EXPLORATION OF RARE-EARTH ION TRANSITIONS AND HOST MATERIALS FOR SPECTRAL HOLE BURNING APPLICATIONS AND QUANTUM INFORMATION SCIENCE

by

Aaron Daniel Marsh

A dissertation submitted in partial fulfillment

of the requirements for the degree

of

Doctor of Philosophy

in

Physics

MONTANA STATE UNIVERSITY

Bozeman, Montana

July 2021

ACKNOWLEDGEMENTS

I am grateful to acknowledge all those whom I have worked with to make the work presented here possible. First, I must thank my co-advisors Dr. Rufus Cone and Dr. Charles Thiel for their expertise, guidance, and the opportunity to work in the lab; there is no way to adequately express their contributions to every part of this work. I was also very excited to be selected to be a part of QISE-NET and the resulting NSF Triplet with Montana Instruments and Dr. Josh Doherty. Alexander Bengtsson of Dr. Stefan Kröll's group at Lund University was instrumental in the lab work presented in chapter 3. Everyone in the Cone-Thiel Rare Earth Spectroscopy Group is very happy with his enthusiasm, intelligence, and intuition and was pleased to conduct research with him during his visit. Dr. Josh Slater of Dr. Wolfgang Tittel's group at TU Delft visited us for the study presented in six. His energy and insights in and out of the lab made that challenging project not only possible, but also turn out very well. Dr. Shermane Benjamin and Dr. John Neumeier were both critical in the crystal growth presented in chapter 5 and taught the author how to prepare vacuum sealed quartz tubes. Shermane and John were both wonderful to interact and work with and generously provided materials and technical assistance. I am also very pleased to have worked with my fellow students and PhD's in the lab, including Tino Woodburn, Kyle Olson, Dr. Thomas Rust, Adam Olivera, Dr. Thomas Böttger, Dr. Rose Ahlefeldt, and many others. Without all of them, the work would have been impossible. Additionally, I am indebted to Normal Williams for his expertise and assistance in the machine shop and the construction of apparatus. Finally, my wife Sarah has been my bedrock through grad school, during both the moments of triumph and disaster. This thesis is as much hers as it is mine. Likewise, all my family has been an endless wellspring of support and motivation.

TABLE OF CONTENTS

1. INTRODUCTION 1

Essential Concepts 8
The Study of Rare Earths 8
Overview of Electronic Structure 10
Kramers Ions 12
Linewidths, Coherence, and Lifetimes 13
Inhomogeneous Broadening 14
Bloch Sphere and Bloch Equations 15
Symmetry 18
Units 23

2. CHARACTERIZATION OF CRYOSTATS FOR QUANTUM INFORMATION SCIENCE RESEARCH WITH RARE-EARTH DECOHERENCE 25

Quantum Information Science Cryostats 26
Measurement Techniques 29
Photon Echoes 29
Stark Absorption Spectroscopy 34
Zeeman Absorption Spectroscopy 35
Experimental Setup 36
Samples 36
Sample Thermometry and Mechanical Isolation – Photon Echoes 37
Magnetism – Zeeman Spectroscopy 39
Results 40
Photon Echoes in the C_2 Cryostation 40
Photon Echoes in the xp100 41
Static Stress Effects 44
Permanent Magnet Integration 46
Conclusion 49

3. SUPPRESSION OF NON-RADIATIVE RELAXATION IN TRIVALENT THULIUM-DOPED LOW-DEBYE TEMPERATURE HOSTS FOR OXYGENATION-SENSITIVE ULTRASOUND-OPTICAL TOMOGRAPHY 52

Ultrasound Optical Tomography and Rare Earths 53
Experimental 59
Spectral Holeburning: Experiment Primer 63
Results 67

TABLE OF CONTENTS CONTINUED

Tm^{3+}:CaF_2 67
Tm^{3+}:BaY_2F_8 69
Tm^{3+}:$YLiF_4$ 70
Tm^{3+}:LaF_3 70
Tm^{3+}:KPb_2Br_5 81
Discussion 82
Conclusion 84

4. DECOHERENCE AND MAGNETISM OF THULIUM-DOPED LANTHANUM TRIFLUORIDE FOR ULTRASOUND-OPTICAL TOMOGRAPHY 86

Introduction 86
Experimental 88
Zeeman Spectral Holeburning: Experiment Primer 89
Enhanced Nuclear Zeeman Effect 93
Optical Coherence of Tm^{3+}:LaF_3 94
Persistent Spectral Hole Burning 96
Spin Lattice Relaxation 97
Enhanced Nuclear Zeeman Effect 100
Quadratic Zeeman Effect 103
Discussion 104
Homogeneous Linewidth and Filter Simulations 106
UOT System Design 109
Conclusion 109

5. GROWTH AND SPECTROSCOPY OF RARE-EARTH DOPED ALKALI LEAD HALIDES FOR TELECOM BAND SIGNAL PROCESSING, QUANTUM INFORMATION, AND LASER CHARACTERIZATION 111

Introduction 112
Experimental 115
Samples 115
Apparatus and Methods 117
Crystal Growth 120
Homemade Littrow Laser Design 126
Spectroscopy of Pr^{3+}:$RbPb_2Br_5$ 128
Absorption 128
Site Selective Spectroscopy 130
Time-Resolved, Gated Spectral Hole Burning 132
Time Resolved Fluorescence 138
Photon Echoes 143

TABLE OF CONTENTS CONTINUED

Fluorescence Spectrum 148
Spectroscopy of Tm^{3+}:KPb_2Br_5 149
Discussion 153
Conclusions 158

6. INVESTIGATION OF THE TELECOM $^3F_4 \Leftrightarrow {}^3H_4$ TRANSITION IN TRIVALENT THULIUM FOR THE DEVELOPMENT OF EXCITED STATE TRANSITIONS FOR CLASSICAL AND QUANTUM SIGNAL PROCESSING 159

Introduction 160
Experimental 164
Results 166
White Light Absorption 170
Fluorescence Spectra 173
Laser Absorption 176
Time Resolved Fluorescence 177
Excited State Spectral Hole Burning 179
Discussion 180
Conclusion 181

7. SUMMARY AND CONCLUSIONS 182

REFERENCES CITED 185

APPENDIX 202

Modeling the Tm^{3+}:LaF_3 Energy Level System 203
Population Transfer Efficiency Expression 204
Absorption profile 205

LIST OF TABLES

Table 1. The character table of the octahedral group *O* 21

Table 2. A character table of the full rotation group under the listed symmetry operations. 22

Table 3. Compatibility table of the octahedral symmetry group *O* with the full rotation group 22

Table 4. Comparison of host crystals 59

Table 5. Summary of the $^3F_3$ survey results 67

Table 6. Observed linecenters of $^3H_6 \Leftrightarrow {}^3F_3$ transitions in Tm^{3+}:BaY_2F_8 with laser absorption at 3K. 69

Table 7. Observed energy levels from absorption and fluorescence 74

Table 8. Energies of side holes and antiholes in a spin-1/2 system 92

Table 9. Structural crystal properties of KPb_2Br_5 and $RbPb_2Br_5$ 117

Table 10. Crystal growth parameters used for all materials grown. 123

Table 11. Summary of spectroscopy of $^3F_3$ 131

Table 12. Observed energy levels from unpolarized fluorescence measured from $^3F_3$ in the sample of 0.1% Pr^{3+}:RPB 149

Table 13. Observed $^3F_3$ levels of Tm^{3+}:KPb_2Br_5. 151

Table 14. Observed energy levels in absorption and fluorescence of the $^3H_6$ and $^3F_4$ manifolds of Tm^{3+}:$YAlO_3$ 168

Table 15. Observed energy levels in absorption and fluorescence of the $^3H_5$ and $^3H_4$ manifolds of Tm^{3+}:$YAlO_3$. 169

LIST OF FIGURES

Figure 1. Highlights of the rare-earth elements in the periodic table 2

Figure 2. Sample of $RbPb_2Br_5$ doped with the lanthanide Pr^{3+} 5

Figure 3. Splittings of the rare-earth manifolds 12

Figure 4. Inhomogeneously broadened absorption 15

Figure 5. Bloch sphere representation 18

Figure 6. Schematic of a two-pulse photon echo experiment 31

Figure 7. Example traces of Rabi oscillations measured in 0.1% Pr^{3+}:$RbPb_2Br_5$ at 1.6K on the $^3H_4 \Leftrightarrow {}^3F_3(1)$ transition of site 4 34

Figure 8. Basic laser absorption experiment schematic 35

Figure 9. An example of the 1% Tm^{3+}:YGG mounting arrangement. A copper clip screwed into the mount lightly presses the crystal into the mount, with the interfaces filled with silver paint 38

Figure 10. Photon Echoes from the lowest to lowest transition of $^3H_6$ to $^3H_4$ in 1% Tm^{3+}:YGG in the C_2 Cryostation 42

Figure 11. Two-pulse photon echo decays from the lowest-to-lowest transition of $^3H_6 \Leftrightarrow {}^3H_4$ in 1% Tm^{3+}:YGG in the prototype xp100 cryostat 43

Figure 12. Temperature dependence of the homogeneous linewidth of the lowest to lowest transition of $^3H_6 \Leftrightarrow {}^3H_4$ in 1% Tm^{3+}:YGG in the prototype xp100 cryostat 44

Figure 13. Measurements on the $^4I_{13/2} \Leftrightarrow {}^4I_{15/2}$ telecom transition (~1538.8 nm) in Er^{3+}:YSO 46

Figure 14. Boltzmann populations of Zeeman levels versus temperature of 0.02% Er^{3+}:YSO 48

Figure 15: Schematic example of a UOT system using spectral holeburning (SHB) detection 55

Figure 16. Modifying the Debye density of states 57

Figure 17: Approximate energy level structure of Tm^{3+} in LaF_3 58

LIST OF FIGURES CONTINUED

Figure 18. Spectral holeburning concept 63

Figure 19. Spectral Holeburning experiment schematic 66

Figure 20. Time resolved fluorescence decay of the $^3F_3$ level in the C_{4V} site in Tm^{3+}:CaF_2. 68

Figure 21. Time resolved fluorescence decay of the $^3F_3$ level in the C_{3V} site in Tm^{3+}:CaF_2. 69

Figure 22. Time resolved fluorescence decay of the $^3F_3$ level in Tm^{3+}:BaY_2F_8. 70

Figure 23. Broadband polarized absorption spectra of Tm^{3+}:LaF_3 at 4.7 K 72

Figure 24. Fluorescence spectrum of Tm^{3+}:LaF_3 at 4.3 K 73

Figure 25: Laser absorption for Tm^{3+}:LaF_3 at 4.0 K 75

Figure 26: Temperature dependence of the lowest to lowest absorption of $^3F_3$ and the comparison of the Raman and direct process models 76

Figure 27: FID in Tm^{3+}:LaF_3, measured at 4 K 79

Figure 28: Time-resolved transient hole area decay of Tm^{3+}:LaF_3 81

Figure 29. Time-resolved transient fluorescence decay of the lowest level of $^3F_3$ of Tm^{3+}:LaF_3 82

Figure 30. Example of spin-½ system split by magnetic fields, and the depiction of the hole and antihole structure that emerges in Zeeman SHB 92

Figure 31: Temperature dependence of Tm^{3+}:LaF_3 homogeneous linewidth 95

Figure 32: Example dependence of the “slow” persistent spectral hole lifetime burned into the $^3H_6 \Leftrightarrow {}^3F_3(1)$ transition in a field of 100 mT in Tm^{3+}:LaF_3 on temperature 97

Figure 33. Processes of spin-lattice relaxation 99

Figure 34: Dependence of the persistent hole relaxation rate ($1/T_1$) burned into the $^3H_6 \Leftrightarrow {}^3F_3$ transition in Tm^{3+}:LaF_3 on applied field 100

Figure 35: Split rates of the observed side hole and antihole structures of 0.5% Tm^{3+}:LaF_3 102

LIST OF FIGURES CONTINUED

Figure 36: Quadratic shift of the holeburning spectrum in Tm^{3+}:LaF_3, burned into the lowest to lowest transition of $^3H_6 \Leftrightarrow {}^3F_3(1)$ 104

Figure 37. White light absorption spectrum of $^3H_6 \Leftrightarrow {}^3H_4(1)$ at 4.7 K 105

Figure 38: Simulated absorption profiles of the first and last 0.1 mm thick slice of the crystal 108

Figure 39. The $^3H_4 \Leftrightarrow {}^3F_3$ transition of Pr^{3+} and adjacent manifolds 115

Figure 40. Examples of crystal growth results, with pieces of 0.2% Tm^{3+}:KPb_2Br_5 and of 0.1% Pr^{3+}:$RbPb_2Br_5$ 117

Figure 41. Homemade Bridgman growth system 122

Figure 42. Homemade modular Littrow laser in use 127

Figure 43. Liquid helium temperature absorption of 0.1% Pr^{3+}:$RbPb_2Br_5$ 129

Figure 44. Laser absorption of the lowest-to-lowest transitions 0.1% Pr^{3+}:$RbPb_2Br_5$ at 3.5 K 130

Figure 45. SHB on the ions designated site 1 of the $^3H_4 \Leftrightarrow {}^3F_3(1)$ transition of 0.1% Pr^{3+}:$RbPb_2Br_5$ at 1584.458 nm at 1.6 K. 134

Figure 46. SHB on the ions designated site 2 of the $^3H_4 \Leftrightarrow {}^3F_3(1)$ transition of 0.1% Pr^{3+}:$RbPb_2Br_5$ at 1584.356 nm at 1.6 K. 135

Figure 47. SHB on the ions designated site 3 of the $^3H_4 \Leftrightarrow {}^3F_3(1)$ transition of 0.1% Pr^{3+}:$RbPb_2Br_5$ at 1584.239 nm at 1.6 K. 136

Figure 48. SHB on the ions designated site 4 of the $^3H_4 \Leftrightarrow {}^3F_3(1)$ transition of 0.1% Pr^{3+}:$RbPb_2Br_5$ at 1584.065 nm at 1.6 K. 137

Figure 49. SHB on the ion designated site 4 of the $^3H_4 \Leftrightarrow {}^3F_3(2)$ transition of 0.1% Pr^{3+}:$RbPb_2Br_5$ at 1584.458 nm at 1.6 K. 138

Figure 50. Time resolved fluorescence from $^3F_3$ in site 1 of 0.1% Pr^{3+}:RPB at 3.3 K. 139

Figure 51. Time resolved fluorescence from $^3F_3$ in site 2 of 0.1% Pr^{3+}:RPB at 3.3 K. 140

Figure 52. Fluorescence from $^3F_3$ in site 3 of 0.1% Pr^{3+}:RPB at 3.3 K. 141

LIST OF FIGURES CONTINUED

Figure 53. Fluorescence from $^3F_3$ in site 4 of 0.1% Pr^{3+}:RPB at 3.3 K. 142

Figure 54. Modulated two-pulse photon echoes on the ions designated site 1 of the $^3H_4 \Leftrightarrow {}^3F_3(1)$ transition of 0.1% Pr^{3+}:RPB at 1584.458 nm at 1.6 K..... 144

Figure 55. Modulated two-pulse photon echoes on the ions designated site 2 of the $^3H_4 \Leftrightarrow {}^3F_3(1)$ transition of 0.1% Pr^{3+}:RPB at 1584.337 nm at 1.6 K..... 145

Figure 56. Modulated two-pulse photon echoes on the ions designated site 3 of the $^3H_4 \Leftrightarrow {}^3F_3(1)$ transition of 0.1% Pr^{3+}:RPB at 1584.236 nm at 1.6 K..... 146

Figure 57. Modulated two-pulse photon echoes on the ions designated site 4 of the $^3H_4 \Leftrightarrow {}^3F_3(1)$ transition of 0.1% Pr^{3+}:RPB at 1584.065 nm at 1.6 K..... 147

Figure 58. Fluorescence spectra of 0.1% Pr^{3+}:RPB at 10K to identify the structure of the ground manifold..... 148

Figure 59. White light absorption spectra of 0.2% Tm^{3+}:KPb_2Br_5..... 150

Figure 60. Examples of traces of (left) ungated and (right) gated spectral holeburning in Tm^{3+}:KPb_2Br_5..... 152

Figure 61. Spectral hole decay of trenches burned into the $^3H_6 \Leftrightarrow {}^3F_3(1)$ transition of Tm^{3+}:KPb_2Br_5..... 153

Figure 62. Energy level diagram of Tm^{3+} 163

Figure 63. Pumping schematic of the double-pump time-resolved fluorescence measurement 166

Figure 64. Unpolarized absorption spectrum of $^3H_6 \Leftrightarrow {}^3H_5$ in Tm^{3+}:$YAlO_3$ at 4K..... 171

Figure 65. Unpolarized absorption spectrum of $^3H_6 \Leftrightarrow {}^3H_4$ in Tm^{3+}:$YAlO_3$ at 4K..... 172

Figure 66. Unpolarized fluorescence spectra of $^3F_4 \Leftrightarrow {}^3H_6$ in Tm^{3+}:$YAlO_3$ at 10K 173

Figure 67. Unpolarized fluorescence spectra of $^3H_4 \Leftrightarrow {}^3H_6$ in Tm^{3+}:$YAlO_3$ at 10K..... 174

Figure 68. Unpolarized fluorescence spectra of $^3H_4 \Leftrightarrow {}^3F_4$ in Tm^{3+}:$YAlO_3$ at 10K 175

Figure 69. Unpolarized laser absorption of the $^3F_4 \Leftrightarrow {}^3H_4$ transition at 4K 176

Figure 70. Double-pumped fluorescence decay of 0.1% Tm^{3+}:$YAlO_3$. 178

LIST OF FIGURES CONTINUED

Figure 71. Ungated SHB spectrum burned onto the ~1451 nm telecom $^3F_4 \Leftrightarrow {}^3H_4$ transition at 4K..... 179

Figure 72: Level structure used in the filtering model..... 204

ABSTRACT

Due to their capacity for generating and manipulating light, the rare-earths are a foundational part of many cutting-edge technologies, ranging from lighting to quantum communications. Optical applications based on rare-earth doped materials are restricted to their transition energies. There are large bands, including the telecom window, where available rare-earth transitions typically have poor properties at liquid helium temperatures. The limitations are determined by the fundamental interactions between rare-earth ions and their host materials; comprehension of the interactions can be leveraged to significantly improve the properties of rare-earth quantum states.

Three unexplored rare-earth optical transitions are investigated in this thesis: the Tm^{3+} $^3H_6 \Leftrightarrow {}^3F_3$ at ~690 nm, the Pr^{3+} $^3H_4 \Leftrightarrow {}^3F_3$ at ~1584 nm, and the Tm^{3+} $^3F_4 \Leftrightarrow {}^3H_4$ at ~1451 nm. The first transition suppresses non-radiative relaxation through engineering of the host material phonon spectrum. The $^3F_3$ lifetime is extended to ~100 μs in Tm^{3+}:KPb_2Br_5. The material Tm^{3+}:LaF_3 is also prepared for high-contrast spectral filtering in ultrasound-optical medical imaging sensitive to blood oxygenation at ~690 nm. Narrow 380 kHz holes are burned; simulations of hole burning indicate that ~60 dB of filtering contrast at ~3MHz is possible. Likewise, non-radiative relaxation is suppressed on the Pr^{3+} transition at ~1584 nm in the low-phonon energy host $RbPb_2Br_5$. Four sites are revealed, with ~2-5 GHz spectrally resolved inhomogeneous broadenings, ~0.5-1 ms T_1 lifetimes, pseudoquadrupole level storage, and ~750 ns coherence times. This material is discussed for use as an L-band quantum memory. The excited state transition of Tm^{3+} at ~1451 nm is then explored for quantum memories. High-resolution spectroscopy finds ~1 GHz inhomogeneous broadenings, ~6 ms lifetimes, and laser-limited ~30 MHz holes are burned. Techniques for measuring the properties of excited state transitions are described. Throughout, experimental methods and applications demonstrate the close relationship between lanthanide research and devices. Rare-earth doped crystals are used as an all-optical, high-resolution sensor package for characterizing cryostats in situ, and spectral hole burning characterizes laser performance as a real-time, ~1 MHz resolution spectrum analyzer. The exploration of rare-earth transitions is found to enable new research and new applications, with many other transitions yet to be explored.

CHAPTER ONE

INTRODUCTION

The rare-earth elements have played an ever-increasing role in modern technology, and are referred to as the vitamins of modern science and industry [1]. The term rare-earth or lanthanide refers to any of the elements belonging to the first row of the f-block of the periodic table, shown in fig. 1, as well as scandium and yttrium. They are found in high-grade permanent magnets, metal alloys, electric motors, abrasives, batteries, displays, consumer electronics, catalytic converters, phosphors and lighting, lasers, magnetic resonance imaging (MRI) and medical imaging devices, high-temperature superconductors, optics, quantum memories, and many, many other places [1-4]. One critical use of rare earths is in erbium-doped optical amplifiers, which regenerate optical signals to span long-haul fiber-optic internet links, thus enabling the modern internet. There is also ~1 kg of rare-earths in the modern automobile. While this is only a small fraction of the overall mass, the rare-earths used in its construction are not substituted with any other elements without consequence or even at all; the same can be said for the overwhelming majority of other applications of lanthanides. Summarily, rare-earth elements are essential to modern life and science.

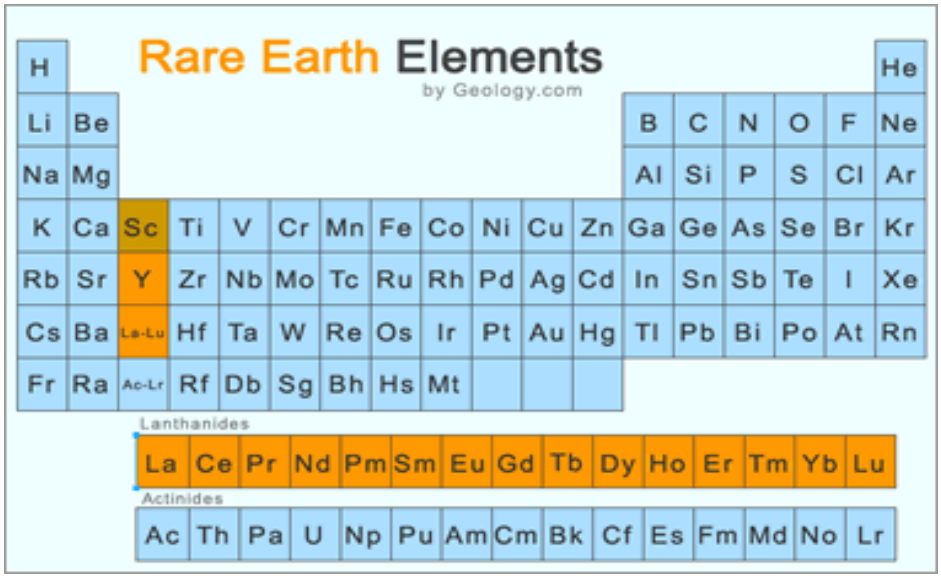

Figure 1. Highlights of the rare-earth elements in the periodic table, from Geology.com [1].

One way in which lanthanides have greatly impacted technology is through their luminescence properties. Rare-earth elements are particularly suited for the creation and manipulation of light. These properties are due to an electronic structure that limits their interaction with the surrounding environment, even when included in a solid. As a direct consequence, they have found extensive application in every imaginable form of lighting, from common displays, lights, and phosphors [1, 5-9], to high-tech solid-state lasers and optical amplifiers [2, 4, 10-29], to state-of-the-art signal processing, quantum memories and transducers in quantum communication [12, 18, 28, 30-41]. Energetic scientific research continues on all of these categories, but quantum information science (QIS) and quantum communications motivate the most intensive studies of rare-earths at temperatures at and below 4 Kelvin. Quantum communication stands to provide completely secure internet links between nodes and network quantum computers. However, entangled photons cannot be amplified without collapsing the quantum state, and so long-haul quantum internet links must be constructed with quantum

repeaters. Repeaters rebroadcast stored photons on demand to distribute entanglement from one terminal to another, and the core element of the quantum repeater is the quantum memory, which stores the photon's quantum state. Extensive research on rare-earth memories has been conducted. Similarly, by virtue of having both excellent microwave and optical transitions, rare-earths are being studied for microwave-optical quantum transducers. The transducer converts microwave photons from superconducting qubits into optical photons, that can be transmitted long distances with quantum repeaters, or visa-versa, to connect one quantum computer to another. Another strong motivation in rare-earth research is spatial-spectral holography and spectral hole burning (SHB) devices, which enable all-optical signal processing, filtering, and frequency references, by leveraging the spectral properties of rare-earth elements [12, 17-20, 28, 36, 37, 41-68]. In all these cases and more, the principal aims are to study the atomic-scale physics of rare-earth ions, but also to engineer the cutting-edge technologies of tomorrow by implementing data-processing protocols with them [64, 69-71]. Absolutely essential to these efforts are the materials under study, whose extensive suite of features must be mapped out to fully comprehend the atomic environment. An essential parameter is the coherence time, T_2, which characterizes the exponential rate at which the phase of a quantum state stored with rare-earths is corrupted. The parameter space that determines T_2 is expansive, providing ultra-sensitive exposure to many dynamic processes in the atomic environment; the physical insight that studies of rare-earth coherence provides cannot be overstated. Consequently, understanding of rare-earth doped materials has exploded in large part due to the invention and subsequent development of the laser, high-resolution spectroscopic instruments, and the effort and intelligence of the research community. Research on rare-earths has enabled quantum states to be

stored in rare-earths out to six hours in Eu^{3+}:Y_2SiO_5, indicating an impressive level of maturity in the field [5, 19, 32, 72-76].

Practical applications with rare-earths are restricted to their optical transition energies, which do not always coincide with requirements or aim, but many modifications can be made to shift energies or pioneer new transitions for use. An excellent example is found in ultrasound-optical tomography (UOT), a non-invasive medical imaging technique in which an ultrasound beam modulates laser light illuminating the human body [28, 37, 38, 40, 41, 50, 77, 78]. Ideally, the laser light used would be at the lowest-loss wavelengths for the human body to maximize penetration depth and blood oxygenation sensitivity. For this application, SHB optical filters are needed to adequately filter the strong carrier from the weak ~5 MHz sideband produced by the ultrasound tissue modulation of incident laser light. An SHB filter near ~700 nm in the tissue-optical window would significantly improve device performance, and the $^3F_3 \Leftrightarrow {}^3H_4$ transition of trivalent thulium is at the correct wavelength. However, the $^3F_3$ state has not been used because it generally possesses a short lifetime (<1 μs) due to non-radiative relaxation via phonons to nearby energy levels. In this thesis, this fast relaxation pathway is suppressed through host-material engineering and modification of the phonon spectrum. Consequently, the transition becomes fluorescent and good hole-burning properties are obtained. The same powerful ideas can be applied to a very similar problem, which is the dearth of suitable rare-earth optical transitions in the telecom window. The telecom window ranges from about 1260 nm in the O-band to about 1675 nm in the U-band [79], with the more ideal lower loss bands between 1460-1625 nm for long-distance transmissions. Only the lanthanide erbium possesses a consistently “good” transition $^4I_{15/2} \Leftrightarrow {}^4I_{13/2}$ for SHB or QIS applications, and is found between approximately 1514-

1545 nm [64], depending on the host. This restricts many system design choices, especially when seeking to multiplex signals across the telecom window. In turn, this leads to more complicated schemes of converting light from the appropriate transmission wavelengths to the device operating wavelength, or simply working in the device band. These approaches inevitably increase device loss, error rates, and complexity, and the tolerance for any of these in the single-photon case is very low already. These frustrations can be overcome though by realizing there are numerous rare-earth transitions all across the telecom window – one only needs to understand their basic limitations through careful study and manipulate them. In this thesis, the Pr^{3+} $^3H_4 \Leftrightarrow {}^3F_3$ and the Tm^{3+} $^3F_4 \Leftrightarrow {}^3H_4$ excited state transitions were pioneered due to their presence at ~1580 nm and ~1450 nm, respectively. Non-radiative relaxation on the praseodymium transition was suppressed to the point of obtaining measurable optical coherence, while holes were burned on the excited state transition of thulium with innovative spectroscopic techniques.

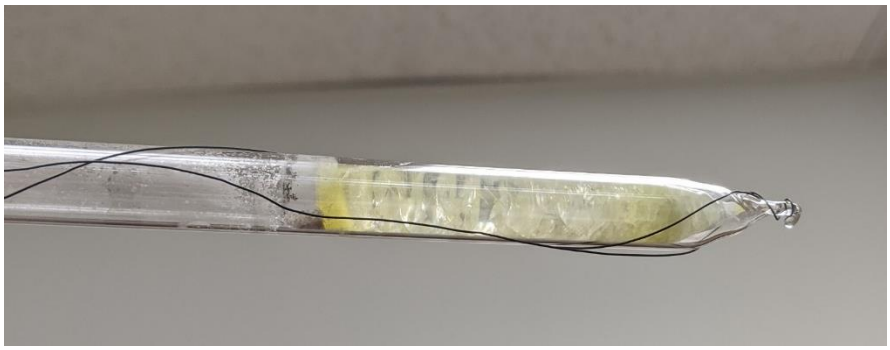

Figure 2. Sample of $RbPb_2Br_5$ doped with the lanthanide Pr^{3+}, grown in-lab for low-temperature spectroscopy, with great assistance from Dr. Shermane Benjamin and Dr. John Neumeier in working with preparing and sealing the quartz ampules.

A closely related problem in the modern day is the expense of helium [80]. Essential research will undoubtedly continue despite this, but this situation negatively affects many researchers by constraining their ability to test new ideas or conduct routine work in a cost-effective manner.

Closed-cycle cryostats are one solution for economical helium use while still obtaining liquid helium temperatures (<4K). Questions remain as to how effective and reliable these systems are for QIS-level research, in which experiments are very sensitive to their conditions. Experimental artifacts are very easy to introduce in many ways. However, the levels of extreme sensitivity provided by rare-earth elements to their dynamic macroscopic and microscopic environment can be probed through measurements of their properties. In this thesis, rare-earth doped materials are used as an all-optical, non-contact, in-situ sensor package. Using this sensing suite, a quantitative understanding of the critical issues is developed, aiding in pushing cryostat performance to the levels needed for QIS-grade work.

Overall, there is significant motivation to expand the toolkit of rare-earth optical transitions and develop techniques to explore them. In this thesis, these issues are addressed, and solutions are demonstrated. Practical experimental issues related to closed-cycle cryostats are studied by means of the sensitivity of rare-earths to variations in temperature, magnetic fields, pressures, and vibration in chapter 2. Because the sample environment is viewed with the high resolution provided by lanthanide coherence, technical problems are systematically identified and eliminated in a variety of spectroscopy experiments. This demonstrates a purely optical method for properly preparing cryogenic hardware for QIS research at low temperature. The knowledge gained is applied throughout this work. A survey of the trivalent thulium $^3H_6 \Leftrightarrow {}^3F_3$ transition is undertaken in chapter 3 across materials of decreasing maximum phonon energy, namely, Tm^{3+}:CaF_2, BaY_2F_8, $YLiF_4$, LaF_3, and KPb_2Br_5. Coupling to phonon modes that cause non-radiative relaxation is suppressed by decreasing the Debye frequency. The fluorescence lifetime there is taken from the sub-microsecond regime in Tm^{3+}:CaF_2 all the way to ~100 μs in

Tm^{3+}:KPb_2Br_5. Good hole burning properties are reported in Tm^{3+}:LaF_3 for UOT at ~690 nm. Tm^{3+}:LaF_3 is then focused on in chapter 4, for oxygenation-sensitive UOT on the $^3H_6 \Leftrightarrow {}^3F_3$ transition. The apex of an optical SHB filter performance is determined by sensitively probing its limiting coherence and magnetic properties. Coherence times of 2.7 μs are measured. Spectral hole lifetimes out to ~2 hours are possible in magnetic fields at 4K. Simulations of spectral holes burned into the absorption of $^3H_6 \Leftrightarrow {}^3F_3$ indicate that high-contrast filtering for oxygenation-sensitive UOT and other SHB filtering applications is expected. The alkali lead halides Pr^{3+}:$RbPb_2Br_5$ and Tm^{3+}:KPb_2Br_5 are grown and studied in chapter 5. The principles of suppressing phonon-mediated non-radiative relaxation in more extreme cases are applied. The conventionally non-radiative transition of $^3H_4 \Leftrightarrow {}^3F_3$ at ~1584 nm in Pr^{3+} is shown to have four separate sites in $RbPb_2Br_5$. Their inhomogeneously broadened transitions are 2-5 GHz in width and with ~10 GHz spacings, with each possessing ~0.5-1.0 millisecond T_1 lifetimes and T_2 coherence times of ~750 ns. Zero-field ground-state nuclear storage was observed in hole burning on each, with the hole lifetime of site 4 being measured as long as ~2.25 s. The impact of this material is discussed in the context of QIS and SHB applications at telecommunications wavelengths. Then, Tm^{3+}:KPb_2Br_5 is used to characterize a homemade laser for spectroscopy, by using the hole burning properties of the $^3H_6 \Leftrightarrow {}^3F_3$ transition at ~690 nm as a high-resolution spectrum analyzer. The essential spectroscopic properties of Tm^{3+}:KPb_2Br_5 at liquid helium temperatures are reported. For the purpose of identifying a suitable host for implementing a quantum memories, spectroscopy of the excited state transition of $^3F_4 \Leftrightarrow {}^3H_4$ in Tm^{3+}:$YAlO_3$ is undertaken in chapter 6. The ~30 MHz holes are burned on the ~1 GHz inhomogeneously broadened transition. Time-resolved fluorescence demonstrates long optical lifetimes.

Altogether, three rare-earth optical transitions, Tm^{3+} $^3H_6 \Leftrightarrow {}^3F_3$ at ~690 nm, the Pr^{3+} $^3H_4 \Leftrightarrow {}^3F_3$ at ~1584 nm, and the Tm^{3+} $^3F_4 \Leftrightarrow {}^3H_4$ at ~1451nm, are explored and developed due to their desirable wavelengths. The spectroscopic techniques by which they are explored shown to be practical and of use to general researchers. All these results demonstrate that many unexplored optical transitions of the lanthanides have many interesting phenomena to probe. The information obtained also simultaneously prepares them for use in advanced applications. It is shown that the development of new optical applications is explicitly dependent on fundamental research of new materials. Altogether, the physical insight provided by spectroscopy of lanthanides blazes inroads into previously disbarred regimes.

Essential Concepts

In this section, a brief tour of background topics is undertaken to prime the reader for the following chapters and sections. Experiments and their layouts are discussed in the context that they are made in, within the subsequent chapters.

The Study of Rare Earths

Rare-earths are of variable actual rarity, and it is in fact the difficulty of separating rare-earths from each other, caused by their chemical similarity, that has given them their names and defined their place in history [1, 5, 81]. The first report of rare-earths was made in 1752 by the mineralogist Crondstedt, who found an unusual heavy mineral in a mine near Ryddarhyttan, Sweden. The sample was only accurately identified as a lanthanide mineral in retrospect in 1794, after Gadolin isolated a mixture of lanthanides from another mineral found near the town Ytterby, Sweden. The trend of misidentification continued for the next century as more

lanthanides were separated from each other, usually through extensive fractional recrystallization efforts. Many erroneous claims of new lanthanides were made through the 19th century, and Mendeleev was confounded by the rare-earths in designing the periodic table [3]. Rare-earths were not fully isolated from each other until 1909 (an exception is promethium, which has no stable isotopes), when Bohr correctly placed the fourteen lanthanides in a separate block of the periodic table. Efforts in rare-earths then turned from isolation to purification. This was greatly expedited by the Manhattan project of the second world war, out of which developed chromatographic lanthanide ion-exchange, one of the leading industrial methods of modern rare earth isolation [1, 5].

Spectroscopy of the atomic transitions of rare-earths paralleled their increasing refinement and the development of quantum mechanics. Measurements were made on rare-earths as early as 1866 by Bunsen, who observed unusually sharp transitions and strong luminescence. After quantum mechanics was developed, the consistent spectra of rare-earths were interpreted as 4f intra-shell transitions by Bethe, Kramers, and Becquerel. Van Vleck explained the parity-forbidden f^N-f^N transitions due to small admixtures of 5d into the nominally 4f configuration [82]. Researchers from this time also realized that the cause for the consistent spectra from host to host was because the smaller radius of the unfilled, optically-active 4f shell relative to the core shells limited its role in chemical bonding [83]. The theoretical framework laid down by Racah and others enabled quantitative analysis of rare-earth spectra in the 1940’s and 50’s. That work culminated in independent publications of Judd and Ofelt in 1962 [82, 84, 85], the aim of which was to predict and describe lanthanide intensities. The means to calculate the wavefunctions based on experimental observations was carried out by Dieke, Carnall, Crosswhites, Wybourne,

and others. Expansive maps rare-earth optical transitions, particularly in the host material LaF_3, continue to serve as a guide of rare-earth research into the modern day [75, 86, 87]. From this point in history, rare-earth research rapidly spreads and subdivides into many areas, as the invention of tunable lasers enabled many new measurements to be made by many researchers, such as Macfarlane and Shelby [19, 88-91], with many applications motivating yet more exploration.

Overview of Electronic Structure

The unfilled 4f shell of rare-earths is the source of their luminescence properties, in large part because the average radius of the 4f wavefunctions are predominantly contained within the core shells 5s, 5p, 3d, and 4d [83]. Since the ligands of the host material ions have little overlap with 4f wavefunctions, the 4f shell experiences the environment as a weak perturbation compared to intraatomic effects such as spin-orbit coupling. The net effect of this structure is a class of ions that behave close to the free ion even when in a solid and quantum states.

Additionally, the f^N-f^N transitions should be forbidden by parity, as the angular momentum of the state remains unchanged [92], but weak configurational mixing between $4f^N$ and $4f^{N-1}5d$ enables forced-electric dipole transitions with oscillator strengths on order of magnetic-dipole transitions [83]. By Fermi's golden rule, the small transition moment between those states slows the rate of optical relaxation [92]:

$$w_{i\to \mathrm{f}} = \frac{2\pi}{\hbar}|V_{if}|^2\rho(E_f) \tag{1}$$

In eq. (1), the transition rate between states i and f is proportional to density of final states $\rho(E_f)$ and the square of the matrix element V_{if} that couples the initial and final states. The Hamiltonian for rare-earths is given eq. (4), in which the forced electric dipole transition is encapsulated and

then expressed in eq. (1) through the matrix element V_{if}. This perspective would lead one to assume that all the excited states of rare-earths have ~100 μs – 10 ms T_1 lifetimes. However, rare-earth ions doped into crystals can relax by the multi-phonon process. The Hamiltonian of that system is given by Orlovskii et al. [93] and Ermeneux et al. [94]:

$$\hat{H} = \hat{H}_i + \hat{H}_L + \hat{H}_{e-L} \tag{2}$$

In eq. (2), the Hamiltonian of the ion is $\hat{H}_i$, the Hamiltonian of the lattice is $\hat{H}_L$, and the rare-earth electron-lattice interaction is $\hat{H}_{e-L}$. Because rare-earth 4f shell is weakly coupled to the lattice, the term $\hat{H}_{e-L}$ can be expanded in a Taylor series for small ion displacements u from equilibrium:

$$\hat{H}_{e-L} = \hat{V}^{(0)} + \hat{V}^{(1)} \cdot u + \hat{V}^{(2)} \cdot u^2 + \ldots \tag{3}$$

In eq. (3), $V^{(n)} = (\frac{\partial \hat{H}_{i-L}}{\partial r^n}/n!)_{r=R_0}$ depends on just the electron coordinates r and the equilibrium ion position R_0. There are several approaches to calculating the non-radiative relaxation rate from eqs. (1)-(3). In the linear relaxation scheme, only the linear term $V^{(1)} \cdot u$ is used to calculate the n-phonon process, which results in the classic non-radiative decay rate of $w = C \cdot e^{-\alpha \cdot \Delta E}$ [94]. The parameters C and α are particular to the host material, temperature, and number of phonons, while ΔE is the energy gap. States dominated by non-radiative relaxation will rapidly decay in as little as nanoseconds [93-96]; the radiative rate is roughly equal to the non-radiative rate when $\Delta E \sim 5\hbar\omega_D$, where ω_D is the Debye frequency. However, the non-radiative rate can be throttled with the proper selection of host material, as will be seen in chapter 3 and 5.

The lanthanide energy levels are split by the multi-electron Hamiltonian:

$$\hat{H} = \hat{H}_0 + \hat{H}_{e-e} + \hat{H}_{S-O} + \hat{H}_{Crystal} + \ldots \tag{4}$$

In eq. (4), $\widehat{H}_0$ describes the interaction of the central electric field due to the nucleus with the bound electrons and their kinetic energy, $\widehat{H}_{e-e}$ describes the mutual electron-electron Coulomb interactions, $\widehat{H}_{S-O}$ encapsulates all of the spin-orbit couplings, and $\widehat{H}_{Crystal}$ describes the crystal field, that is, the interaction of the host ions with the material [83, 97]. Ellipses are left to indicate that even more interactions, such as the Zeeman, hyperfine, and nuclear quadrupole interactions and others are possible, but the first few terms are of interest for now. The truncated Hamiltonian gives rise to level structure described by fig. 3.

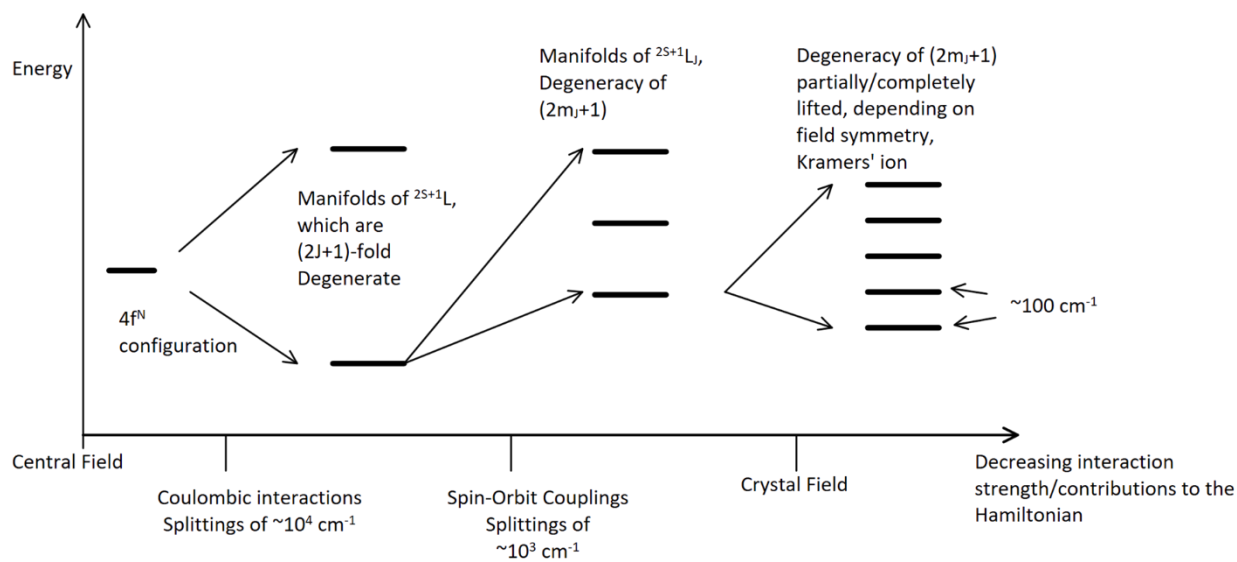

Figure 3. Splittings of the rare-earth manifolds by additional interactions. Crystal field levels are directly observed in experiments. Further degeneracies caused by Kramers ions, nuclear levels, or certain crystal field symmetries can be lifted with additional interactions [83].

Intermediate coupling levels produced from eq. (4) are labeled with the dominant $^{2S+1}L_J$ state, where S is the total spin angular momentum, L is the total orbital angular momentum, and J is the total angular momentum [74, 83]. The symbols used are from the Russel-Saunders (or L-S) angular momentum coupling limit. Since the central field interaction and spin-orbit couplings in rare-earths are of the same order, S and L are not good quantum numbers. The more accurate

intermediate angular momentum coupling scheme derives from the L-S limit, and so the labels $^{2S+1}L_J$ should be regarded with the implicit understanding that they are actually linear combinations of SLJ wavefunctions, with the leading contribution serving as the label [83].

Kramers Ions

Kramers ions possess an odd number of electrons. These ions therefore possess half-integer spins S (even values of 2S+1), which by time reversal symmetry requires that the crystal field levels be at least doubly degenerate [83, 98, 99]. For the trivalent rare-earths, cerium, neodymium, samarium, gadolinium, dysprosium, erbium, and ytterbium all have unsplit crystal field levels absent a magnetic field. Conversely, praseodymium, promethium, europium, terbium, holmium, and thulium can have singlet levels. The distinction between Kramers and non-Kramers ions has important implications, not the least of which is the scale of the magnetically mediated decoherence and the associated spin transitions. In many cases, Kramers ions require applied magnetic fields to achieve good hole burning and coherence properties, leading many researchers to naturally gravitate toward the logistically simpler non-Kramers ions [67]. However, many excellent properties have been measured on many Kramers ions, with erbium being a principal focus due to its $^4I_{15/2} \Leftrightarrow {}^4I_{13/2}$ telecom wavelength transition [17, 20, 45, 46, 65, 66, 68, 100-104].

Linewidths, Coherence, and Lifetimes

Optical resonances, where ions are driven by photons or emit photons to transition from one state to another, have a finite width called the homogeneous linewidth Γ_h. The relationship between linewidths and lifetimes of atomic states is inextricably coupled through Fourier relations and quantum mechanics, and is expressed in the following equations [92, 105]:

$$\Gamma_h = \frac{1}{\pi T_2} = \frac{1}{2\pi T_1} + \frac{1}{\pi T_2'} \tag{5}$$

In eq. (5), Γ_h is the homogeneous atomic linewidth, T_1 is lifetime of the excited state, the pure dephasing time T_2', which encapsulates many effects [17, 67, 74, 101, 104, 106-109], and T_2 is the overall coherence time of the transition [60]. The coherence time bears that name because it parameterizes the rate at which the precessing phase of the atomic transition moment associated with the transition is perturbed after being prepared in an experiment. The coherence time T_2 fundamentally limits the homogeneous linewidth Γ_h. In turn, T_2 is fundamentally limited by the T_1 lifetime by the inequality $T_2 \leq 2T_1$, which can be seen by taking the limit of the pure dephasing time T_2' to infinity. Ultimately, effects that lengthen the T_1 and T_2 narrow the transition width Γ_h, and visa-versa for those that broaden it. Broadening mechanisms include phonon absorption, emission, and scattering, spin flips and flip-flops, and far more, all of which can be measured as a snapshot of the dynamic atomic environment. Researchers have subsequently devised many ways to measure coherence, and it is of paramount importance in QIS. The most reliable and informative of these used for rare-earth doped materials is the photon echo, which will be discussed in more detail in chapter 2 [110-112]. Coherence times in rare-earths range from short (<1 μs or even ~1 ps) to hours long, depending on the ion, transition, host, and experimental configuration [72].

Inhomogeneous Broadening

The need for photon echoes to measure the homogeneous width Γ_h becomes readily apparent in the presence of inhomogeneous broadening. In the case of rare-earths doped into solids, homogeneous broadening of ions decreases with temperature. At liquid helium temperatures (<4.2K), the regime where SHB and QIS devices operate, the homogeneous linewidths Γ_h are

smaller than the perturbative shifts in the atomic transition energy caused by microscopic variations in the crystal lattice. Additionally, during measurements of the $4f^N$-$4f^N$ transitions, the average effect across all possible perturbations is observed. The result is spectra like that of fig. 4, where homogeneous lines of individual ions are buried in a smooth distribution of other homogeneous lines. More complicated inhomogeneously broadened spectra do arise. The drive to probe the actual atomic properties within the inhomogeneously broadened line evolved many techniques of scientific and practical utility, including spectral hole burning, which is discussed in more detail in chapter 3 [12, 42].

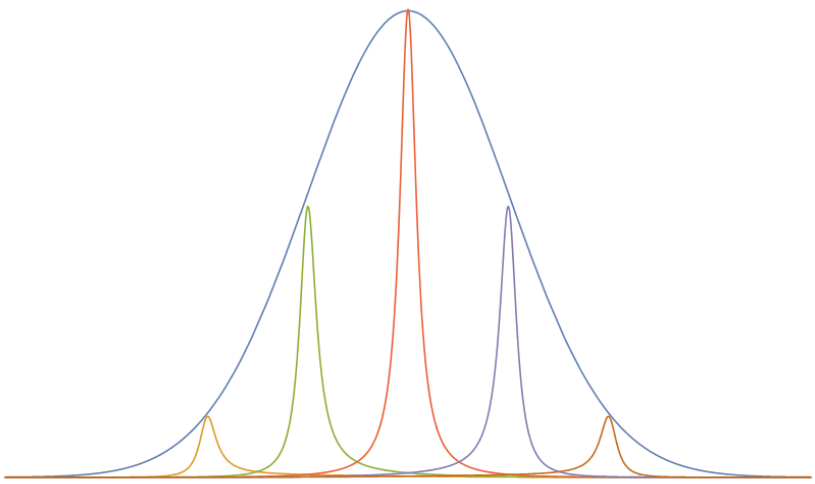

Figure 4. The inhomogeneously broadened absorption of a species of ion doped into a host is due to the microscopic variations of the host material itself.

Bloch Sphere and Bloch Equations

The Bloch sphere, shown in fig. 5, is a powerful conceptual tool for visualizing quantum states prepared in light-matter interaction. Therefore, these concepts underpin any discussion involving rare-earth coherence, especially in the context of spin-wave quantum memories and photon echoes [17, 20, 32, 66, 69, 74, 110, 111, 113-118]. The full quantitative details are not

reproduced here, but the importance is emphasized in that many important experiments and ideas are intuitively understood within this framework, including optical nutation, echoes, dephasing, decoherence, and more.

The evolution of a two-level quantum superposition state under illumination by coherent light is governed by the optical Bloch equations [112, 119]. The optical Bloch equations for a two-level system are written as [120]:

$$\begin{cases} \dot{u} = -\Delta \cdot v - u/T_2 \\ \dot{v} = \Delta \cdot u + \Omega \cdot w - v/T_2 \\ \dot{w} = -\Omega \cdot v + (w - w_0)/T_1 \end{cases} \tag{6}$$

The functions $u(t)$, $v(t)$, and $w(t)$ are linear combinations of elements of the density matrix $\boldsymbol{\rho}(t)$, which itself is from the wavefunctions of a two-level ion interacting with a time-dependent sinusoidal light field $\boldsymbol{E}(t)$. The absorptive function $v(t)$ couples the system to the field $\boldsymbol{E}(t)$ through the transition moment $\hat{p}$, and the dispersive function is $u(t)$. The function $w(t)$ denotes the population difference between the ground and excited states. All three functions are related through conservation of probability: $1 = u^2 + v^2 + w^2$. The Rabi transition frequency is denoted as Ω, the detuning from the resonance frequency is Δ, and the equilibrium population is w_0. Finally, the vector $\mathbf{B} = (u, v, w)^T$ represents the quantum state $|\psi\rangle$ of the system mapped to the Bloch sphere, shown in fig. 5. The solutions to eq. (6) were made by Torrey [105, 121]:

$$x_i(t) = A_i \cdot e^{-a_i t} + [B_i \cdot cos(s_i \cdot t) + \frac{C_i}{s_i} sin(s_i \cdot t)]e^{-b_i t} + D_i \tag{7}$$

where x_i denotes u, v, or w. The constants in eq. (7) depend on Ω, Δ, w_0, T_1, T_2, and the form of $\boldsymbol{E}(t)$. Due to the size and complexity of each constant, and the variety of forms they can take in specific limiting cases, they are not given here explicitly.

The solutions $x_i(t)$ express how a Bloch vector **B** evolves on the Bloch sphere in response to a field $\boldsymbol{E}(t)$, which have the effect of applying "torques" to **B**. Standard pulses applied to the ensemble of $\mathbf{B}_i$ are referred to in fractions of π of phase accumulation of the transition dipole $\hat{p}_i$. For example, when a system is fully relaxed into the ground state, a "π/2" pulse applies a torque to $\mathbf{B}_i$ in the direction of the $\boldsymbol{u}$-axis. The resulting state points along the $\boldsymbol{v}$-axis. The timings and intensities of light needed to generate that exact amount of phase accumulation are discussed in chapter 2. The state then freely evolves, such that $\mathbf{B}_i$ precesses about the $\boldsymbol{w}$-axis at the natural frequency of the transition while decaying back to the ground state exponentially by the T_1 lifetime. If a π pulse is applied at some later time τ, before the state fully decays, the π pulse will flip the entire ensemble over in the Bloch sphere; the pulse has the effect of inverting the direction of phase precession of each dipole moment $\hat{p}_i$ mapped to the Bloch sphere. As a direct consequence, at time 2τ, the ensemble of radiating dipoles rephases, and a net material polarization reforms to emit a burst of coherent radiation – this is the mechanism behind a photon echo. Other effects that are consequences of the transition dipole moments of atoms, such as the Rabi cycle, the optical nutation, the free induction decay, and rephasing and dephasing can also be intuitively understood with the insight that the Bloch sphere affords. For the experimentalist, the Bloch sphere also is an effective way to visualize experiments involving the coherence of lanthanides.

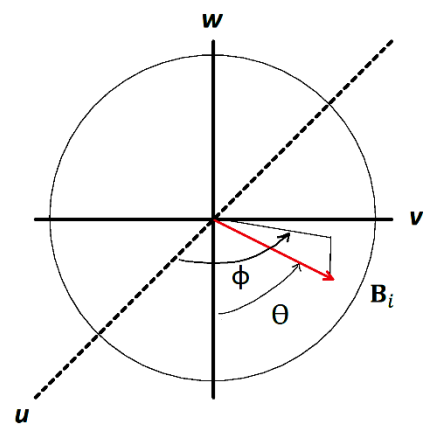

Figure 5. Bloch sphere representation, with Bloch vector $\mathbf{B}_i$ shown as a red vector, with phase angles to locate it on the unit sphere. The $\boldsymbol{u}$ and $\boldsymbol{v}$ axes are related to the precession of the atomic transition moment $\hat{p}_i$, while $\boldsymbol{w}$ tracks the probability in being in either the excited or ground state. "Torques" may be applied on this vector by timed laser pulses to send it on paths across the surface to the sphere as it evolves naturally; together with other states of other atoms in the ensemble, realigning and rephasing populations of dipoles is the mechanism behind the photon echo.

Symmetry

The most useful theoretical tool in the study of rare-earth doped materials is undoubtedly symmetry and the associated group theory. The concept of symmetry plays a fundamental role in all of quantum mechanics, and the point group symmetry of rare-earths in crystals is no exception. There are numerous and extensive discussions of this topic in many places [82, 83, 122]. The fundamental concept is that if there were an unknown wavefunction ψ with a known Hamiltonian $\hat{H}$, the problem of what the properties of ψ are could be informed by any other observable operator $\hat{O}$ that commuted with $\hat{H}$ [92, 122]. That is, $[\hat{H}, \hat{O}] = \hat{H}\hat{O} - \hat{O}\hat{H} = 0$, and so they are compatible observables with simultaneous eigenstates $|E, \varphi\rangle$. Therefore, $\hat{O}$ can be used to diagonalize $\hat{H}$, since if a matrix representation of $\hat{O}$ were diagonalized, it is impossible for $\hat{H}$ to connect functions of different symmetry, as that would require $[\hat{H}, \hat{O}] \neq 0$. In the case of the lanthanide Hamiltonian $\hat{H}$, the eigenvalues $\hat{J}$ of the total angular momentum operator label the

energy eigenstates, while the eigenvalues of the total orbital angular momentum $\hat{L}$ and spin angular momentum $\hat{S}$ label the basis states used in diagonalizing the intermediate coupling Hamiltonian matrix. The indirect nature of the approach is emphasized though – symmetry only exposes which matrix elements $\langle E', \varphi' | \hat{H} | E, \varphi \rangle$ must be zero, and it does not give the values of the non-zero elements. However, the eigenfunctions of the lanthanide Hamiltonian $\hat{H}$ doped into a crystal already defy direct calculation, and so any simplification or shortcut is extremely useful.

Physical symmetry operators $\hat{R}$, such as rotations which act on the Hamiltonian but bring the system back onto itself, are one useful type that commutes with the Hamiltonian $\hat{H}$. All symmetry operations $\hat{R}$ that commute with the rare-earth Hamiltonian $\hat{H}$ form a group *G* that has simultaneous eigenstates with $\hat{H}$. Therefore, once the symmetry of the system is identified, the machinery of group theory informs the researcher of which transitions are allowed or forbidden, which levels are degenerate or split, and more. To the experimentalist, symmetry and group theory are powerful tools to be aware of to quickly explain observations or predict what cannot happen.

A brief example on how degeneracies of rare-earth states are predicted in a certain symmetry of crystal field is now worked to illustrate the concepts. Here, a non-Kramers rare-earth ion is placed in an octahedral crystal field of symmetry *O,* in Schönflies notation. This example parallels the discussion in Tinkham [122]. It is important to point out that throughout this thesis, the site symmetries of rare-earth dopants are much lower than *O*, even as low as C_1, in which case all levels are expected to be split. The high symmetry case is instead chosen because it demonstrates the variety of degeneracies and splittings that can occur.

The character χ is the trace of the matrix representation $M(\hat{R})$, where $M(\hat{R})$ expresses a symmetry element $\hat{R}$ of group *G* in matrix form, such that $\chi^{(M)}(\hat{R}) = Tr(M(\hat{R}))$. Any representations $M(\hat{R})$ which have the same character $\chi^{(M)}(\hat{R})$ all belong to the same class in the group *G*; a class is a collection of symmetry elements in a group that are related by a similarity transformation $\hat{R}^{(1)} = \hat{U}^{-1}\hat{R}^{(i)}\hat{U}$, where $\hat{U}$ is another rotation operator that brings the system onto itself. Regardless, the character $\chi^{(M)}(\hat{R})$ is a useful identifier of a class of symmetry elements, in that it enables rapid inspection and comparison of matrices.

With this information, the character table of *O* can now be constructed; a character table exposes the relationship between the character $\chi^{(M)}(\hat{R})$ and the classes of symmetry operations. In this example, the Hamiltonian $\hat{H}$ of the ion must possess symmetry *O* because of the prescribed crystal field. There are five classes of symmetry operations in the group *O* to be considered: *E* (identity), 8*C_3, 3*C_2, 6*C_2', and 6*C_4, where the prefactor indicates the number of times that symmetry element appears in *O*. Note there are two distinct classes of C_2 rotations, which are not related to each other through a similarity transformation. The character table of the group *O* is now given in table 1 [122]:

O	***E***	***8C₃***	***3C₂***	***6C₂'***	***6C₄***
A₁	1	1	1	1	1
A₂	1	1	1	-1	-1
E	2	-1	2	0	0
T₁	3	0	-1	-1	1
T₂	3	0	-1	1	-1

Table 1. The character table of the octahedral group *O*. The classes of symmetry operations $\hat{R}$ head each column; irreducible matrix representations $M(\hat{R})$ of these operations head each row. Each table entry is $\chi^{(M)}(\hat{R})$, the trace of the matrix $M(\hat{R})$. The 2x2 matrix *E* in the third row is not to be confused with the identity symmetry element *E* in the first column.

The notation for the irreducible representations $M(\hat{R})$ in table 1 follows Tinkham [122]: A_i is reserved for one-dimensional matrices, E_i is for two-dimensional matrices, and T_i is reserved for three-dimensional matrices. An intuitive way to understand the standardized matrix representations $M(\hat{R})$ is that there is more than one way to represent the same symmetry operation $\hat{R}$ with a matrix.

For a free ion in isotropic symmetry, the character χ of a transformation matrix $M(\hat{R})$ that produces a given rotation α about some axis for an ion of orbital angular momentum J is given by [92, 122, 123]:

$$\chi^{(J)}(\alpha) = \frac{sin((J + 1/2)\alpha)}{sin(\alpha/2)} \tag{8}$$

Eq. (8) allows the character $\chi^{(J)}(\alpha)$ of the matrix representations $D_J(\hat{R})$ of the full rotation group to be specified. Note that in isotropic symmetry, all rotations of angle α belong to the same class. Using eq. (8) and the symmetry elements in *O*, the character of the reducible representation $D_J(\hat{R})$ may be written as in table 2:

O	***E***	***8C₃***	***3C₂***	***6C₂***	***6C₄***
$\boldsymbol{D_0}$	1	1	1	1	1
$\boldsymbol{D_1}$	3	0	-1	-1	1
$\boldsymbol{D_2}$	5	-1	1	1	-1
$\boldsymbol{D_3}$	7	1	1	1	-1
$\boldsymbol{D_4}$	9	0	1	1	1
$\boldsymbol{D_J}$	…	…	…	…	…

Table 2. A character table of the full rotation group under the listed symmetry operations. As the environmental symmetry is lowered from isotropic to octahedral *O*, comparison of the character tables enables rapid insight into which irreducible representations of discrete symmetry operations $M(\hat{R})$ must be added together to decompose the reducible representations of the full rotation group $D_J(\hat{R})$. In other words, the comparison of the character tables identifies how the matrices must transform in the presence of the lower symmetry crystal field and therefore which levels cannot be degenerate any longer. This enables compatibility tables to be written [123].

The characters $\chi^{(M)}(\hat{R})$ provide a concise means to quickly identify which pieces of irreducible matrices $M(\hat{R})$ of the discrete rotation group compose the reducible matrices $D_J(\hat{R})$ of the full rotation group. By adding the rows of table 1 to reproduce the rows of table 2, the compatibility table [123] of the full rotation group with *O* may be constructed, shown in table 3:

$\boldsymbol{D_J(\hat{R}) \rightarrow M(\hat{R})}$	**Comment**
$D_0 \rightarrow A_1$	One-dimensional J = 0 states cannot split.
$D_1 \rightarrow T_1$	J = 1 states are not split in an octahedral crystal field.
$D_2 \rightarrow E + T_2$	J = 2 states split into a singlet and triplet.
$D_3 \rightarrow A_2 + T_1 + T_2$	J = 3 states split into a singlet and two triplets.
$D_4 \rightarrow A_1 + E + T_1 + T_2$	J = 4 states split into a singlet, doublet, and two triplets.

Table 3. Compatibility table of the octahedral symmetry group *O* with the full rotation group. Note that this table is truncated and could continue for J = 5, 6, 7…

Table 3 represents just one simple example of the power of group theory – the framework enables the calculation of which degeneracies are lifted in lower symmetry environments. However, it does not give the magnitude of those splittings. The practical application to researchers is that this assists in knowing how many levels to expect, which is extremely useful in that it informs if a transition is missing from a measured spectrum, in assigning site symmetries, and more.

It is noted that Kramers ions require the use of double groups to capture the effect of non-integral values of angular momentum $\hat{J}$. Additionally, many other applications of the theory exist, such as the determination of forbidden and allowed transitions [92, 123]. More detailed explanations and tables are provided in Tinkham [122].

Units

Unless otherwise stated, units in this thesis are in SI. The predominant exception is the use of the spectroscopic wavenumber, in units of inverse centimeters. The wavenumber cm^{-1} emerged during times when precision of spectral measurements were outstripping the precision of measurements of the speed of light, and has remained a traditional unit of energy in experimental spectroscopy with the speed of light set to a value of 1. In all cases, the use of the term is not to be confused with propagation vector $\boldsymbol{k}$ of light, often called a wavenumber as well.

Wavenumbers (cm^{-1}) per GHz	29.9792458
Wavenumbers (cm^{-1}) per Kelvin	0.695
Wavenumbers (cm^{-1}) per eV	8065.54
Wavenumbers (cm^{-1}) per Joule	5.034×10^{22}
Bohr Magneton μ_B (J/T)	9.274×10^{-24}
Nuclear Magneton μ_N (J/T)	5.051×10^{-27}
μ_B/μ_N	1.836×10^{3}
Fine Structure Constant	$0.007297352 \approx 1/137$
Planck's constant (J/Hz)	$6.62607015 \times 10^{-34}$
Reduced Planck's constant $(J \cdot s)$	$1.054571817 \times 10^{-34}$

CHAPTER TWO

CHARACTERIZATION OF CRYOSTATS FOR QUANTUM INFORMATION SCIENCE RESEARCH WITH RARE-EARTH DECOHERENCE

In this chapter, the reader is introduced to the nuts and bolts of rare-earth spectroscopy, with the intention of demonstrating how rare-earth coherence can be used to characterize cryogenic hardware and optimize it for QIS-level research. Pieces of Tm^{3+}:YGG and Er^{3+}:YSO are loaded into two closed-cycle cryostats and compared to measurements made in conventional helium bath cryostats. The principle interest is the incredible sensitivity of rare-earth ions to a wide range of effects, including temperatures, fields, sample mounting procedures, pressures, and more, and how the measurements can be used to probe and control experimental artifacts in non-contact, all optical method. It is shown that the microscopic physical interactions that take place within these materials can directly drive the development of QIS hardware through sensing.

Critical to these efforts was QISE-NET and the NSF Triplet awarded to the author, his co-advisors Dr. Rufus Cone and Dr. Charles Thiel, and Dr. Josh Doherty at Montana Instruments. The author remains indebted for the cooperative support, expertise, and the instrumentation provided by the other members of the triplet [124, 125]. The Cone-Thiel Rare-Earth Spectroscopy Group is grateful for the opportunity to work with Montana Instruments, and the multi-year effort in working with them on the xp100 prototype. The author is also grateful to both Dr. Charles Thiel for providing measurements of strain, damage, and stray fields in samples, greatly adding depth to the overall discussion.

Quantum Information Science Cryostats

Fundamental to the success of quantum information science (QIS) research using quantum states of solids is the cryostat. One of the principle considerations in limiting decoherence in rare-earth-activated materials, for example, lies in the strongly temperature-dependent phonon-mediated relaxation and decoherence processes. These processes can be incrementally "frozen out" by low temperatures, approximately ~2 K or lower for many materials, a temperature range that is below the floor of many commercial cryocoolers [64, 109]. Another important consideration in mitigating decoherence is the inherent electronic and nuclear magnetism of most rare-earth ions, with electronic and nuclear spin flips (relaxation) and spin flip-flops (diffusion) leading to decoherence and spectral diffusion through the magnetic coupling [17, 54, 72, 109, 126]. Application of a magnetic field with an optimal magnitude and direction can suppress these effects by either inhibiting spin dynamics or minimizing the magnetic spin-ion and spin-spin coupling [64, 101, 103, 109]. Consequently, QIS-oriented cryostats measuring these atomic-scale properties must reach low temperatures, provide electrical and optical access, large sample space, magnetic field control, and more. Traditional open-cycle liquid helium bath or gas-flow cryostats have been used for decades and have solved many of these problems, but the current helium shortage makes these an unsustainable solution for many use-cases. Demagnetization, sorption, and dilution refrigerators reach very low temperatures. However, these are expensive to purchase and maintain, difficult to operate, have very limited cooling power, and generally have limited access to the sample chamber. Conversely, a mechanical refrigeration system, such as the Montana Instruments (MI) Cryostation (C_2), is simple to use and specifically designed for low vibration, high customizability and accessibility, and economic use of helium. Because of these

advantages, these kinds of systems, from MI and from other companies such as Photon Spot and Cryomech, are already widely employed in the QIS community for routine work. However, their use in advanced applications has been limited since cryocoolers typically do not reach below 3K under normal thermal loads. A mechanically stable sub 2K cooling stage with integrable magnetic field options would extend a convenient closed-cycle cryocooler to the lower temperatures and fields needed for characterization of QIS systems, while also optimally suppressing decoherence in rare-earth materials as well as the broader class of systems exploiting spin-based qubits. However, cold finger cryostats rely on mechanical interfaces to cool samples, which leads to critical performance issues that need to be investigated and addressed:

1. ***Thermal contact and heating of samples*** - Mechanical interfaces are intrinsically difficult to thermally bridge adequately, especially at very low temperatures where heat capacity is very low, and the thermal conductivity of many materials is poor. In addition, limited vacuum quality is a potential source of heating, which is especially important in cryo-pumped vacuum systems that are regularly exposed to atmosphere and handled by users. Finally, optical cryostats expose the sample to the ~300 K laboratory through windows, causing radiative heating of the sample even with shielding already in place. The net result is that the real sample temperature is difficult to reliably correlate to a temperature sensor readout.
2. ***Sample vibration*** **-** Vibrations generated from the normal operation cycle of the cryostat travel along the mechanical linkages needed for the cooling of samples, which can cause periodic bursts of decoherence with the same period as the cooling cycle. However, mechanical isolation can also negatively impact cooling power.

3. ***Mechanical Stress*** – Rare-earth materials are known to be sensitive to pressures that would assist in thermally linking the sample to the cold finger, causing inhomogeneous strain broadening and even nanoscale plastic deformation that can permanently degrade the sample in the worst cases.
4. ***Magnetic fields and sample chamber configurability*** - Magnetic fields are needed for optimal control of the rare-earth doped material properties. In addition, samples and experiments can often require custom mounting solutions, highlighting the need for a modular, spacious, and customizable sample chamber.

To adequately address all these difficulties, a variety of sensors are needed to fully characterize the interaction of the cryostat with the sample. Fortunately, the well-quantified sources of decoherence in rare-earth doped materials can be used to characterize cryostat performance at a level far beyond that achievable with traditional techniques, using the sample itself as a uniquely sensitive sensor. Measurements of these materials can therefore probe dynamics driven by undesirable thermal, mechanical, and electromagnetic perturbations, and then be used to optimize a cryocooler solution. In this work, measurements on thulium-doped yttrium gallium garnet (Tm^{3+}:YGG) and erbium-doped yttrium orthosilicate (Er^{3+}:YSO) in the Montana Instruments C_2 and prototype xp100 systems are performed to explore appropriate use cases and determine best practices for this class of cryostat. The effects of different sample mounting procedures are explored, and silver paint with mild pressure from a copper spring clip is identified as being effective, with good thermal conduction, relatively low mechanical stress. Decoherence from the cryostat operation pump cycle is not detected, and radiation heating is low. Permanent magnets are directly integrated into the cryostat for a simple, straightforward

magnetic field option, and their effects on base temperature are characterized. The results indicate that with the correct setup and techniques, the xp100 is capable of delivering the necessary performance for general low-temperature spectroscopy and exploratory QIS research, but with the incorrect approach, its performance is reduced to less than that of the previous-generation C_2 cryostat. This result underscores the need for fully understanding system performance. Summarily, the general utility of rare-earth decoherence as a compact, all-optical sensor suite for quantifying device performance is demonstrated, and greatly facilitates researchers' understanding of their own equipment to achieve accurate results. The methods developed in this chapter are used directly to inform and improve the research and discussion in the subsequent chapters.

Measurement Techniques

In this section, a primer on the spectroscopy techniques used in these specific measurements is given. These will be referenced in the subsequent sections and chapters.

Photon Echoes

Photon echoes are the optical frequency analog of the spin echo, a technique pioneered by Erwin Hahn, which was utilized for Nuclear Magnetic Resonance (NMR) and Electron Paramagnetic Resonance (EPR). Photon echoes were then pioneered by Kurnit after the invention of the laser [111], in which pulses of laser light are passed through samples instead of radio frequency pulses [19, 111, 116]. Altogether, this family of spectroscopy techniques provides a direct probe of the atomic-scale environment, whose dynamic processes are linked to the host material composition, temperature, and applied and intrinsic fields [19]. Beyond

fundamental scientific research, the photon echo is a key technique in the storage and recall of single photons for use in quantum memories, microwave-optical transduction, spatial-spectral holography, and many other scientific measurement methods [12, 20, 30-32, 34, 35, 42, 64, 67, 69-71, 74, 114, 127-132]. Theoretical treatments of photon echoes are discussed extensively in many places, and only the qualitative overview is given here [17, 19, 54, 67, 74, 100, 101, 104, 106, 108, 111, 112, 133-138].

In the simplest echo experiment, depicted in fig. 6, two tightly focused laser pulses delayed by time τ are applied in resonance with an atomic transition, whose pulse areas are equivalent to $\pi/2$ and π radians of phase accumulation for the transition moments [139]. Put another way, the $\pi/2$ pulse places the ensemble of atoms in a superposition of excited and ground states, and then the atomic transition moments freely precess between excitations. The initial net material polarization **P** rapidly decays as the individual atomic transition moments have slightly different precession frequencies from each other, each determined by their specific atomic configuration, but the phase of each atomic moment continues to precess independently of all the others. However, the phase of each atom is corrupted at a rate inversely proportional to the coherence time T_2, caused by dynamic processes in the host environment. After a chosen delay τ, the direction of the transition moment precession is inverted with the π pulse. Another interval τ later, the radiating atomic moments whose phase has not been perturbed by decohering processes return to their initial state. The ensemble then rephases to regenerate the net material polarization **P** and emits a burst of coherent radiation called an echo [112]. In simple cases, the echo intensity decays as $\sim e^{-4t/T_2}$, that is, exponentially by the coherence time T_2 as the delay τ is increased. The homogeneous linewidth Γ_h of the transition is then given by $\Gamma_h = 1/(\pi T_2)$. From there, the

atomic-scale processes that give rise to the overall coherence time T_2 can be analyzed based on extrinsic factors such as sample temperature and applied fields, and intrinsic factors such as magnetic coupling, spin flips, and host material composition.

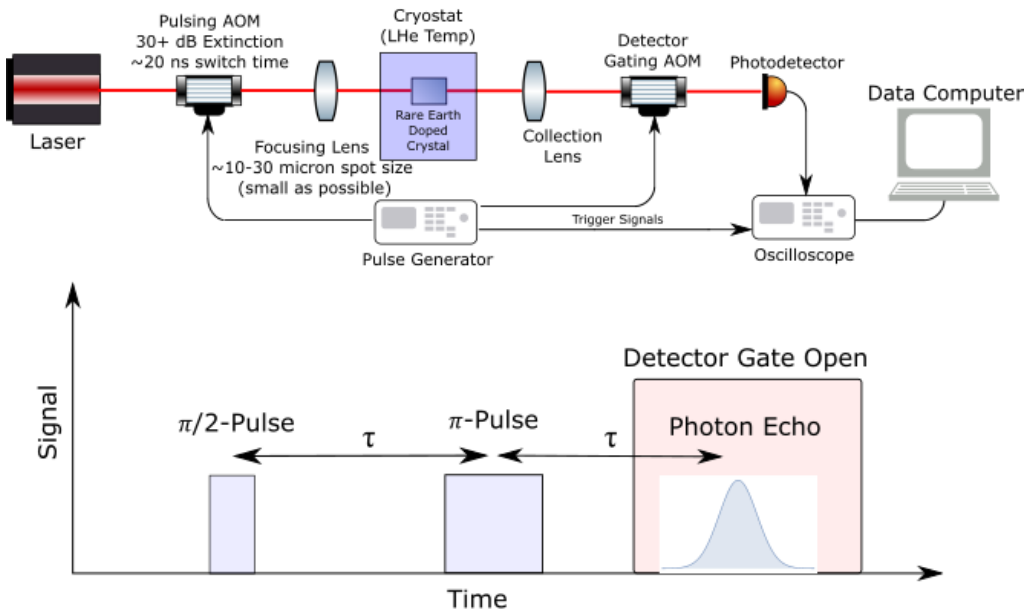

Figure 6. (Top) Schematic of a two-pulse photon echo experiment. Not shown are the focusing and collecting lenses for the acousto-optic modulators (AOMs). Tightly focused beams into AOMs enable fast switching at the cost of mode quality. (Bottom) The first two pulses are generated through switching of the pulsing AOM. The echo is often much weaker than the excitation pulses, and so the gate prevents detector saturation and associated artifacts when searching for a weak signal on the background of a strong signal. The signal strength of the photon echo decays exponentially with delay τ by the coherence time T_2. Image produced with Component Library [140].

More complex decay dynamics, including effects like spectral diffusion, are described by an empirical Mim's decay $\sim e^{-2(2t/T_M)^x}$, with the phase memory time T_M and fit parameter x. An effective homogenous linewidth $\Gamma_{Eff} = 1/(\pi T_M)$ is used in analogy to the simple case of $\Gamma_h = 1/(\pi T_2)$ [17, 56, 64, 67, 107, 108, 137, 141]. In addition, optically driven spin flips of neighboring ions can appear in the decay as damped oscillations of the envelope curve [19, 58, 66-68, 72, 91, 117, 142-145]. Regardless of the specifics, the longevity of the quantum

coherence stored in the material is critically sensitive to the atomic environment, and long coherence times provide extremely high sensitivity to the sample conditions.

Depending on the material and measurement configuration, the echo effect may be difficult to detect in practice. The intensity of the echo scales as the cube of the laser light field intensity, if both excitation pulses are the same intensity [133]. Therefore, optimizing for large echoes generally requires tight focus (~10-30 microns, or as small as possible) at the front of the sample to ensure that the absorption of the material being studied does not attenuate the excitation light before reaching the focus of the beam. The focal position must be simultaneously adjusted in concert with the excitation pulse times, which in practice are not a factor of two from each other because of optical thickness and absorption effects [139]. Pulse areas that are too high can also create multiple convoluted echoes that distort the results. The right balance of absorption, path length, and beam waist are is also imperative [104]. Detector gating is extremely helpful, as fast and strong excitation pulses can cause non-linear detector recovery artifacts that obscure the comparatively small echo pulses. Photomultiplier Tubes (PMTs) or avalanche photodiodes are ideal optical detectors for these measurements where available. Another critical factor is the laser stability, especially in the case of long coherence times, where the laser may drift in frequency between excitation pulses, resulting in an echo decay curve that merely characterizes the laser stability. Such a decay curve is useful studying laser stability over time but is not discussed further in this work.

Photon echo measurements are frequently difficult to initiate due to the difficulty of producing a starting signal to optimize in the first place. One method to initiate an echo experiment and determine if the system parameters are close is to measure the Rabi oscillations

of the transition [146]. An example is shown in fig. 7. The Rabi cycle directly measures the in-phase oscillations of ions between the ground and excited states, and it is generally easier to spot in practice. A single square pulse longer than the dephasing time is all that is needed to observe them; a quarter of the period of the Rabi oscillation corresponds to the duration of $\pi/4$ of phase accumulation on the Bloch sphere, and half the oscillation corresponds $\pi/2$ of phase accumulation [32]. To bootstrap an echo measurement, optics are adjusted to increase the frequency of oscillation and amplitude until the maximum point is reached, and then the experiment is changed over to an echo experiment simply by changing the pulse numbers and timings. Further timing and alignment adjustments are needed thereafter for final optimization.

The Rabi oscillation itself can be used to measure the coherence time. In practice though, the photon echo itself is more practical. The echo is a zero-background measurement, the linewidth and jitter of the laser is not a factor, and drift is a minor consideration except at long timescales where the laser wanders between pulses. The effects of laser drift are noted in chapter 5 when spectral hole burning is used to characterize the laser drift and jitter.

It is also important to note that in many spectroscopic measurements presented in this thesis, including photon echoes, the random error is often far less than any systematic errors. This results in plots where error bars on datapoints are smaller than any displayed point. It is assumed this is the case throughout this thesis if the error bars are not included in any given plot.

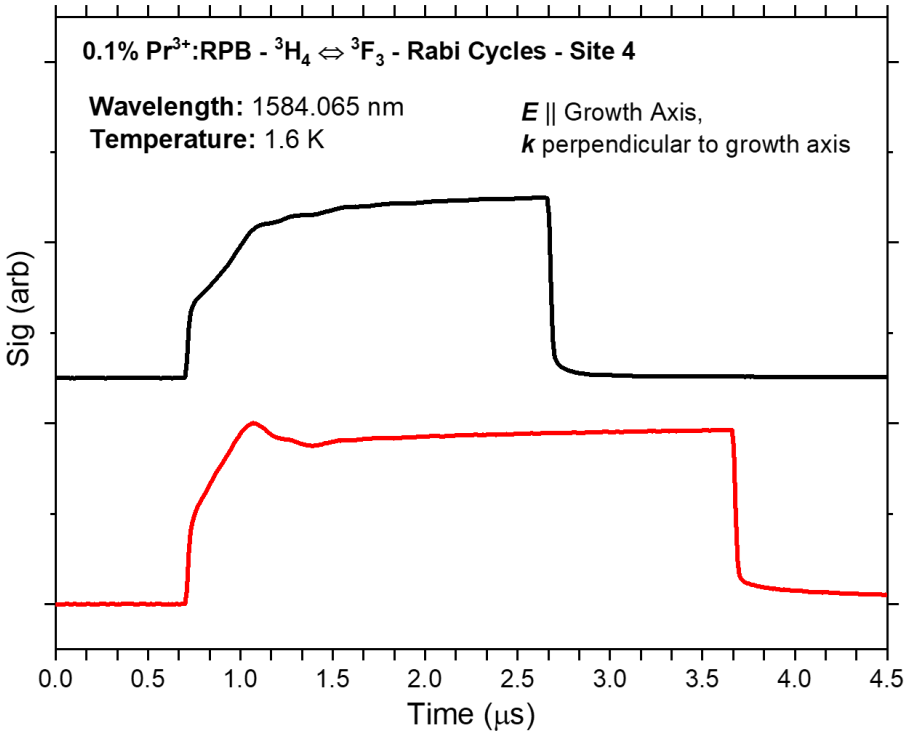

Figure 7. Example traces of Rabi oscillations measured in 0.1% Pr^{3+}:$RbPb_2Br_5$ at 1.6K on the $^3H_4 \Leftrightarrow {}^3F_3(1)$ transition of site 4. These oscillations assisted in determining the timings and laser intensity required to produce echoes.

Stark Absorption Spectroscopy

Stark absorption spectroscopy is a classical technique that measures atomic absorptions and emissions in the presence of electric fields [147]. Stark shifts play an important role in the CRIB quantum information protocol [30, 32, 34, 71, 107, 148]. It is important to note that the energy level manifolds of rare-earth ions in rare-earth doped crystals are already split and shifted by the crystalline electric fields of their host materials according to the symmetry of the field and the ion's polarizability [73, 74, 134, 146, 149]. Further broadening or shifting of transitions from external fields or applied pressures depends the magnitude, direction, and host material composition [150].

As in all absorption measurements, precise measurement of the background level and measuring with very low spectral density to avoid bleaching the absorption is essential. Leakage of light around the sample must be eliminated. Optimal results also require absorptions that are neither too faint, causing poor sensitivity, nor too dark, such that the material is considered optically thick and causes non-linear distortions. The basic experimental layout is given in fig. 8.

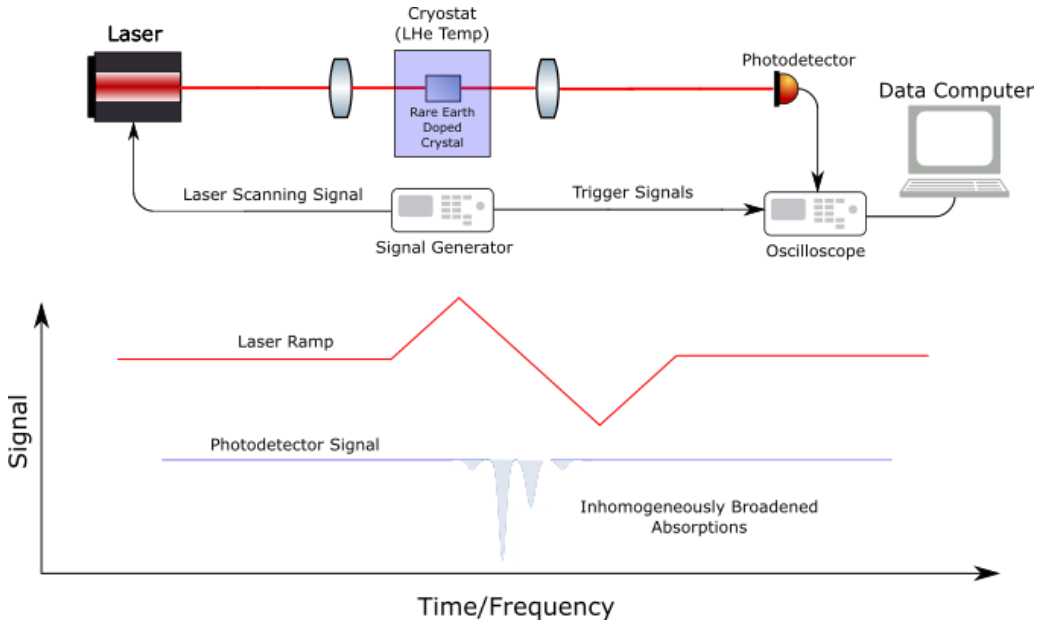

Figure 8. Basic laser absorption experiment schematic. All laser absorption measurements, including Stark spectroscopy, Zeeman spectroscopy, and SHB measurements, are all variations on this basic arrangement. Fields are applied in the cryostat with Helmholtz coils, permanent magnets, and electrodes. Classical white light absorption spectroscopy is also used for both Stark and Zeeman where the splittings, broadenings, and shifts are large enough for to be resolved by spectrometer. In that case, the laser is exchanged for a lamp and the measurement is spectrally resolved by a computer-controlled spectrometer, rather than by tuning a laser with a signal generator. Image produced with Component Library [140].

Zeeman Absorption Spectroscopy

Zeeman spectroscopy is another classical technique that measures the behavior of absorptions or emissions in the presence of a magnetic field [151]. This family of techniques is typically used to measure the g-values of the levels of ions under investigation. In crystals, the

magnetic interaction at low field strengths is governed by the local symmetry of the ionic environment, and in the general case is described by a g-tensor with anisotropic behavior. Zeeman spectroscopy is frequently performed in the optical regime where the observed splittings are the result of the net effect of both the ground and excited electronic state g-tensors [100, 101, 103].

Experimental Setup

These experiments are laid out according to fig. 6 and fig. 8 in the preceding section.

Samples

Ideal rare-earth materials for probing the new cryostat's performance include thulium-doped yttrium gallium garnet (Tm^{3+}:YGG) and erbium-doped yttrium orthosilicate (Er^{3+}:YSO), as these materials have had their thermal and magnetic behavior at low temperature well-characterized [100, 101, 103, 104, 107, 137]. In particular, the very long optical coherence time of Tm^{3+}:YGG has a well-characterized thermal dependence and is optically isotropic, making it a relatively uncomplicated probe of the sample temperature and mechanical stability [152]. The absorption of the lowest-to-lowest transition of $^3H_6 \Leftrightarrow {}^3H_4$ is also well-understood, and relatively ideal for measuring stress-induced broadening. On the other hand, the lowest-to-lowest transition of $^4I_{15/2} \Leftrightarrow {}^4I_{13/2}$ in Er^{3+}:YSO has strong, narrow absorptions and large g-values, making it ideal for characterizing magnetic systems as well as measuring temperatures through comparison of absorption of optically-resolved splittings to Boltzmann population models [101, 103].

Sample Thermometry and Mechanical Isolation – Photon Echoes

The effect of sample mounting on actual sample temperature and the effect of the cryostat refrigeration cycle on measurements was determined by comparing coherence times of 1% Tm^{3+}:YGG at zero field in the xp100 and C_2 cryostats, to coherence times made in bath cryostats in literature [107, 137].

- ***Laser:*** Coherent 899-21 Ti:Sapphire Ring Laser
- ***Pulse/Delay Generator:*** Stanford Research Systems DG645
- ***Laser Gating:*** Two Synchronized 200 MHz Acousto-Optic Modulators
- ***Frequency Reference:*** Burleigh WA-1500 Wavemeter
- ***Detector Gating:*** 200 MHz Acousto-Optic Modulator
- ***Detector:*** Hamamatsu R928 PMT
- ***Sample Mounting:***
    - Sample copper-taped to mount, completely encased to suppress radiation heating
    - Copper sheet/shim spring clip and interfaced with Ted Pella brand silver paint onto gold-electroplated OFHC copper mount, shown in fig. 9, in accordance with ref. [152].
- ***Cryostats:***
    - Montana Instruments C_2 Cryostation
    - Montana Instruments Prototype xp100 sub-2 K Cryostat

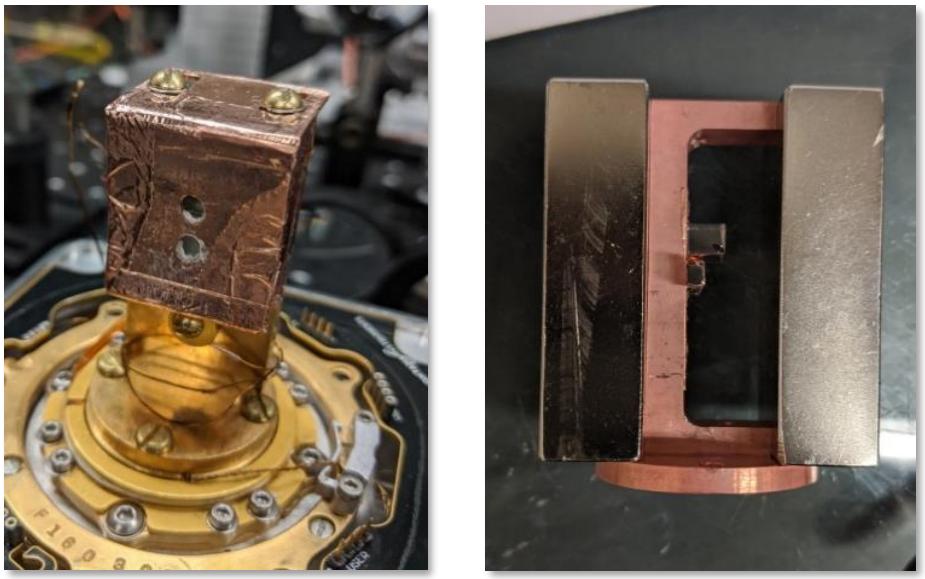

Figure 9. (Left) An example of the 1% Tm^{3+}:YGG mounting arrangement. A copper clip screwed into the mount lightly presses the crystal into the mount, with the interfaces filled with silver paint. Holes in the mount and clip provide optical access to the sample. In this case, the crystal sits at the lower aperture. Copper tape finishes the sample enclosure, creating a low-temperature stage radiation shield. (Right) is an example of the 0.02% Er^{3+}:YSO mounting arrangement. NdFeB bar magnets provide a fixed, uniform field to suppress magnetic decoherence. A copper clip (not shown) and silver paint are also used to thermally link the sample to the mount, while copper tape is used to completely enclose the sample and further shield against radiation heating.

The sample was cooled to the base temperature and the laser, tuned to the lowest to lowest transition of $^3H_6 \Leftrightarrow {}^3H_4$ at 795.325 nm, was tightly focused onto the sample. A pair of 300 and 500 ns pulses were generated by the DG645 and applied to the two synchronized AOMs to generate excitation laser pulses with very high suppression (>90 dB). The transmission through the sample was collected and passed through a gating AOM, timed to reject the excitation laser pulses while admitting the echo to pass through to the detector. The PMT response time was optimized with a short cable and low impedance, and its signal was recorded on an oscilloscope. The recorded traces were analyzed digitally, and the area under the echo curve was recorded as a

function of the delay. The temperature dependence of the coherence time was then compared to measurements and fits reported in literature.

Magnetism – Zeeman Spectroscopy

Zeeman Spectroscopy was done on 0.02% $Er^{3+:}$YSO to determine the utility and practicality of mounting NdFeB button magnets directly in the sample spaces of cryostats for magnetic studies, as well as any effects on the cryostat temperature they might have. The crystal was mounted in the cryostat with silver paint and mild pressure applied to the crystal on the mount with a copper spring clip. Bar magnets were held onto the mount through their magnetic attraction to each other, with the mount placed between as a spacer.

- ***Light Source:*** New Focus Velocity Laser Model 6326, Range: 1470 – 1551 nm
- ***Function Generator:*** Stanford Research Systems DS345
- ***Frequency References:*** Burleigh WA-1500 Wavemeter and 7.94 GHz Mach-Zehnder interferometer
- ***Detector:*** New Focus 1811 Photoreceiver
- ***Polarization:*** Fiber Polarization Controller
- ***Magnetic Fields:*** NdFeB N52 grade 1”x2”x.5” block magnets
- ***Sample Mounting:*** Copper sheet spring clip and interfaced with Ted Pella silver paint on OFHC copper mount, as in fig. 9.
- ***Cryostats:*** Montana Instruments C_2 Cryostation; Montana Instruments xp100 Prototype sub-2K Cryostat

The sample was cooled to the base temperature, with the light from the laser passed through the sample and then imaged onto the detector. Power and intensity of the beam within the sample

was minimized to mitigate readout-induced hole burning. The absorption spectrum of the lowest-to-lowest transition of the $^3I_{15/2} \Leftrightarrow {}^4I_{15/2}$ manifolds of the dopant erbium ions was measured by scanning the laser frequency with an external voltage applied to the laser piezo from the function generator at a low rate. The frequency scan of the laser in time was calibrated by sending part of the laser through the Mach-Zehnder interferometer and the constructive and destructive interference was recorded concurrently with the sample transmission signal on the oscilloscope and captured with a computer program.

Results

The sample of 1% Tm^{3+}:YGG was loaded into both the C_2 Cryostation and the prototype xp100. Baselines were determined and the performance of the two cryostats were compared not only with literature, but also with each other in a variety of configurations that researchers would commonly employ. The same sample was initially mounted with copper tape in both cryostats, before mounting with silver paint and a spring clip. The spring clip arrangement is shown in fig. 9.

Photon Echoes in the C_2 Cryostation

The measurements, shown in fig. 10, quantitatively determine that even a well-mounted crystal sample was significantly warmer than what the thermal sensor was measuring when using copper tape, even when the temperature sensor was mounted directly adjacent to the sample. Interfacing the sample with Apiezon-N cryogenic grease yielded similar temperature offsets for the sample. Conversely, measurements made with a copper spring clip applying mild pressure with silver paint to interface the sample to the cryostat possess superior temperature floors and temperature sensor accuracy. The results are in agreement with the literature on the temperature

dependence of 1% Tm^{3+}:YGG [108]. The echo measurements did not detect any mechanical noise affecting the crystal, indicating a high degree of mechanical isolation.

The effect of sample chamber contamination was also explored by exposing the sample mount and sample to ambient atmosphere for ~24 hours, then re-mounting the sample holder in the C_2 Cryostation to repeat the echo measurements. A clear performance degradation is visible in fig. 10, yielding similar performance to mounting the 1% Tm^{3+}:YGG sample with copper tape or with Apiezon-N grease. Sonication, washing the sample mount in solvents, and then remounting restored the performance. This experiment demonstrates the detrimental effects of contamination in the sample chamber and highlights the need for regular cleaning of the mounts, samples, and chamber.

Photon Echoes in the xp100

As shown in fig. 11, copper tape alone was found to increase the actual internal sample temperature in the xp100 to that of the C_2 cryostat, nullifying any advantages of the more advanced system. Furthermore, a simple aluminum radiation shield was mounted on the 1.6 K stage with the copper tape sample mounting to check for additional radiation heating not managed by the standard high and low temperature radiation shields. An improvement in the sample base temperature was observed but was not the dominant source of heating. A turbo pump was also used to improve the initial vacuum, but better starting vacuum did not measurably impact low temperature results in this case. The greatest improvements in the coherence time came from interfacing the sample with (Ted Pella-brand) silver paint to the sample mount and

applying mild pressure with a copper spring clip. As was the case for the C_2 cryostat, echo measurements did not detect any mechanical noise affecting the crystal.

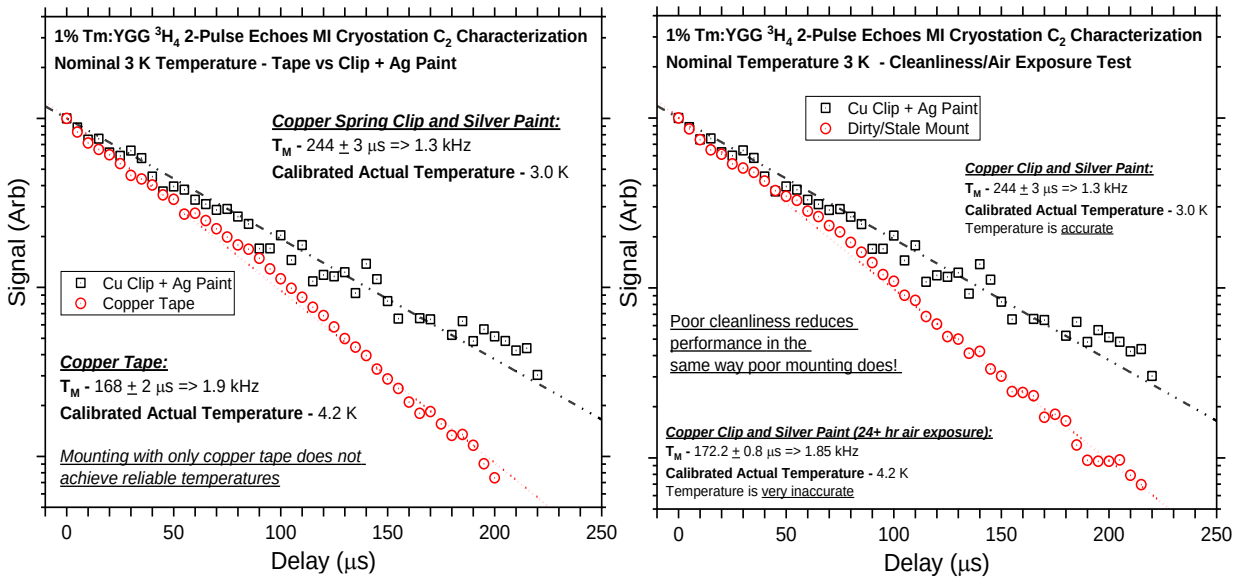

Figure 10. (Left) Photon Echoes from the lowest to lowest transition of $^3H_6$ to $^3H_4$ in 1% Tm^{3+}:YGG in the C_2 Cryostation, comparing the effect of different sample mounting procedures. The coherence time improves by ~76 μs changing the mounting method, and the actual sample temperature improves by lowering an additional 1.2 K to match the sensor. (Right) The effect of contamination on coherence time is nearly identical to mounting with coper tape. This result indicates that the copper tape adhesive adversely affects the thermal linkage of the crystal to the cryostat in the same way that dirt and contamination do. Error bars are not included on the points because the random error is very small.

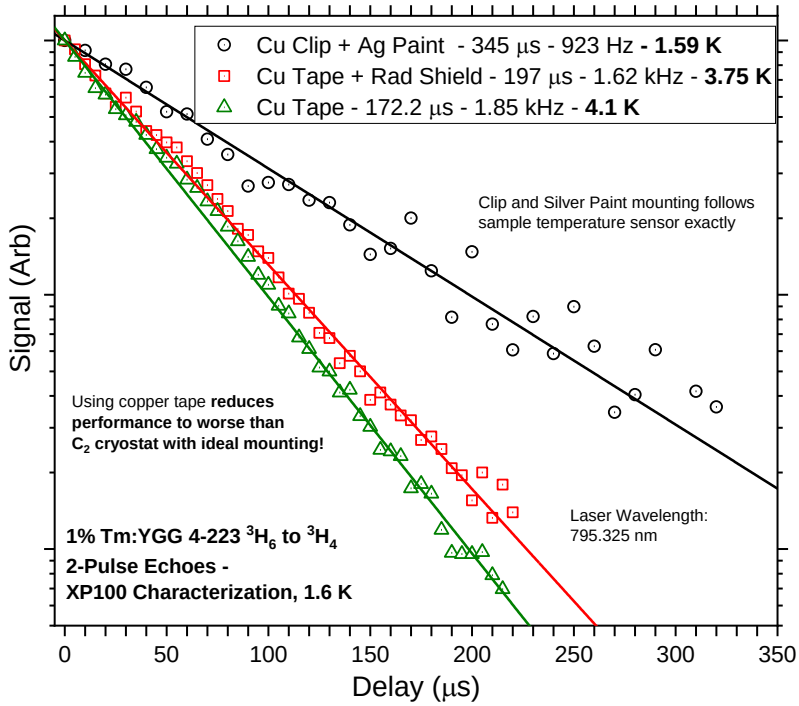

Figure 11. Two-pulse photon echo decays from the lowest-to-lowest transition of $^3H_6 \Leftrightarrow {}^3H_4$ in 1% Tm^{3+}:YGG in the prototype xp100 cryostat, comparing mounting procedures. The differing coherence times clearly show that it is not the cooling power in the C_2 limiting the sample temperature floor, but that the limited thermal conductivity of the sample mounting method. The comparison also shows that radiation heating is found to be a small but measurable contribution to the crystal temperature.

Reaching the sub-2 K regime is critical for evaluating the performance of both rare-earth-doped crystals and QIS materials in general, where many temperature effects are effectively frozen out and can be characterized [109]. Fig. 12 compares the echo decays measured in the xp100 to those measured in the literature and demonstrates how the increased temperature performance promised by xp100 is only realized with an optimized mounting procedure. These results highlight the need for adequate mounting techniques and actual sample temperature monitoring in general low-temperature research. Also, fig. 11 and fig. 12 both demonstrate the direct improvement in temperature performance of the xp100 over the C_2 Cryostation, and clearly indicate the relative capabilities and appropriate use cases of either system.

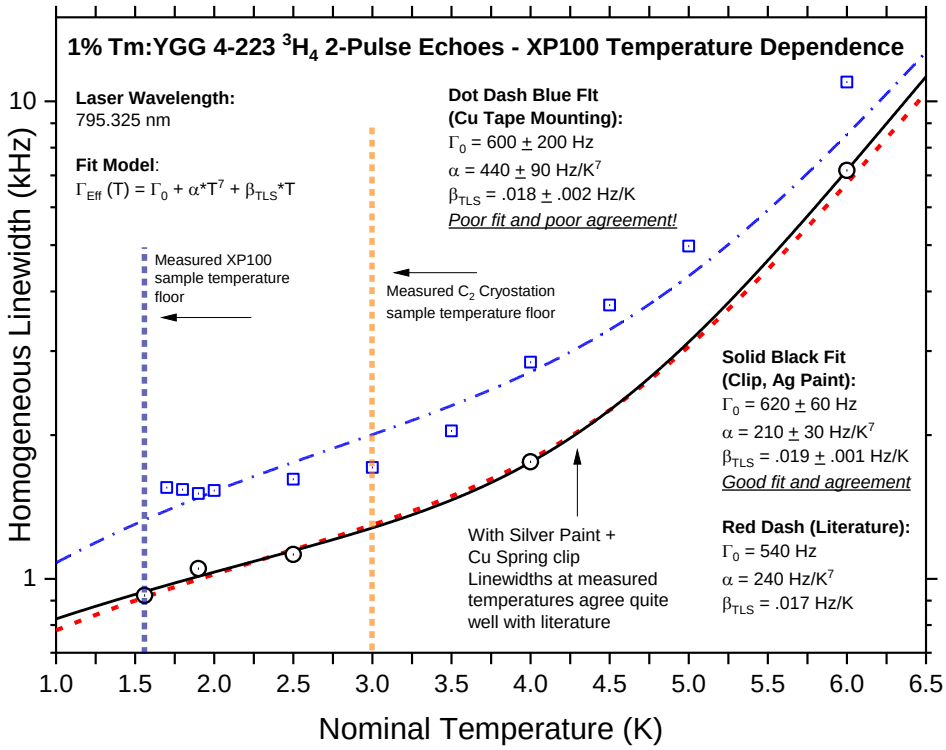

Figure 12. Summary of the temperature dependence of the homogeneous linewidth of the lowest to lowest transition of $^3H_6 \Leftrightarrow {}^3H_4$ in 1% Tm^{3+}:YGG in the prototype xp100 cryostat, in which the curves are compared to the curve described in ref. [108]. Improvements in the sample mounting strategy greatly increased the effective temperature range of the xp100, allowing it to access regimes critical for QIS research, well beyond the capabilities of the C_2 Cryostation.

Static Stress Effects

No broadenings or shifts were detected in the sample of 1% Tm^{3+}:YGG. This result is not unexpected due to low sensitivity the broad inhomogeneous absorption provides, which results from already extant static disorder in the material [137]. To use rare-earth ion doped materials as a sensor of static strain, the sharp lines of the $^4I_{13/2} \Leftrightarrow {}^4I_{15/2}$ transition in Er^{3+}:YSO are far more sensitive.In unpublished work provided by Thiel, mount-induced sample strains were investigated in a piece of 0.001% Er^{3+}:YSO (sample #1-544T) through measurement of the telecom transition $^4I_{13/2} \Leftrightarrow {}^4I_{15/2}$ absorption spectrum, using a laser tuned across the inhomogeneous line [150]. The sharp line of this transition of erbium in this host material provides excellent sensitivity to even

minor changes in applied pressures and external fields, shown in fig. 13. The crystal was mounted in a bath cryostat cooled to 5 K with tape and a baseline measurement taken, and then the sample was strongly clamped into its mount, and the inhomogeneous linewidth remeasured. They found that the measured samples were sensitive to pressure. The microscopic plastic deformation, detected in the absorption measurements shown in fig. 13a and b, permanently degraded the homogeneity of the bulk sample in the form of shifts and broadenings. Mounting with a hard clamp clearly introduces glass-like defect structure, increasing decoherence through local vibrational modes. These results indicate that any mounting procedure strongly requires as low amount of applied stress to the crystal as needed to make good thermal contact. Note that sensitivity to stress varies from material to material, and even sample to sample. Sharper lines and more sensitive host materials may also not tolerate any applied pressure at all, and these types of materials may strictly require mounting with no solid connections and or cooling with bath cryostats.

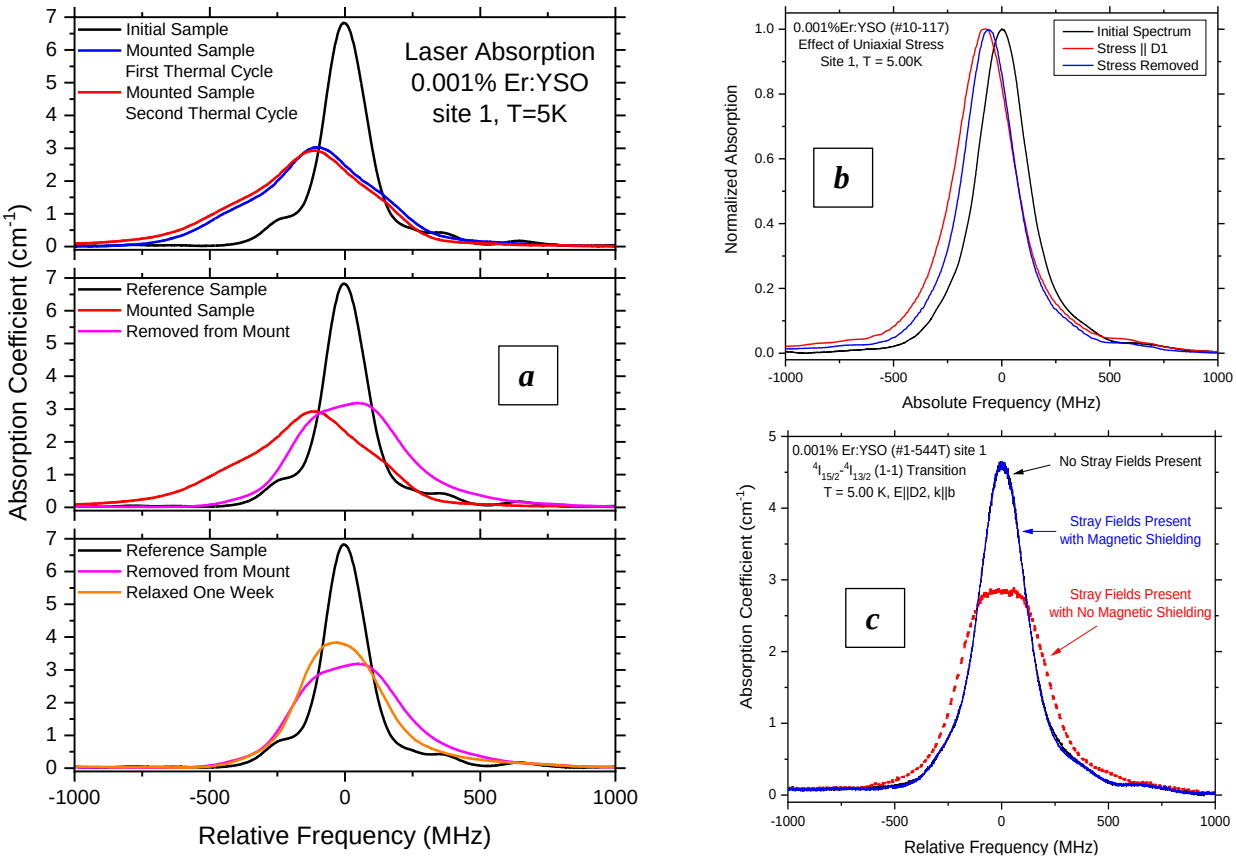

Figure 13. Measurements on the $^4I_{13/2} \Leftrightarrow {}^4I_{15/2}$ telecom transition (~1538.8 nm) in Er^{3+}:YSO, provided by Thiel. (Left - ***a***) The hysteresis of the absorption width and position is shown, beginning with the undamaged spectrum, then showing the effects of heavily clamping the sample down to the cooling stage, next removing the pressure, and finally allowing the damage to relax for a week. (Right, Top – ***b***) A similar effect is shown with carefully directed pressure, where the absorption peak is permanently shifted in frequency. In both ***a*** and ***b***, the broadening and shifts are irreversible. (Right, Bottom – ***c***) Mu-metal is used to shield the highly-sensitive erbium ions in YSO from stray magnetic fields, showcasing the feasibility of this simple and effective method for controlling magnetism in and around the confined spaces of a cryostat sample space.

<u>Permanent Magnet Integration</u>

Magnetic fields are essential for suppressing decoherence mechanisms in QIS research. A sample of 0.02% Er^{3+}:YSO and high-grade NdFeB bar magnets were first loaded into the xp100 cryostat to investigate the potential of a simple, fixed, and uniform magnetic field solution capable of reaching ~500 mT. The integrated absorption areas are plotted versus temperature in

fig. 14. From the fit, the sample base temperature is raised by ~170 mK above sample mount sensor reading. Because the sensor readings still achieved the base temperature of the system, the sample stage does not have a uniform temperature profile, and therefore the offset should be interpreted as resulting from the difficulty in cooling the bar magnets themselves, rather than a lack of cooling power of the cryostat. Further improvements in thermally sinking the magnets may further reduce the offset.

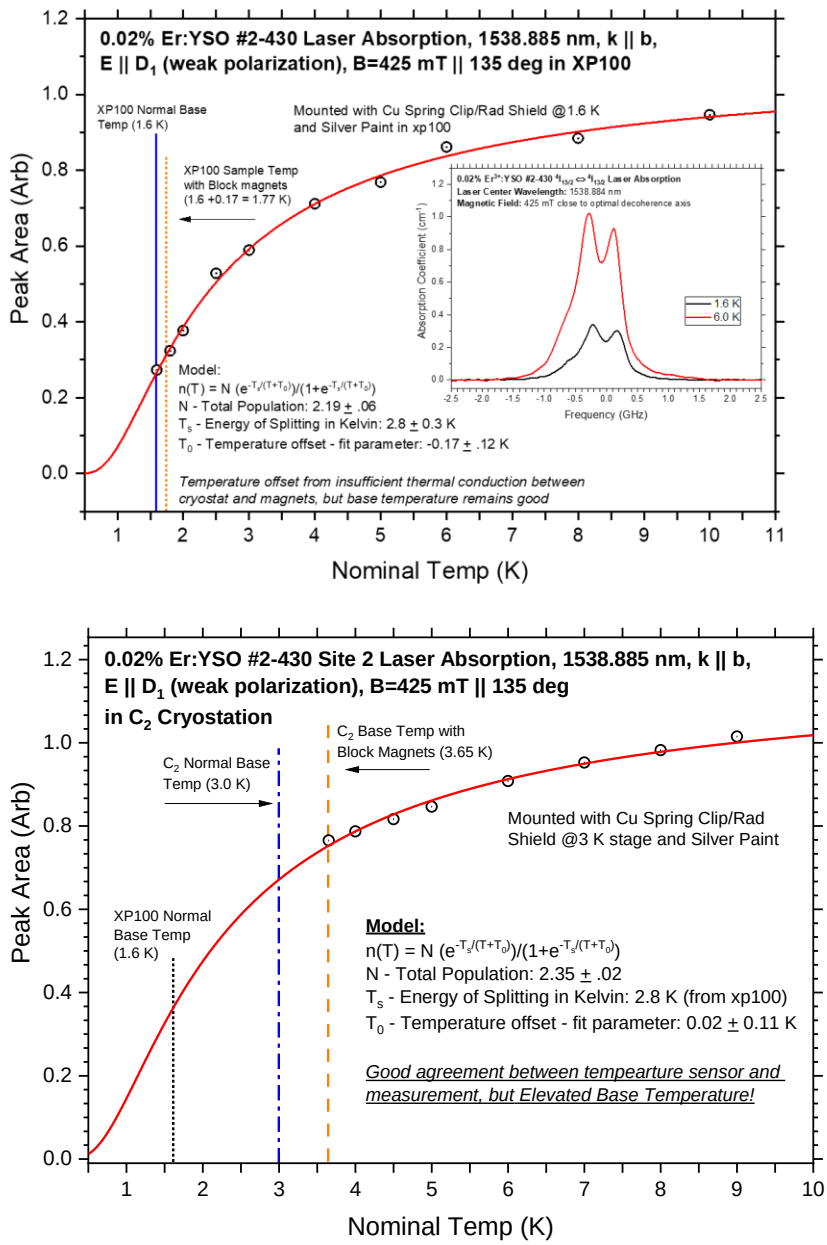

Figure 14. Boltzmann populations of Zeeman levels versus temperature of 0.02% Er^{3+}:YSO determined by optical absorption for the xp100 (top) and the C_2 (bottom), where the curve fit parameters are used to calibrate the actual sample temperature. Integration of the large permanent magnets does not significantly affect the xp100 performance, and the offset may be further improved through better thermal links to the magnets. Conversely, the C_2 is unable to cool the additional thermal mass as effectively as the xp100. This arrangement demonstrates the customizability and cooling power of the xp100 over the C_2. Error bars are not included on the points because the random error is very small.

Similar measurements were performed in the C_2 Cryostation. As seen in fig. 14, there is insufficient cooling power in the C_2 Cryostation to fully cool the sample with the large block magnets present. This conclusion is reached because the sensor itself no longer reaches the base temperature, but the sensor reading remains in good agreement with the relative populations of rare-earth ions. Consequently, the entire cold stage reached an elevated but uniform temperature equilibrium. The elevated base temperature is also too high for coherence spectroscopies of many rare-earth-doped crystals, especially in magnetically sensitive systems such as Kramer's ions [64]. Even if improvements to restore the C_2 base temperature were possible, 3K would still be marginal for fully investigating many materials' coherence properties. From this perspective, the cooling power afforded by the xp100 is superior to the C_2 in that the xp100 provides enough cooling power to support customizations that increase the thermal loads for QIS materials research, but only with the appropriate preparation and configurations.

Further unpublished work by Thiel, shown in the Zeeman laser absorption measurement of fig. 13c, also demonstrates the viability and utility of simple magnetic shielding of mu-metal for controlling small-scale stray magnetic fields inside the confined sample spaces of cryostats. This result has important implications for shielding in situations where magnetically sensitive components must be operated near a magnetic field; this situation arises frequently in the design of rare-earth microwave-optical transducers [150].

Conclusion

Progress in the QIS field of quantum communications depends heavily on expanding the toolkit of materials, which can only be done through studies of the fundamental processes at low temperatures and fields offered by advanced cryogenic systems under practical operating

conditions. Cryostats must therefore function as a tailor-made decoherence control suite in which researchers can reliably and easily access as much of the parameter space as possible. With this perspective, MI cold finger closed-cycle cryostats have been explored to investigate potential problems that a QIS researcher might face when working with this class of cryocooler.

The study uncovered several potential pitfalls and their solutions in working with cold-finger cryostats. First, adhesive-backed copper tape mounting was not reliable for the lowest temperatures, and the data strongly indicates that contamination can significantly influence the achievable base temperature. In contrast, light pressure applied to the sample with a high thermal conductivity, pliable interfacing material such as silver paint produced excellent thermal contact. Good vacuum hygiene was therefore absolutely essential, especially in situations where cooling power was already limited. Second, mechanical pump cycles were not detected in coherence measurements in either the C_2 or xp100 at the available level of sensitivity, indicating a high degree of mechanical isolation. Third, cooling-stage radiation shields help alleviate heating problems, and should be incorporated into sample mount designs. Fourth, no stress effects from the mounting were detected in the 1% Tm^{3+}:YGG sample, but in the highly sensitive, sharp-lined Er^{3+}:YSO sample measured by Thiel, the damage was easily seen from clamping the samples or applying uniaxial stress to them. The conclusion is that for materials with more intrinsic static disorder and broader inhomogeneous lines, the silver-paint and clip method of mounting should be sufficient. However, sensitive materials may need an entirely different mounting method or an entirely different type of cryostat. Fifth, button magnets integrated into the sample space are useful for mid-sized, fixed fields. Basic magnetic shielding is also shown to be sufficient in protecting samples from stray fields that could interfere with device operation.

In conclusion, this study has shown that leveraging the fundamental coherence properties of rare-earth ions for high-resolution sensing enables systems like the xp100 cryostat to serve as an ideal platform for low-temperature, high-resolution spectroscopy. The work outlines a generally useful, all-optical approach for characterizing QIS research equipment and diagnosing critical issues. Researchers can use these methods with rare-earth-doped materials to characterize their own hardware in situ to detect and correct issues, including QIS systems employing different material platforms, and these methods are used throughout this thesis to optimize and accurize measurements.

CHAPTER THREE

SUPPRESSION OF NON-RADIATIVE RELAXATION IN TRIVALENT THULIUM-DOPED LOW-DEBYE TEMPERATURE HOSTS FOR OXYGENATION-SENSITIVE ULTRASOUND-OPTICAL TOMOGRAPHY

In this chapter, the first of the three rare-earth optical transitions explored in this thesis is considered. The trivalent thulium $^3H_6 \Leftrightarrow {}^3F_3$ transition is located roughly between 690-700 nm. This wavelength regime is sought after for UOT applications, where the human body has an optimum balance of low absorption to light and contrast in oxygenated versus deoxygenated hemoglobin. The $^3H_6 \Leftrightarrow {}^3F_3$ transition is in exactly the right position in the spectrum, but its typical homogeneous linewidths are too broad for any SHB applications. The research presented here shows that hard crystals commonly used as rare-earth hosts cause the fluorescence from $^3F_3$ to be quenched and phonon-mediated decoherence to broaden the homogeneous lines through the direct phonon process. To counteract these effects, softer, denser materials are surveyed to reduce phonon energies and therefore enable good hole burning properties on the $^3H_6 \Leftrightarrow {}^3F_3$ transition in Tm^{3+}:LaF_3 and long T_1 lifetimes in Tm^{3+}:KPb_2Br_5. These results demonstrate the connection between advanced application development and fundamental physics research in the context of a medical imaging application leveraging SHB filters.

The work presented here was in direct cooperation with Dr. Stefan Kröll and Alexander Bengtsson of Lund University. The research visit by Alex was both a pleasure and extremely productive. We are grateful for the samples of Tm^{3+}:LaF_3 provided by Dr. Roger Macfarlane.

Ultrasound Optical Tomography and Rare Earths

Non-invasive optical-contrast imaging of deep-lying organs in humans is sought after for medical applications such as detecting ischemic heart disease, the leading cause of death worldwide, as well as tumor detection and monitoring [37, 40, 153]. Ultrasound optical tomography (UOT) is being explored for these applications [28, 38-40]; images combining optical contrast and ultrasound spatial resolution can be obtained by recording the intensity of frequency-shifted light generated by the interaction between the ultrasound beam and incident light as a function of ultrasound position, shown schematically in fig. 15.

One of the major challenges of UOT is discriminating the weak optical sideband from the strong carrier wave after the light has passed through highly scattering media. Rare earth-ion-doped crystals have been found to be good spectral filters for UOT. They are also useful for many other spectral applications, including laser line-narrowing and stabilization devices [65], RF spectral analysis and signal processing [64, 104, 134], and quantum memories and transducers [17, 54, 67, 106, 107, 126, 136, 137]. With respect to UOT, these crystals can be engineered to create large etendue, high-contrast spectral hole burning (SHB) filters at the wavelengths of rare earth optical transitions [28], which could enable UOT to reach theoretical imaging depths as large as ~6 cm in real biological tissue [37]. Recent implementations based on praseodymium-doped yttrium orthosilicate (Pr^{3+}:YSO) near 606 nm and thulium-doped yttrium aluminum garnet (Tm^{3+}:YAG) near 795 nm showcase the feasibility of SHB-enabled UOT [18, 36, 40, 41, 50]. However, the high absorption by blood at the required 606 nm operating wavelength of Pr^{3+}:YSO filters limits the imaging depth. Conversely, thulium $^3H_6 \Leftrightarrow {}^3H_4$ transition filters at 795 nm have operated very close to the isosbestic point of oxygenated (HbO_2)

and de-oxygenated hemoglobin (Hb), where the detected UOT signal strength is least sensitive to changes in tissue oxygenation, as shown in fig. 15. To achieve practical penetration depth, another new optical transition in an SHB-material closer to 700 nm, where the absorption from muscle tissue is low and oxygenation contrast is high, should be identified and characterized for oxygenation-sensitive UOT.

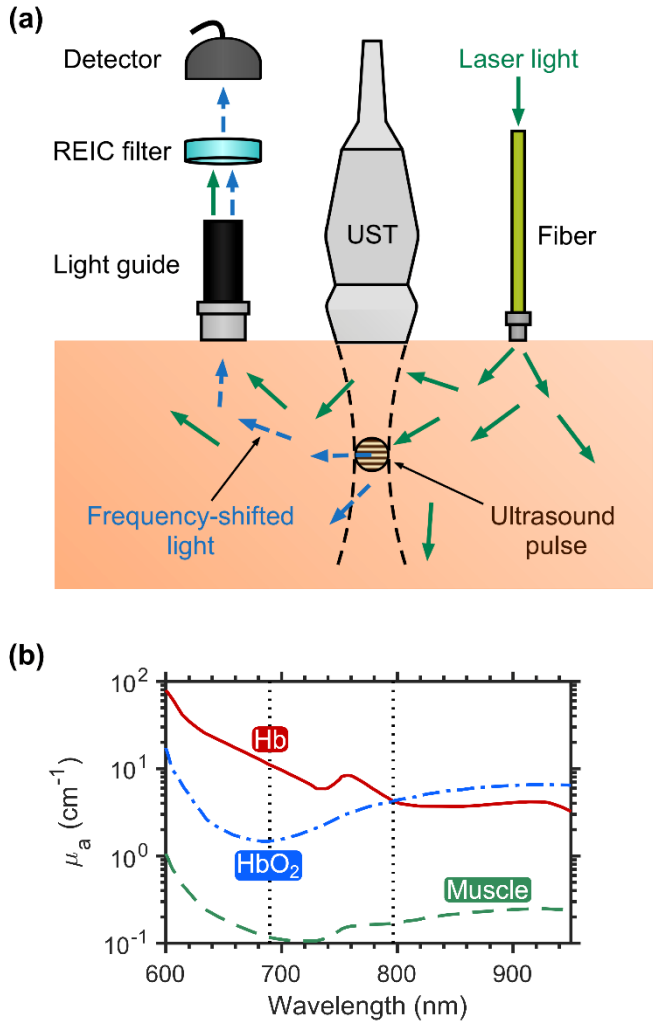

Figure 15: (a) Schematic example of a UOT system using spectral holeburning (SHB) detection. Ultrasonic pulses and laser light are delivered into the target tissue by an ultrasound transducer (UST) and through an optical fiber, respectively. Photons traversing the ultrasound pulse are frequency-shifted via the acousto-optic effect. Frequency-shifted photons (blue dotted arrows) are collected from the target and filtered from the unshifted photons (green arrows) through the rare-earth-ion-doped crystal (REIC). (b) 690 nm light can distinguish between changes in blood oxygenation due to the large difference in absorption coefficient (μa) for oxygenated (HbO_2) and de-oxygenated hemoglobin (Hb) at this wavelength. By comparing to a signal using 795 nm light, changes that are not caused by changes in tissue oxygenation can be detected and the effect of these can then be removed from the 690 nm signal. Absorption spectra of Hb and HbO_2 provided by ref. [154]. Absorption spectrum of muscle tissue is calculated from ref. [154] assuming Hb and HbO_2 are the only absorbers in the tissue, and there is 4% blood content with 85% average oxygen saturation.

Thulium is an attractive dopant for the desired SHB filter material for several reasons. First, its $^3H_6 \Leftrightarrow {}^3H_4$ transition near 795 nm is already used for UOT, and thulium also possesses the $^3H_6 \Leftrightarrow {}^3F_3$ transition near 690 nm, shown in fig. 17. Having two transitions in the tissue-optical window could also enable two-color UOT within the same SHB material [37, 77]. Furthermore, trivalent thulium possesses a simple spin-1/2 nuclear magnetic structure and has weaker coupling to environmental magnetic perturbations compared to other rare earths, which mitigates the need for external magnetic fields to control decohering magnetic interactions that broaden spectral holes. The spin-1/2 also means there is no zero-field hyperfine structure [109]. Finally, both the $^3H_6 \Leftrightarrow {}^3H_4$ and $^3H_6 \Leftrightarrow {}^3F_3$ transitions are in the span of commercially available diode lasers. While these features make thulium-doped materials good candidates, the properties of the $^3H_6 \Leftrightarrow {}^3F_3$ transition are conventionally expected to be too poor for SHB filtering due to rapid nonradiative-relaxation to the $^3H_4$ multiplet, which increases the homogeneous linewidth with corresponding increases in the UOT filter bandwidth. This is due to the fundamental relationship between homogeneous atomic linewidth Γ_h, the T_1 lifetime of the excited state, the pure dephasing time T_2', which encapsulates many effects [17, 67, 74, 101, 104, 106-109], and the overall T_2 coherence time of the transition [60]:

$$\Gamma_h = \frac{1}{\pi T_2} = \frac{1}{2\pi T_1} + \frac{1}{\pi T_2'} \tag{9}$$

The nonradiative multiphonon decay rate is conventionally equal to the radiative decay rate when the energy gap to the next lowest level is $\sim 5\hbar\omega_D$, or five times the maximum phonon energy [93-96, 155-157]. For states dominated by phonon-mediated non-radiative relaxation, the T_1 lifetime is reduced to <1 μs or even as low as ~1 ns, giving rise to broad homogeneous linewidths that limit the minimum spectral hole width. Therefore, the minimum spectral filter

bandwidth in these cases should be lowered if the T_1 lifetime can be improved by slowing the phonon relaxation rate. Transitions like $^3H_6 \Leftrightarrow {}^3F_3$ should have their low-temperature homogeneous linewidths improved in softer, denser host materials compared to the less-dense, hard-oxides that are typically used as lanthanide hosts, because of the relationship between the material hardness, the density, and the maximum phonon energy, the Debye frequency [158]. This is most easily seen in the Debye model of phonons in a three-dimensional solid, where both the Debye temperature θ_D and phonon cutoff frequency ω_D go as:

$$\theta_D, \omega_D \propto n^{1/3}\sqrt{M/\rho} \tag{10}$$

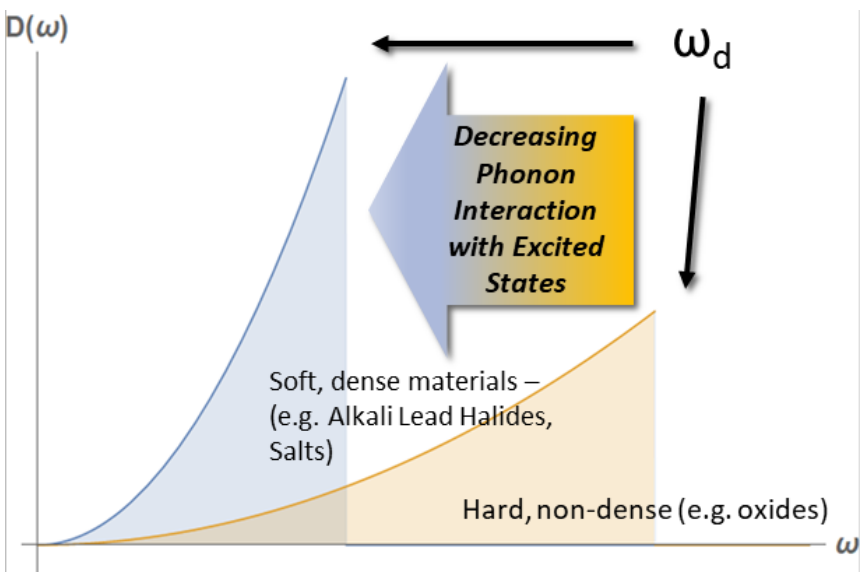

Figure 16. Modifying the Debye density of states in accordance with eq. (10). The maximum allowed phonon energy is lowered, and therefore, the multiphonon process that enables the rare-earth ion to relax non-radiatively is stopped.

In eq. (10), the number of ions per unit volume is n, elastic modulus is M, and the material density is ρ. The elastic constants depend on the type of the phonon being considered, but in general refers to the stiffness of the material, analogous to a spring constant for a mass on the end of a spring. By increasing the mass and reducing the coupling strength, the phonon spectrum

must shift towards lower energy, as in fig. 16. The room-temperature Mid-IR (3-10 μm) laser material family, the alkali lead halides, leverage this property to suppress non-radiative relaxation [159]. Furthermore, hole burning spectroscopy by Macfarlane in ref. [59] on Tm^{3+}:LaF_3, with a Debye temperature of 360 K, also supports this perspective by suggesting that the homogeneous linewidth of the $^3H_6 \Leftrightarrow {}^3F_3$ transition could be less than 1 MHz at temperatures below 5K [160]. Consequently, the Debye temperature should be a figure of merit that gauges the phonon-mediated non-radiative relaxation rate and is useful for identifying a host material that could make a transition suited for sub-MHz holeburning.

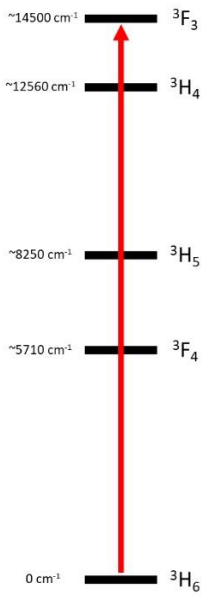

Figure 17: Approximate energy level structure of Tm^{3+} in LaF_3, based on measurements from ref. [160] and this chapter. The transition wavelength is near 690 nm.

In this chapter, a survey of the homogeneous linewidth of the $^3F_3$ transition for progressively denser and softer media determines the point at which the non-radiative relaxation is adequately suppressed for UOT. Trivalent thulium-doped CaF_2, BaY_2F_8, $YLiF_4$, LaF_3, and KPb_2Br_5 are identified as possible host materials because of their incrementally lower Debye temperatures.

Samples of each material are surveyed with absorption, fluorescence, and holeburning spectroscopies. The reduction of phonon-mediated homogeneous line broadening mechanisms in lower Debye temperature host materials allowed the burning of 380 kHz-wide spectral holes in Tm^{3+}:LaF_3, an improvement of over 2 orders of magnitude across the range of studied materials. The lifetime of the lowest level of $^3F_3$ reaches ~100 μs in Tm^{3+}:KPb_2Br_5, projecting a T_1 lifetime-limited SHB filter bandwidth of 1.6 kHz, though this is likely to be limited by T_2' broadening. The survey determines that a UOT device operating at 690 nm would be feasible in Tm^{3+}:LaF_3 because of its strong absorption and narrow holes.

Experimental

Host materials were selected with the aim of suppressing non-radiative relaxation pathways. Fluoride salts with their long history of study, the availability of samples with a range of Debye temperatures, and their resistance to moisture were the focus as summarized in table 4. All samples were clear, colorless, and optically polished. Ranges of Debye temperatures are reported for many of the materials in table 4 because the determination is sensitive characterization technique and analytical approach [161-167]. The concentration of dopant rare earths does not have great effect on the Debye temperature of a host material [168].

Crystal	YAG	YSO	**CaF_2**	**BaY_2F_8**	**$YLiF_4$**	**LaF_3**	**KPb_2Br_5**
Debye Temp. (K)	760-500 [161, 162]	580 [163]	510 [164]	500 [162, 165]	560-460 [162, 166]	360 [167]	292 [169]

Table 4. Comparison of host crystals. Crystals that are surveyed in this work are bolded. The listed values are representative of the range of values reported for each crystal in literature.

Measurements on Tm^{3+}:CaF_2 were performed on a deuterated 0.03% Tm^{3+}:CaF_2. CaF_2 is cubic, with a lattice parameter of 5.40 angstroms. There are two rare earth sites in CaF_2 of C_{3V} and C_{4V} symmetries [170].

Measurements on Tm^{3+}:BaY_2F_8 were made on a sample of 0.75% Tm^{3+}:BaY_2F_8 obtained from AC Materials. BaY_2F_8 is monoclinic with an angle **β** of 99.7 degrees, and lattice parameters 6.99, 1.05, and 4.2 Angstroms for ***a***, ***b***, and ***c*** respectively [24, 26, 171].

Measurements on Tm^{3+}:$YLiF_4$ were performed on a sample of 2% Tm^{3+}: $YLiF_4$ (No. 11-3-52), also from AC Materials. $YLiF_4$ is a Scheelite or tetragonal structure, with lattice parameters ***a*** = 5.04 Angstroms and ***c*** = 10.61 Angstroms. Rare earths occupy an S_4 symmetry site in the lattice [172].

Measurements of Tm^{3+}:LaF_3 were performed on a sample of 0.1% and 0.5% Tm^{3+}:LaF_3 obtained on loan from Dr. Roger Macfarlane of IBM. The dimensions of the 0.1% sample were 2.00 mm (***c***-*axis)* x 6.97 mm (***k***-direction) x 1.8 mm, while the dimensions of the 0.5% sample were 2.14 mm (***k***-direction) x 3.74 mm (***c***-axis) x 3.2 mm. The trigonal unit cell is comprised of 6 units of LaF_3. The space group of the crystal is D_{3d}^4, with lattice parameters ***a*** = 7.2 Angstroms and ***c*** = 7.4 Angstroms, where ***c*** is the conventional symmetry axis [173]. Rare earths occupy the lanthanum site with nine-fold coordination and C_2 symmetry in the lattice, whose site symmetry axis is perpendicular to the crystal ***c***-axis [55, 173].

Measurements of ~0.2% Tm^{3+}:KPb_2Br_5 were performed on a homemade sample, which was grown in vacuum-sealed quartz tubes on a homemade Bridgeman growth setup following the procedure described in ref. [16]. The unit cell is monoclinic with an angle **β** very close to 90 degrees, and lattice parameters ***a*** = 9.26, ***b*** =8.37, ***c*** = 13.03 Angstroms [174]. The high rejection

coefficient of thulium in this material made only low concentrations possible, and the sample was irregularly cut and unoriented, but optically polished for basic investigations. The growth and characterization of this material is discussed in more detail in chapter 5.

All measurements were carried out in a Montana Instruments C_2 Cryostation cooled to 4 K, with windows anti-reflection coated for 633-1050 nm. For all samples except the ~0.2% Tm^{3+}:KPb_2Br_5, an EOSI Littman-Metcalf type external cavity diode laser supplied coherent light with a ~100 kHz-linewidth for studying the $^3H_6 \Leftrightarrow {}^3F_3$ transitions. The absolute wavelength of the laser was measured with a Burleigh WA-1500 wavemeter. All scans were driven by pulses from a Stanford Research Systems DG645 and triangle ramps from a DS345. Piezo-scans of the frequency of the EOSI laser were calibrated with a home-built confocal scanning Fabry-Perot for laser absorption measurements with a free spectral range of 1.9 GHz. The laser was gated with a single Crystal Technology Inc. 3080-125 acousto-optic modulator (AOM) driven at 80 MHz, with greater than 30 dB of measured extinction and 20 ns of rise time. The sample of ~0.2% Tm^{3+}:KPb_2Br_5 was measured similarly, but with a home-built Littrow laser, scanned externally by sweeping the drive frequency on the AOM; the design and construction of this laser is discussed more in chapter 5. This laser was used because the EOSI laser lacked sufficient tuning range to reach this transition without modification. All laser measurements were digitized by a Tektronix TDS 754C oscilloscope.

To map out the $^3F_3$ excited manifold structure of Tm^{3+}:LaF_3, white light from a 12-Watt tungsten-halogen bulb was passed through a Polaroid sheet polarizer, focused onto the 0.5% sample of Tm^{3+}:LaF_3, and analyzed by an Advantest Q8347 Optical Spectrum Analyzer with ~900 MHz resolution. Laser absorption of the lowest-to-lowest $^3H_6 \Leftrightarrow {}^3F_3$ transition in both the

0.1% and 0.5% samples of Tm^{3+}:LaF_3 precisely determined the transition's frequency, absorption coefficient, and temperature dependence. Transmission was detected with a Newfocus 1801 visible photodetector.

The ground state structure of Tm^{3+}:LaF_3 was measured with fluorescence from the 0.5% sample, excited with the EOSI laser tuned to the lowest energy transition of $^3H_6 \Leftrightarrow {}^3F_3$. Light was collected 90 degrees to the beam path by a lens and passed through a SPEX 1401 double monochromator. Time-resolved fluorescence from the 0.1% sample was used to determine the $^3F_3$ state lifetime by AOM-gating the EOSI laser. Emission was collected 90 degrees to the beam path through a lens tube fitted with sharp interference filters to create a passband of 700 nm – 750 nm to illuminate a Hamamatsu R928 PMT biased to -1.05 kV. The sample chamber was masked with neoprene gaskets in a dark room to suppress background light. This experimental arrangement was also used to measure the lifetime of the $^3F_3$ state in Tm^{3+}:KPb_2Br_5, except that the home-built Littrow laser was used for excitation.

The homogeneous linewidths of the lowest-to-lowest $^3H_6 \Leftrightarrow {}^3F_3$ transitions in all the surveyed materials were measured by burning narrow transient holes and probing them with a frequency-swept laser. Hole widths were optimized by using minimal burn and probe power and illumination times. The resulting signal was detected with a New Focus 1801 detector.

Time-resolved holeburning was used to determine the spectral hole lifetimes without a field in the 0.1% Tm^{3+}:LaF_3 sample. These were optimized for long measurement times by burning trenches with 50 μs burn times and high intensity into the $^3H_6 \Leftrightarrow {}^3F_3$ transition.

Spectral Holeburning: Experiment Primer

Spectral holeburning (SHB) is a measurement performed by selectively exciting a portion of an inhomogeneously broadened absorption. At liquid helium temperatures where the underlying homogeneous lines are narrow relative to the width of inhomogeneous line, illumination selectively "burns" a notch of decreased absorption in the inhomogeneous line, as in fig. 18. The resulting hole relaxes by the lifetimes of the excited states that the atom traverses as it returns to the ground state [12, 18, 19, 28, 36, 41, 42, 44, 50, 54, 55, 59, 62, 65-67, 90, 175]. This can be used in a wide variety of useful ways, both to the experimentalist and to the optical engineer. A basic experimental setup is shown in fig. 19.

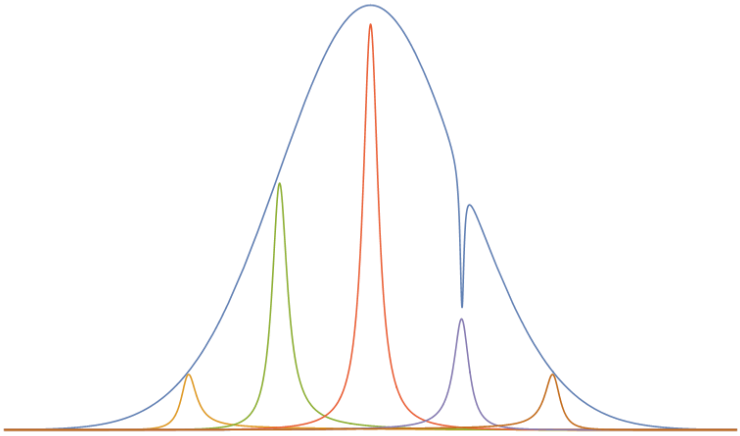

Figure 18. Spectral holeburning concept. A notch is "burned" into the inhomogeneously broadened line upon illumination with a laser, due to absorption in the underlying homogeneously broadened absorptions.

One immediately obvious use is in ultra-narrow bandpass spectral filtering applications, such as UOT, and other quantum and classical optical signal processing applications [28, 37, 38, 44, 64, 74, 104, 134, 136]. The procedure can be used to also measure lifetimes of excited states

without confusion from radiation trapping [176, 177], or complications of from multiple crystallographic sites fluorescing at similar wavelengths.

Direct measurement of the homogeneous linewidth in the transition is made by burning the narrowest possible hole into the inhomogeneous line. This is achieved by minimizing the laser intensity as much as possible, and stabilizing the laser frequency [19, 60, 105]. However, this method for measuring the homogeneous width Γ_h is often regarded as inferior to photon echoes for measuring the homogeneous width. This is because the measurement is very sensitive to the stability and width of the laser itself, leading to gross overestimations of the true homogeneous width. Photon echoes implicitly eliminate all effects of inhomogeneous broadening without penalty and enable direct viewing of the atomic scale dynamics. Note that the sensitivity of SHB to laser behavior can be extremely useful in gauging laser performance and can directly inform researchers as to laser stability and quality. This technique is used in chapter 5 to validate the correct mono-mode operation of a homebuilt laser to explore a new material, Tm^{3+}:KPb_2Br_5. SHB can also be a very efficient and simple way to quickly identify hole burning transitions with numerous narrow absorptions and perturbed sites in a survey, requiring less setup and fine-tuning than an echo. That approach is used to rapidly identify multiple sites with overlapping but seperate energy level structures in chapter 5, in the study of both Tm^{3+}:KPb_2Br_5 and Pr^{3+}:$RbPb_2Br_5$. In many cases, the lowest-to-lowest transition between two manifolds is often regarded as the only hole burning transition to be found. However, this is not guaranteed except by the difficulty of suppressing phonon relaxation and excitation to and from other crystal field levels. Therefore, in cases where the phonons that bridge these energy gaps might be suppressed

or not be allowed in the first place, excited states should be holeburning transitions as well. A possible case of this is pointed out in chapter 5 in Pr^{3+}:$RbPb_2Br_5$.

SHB is also sensitive to magnetic fields, in that it can be used for Zeeman spectroscopy [19, 126, 151, 178]. The atomic structure in the magnetic field obscured by the inhomogeneous line is revealed in the resulting hole and anti-hole pattern. Persistent SHB (PSHB) is also possible through a variety of mechanisms [19, 32, 59, 66, 67]. In this thesis, PSHB occurs in optically pumping the ground states of either split doublets of nuclear spins in thulium or in nuclear pseudoquadrupole levels of praseodymium, which relax by the spin-lattice relaxation time at liquid helium temperatures [66, 67, 72, 91, 144]. More on Zeeman hole burning spectroscopy and a case of PSHB is discussed in chapter 4.

Readouts of very narrow holes, generally assumed to be <1 MHz (but much narrower holes have been measured [19]) produces ringing in the signal. The cause of this may be viewed in one of two equivalent ways. The first is that Fourier conjugate pairs of time and frequency require that the probing laser linger on the narrow spectral feature long enough to fully resolve it. The second perspective is the interference of the decaying precession of the excited ionic transition moments, called the free induction decay or FID, beats with the scanning probe beam to produce oscillations [19, 90, 179-182]. At first, this interference effect seems a major impediment to extracting material parameters with spectral holeburning, but the decay envelope of the beating between the FID and the probe beam directly yields the width of the hole. The FID is discussed further in the context of SHB measurement of Tm^{3+}:LaF_3 later on in this chapter.

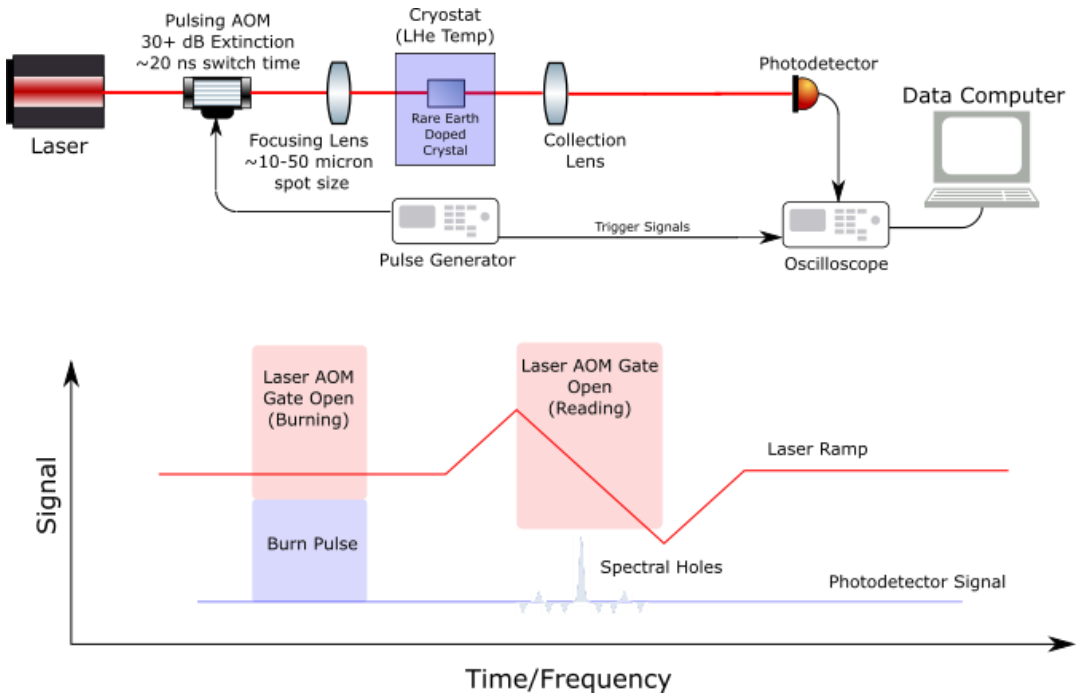

Figure 19. Spectral Holeburning experiment schematic. A burn pulse of variable length burns a pattern into an absorption, and a laser frequency scan is synchronized with another open gate to probe the burned pattern. The shown hole spectrum, comprising of sideholes and antiholes, emerges in a spin-1/2 system (as in thulium) in a magnetic field at liquid helium temperatures. Created using component library [140].

Results

Time-resolved fluorescence was recorded and spectral holes were burned and probed on the lowest-to-lowest $^3H_6 \Leftrightarrow {}^3F_3$ transitions, and the results are summarized in table 5. Discussion of the details follow.

	CaF_2: C_{4V}	**CaF_2: C_{3V}**	**BaY_2F_8**	**$YLiF_4$**	**LaF_3**	**KPb_2Br_5**
Wavelength (nm)	682.156	694.502	688.78	685.07	689.556	698.637
T_1 Lifetime (μs)	0.61	1.30	0.69	-	1.31	99.9
Narrowest Spectral Hole Measured (MHz)	25.9	-	10.9	8.4	0.38 (Temperature-limited)	~20 (Laser-limited, homemade Littrow laser)

Table 5. Summary of the $^3F_3$ survey results. The $^3H_6 \Leftrightarrow {}^3F_3$ lowest to lowest transition of the Tm^{3+}:KPb_2Br_5 material was not reachable with the Littman-Metcalf EOSI laser. The Littrow configuration has broader linewidth, resulting in a much higher upper bound on the transition linewidth. No holeburning was measurable on the C_{3V} site of CaF_2, and the lifetime of the Tm^{3+}:$YLiF_4$ transition was not measured due to insufficient signal. The general trend is that the width of the spectral hole decreases with lower Debye Temperature. The T_1 is markedly increased in the case of Tm^{3+}:KPb_2Br_5, with the lowest Debye temperature, indicating that the non-radiative relaxation rate from $^3F_3$ has fallen off significantly. The spectral hole measured in Tm^{3+}:KPb_2Br_5 was limited by the laser used to reach that transition and experimental conditions and does not measure the true homogeneous linewidth.

Tm^{3+}:CaF_2

Strickland and Jones measured the absorption and fluorescence of many of the multiplets of Tm^{3+} in deuterated CaF_2 [170]. While many of the line positions of the multiplets have been mapped out, time-resolved fluorescence and coherence measurements of $^3F_3$ have not been performed previously.

In this survey, fluorescence measurements showed that the C_{4V} site and C_{3V} site had lifetimes of 0.624 and 1.300 microseconds, respectively. Holes were burned to identify the lowest lines in

the spectrum belonging to the C_{4V} site. Only holes burned with long burn times of ~100 μs and focused power ~5 mW were detectable, resulting in a spectral hole width of 25.9 MHz. The short lifetime and poor holeburning properties render the C_{4V} site as unsuitable for UOT and SHB applications.

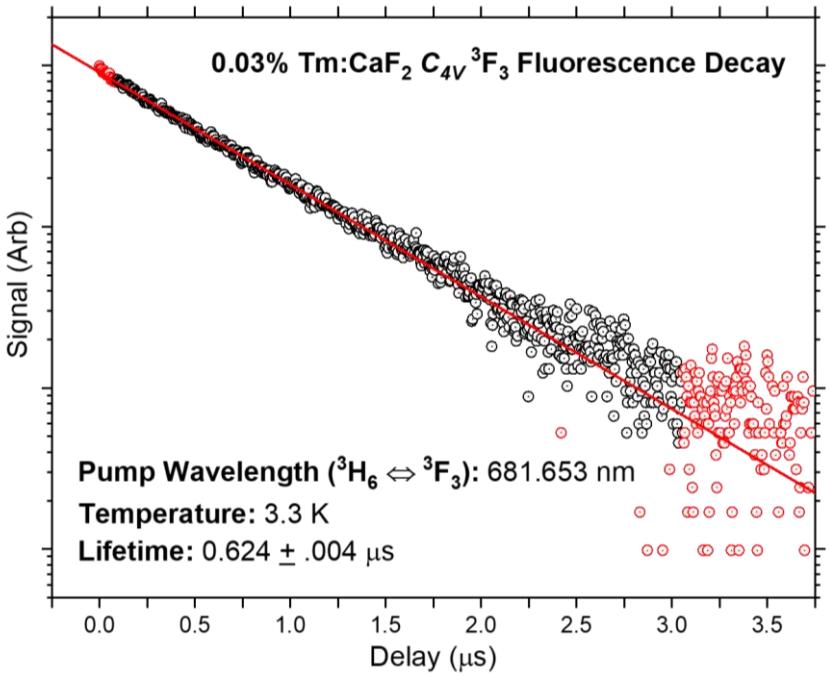

Figure 20. Time resolved fluorescence decay of the $^3F_3$ level in the C_{4V} site in Tm^{3+}:CaF_2.

The same measurements were attempted for the C_{3V} site, but the laser could not tune to the lowest-to-lowest transition for holeburning measurements. Since the C_{3V} site has a longer lifetime, it may have superior properties compared to the C_{4V} site. However, they are likely to be limited by non-radiative relaxation.

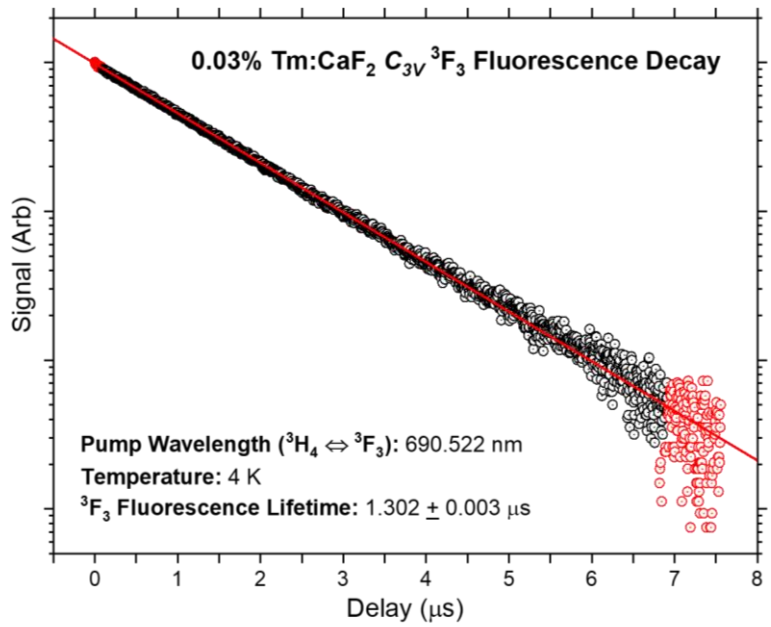

Figure 21. Time resolved fluorescence decay of the $^3F_3$ level in the C_{3V} site in Tm^{3+}:CaF_2.

<u>Tm^{3+}:BaY_2F_8</u>

Little in the way of low-temperature spectroscopy has been found in current literature on Tm^{3+}:BaY_2F_8, though it has been investigated as a laser material [24, 26, 171].

In our measurements, line centers of the crystal field levels in the $^3F_3$ multiplet were mapped out by tuning the laser to places of minimum transmission and recording their position with the wavemeter are shown in table 6. Fluorescence from the $^3F_3$ manifold was weak but measurable, with a lifetime of 0.69 microseconds. In the low-power limit, 10.9 MHz-wide holes were burned.

Line centers (nm):	684.59	685.24	686.55	686.65	688.78

Table 6. Observed linecenters of $^3H_6 \Leftrightarrow {}^3F_3$ transitions in Tm^{3+}:BaY_2F_8 with laser absorption at 3K.

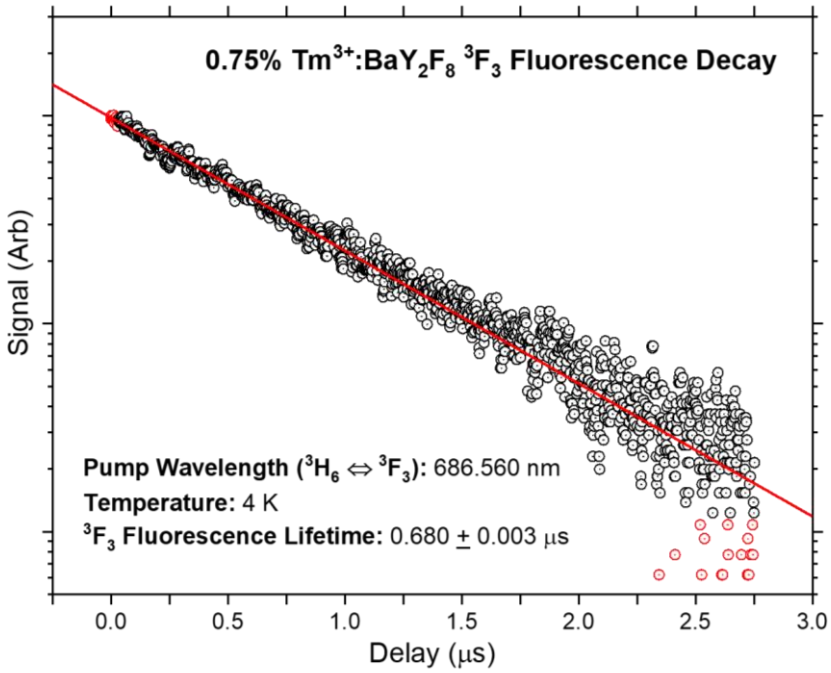

Figure 22. Time resolved fluorescence decay of the $^3F_3$ level in Tm^{3+}:BaY_2F_8.

<u>Tm^{3+}:$YLiF_4$</u>

Dulick et al. measured the low-temperature white-light absorption spectrum of Tm^{3+}:$YLiF_4$, and determined the energy level structure and transition energies down to 10 K [172].

In our survey, fluorescence intensity was very low upon excitation to the $^3F_3$ manifold down to 4 K with the EOSI laser, and the T_1 lifetime was not measured. Holeburning on the lowest to lowest $^3H_6 \Leftrightarrow {}^3F_3$ transition with long burn times and high intensity revealed a spectral hole width of 8.4 MHz, too large for UOT filtering, but improved over the CaF_2 and BaY_2F_8.

<u>Tm^{3+}:LaF_3</u>

Tm^{3+}:LaF_3 has been investigated in the past in detail [55, 56, 59, 75, 160, 183], with some SHB measurements of the $^3H_6 \Leftrightarrow {}^3F_3$ transition in LaF_3 nanocrystals by Macfarlane et al. In those measurements, strong fluorescence from the $^3F_3$ multiplet was reported.

For our survey reported here, the T_1 lifetime of $^3F_3$ was measured by exciting to the upper states of the $^3F_3$ multiplet, resulting in a single exponential decay of 1.31 μs from the lowest level. By way of eq. (9), this corresponds to a T_1-limited homogenous linewidth of ~122 kHz. Broadband absorption and fluorescence spectra were measured at 4 K, and polarized absorption spectra are shown in fig. 23. Fluorescence excited at the lowest level of $^3F_3$ was measured from $^3H_4$, producing an indistinct spectrum at lower energies with peaks obscured by satellite lines and a long tail from defects, shown in fig. 24. This prevents completely certain level assignments of $^3H_6$ levels for every case. This fluorescence structure likely arises from energy transfer to local structure defects in the crystal samples, as additional thulium sites were not observed by pumping other levels or in hole burning. Regardless, knowledge of the lowest-to-lowest absorption line positions and polarizations is sufficient for UOT and other SHB-based applications; typically only the lowest levels have good holeburning properties, though it is possible for transitions to upper crystal field levels to have good properties as well. The line centers were obtained by fits and are included in table 7.

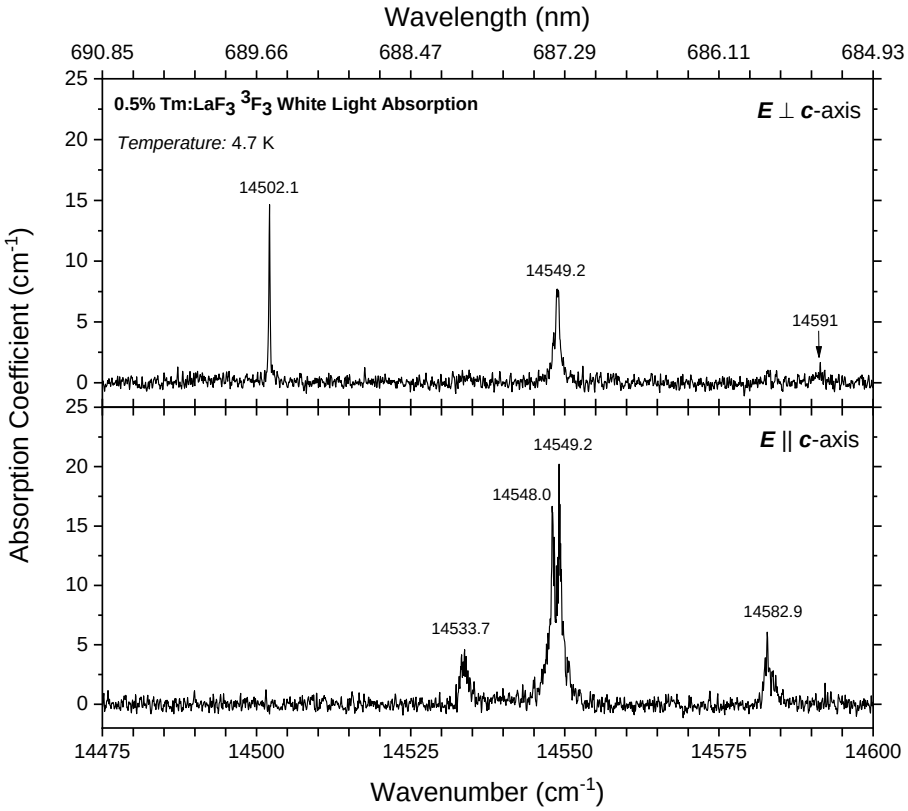

Figure 23. Broadband polarized absorption spectra of Tm^{3+}:LaF_3 at 4.7 K. (a) Top is polarized perpendicular to the crystal symmetry axis, and (b) bottom is polarized parallel to the c-axis.

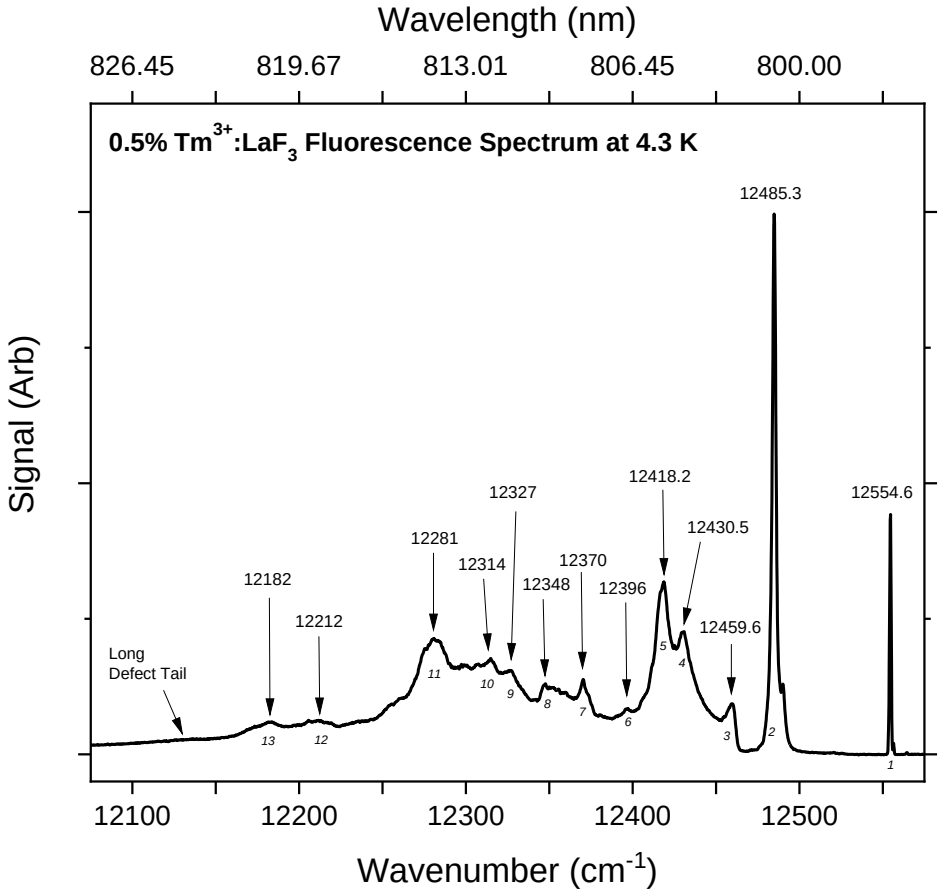

Figure 24. Fluorescence spectrum of Tm^{3+}:LaF_3 at 4.3 K, measured from the $^3H_4$ level. Peaks with obscured lineshapes were located by their maximum value instead of fitting. Distinct satellite lines such as on the second level are noted in table 7, but otherwise not attributed to the main energy level structure.

Manifold	Level	Energy (cm^{-1})	Comment
			Unpolarized fluorescence from $^3H_4$:
$^3H_6$	1	0	Strong, small satellite peak present
	2	69.3	Strong, satellite peak present
	3	95	
	4	124.1	
	5	136.4	
	6	159	Indistinct
	7	185	
	8	207	Indistinct
	9	228	Indistinct
	10	241	Indistinct
	11	274	
	12	343	Weak, broad
	13	373	Weak, broad
			In polarized absorption from $^3H_6$:
$^3H_4$	1	12554.6	Strongly polarized ⊥ ***c***-axis, [55]
			In polarized absorption from $^3H_6$:
$^3F_3$	1	14502.1	Strongly polarized ⊥ ***c***-axis
	2	14533.7	Polarized ‖ ***c***-axis
	3	14548	Polarized ‖ ***c***-axis
	4	14549.2	Polarized ‖ ***c***-axis
	5	14582.9	Strongly polarized ‖ ***c***-axis
	6	14591	

Table 7. Observed energy levels from absorption and fluorescence. Previous work on this structure at liquid helium temperatures can be seen in ref. [160].

Continuing with our measurements, laser absorption of the lowest to lowest transition of $^3H_6 \Leftrightarrow {}^3F_3$ was performed to precisely measure its transition frequency as a function of temperature and absorption coefficient. The absorption coefficient propagating and polarized perpendicular to the ***c***-axis was found to be sufficiently strong for UOT filtering requirements in the 0.5% sample at 15.2 cm^{-1}. In comparison, the absorption coefficient of the $^3H_6 \Leftrightarrow {}^3H_4$ transition was measured to be 2.8 cm^{-1} in the 0.5% sample. The absorption of the 0.1% and 0.5% samples are plotted alongside each other in fig. 25. No absorption was measurable polarized parallel to the ***c***-axis.

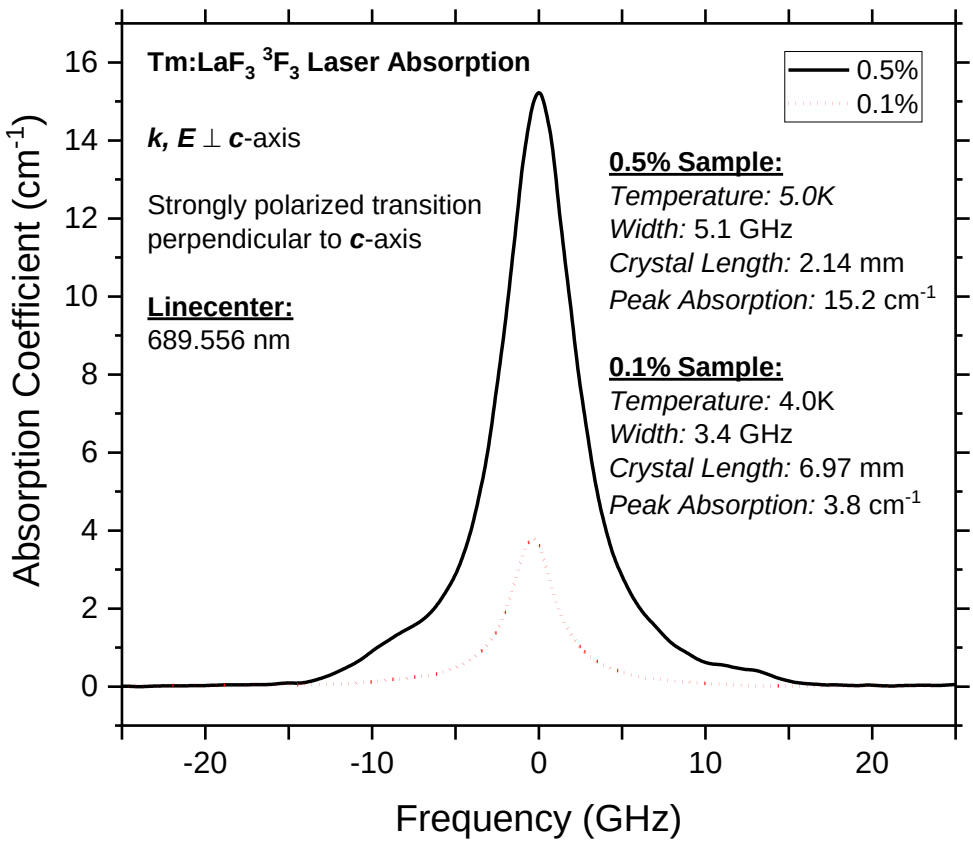

Figure 25: Laser absorption for Tm^{3+}:LaF_3 at 4.0 K, both polarized and propagating perpendicular to the ***c***-axis. No absorption was measurable polarized parallel to the ***c***-axis.

The linecenter of the transition was then measured with increasing temperature out to 30 K. The results are plotted in fig. 26. The data were fit to the non-resonant process of McCumber [184-186] and with the direct process model described by Böttger et al. [106], which was derived from the general form of Imbusch [187]. The resonant process described by Böttger et al. more accurately describes the lineshift due to the presence of nearby crystal field levels that readily exchange phonons. This effect overshadows the non-resonant processes that dominate the isolated energy levels that McCumber originally modeled in ruby, described by the Raman 2-phonon model in fig. 26. The respective limits of the energy level structures are discussed in ref. [57].

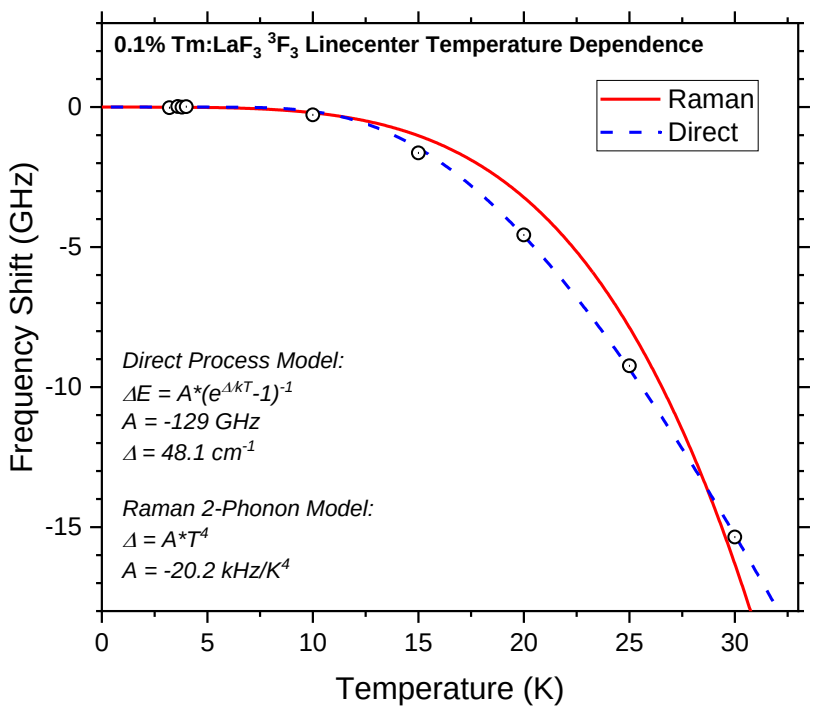

Figure 26: Temperature dependence of the lowest to lowest absorption of $^3F_3$ and the comparison of the Raman and direct process models. Here the resonant phonon interaction better explains the lineshift. Error bars are not included on the points because the random error is very small, and much less than any possible systematic error.

Narrow holes were burned and probed in the lowest-to-lowest transition of $^3H_6 \Leftrightarrow {}^3F_3$ to estimate the homogeneous linewidth and the minimum filter width possible. Beats of the probe beam with the free induction decay (FID) were detected, shown in fig. 27. The FID is the coherent precession of excited atoms in the bandwidth of the hole. The FID is generated when the excitation pulses induce a net polarization $\boldsymbol{P}$ in the ensemble atomic transition moments, all initially phased relative to the excitation laser. The re-radiation of $\boldsymbol{P}$ decays as the atoms dephase relative to each other, and then the excited population incoherently fluoresces instead. The FID can be detected on an optical detector by beating it with a probe beam [19, 90, 179].

The FID decays at the rate dictated by its Fourier relationship to the holewidth, and both the laser and homogeneous linewidth contribute to the burned hole. From Macfarlane in ref. [180], the explicit relationship of the FID decay time T_{FID} to the coherence time T_2 is given as $T_2 = 2T_{FID}$ in the zero-intensity limit. However, $2T_{FID}$ will almost always be shorter than the coherence time T_2, due to the contributions of the laser width to the width of the burned hole. Therefore, the relation should be relaxed to $T_2 \geq 2T_{FID}$, and the longest measurable T_{FID} is sought to determine the intrinsic material properties by minimizing the laser contributions to the hole width [19, 112, 175]. The narrowing of the burned hole may be accomplished principally by limiting the laser burn time and laser power as much as possible without fully eliminating the signal, which was done for these measurements. Further improvements can be made by narrowing and stabilizing the burning and probing laser itself. The FID decay time is then maximized to determine the minimum measurable holewidth.

The upper bound on the width of the homogeneous linewidth from an FID measurement may therefore be estimated as $\Gamma_h \leq 1/(2\pi T_{FID})$. From the zero-power limit and derived from the Bloch equations, the minimum width of a spectral hole Γ_{SH} that can be burned in this transition is $2\Gamma_h$, twice the homogeneous linewidth [19, 60, 175]. Note that in ref. [175] and in many other places, the full width at half-maximum determined from the steady-state Bloch equations is given in angular frequency, and is converted to frequency by dividing by a factor of 2π.

The FID decay constant T_{FID} was measured to be 0.83 μs, resulting in an upper bound on the homogeneous width Γ_h of 190 kHz, which also implies that T_2 is at least 1.7 μs. By means of $\Gamma_{SH} = 2\Gamma_h$, the hole burned is 380 kHz [60]. The T_1 contribution is 122 kHz, which is determined from the fluorescence lifetime of 1.31 μs and eq. (9). Subtracting the lifetime contribution from the homogeneous width, 68 kHz of additional broadening in Γ_h remains unaccounted for. The remaining sources of broadening are likely to be dominated by the relatively high temperature (4K) of the sample and the laser width. Further cooling of the sample and stabilization of the laser could eliminate the remaining broadening.

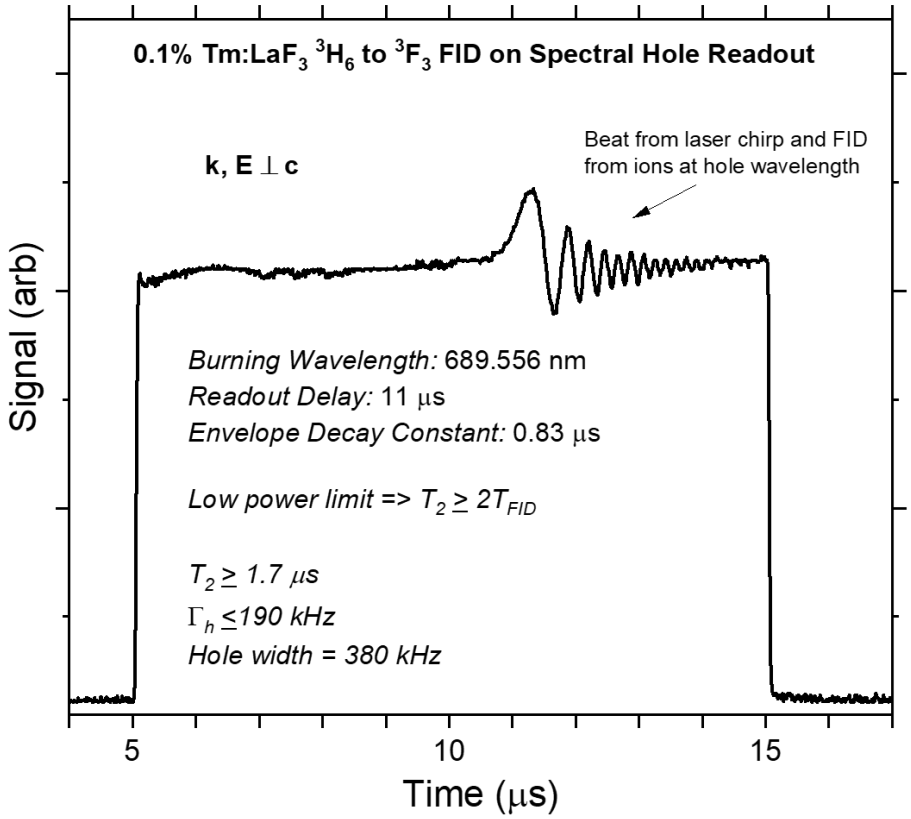

Figure 27: FID in Tm^{3+}:LaF_3, measured at 4 K. The excited ions freely precess after the burning pulse (not shown) is shut off, and the scanned laser (shown) beats with the excited ions of the hole.

To check whether the other observed transitions in the absorption spectrum arise from only higher $^3F_3$ crystal field levels or from differing thulium sites, attempts were made to burn holes in each absorption. Holeburning was only observed on the lowest energy transition at 689.556 nm, and no additional hole structure was observed on that transition, suggesting that there is only a single thulium site.

The lifetime of spectral holes affects the intervals at which the UOT filter must be refreshed by re-burning, which in turn affects image integration times. Time-resolved holeburning was used to monitor the population dynamics of relaxation from $^3F_3$ that affect the hole lifetime as

shown in fig. 28. The spectral hole area was measured at each point instead of the amplitude, to account for fluctuations of hole depth and width.

A three-level system of $^3H_4$, $^3F_4$, and $^3H_6$ was assumed, since all the population in the relatively short-lived upper crystal field levels and $^3F_3$ and $^3H_5$ manifolds decay rapidly compared to the long-lived bottleneck states below them. For lifetimes τ_i, branching ratio β, and population fraction $N(t)$ in the ground state, these assumptions result in the following population model:

$$N(t) = \left(1 - e^{-\frac{t}{\tau_1}}\right) + \frac{\beta\tau_2}{\tau_2 - \tau_1}\left(e^{-\frac{t}{\tau_1}} - e^{-\frac{t}{\tau_2}}\right) \tag{11}$$

In eq. (11), $^3H_4$ is level 1, and is populated through non-radiative relaxation from $^3F_3$. The bottleneck $^3F_4$ is identified by level 2 subscripts. Because the pumping manifold, $^3F_3$, is not part of the analysis, this formula differs from that in ref. [67]. The branching ratio is divided by two because the stimulated emission term in that case is not present in this population model.

By fitting to eq. (11), the lifetime of the lowest level of $^3H_4$ was found to be 3.4 ms, the lifetime of the lowest level of $^3F_4$ was determined to be 15.7 ms, and 39% of the $^3H_4$ population decayed to $^3F_4$. These values are consistent with the measurement by Hong et al. in ref. [183] and other measurements of thulium-doped materials [138].

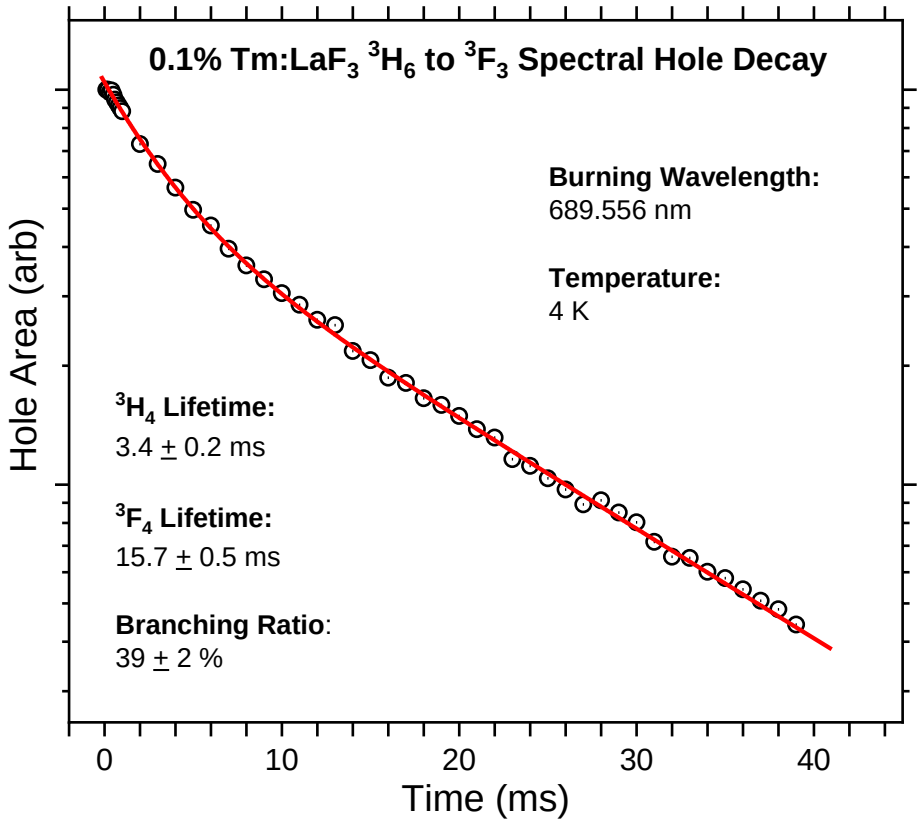

Figure 28: Time-resolved transient hole area decay of Tm^{3+}:LaF_3. The fit to the multi-level decay described by eq. (11) is indicated by the solid line.

<u>Tm^{3+}:KPb_2Br_5</u>

Extensive work has been done on the alkali lead halides for Mid-IR lasers [174], though little of their properties appear to have been investigated at liquid helium temperatures.

In our measurements on our homegrown sample of Tm^{3+}:KPb_2Br_5, the lowest energy absorption peak was measured with white light to be 689.63 nm at 4K. Weak polarization dependence was observed, with an unpolarized absorption coefficient of 1.7 cm^{-1}. Using the homemade Littrow laser tuned to the lowest-to-lowest energy transition, laser-limited holes ~20 MHz wide were burned into the transition that lasted ~100 ms. AOM-pulsed time-resolved

fluorescence measured the $^3F_3$ lifetime as being ~100 μs, as shown in fig. 29. More of these measurements are discussed in chapter 5.

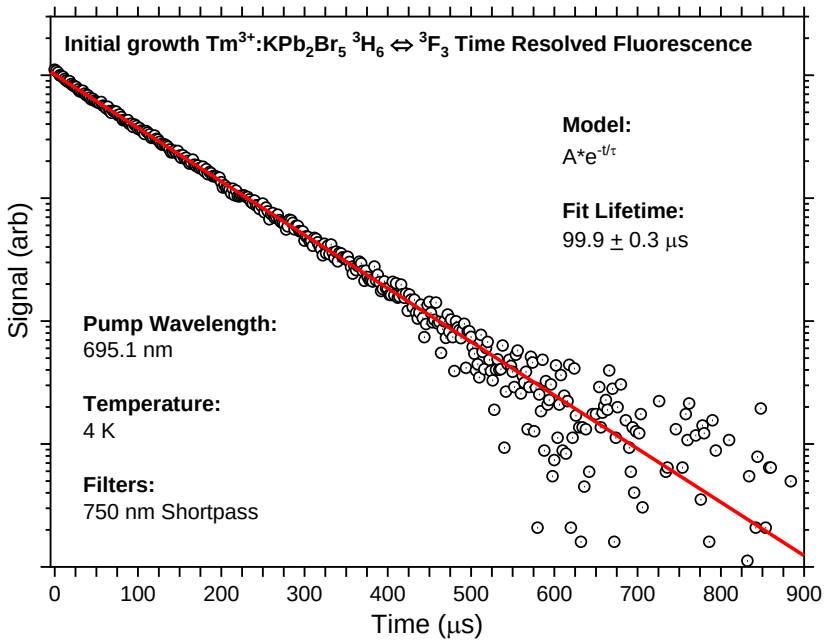

Figure 29. Time-resolved transient fluorescence decay of the lowest level of $^3F_3$ of Tm^{3+}:LaF_3, and fit to a single exponential decay. A 750 nm short pass filter is used to filter out the decay of $^3H_4$ at ~795 nm and longer.

Discussion

The principal goal of these experiments was to identify a rare-earth optical transition around 690 nm with low phonon-mediated relaxation and decoherence, and strong absorption. The results, summarized in table 5, demonstrate the impact on the homogeneous linewidth of the $^3H_6 \Leftrightarrow {}^3F_3$ transition of thulium by selecting host materials with lower Debye temperatures. LaF_3 and KPb_2Br_5 show the greatest improvements to the T_1-limited minimum filter bandwidth on the $^3H_6 \Leftrightarrow {}^3F_3$ transition. The Debye temperature can therefore be used as a figure of merit for improving the properties of optical transitions limited by non-radiative decay, since it

encapsulates several relevant material parameters, such as hardness, density, and the speed of sound of the host material. Other transitions may likewise be engineered for SHB applications in a similar manner. For example, holmium is also a non-Kramer's ion that has several transitions in the tissue-optical window that are non-radiatively limited and that may be useful for UOT [178, 188]. Other ions likewise have many potentially interesting transitions for many applications [75]. Semiconductors and their optical applications should not be overlooked, as many possess low Debye temperatures as well [11, 29, 189-192]. Overall, this approach is a generally useful framework for enabling applications based on rare-earth transitions that were previously unusable due to non-radiative relaxation via phonons to nearby energy levels.

The spectroscopy of Tm^{3+}:LaF_3 performed in this survey reveals several attributes that make it attractive for UOT. This crystal system is among classic optical spectroscopy materials and is available in centimeter or larger sizes [183]. Consequently, large filters of LaF_3 can be fabricated for high etendue. In addition, if the ***c***-axis is oriented parallel to the light propagation axis ***k***, the optical properties of LaF_3 become isotropic and insensitive to polarization. This feature allows the depolarized scattered light collected from the tissue to be used directly for greater throughput and potentially superior carrier suppression in comparison to Pr^{3+}:YSO systems, which are polarization-sensitive [36]. Transient holes can be burned at 3K for inscribing filters onto the transition, which is within the temperature span of many commercial cryocooler systems. Long-lived persistent holes could also be burned into the nuclear spin levels of thulium by applying a magnetic field for even longer image integration times. For two-color UOT devices [37], the work in this paper and by Macfarlane in ref. [55] shows that holeburning may be performed on both the $^3H_6 \Leftrightarrow {}^3F_3$ and $^3H_6 \Leftrightarrow {}^3H_4$ transitions simultaneously in the same crystal. Considering that

the narrowest spectral hole reported here were temperature and laser-limited, further investigations into the ultimate limits of performance of Tm^{3+}:LaF_3 for oxygenation-sensitive UOT at 690 nm are needed, as well as exploration of magnetic field dependence for long-lived persistent holes.

Tm^{3+}:KPb_2Br_5 is also of interest for UOT at 690 nm with its long T_1 lifetime of ~100 μs. However, several issues limit its practicality. First, the Tm^{3+} ion is small for the Pb^{2+} site, and the segregation coefficient is ~20% in KPb_2Br_5 [159]. Achieving enough absorption for suppression therefore is difficult. The symmetry is also monoclinic and lower than LaF_3; compensating will add to the device complexity. The material is also not as easily obtained commercially and is principally grown in labs for study of mid-IR (3-10 μm) lasers [13, 16, 21, 22, 27, 159, 169, 193, 194]. The lowest-to-lowest transition is also shifted towards 700 nm, where laser diodes able to tune to the transition are harder to obtain.

To determine the limits of performance of the $^3H_6 \Leftrightarrow {}^3F_3$ transition in Tm^{3+}:LaF_3 for general SHB applications, further high-resolution coherence spectroscopy is needed to measure the homogeneous linewidth more accurately. Magnetic field studies are also needed to determine the ground state Zeeman level lifetimes, which can enable persistent holes.

Conclusion

The practicality of any device depends on available materials, and so fundamental materials research is necessary to find and tailor materials to the application. In this case, a survey of SHB materials was undertaken to identify a host material that would support narrow holes on the $^3H_6 \Leftrightarrow {}^3F_3$ transition of thulium. This transition of the rare earth thulium was engineered to suppress non-radiative relaxation from $^3F_3$ through selection of host materials with lower Debye

temperatures, resulting in narrow holes in Tm^{3+}:LaF_3 and long lifetimes in Tm^{3+}:KPb_2Br_5. This study indicates further that the high absorption and sub-MHz holeburning of the $^3H_6 \Leftrightarrow {}^3F_3$ transition of Tm^{3+}:LaF_3 makes it a strong candidate for implementing oxygen-sensitive UOT devices. Overall, the study of this formerly uninteresting transition has provided newly available wavelength to enable the next generation of a high-tech medical imaging device.

If phonons are a limiting factor due to small energy gaps arising from nearby energy levels, the Debye temperature has been shown to be a useful figure of merit that gauges the relative contribution of phonon-mediated non-radiative relaxation and decoherence in a transition. Selection of soft, dense host materials can significantly impact the properties of rare earth transitions and enable new applications on them. This approach to host material design is broadly useful to the larger field of rare-earth doped materials research, which is applied in chapter 5 to the study of the $^3H_4 \Leftrightarrow {}^3F_3$ transition in Pr^{3+}:$RbPb_2Br_5$, located at ~1584 nm, which is also strongly limited by nonradiative relaxation from the $^3F_3$ to the nearby $^3H_2$ manifold.

CHAPTER FOUR

DECOHERENCE AND MAGNETISM OF THULIUM-DOPED LANTHANUM TRIFLUORIDE FOR ULTRASOUND-OPTICAL TOMOGRAPHY

In this chapter, photon echoes and persistent spectral holeburning on Tm^{3+}:LaF_3 are performed to probe the coherence and magnetism of the material and optimize the $^3H_6 \Leftrightarrow {}^3F_3$ transition for spectral filtering applications. Afterwards, simulations of spectral holes burned into $^3H_6 \Leftrightarrow {}^3F_3$ indicate that the transition is suitable for oxygenation-sensitive UOT and other SHB filtering applications. The high-resolution spectroscopy of rare-earths reported here has introduced this transition to both more measurements and advanced applications.

The work presented here was in direct cooperation with Dr. Stefan Kröll and Alexander Bengtsson of Lund University. The research visit by Alex was both a pleasure and extremely productive. We are grateful for the samples of Tm^{3+}:LaF_3 provided by Dr. Roger Macfarlane.

Introduction

The data presented in chapter 3 showed that rare-earth transitions can be engineered to suppress phonon-mediated broadening of the homogeneous linewidth by selecting denser, softer host materials with smaller phonon cutoff energies. The material Tm^{3+}:LaF_3 was also identified as an attractive candidate for oxygen-sensitive UOT filtering at 690 nm with the $^3H_6 \Leftrightarrow {}^3F_3$ transition. However, significant improvements could be made through further exploration of the Tm^{3+}:LaF_3 parameter space. The upper limit on the homogeneous linewidth was measured to be ~190 kHz at 4K and could reach the T_1 limit of ~120 kHz in lower temperature regimes. Narrower linewidths enable sharper filters to be inscribed on the transition, and thus enable

lower-frequency UOT, which has the advantage of greater penetration depths [78]. Moreover, the thulium ion possesses a spin-1/2 nuclear moment for persistent holeburning into the long-lived nuclear states, which would enable more flexibility in engineering system refresh rates and light integration times. The lowest to lowest $^3H_6 \Leftrightarrow {}^3H_4$ transition also has been explored by Macfarlane [55, 56]. The ~795 nm transition shows promise for correlation with the oxygenation-sensitive UOT in an alternative filtering system, or even in a two-color system [37, 38]. Overall, the optimal configuration for Tm^{3+}:LaF_3 should be determined for spectral filtering applications and understanding of the material physics taking place on the atomic scale.

In this chapter, the properties of the lowest to lowest line at 689.556 nm, referred to hereafter as $^3H_6 \Leftrightarrow {}^3F_3(1)$, in Tm^{3+}:LaF_3 are measured with photon echoes and Zeeman spectroscopy to optimize the material for UOT. The temperature dependence of the homogeneous linewidth of the transition was mapped out with photon echo measurements, with a T_1-limited linewidth of 117 kHz at 1.6 K. Instantaneous spectral diffusion (ISD) and spectral diffusion were not detected [17, 56, 64, 67, 107, 109]. Persistent spectral holeburning (PSHB) [19, 62, 66, 67] into the nuclear states of thulium in an applied magnetic field was observed on both the $^3H_6 \Leftrightarrow {}^3F_3(1)$ and $^3H_6 \Leftrightarrow {}^3H_4(1)$ transitions, whose lifetimes depended linearly on the field strength and were measured to last as long as two hours at 500 mT. No spin-flip sidebands were observed in the holeburning spectra, indicating low magnetic coupling to the neighboring fluorine spins. Simulations of filter performance based on the measured properties project are presented, and project that an actual oxygen-sensitive UOT device based on the $^3H_6 \Leftrightarrow {}^3F_3$ transition alone in Tm^{3+}:LaF_3 is both feasible and practical.

Experimental

Measurements were performed on the same samples of 0.1% and 0.5% Tm^{3+}:LaF_3 obtained on loan from Dr. Roger Macfarlane of IBM as described in chapter 3.

A ~100 kHz-linewidth EOSI Littman-Metcalf external cavity diode laser was used for the $^3H_6 \Leftrightarrow {}^3F_3(1)$ transition at 12554.6 cm^{-1}, while a ~100 kHz Coherent 899-21 Ti:Al_2O_3 ring laser was used to study the $^3H_6 \Leftrightarrow {}^3H_4(1)$ transition at 14502.1 cm^{-1}. A Stanford Research Systems DG645 was used to generate pulses to synchronize timings, and a DS345 to make triangle ramps to scan the lasers. The absolute wavelengths of the lasers were measured with a Burleigh WA-1500 wavemeter. The EOSI laser was gated with a single Crystal Technology Inc. 3080-125 acousto-optic modulator (AOM) driven at 80 MHz with a PTS 500 frequency synthesizer, with greater than 30 dB of measured extinction and 20 ns of rise time, and laser diode current chirps were used to scan the EOSI laser to read out spectral holes and features. The Ti:Al_2O_3 laser was gated by two synchronized AOMs in series for more than 40dB of extinction. The laser wavelength was scanned with a double-pass AOM calibrated with the wavemeter. All measurements were digitized by a Tektronix TDS 754C oscilloscope unless stated otherwise.

Coherence times of $^3H_6 \Leftrightarrow {}^3F_3(1)$ transition were measured with echoes in the 0.5% sample in the Montana Instruments (MI) prototype xp100 cryostat. Two-pulse photon echoes were excited with 300 and 400 ns pulses, and three-pulse echoes used 350-350-350 ns pulses. Echoes were detected with an AOM-gated R928 PMT, timed to reject the excitation pulses while admitting echo pulses. Total echo power was measured by integration of time-averaged echo areas after subtracting the background signal.

Measurements of persistent spectral hole burning were performed in magnetic fields up to 750 mT, supplied by the Montana Instruments magneto-optic option, whose temperature floor was limited to 3.5 K. Holes were optimized for long measurement times with ~10 second burn times and high power to burn large, power-broadened trenches to saturation. The spectrum was then probed by scanning the burning laser frequency. The integrated area of the hole and side structure was used to track the total population during the decay. The dependence of the hole spectrum on field strength and orientation was measured by burning holes in a magnetic field and scanning the laser across the spectrum in transmission. These scans were calibrated with two-tone holeburning; that is, two laser frequencies were created by jumping the RF driving signal on the AOM by tens of megahertz and measuring the difference in time on the trace between the two persistent holes. The persistent hole lifetime is long enough that the jump was done manually by directly adjusting the synthesizer. Similarly, the quadratic Zeeman effect of the $^3H_6 \Leftrightarrow {}^3F_3(1)$ transition was measured by tracking the main hole with the laser and measuring the change in wavelength from the initial burning wavelength with the wavemeter as the magnetic field was varied.

Zeeman Spectral Holeburning: Experiment Primer

The practical reasons for studying the Zeeman effect in the context of rare-earth doped materials are manyfold; a few are described here. First, Zeeman measurements are extremely useful in illuminating the critical issues in rare-earth magnetism, and understanding the interactions that drive atomic-scale dynamics is of general scientific interest. Second, in terms of applications, long-lived ground state spin storage systems are essential to QIS and quantum communication research [17, 19, 32, 64, 72, 117, 134, 136, 148, 178]. Both nuclear and electron

spins also have an advantage of possessing very little or no spontaneous emission, due to the very low energy of their transitions [195, 196]. Non-Kramers ions are also frequently seen as an advantage, since the additional electronic magnetism complicates the spectral structure, and the Bohr magneton μ_B is over three orders of magnitude larger than the nuclear magneton μ_N. Therefore, moments arising from electron spins are much more sensitive to magnetic fluctuations in the local host environment compared to moments caused by nuclear spins. The direct consequence of this is that nuclear hyperfine levels can have extremely long lifetimes and their transitions can possess very low decoherence relative to both electron spin and optical transitions. The disadvantage of nuclear spin storage is that their decoherence that cannot be frozen out with low temperatures, as the energy gaps are usually minute relative to the electronic spin storage. Therefore, the limitation to both coherence and spin-lattice relaxation times is understanding of the magnetic environment and mapping out the critical parameters of the system in question. When the material is well-understood, extremely impressive results emerge, such as the six hour coherence time achieved in Eu^{3+}:YSO [72]. This was achieved by leveraging a point in the magnetic field orientation which rendered the ions insensitive to magnetic fluctuations and dynamic decoupling of neighboring spins from the lanthanide dopants.

To investigate the magnetism of rare-earth doped materials, holes can be burned into an inhomogeneously broadened absorption in a magnetic field to probe the spectrally unresolved magnetic splittings hidden in absorption line. This phenomenon occurs by pumping population out of the main hole and into side structure, which are levels shifted in energy by the intrinsic inhomogeneity relative to the burning laser frequency in the main hole. Side peaks of decreased absorption are called side holes, and side peaks of increased absorption are antiholes. In the case

of splittings caused by applied magnetic fields as in the Zeeman effect, the structure that appears is directly determined by the g-values and other magnetic properties [100, 101] at low fields and in inhomogeneously broadened absorptions, making Zeeman SHB extremely useful for mapping out magnetic interactions. Fig. 30 lays out the nuclear spin-1/2 hyperfine levels of thulium and the corresponding hole structure that should be observed in principle. Table 8 organizes the energies of the hole and antihole relative to the main laser frequency. Save for the application of a magnetic field to the sample, the experimental procedure and data collection is the same as the normal SHB layout described in chapter 3.

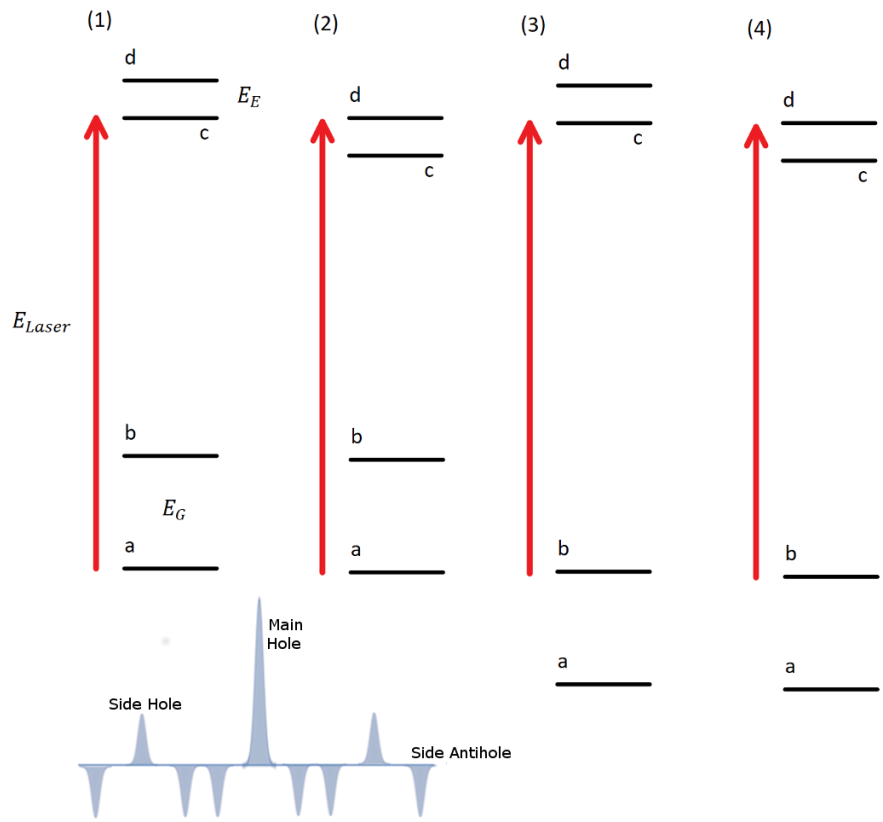

Figure 30. Example of spin-½ system split by magnetic fields, and the depiction of the hole and antihole structure that emerges in Zeeman SHB. Holes, or decreased absorption, that appear are correspond to excited state structure; antiholes, or increased absorption, correspond to sums and differences of ground state structure with excited state structure. The resulting spectrum is shown in the bottom left for the case $E_g > E_e$. Note a different ordering of holes and antiholes will appear with $E_g < E_e$, but antiholes will always emerge first with increasing field from the main hole.

	1	**2**	**3**	**4**
Holes	E_e	$-E_e$	E_e	$-E_e$
Antiholes	$-E_g$ $-E_g - E_e$	$-E_g$ $-E_g + E_e$	E_g $E_g + E_e$	E_g $E_g - E_e$

Table 8. Energies of side holes and antiholes in a spin-1/2 system (e. g. thulium), determined from fig. 30. Holes appear at $\pm E_e$, while antiholes appear at $\pm E_g$, $\pm(E_e + E_g)$, and $\pm(E_e - E_g)$ relative to the main hole, which occurs at the laser frequency.

Enhanced Nuclear Zeeman Effect

The enhanced nuclear Zeeman effect, exhibited by thulium [67, 126], is caused by the second order coupling of a nuclear spin to electronic magnetic moments, induced from $^{2S+1}L_J$ levels mixing in magnetic fields. These enhanced moments bridge the gap between the two extremes of nuclear and electron spins and even beyond [67, 88, 117, 178]. Thulium also has the dual advantages of being a non-Kramer's ion and of possessing a simple nuclear structure from a single stable isotope of spin 1/2. Thulium is therefore a very interesting case for researchers exploring hyperfine storage for applications as well as basic rare-earth magnetism.

Despite the seemingly close parallels in field dependencies and terminology, the mechanism of the enhanced nuclear Zeeman effect [117, 126, 197] is emphasized as being different from the canonical electronic linear and quadratic Zeeman effects [198, 199]. The first arises from a nuclear moment coupling with the magnetic moment generated by the mixing of electronic wavefunctions from an applied field; the latter is a consequence of an electron bound to a nucleus moving in an applied magnetic field. The nuclear Zeeman effect is weaker than either. The hyperfine interaction is likewise different than all of these. It can persist in zero field, because it is caused by the coupling of the nuclear angular momentum to the spin and orbital angular momentum of the electrons through either the nuclear magnetic dipole moment or the nuclear electric quadrupole moment. The case of the pseudoquadrupole moment is seen in chapter 5, in Pr^{3+}:$RbPb_2Br_5$, which has the form of the nuclear electric quadrupole interaction. Overall, all these interactions are quite different in origin, despite appearances.

Optical Coherence of Tm^{3+}:LaF_3

In chapter 3, free induction decay (FID) measurements on the $^3H_6 \Leftrightarrow {}^3F_3(1)$ transition suggested that temperature and laser linewidth contributed up to 68 kHz to the homogeneous linewidth. To determine the limitations to the linewidth, two pulse photon echo measurements as a function of temperature were made on the lowest to lowest transition at 689.556 nm. The results of a temperature sweep, shown in fig. 31, were fit to a model proportional to the direct phonon process, which describes the effect of the emission and resonant absorption of phonons between adjacent atomic energy levels [57, 106, 187]:

$$\Gamma(T) = \Gamma_0 + \frac{A}{e^{\frac{\Delta}{k_B T}} - 1} \tag{12}$$

In eq. (12), Γ_0 is the effective homogeneous linewidth, $k_B$is the Boltzmann constant, T is the temperature, and A and Δ are fit parameters.

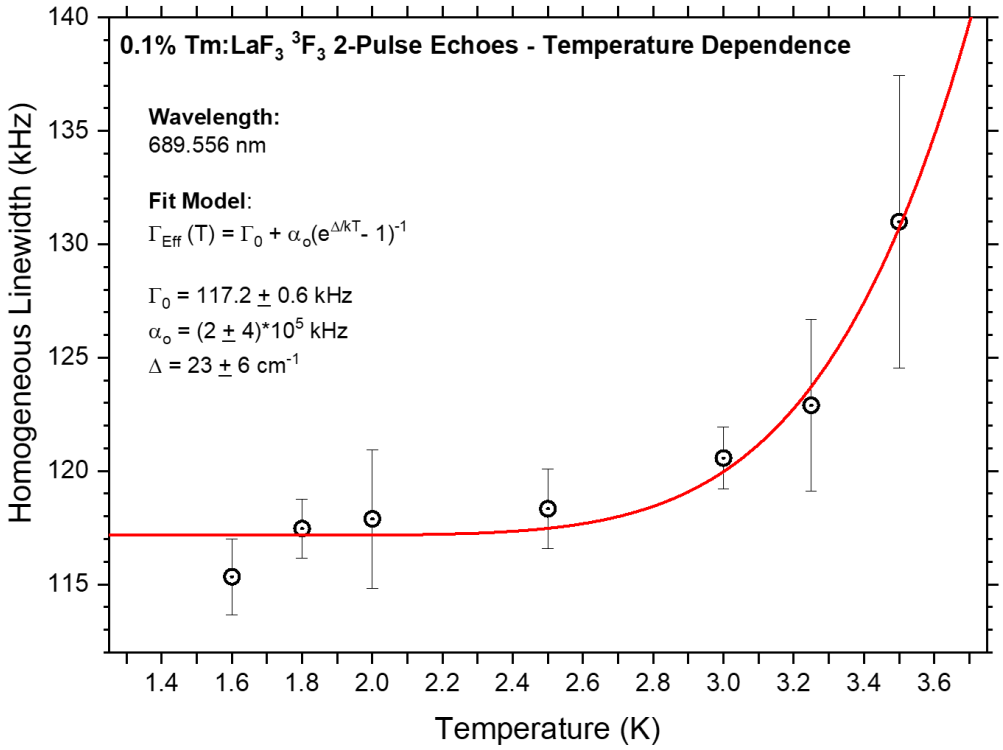

Figure 31: Temperature dependence of Tm^{3+}:LaF_3 homogeneous linewidth, varied between 1.6 and 3.6 K. The fit to eq. (12) is indicated by the solid line.

The fit indicates that a linewidth of 117 kHz for $^3H_6 \Leftrightarrow {}^3F_3(1)$ was achieved, all of which is the lifetime-limited width of 122 kHz measured in chapter 3 with fluorescence. Attempts were made to detect the presence of any other effects. Magnetic fields were applied to detect couplings to neighboring thulium and fluorine nuclear spins in modulated echoes [17], but no modulations were detected, and no change in the coherence properties were detected due to ISD when the excitation power was varied with or without fields [107]. These results are consistent with the T_1 lifetime limit being met. Additionally, three pulse photon echoes on the $^3H_6 \Leftrightarrow {}^3F_3(1)$ transition revealed no dependencies on waiting times, indicating little or no spectral diffusion [67].

The limiting decohering interactions on the $^3H_6 \Leftrightarrow {}^3H_4$ transition at 795 nm, in Tm^{3+}:LaF_3 have been characterized by Macfarlane in ref. [56]. There, Macfarlane measured a homogeneous linewidth of 45 kHz in $^3H_6 \Leftrightarrow {}^3H_4$ at 1.5 K and determined from the non-exponential decays that the decoherence of thulium in LaF_3 was dominated by coupling to fluorine spins [56]. As a crude estimate of a similar effect on the $^3H_6 \Leftrightarrow {}^3F_3(1)$ transition, the measurements of Macfarlane indicate the expected contributions of the fluorine spins to the homogeneous linewidth of the $^3H_6 \Leftrightarrow {}^3F_3(1)$ transition is likely below the T_1-limit.

Persistent Spectral Hole Burning

To extend the lifetime of spectral filters written to the crystal absorption spectrum beyond tens of milliseconds, PSHB through ground state storage in the spin-1/2 nuclear states was achieved through application of a magnetic field parallel and perpendicular to the crystallographic ***c***-axis of LaF_3. The relaxation rate of the persistent holes as a function of temperature and field was mapped out to gain further insight into the relaxation dynamics, shown in fig. 32 and fig. 34.

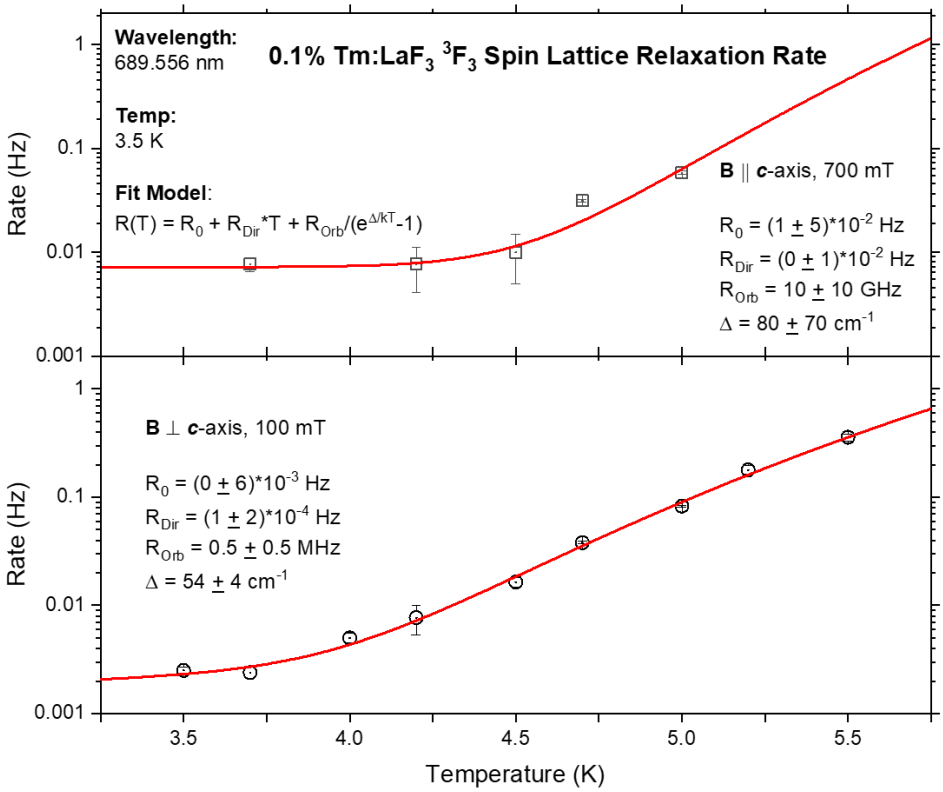

Figure 32: Example dependence of the "slow" persistent spectral hole lifetime burned into the $^3H_6 \Leftrightarrow {}^3F_3(1)$ transition in a field of 100 mT in Tm^{3+}:LaF_3 on temperature (a - top) parallel and (b - bottom) perpendicular to the ***c***-axis and fit to the inset equation. The model is from refs. [200] and [126]. The secondary "fast" lifetime was difficult to measure accurately at higher temperatures and is not shown.

Spin Lattice Relaxation

In fig. 32, the dependencies of the lifetime on the applied field and temperature were fit to the spin lattice relaxation model in refs. [200] and [126], in the limit where the thermal energy is large compared to the spin level splittings, but small compared to splittings of adjacent crystal field levels. This is reasonable at the experimental temperature range of ~3.5K, where the splittings by the nuclear Zeeman effect are not large compared to the thermal energy, but small compared to the next crystal field level (measured in chapter 3 as 69.1 cm^{-1}). These limits in the model yields:

$$\frac{1}{T_1^{SLR}} = R_0 + (R_{Direct} * T) + (R_{Raman} * T^n) + \frac{R_{Orbach}}{e^{\Delta/kT} - 1} \quad (13)$$

The meaning of the various terms is depicted in fig. 33. The first term is a residual relaxation rate at no field and zero temperature. The second term corresponds to the phonon direct process, which is the direct absorption or emission of a phonon, triggering a spin flip. In this limit of this model, the process is just proportional to the temperature T and the fit parameter R_{Direct}. The third term is the Raman process, modeled with $R_{Raman} * T^n$, which describes a phonon scattering off an ion, causing a spin flip, and carrying away with it a gain or loss of the energy difference $h\nu$ between the up and down spin states. In that term, T^n is the temperature, and in the case of thulium, a non-Kramers ion with no unpaired electron spins, a typical value for the exponent n is 7 [200]. However, in fig. 32, the Raman term is actually a negligible contribution at the measured temperature range. The final term describes the Orbach process, a process in which an atom is excited by a phonon of energy Δ from one spin level to a much higher level and relaxes with a phonon of $\Delta \pm h\nu$ to an adjacent spin level. In that term, $R_{Orbach} = r_{Orb}^0 + r_{Orb}^1 \boldsymbol{B}^2$ is fit parameter proportional on the square of the magnetic field, while kT is the thermal energy. The parameter $\Delta = \delta_0 + \delta_1 \boldsymbol{B}^2$ also depends on the square of the magnetic field [126]. At higher temperatures, the relaxation process described by eq. (13) is dominated by the Orbach contribution in the measured temperature range, as shown in fig. 32. In the limit where $\Delta >> kT$, this term may be simplified to $R_{Orbach} * e^{-\Delta/kT}$.

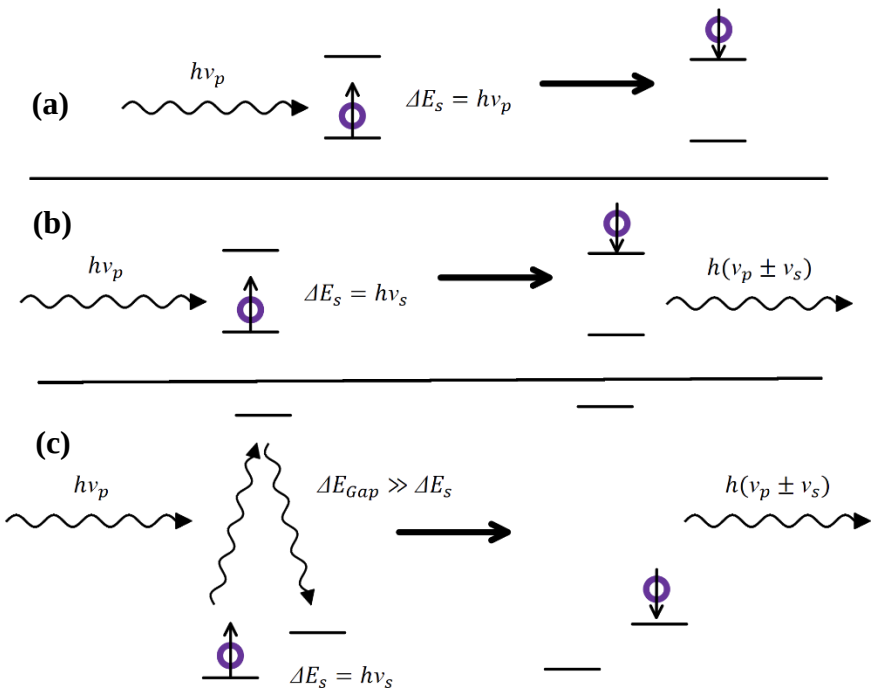

Figure 33. Processes of spin-lattice relaxation. (a) The direct phonon process. Emission is the mirror of this diagram. (b) The Raman process scatters a phonon off an atom, gaining or losing energy as it flips spin state. (c) The Orbach process absorbs a phonon and emits a lower or higher energy one in relaxing into the opposite spin state.

Spectral holes with lifetimes up two hours were measured for fields **B** ⊥ ***c***-axis at 500 mT, shown in fig. 34. Further increases in hole lifetimes may be possible at higher fields. For both directions of applied field, two independent exponential decays were observed, shown in fig. 34. The reason for the appearance of two decays for fields applied parallel to the ***c***-axis is unclear and is not explained by magnetic subsites formed by the projections of the field on rare-earth sites [56, 173]. If the field is parallel to the crystal symmetry axis, all rare-earth sites should possess the same g-value; for an arbitrary field direction perpendicular to the ***c***-axis, there should be three inequivalent magnetic subsites.

The nuclear lifetime was found to increase linearly with applied field ~***B*** across the entire measured range, shown in fig. 34 in terms of the spin lattice relaxation rate. However, the

accepted model is described in ref. [126], such that the lifetime is proportional to the fourth power of applied field strength, $\sim \boldsymbol{B^4}$, in the measured range of fields (<750 mT) and temperatures. The linear magnetic dependence of the spin-lattice relaxation process in Tm^{3+}:LaF_3 is irregular in light of other thulium doped materials such as Tm^{3+}:YAG [126] and accepted theories on spin-lattice relaxation [117].

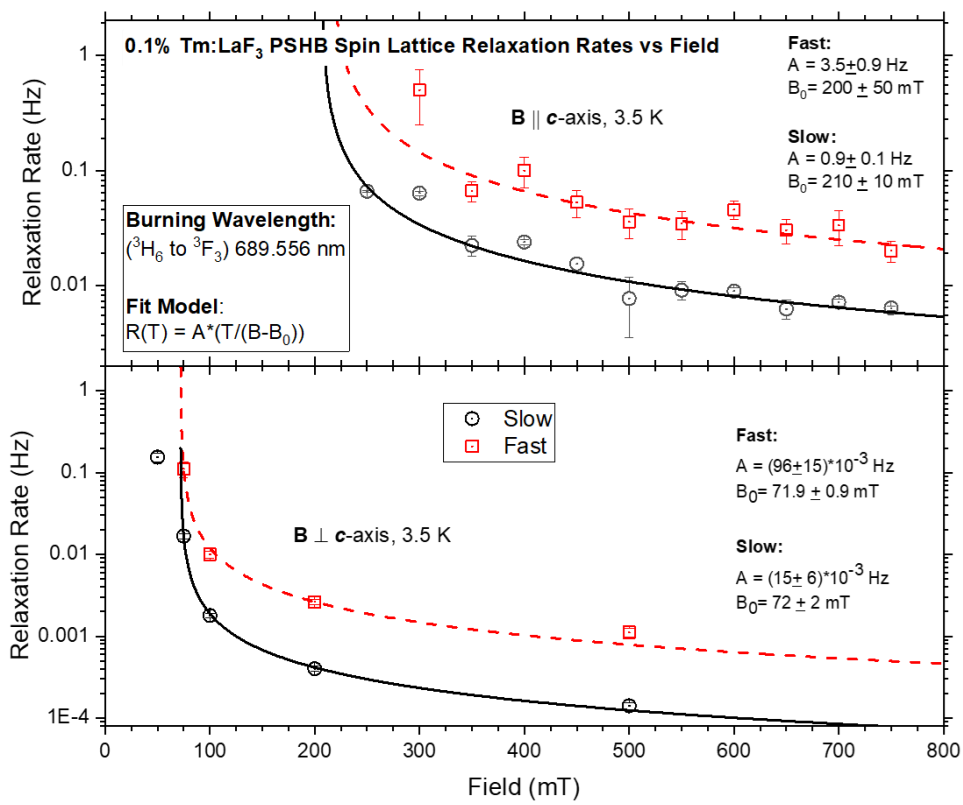

Figure 34: Dependence of the persistent hole relaxation rate ($1/T_1$) burned into the $^3H_6 \Leftrightarrow {}^3F_3$ transition in Tm^{3+}:LaF_3 on applied field (a - top) parallel and (b - bottom) perpendicular to the ***c***-axis. The T_1 lifetime of the nuclear spin states increased linearly with applied field from the minimum field point B_0, the threshold of field needed to observe any persistent holes.

Enhanced Nuclear Zeeman Effect

The implication of multiple magnetic subsites and unusual hyperfine relaxation dependence on field motivated further investigation with Zeeman SHB spectroscopy on both the $^3H_6 \Leftrightarrow {}^3H_4(1)$

and $^3H_6 \Leftrightarrow {}^3F_3(1)$ transitions. Due to technical limitations, full rotation dependence of the enhanced nuclear Zeeman effect with holeburning was not possible at the time of measurement. The dependence of the side structure of the persistent holes on field strength was plotted for both the field oriented parallel and perpendicular to the ***c***-axis, shown in fig. 35(a) and (b). No clear evidence of other magnetic subsites was observed in the Zeeman spectra, but the relative size holes and antiholes compared to the main hole and their ordering indicated that not all of the hole structure was observed.

The gyromagnetic ratio of the nucleus of fluorine is large at ~40 MHz/T, comparable to hydrogen, and inclusion in a crystal does not modify the nuclear moment greatly by itself [68]. Consequently, fluorine spins are often a feature in hole burning spectra as spin-flip sidebands [56, 68]. However, the signal of fluorine was not observed in the hole burning spectrum of Tm^{3+}:LaF_3, shown in fig. 35. The lack of obvious fluorine-induced decoherence or spin-flip sidebands implies there may be a mechanism to inhibit coupling of thulium to the strong magnetic moments of nearest-neighbor fluorine ions, or at least a mechanism to broaden these spin transitions to the point where they are difficult to observe directly. Understanding of this feature could be generally useful in mitigating spin-mediated decoherence.

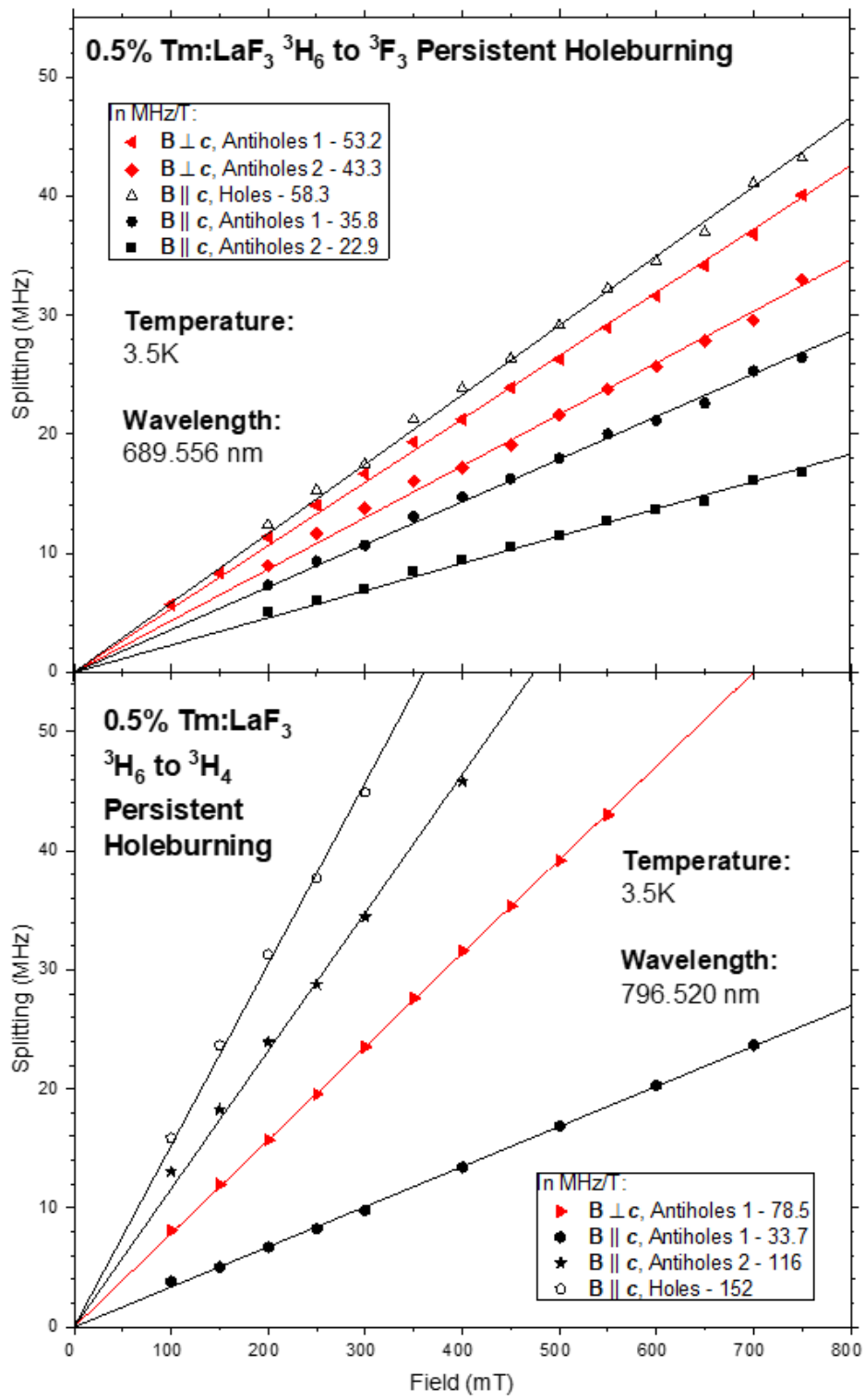

Figure 35: Split rates of the observed side hole and antihole structures of 0.5% Tm^{3+}:LaF_3, burned on (a – top) $^3F_3$ and (b – bottom) $^3H_4$, and fit to a linear dependence.

Quadratic Zeeman Effect

The quadratic Zeeman shifts of the hole spectrum were also mapped out in fig. 36 for the field applied perpendicular to the ***c***-axis. However, the full rotation dependence was not possible to determine the tensor elements, and so the measurements and discussions are restricted to explorations of the field dependence.

As long as the shifts are small relative to the crystal field splittings, the resulting shifts are proportional to $\sim\boldsymbol{B}^2$ [126]. The direction of the shift in fig. 36 is consistent with the spacing of the relative spacing of adjacent crystal field levels measured in absorption and fluorescence in chapter 3 [56, 75, 126, 160, 183]. The magnitude of the energy shift in any level by the quadratic Zeeman effect is inversely proportional to the energy gaps between the level in question and all other crystal field levels. The overall optical frequency shift is proportional to the difference in shifts between the ground and excited states in the transition. This is cast as:

$$\Delta\nu\sim(\sum_{n\neq i}\frac{1}{E_g-E_{g+1}})-(\sum_{n\neq j}\frac{1}{E_e-E_{e+1}}) \tag{14}$$

The gaps between the optical transition levels and the crystal field levels are generally large, such that only the adjacent level in each manifold matters. This results in a simpler form:

$$\Delta\nu\sim(\frac{1}{E_{g+1}-E_g})-(\frac{1}{E_{e+1}-E_e}) \tag{15}$$

From the measurements of chapter 3, the gap in the ground manifold $^3H_6$ is 69.1 cm^{-1}, while the gap in the excited manifold $^3F_3$ is 31.6 cm^{-1}. Consequently, the shift in the energy of the excited level dominates the overall shift in optical transition energy, and pushes the transition towards lower frequency, as seen in fig. 36.

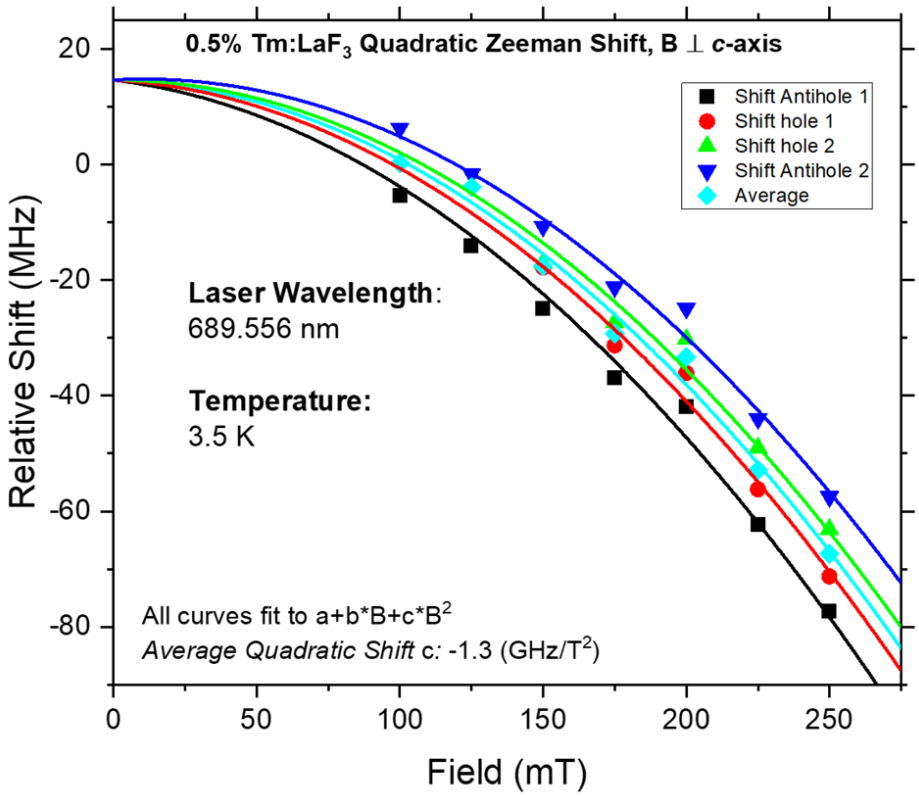

Figure 36: Quadratic shift of the holeburning spectrum in Tm^{3+}:LaF_3, burned into the lowest to lowest transition of $^3H_6 \Leftrightarrow {}^3F_3(1)$. Least squares fits to polynomials are indicated by solid lines, where the constant term was an arbitrary value and the linear term predetermined by distance from the main hole.

Discussion

Tm^{3+}:LaF_3 possesses several attributes which make it attractive for spectral filtering. This host crystal is among classic optical spectroscopy materials and has been grown to large sizes for many years [183], which admits high etendue. In addition, if the ***c***-axis is oriented parallel to the light propagation axis, the optical properties of LaF_3 become isotropic for both the $^3H_6 \Leftrightarrow {}^3H_4$ and the $^3H_6 \Leftrightarrow {}^3F_3$ transitions. This feature allows the depolarized light collected from the tissue to be used directly without polarization selection for superior throughput than anisotropic materials. Narrow holes can also be burned at either 690 nm on the $^3H_6 \Leftrightarrow {}^3F_3$ transition or at ~795 nm on

the $^3H_6 \Leftrightarrow {}^3H_4$ transition for filtering at oxygen-sensitive or insensitive UOT in a two-color arrangement within the same material [56]. However, while the absorption coefficient of the $^3H_6 \Leftrightarrow {}^3F_3(1)$ transition measured in the 0.5% sample in chapter 3 is enough for high-contrast filtering (15.2 cm^{-1} at the peak), the $^3H_6 \Leftrightarrow {}^3H_4$ transitions are comparatively weak at the same concentration of the thulium (~3.75 cm^{-1} at the peak). The absorption spectrum of $^3H_6 \Leftrightarrow {}^3H_4(1)$ is shown in fig. 37. A higher concentration crystal could rectify this issue, but may also introduce and magnify other detrimental effects such as ISD and broader homogeneous linewidths [107]. A thicker sample should be employed instead to optimize the $^3H_6 \Leftrightarrow {}^3H_4(1)$ transition of Tm^{3+}:LaF_3 for SHB applications.

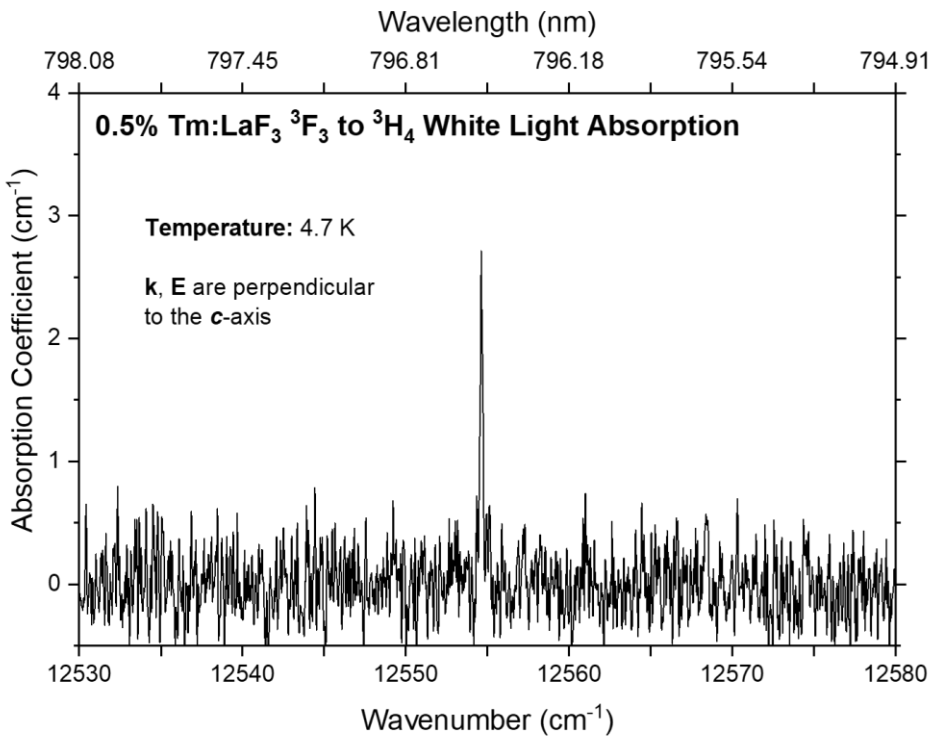

Figure 37. White light absorption spectrum of $^3H_6 \Leftrightarrow {}^3H_4(1)$ at 4.7 K. Only the lowest-to-lowest transition is visible, and the overall absorption is weak relative to the absorption measured in $^3H_6 \Leftrightarrow {}^3F_3(1)$.

More investigation at a larger range of fields and at longer timescales is needed to explore the magnetism, since the observed behavior is unusual and not readily explained in terms of published models. The direct and Orbach processes, which are the leading contributions to the spin-lattice relaxation rate in this case, do not depend linearly on the field magnitude in the case where the ion has an induced electronic moment [126, 201-203]. In that case, the spin-lattice relaxation lifetime should be proportional to the fourth power of applied field magnitude, $\sim \boldsymbol{B}^4$, as described in ref. [126]. Furthermore, multiple thulium sites with different spin lattice relaxation times might explain the multi-exponential persistent spectral hole decay, but no clear evidence of another site in the hole burning pattern was observed, as shown in fig. 35. Since the likelihood is low that the spin lattice relaxation time would increase linearly with field forever, characterization of the higher field regime beyond what was technically accessible in this work could provide insight into and control over the mechanisms responsible for the observed behavior.

Homogeneous Linewidth and Filter Simulations

The measured homogeneous linewidth of the $^3H_6 \Leftrightarrow {}^3F_3$ transition is at the lifetime limit. More typical linewidths for UOT materials are more than an order of magnitude smaller to admit as small of a frequency shift as possible to minimize absorption of ultrasound by tissue [36, 64]. The following simulations indicate that the ~120 kHz homogenous linewidths are adequate for UOT.

Theoretical filter absorption profiles were calculated by Bengtsson [204] with a simple spectral hole-burning simulation based on steady-state solutions to rate equations, using a 0.5 % thulium doped a 1.25x1.25x1.25 cm^3 crystal in a 250 mT field. Since the laser spectrum will be

modified with crystal depth, the model crystal was divided into 125 slices, each 0.1 mm thick. The absorption profile for each crystal slice *N* was calculated and used as the input to the next slice *N+1* using Beer-Lambert's law. This procedure is repeated for the whole crystal length, giving the absorption profile as a function of crystal depth. The filter depth, bandwidth and frequency cutoff were optimized by tuning the simulation input parameters related to the burn intensity and frequency width. Further details on how the Tm^{3+}:LaF_3 system was modelled and the absorption profiles were calculated can be found in the Appendix .

As seen in fig. 38, deep and broad holes are burned at the beginning of the crystal due to the higher laser intensity, but the non-linearity of optically thick SHB materials causes the tails of the pass band to form a more rectangular profile with increasing optical depth. This feature of rare earth doped crystals has been leveraged by Thiel et al. for laser linewidth narrowing and phase noise suppression [65]. The laser burn is not able to completely remove all absorption at the center of the filter due to the Lorentzian tails of nearby ions that reach into the filter pass band.

The attenuation of an optical probe pulse sent through the model filter as a function of frequency detuning compared with the filter center frequency can be estimated in the same manner since the absorption profile for each crystal slice is known. The simulated SHB filter was probed with 1 μs long Gaussian pulses to determine the attenuation as a function of frequency. 4.3 dB of attenuation is at center of the filter, while probe detunings larger than 2 MHz have above 60 dB of attenuation. For a probe detunings of 5 MHz, the ultrasound frequency used for the UOT measurements described in refs. [18, 28], nearly ~80 dB of attenuation is achieved.

Lower ultrasound frequencies are ideal because the human body preferentially absorbs higher frequencies, limiting penetration depth of the ultrasound tissue modulation [37, 38, 78].

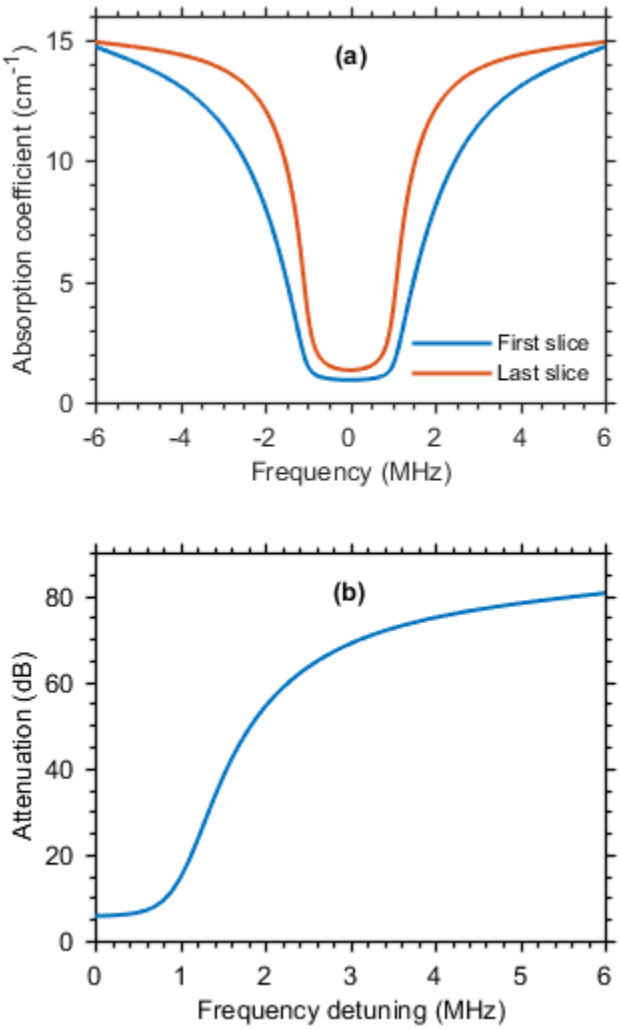

Figure 38: (a) Simulated absorption profiles of the first and last 0.1 mm thick slice of the crystal. (b) Attenuation of a 1 µs long Gaussian pulse sent along the c-axis of a 1.25 cm long crystal as a function of frequency detuning from the center frequency of the filter. Simulation implemented and provided by Alexander Bengtsson [204].

Additionally, a delay caused by the slow light effects within the passband of the filter means that the carrier may be time-gated against the side-band to further improve filter contrast [40]. By

implementing the mathematics put forward by Rebane et al. in ref. [62], the temporal separation of the pulses can be calculated at the crystal output and an estimation of the slow light filter contrast can thus be made. Two 1 μs long pulses are sent simultaneously to the center and +5 MHz outside the filter, as seen in fig. 38. If the time gate is set to cut 5% of the pulse sent at the center of the filter, another 15 dB of suppression of the +5MHz pulse can be obtained from the slow light delay for a total of ~90 dB of contrast. Consequently, Tm^{3+}:LaF_3 crystals operating on the $^3H_6 \Leftrightarrow {}^3F_3$ transition are projected to offer high filter contrast while retaining good penetration depth and sensitivity to tissue oxygenation [18, 36, 40].

UOT System Design

The technical requirements for building a practical system are straightforward. Both the $^3H_6 \Leftrightarrow {}^3H_4$ and $^3H_6 \Leftrightarrow {}^3F_3$ transitions are in the span of commercially available diode lasers, amplifiers, and modulators, other optics for off-the-shelf construction of optical systems. Holes for spectral filtering can be easily burned at 3K, which is within the temperature span of many simple-to-operate and maintain commercial cryocooler systems. Furthermore, the necessary magnetic fields for long-lived persistent holes in Tm^{3+}:LaF_3 can be achieved with high-grade NdFeB button magnets mounted within the cryostat, which obviates the need for any electronics for controlling the magnetic fields.

Conclusion

Optimization of materials for applications determines the practicality and limitations of devices they implement, and so fundamental research of this type is essential. In this study, the material Tm^{3+}:LaF_3 has been characterized with holeburning and coherence spectroscopy to

optimize it for UOT by mapping out its properties and dynamics in high resolution. The results of this study and simulation indicate that the $^3H_6 \Leftrightarrow {}^3F_3$ transition of Tm^{3+}:LaF_3 possesses many ideal properties for implementing an oxygenation-sensitive UOT device and other signal processing applications in the 690 nm band. The homogenous linewidth was found to be at the lifetime limit of ~120 kHz at temperatures <2.5K. The lifetime of spectral holes, and therefore the lifetime of inscribed spectral filters, was greatly extended to over two hours by burning into the nuclear states compared to the transient hole lifetimes measured in chapter 3. The study of the linear and quadratic Zeeman effect continues to identify the dynamics present in this material and how they affect rare-earth properties.

In conjunction with the work in chapter 3, these results strongly underscores how understanding of the fundamental processes in the material directly improve both scientific understanding and practical material properties: the transition of $^3H_6 \Leftrightarrow {}^3F_3(1)$, heretofore considered to have only broad (<10 MHz) homogeneous linewidths and little practical value for luminescence or spectral processing, has been taken from non-radiative to being practical for use a medical tomographic imaging device. The study of $^3H_6 \Leftrightarrow {}^3F_3$ has also pointed out a very interesting class of materials, the alkali lead halides, for growth and high-resolution spectroscopy for new luminescence and signal processing applications, which will be discussed in chapter 5.

CHAPTER FIVE

GROWTH AND SPECTROSCOPY OF RARE-EARTH DOPED ALKALI LEAD HALIDES FOR TELECOM BAND SIGNAL PROCESSING, QUANTUM INFORMATION, AND LASER CHARACTERIZATION

In this chapter, Pr^{3+}:$RbPb_2Br_5$ and Tm^{3+}:KPb_2Br_5 are grown and studied to apply the principles of suppression of phonon-mediated non-radiative relaxation to the development of rare-earth transitions. The applications that their study enables are discussed. The $^3H_4 \Leftrightarrow {}^3F_3$ transition at ~1584 nm in Pr^{3+} reveals four separate sites Pr^{3+} ion sites in $RbPb_2Br_5$ with millisecond lifetimes and narrow inhomogeneous broadenings. Coherence times are ~750 ns with modulations. Spectral holes are burned onto the nuclear pseudoquadrupole levels, with hole lifetimes estimated as ~2.25 s on site 4. This material stands to impact QIS and SHB applications at telecommunications wavelengths. Then, the survey and development of $^3H_6 \Leftrightarrow {}^3F_3$ concludes in Tm^{3+}:KPb_2Br_5 at ~700 nm. The transition is used to characterize and optimize a homemade laser used to study it by leveraging the SHB properties as a high-resolution, real-time spectrum analyzer. Absorption, fluorescence, and hole burning spectroscopy are presented. In both materials, the spectroscopy at these wavelengths immediately leads to new horizons.

The crystal growth was performed with the active and capable assistance of Dr. Shermane Benjamin and Dr. John Neumeier and their equipment, and the author remains indebted for the research they made possible. The author is also extremely grateful to his wife, Sarah, for showing up late at night to help.

Introduction

The alkali lead halide family of crystals, which are of the form XPb_2Y_5, where X is a alkali metal ion and Y is a halogen ion, are very interesting for enabling SHB and QIS applications on rare-earth optical transitions [159]. These materials are specifically studied for their use as low-phonon cutoff energy hosts for rare-earths in room-temperature Mid-IR (~3-10 μm) lasers, on transitions where non-radiative relaxation via multiphonon decay would quench fluorescence in materials such as hard oxides [13-16, 21-23, 27, 159, 169, 193, 194, 205-212]. Consequently, the survey of low-phonon cutoff energy hosts in chapter 3 led that work directly towards the rare-earth doped alkali lead halides, where Tm^{3+}:KPb_2Br_5 demonstrated strong suppression of non-radiative relaxation and a ~100 μs T_1 fluorescence lifetime. Rare-earth doped materials in general have great interest for fundamental atomic-scale physics in solids as well as for many optical and luminescence applications, including phosphors [4, 5, 7, 8, 213, 214], optical amplifiers [10, 11], lasers [13, 15, 16, 21, 22, 27, 169, 174, 193, 210], SHB frequency refs. [19, 20, 49, 53, 64, 215], ultrahigh finesse SHB filters and medical imaging [18, 28, 36-41, 65, 204], spatial-spectral holography [12, 20, 42, 51], quantum sensing [216-219], quantum computing [220, 221], quantum memories [30-33, 48, 52, 64, 69, 70, 72, 127, 132, 134, 137, 148, 221, 222], microwave-optical transduction [35, 129-132], and more. Little in the way of high-resolution spectroscopy has been performed at liquid helium temperatures in any of the alkali lead halides, where many of these cutting-edge applications of rare-earth ensembles must operate. Building on the work in the previous chapters, the alkali lead halides should support many new low-temperature applications on a variety of rare-earth transitions otherwise limited by phonons.

The alkali lead halides could overcome the limitation that for rare-earth and transition metal ions, only the lanthanide erbium possesses a transition with useful optical coherence in the telecom window for classical and quantum signal processing. Even then, across a wide range of host materials, the Er^{3+} $^4I_{15/2}$⇔$^4I_{13/2}$ transition is always found between 1514-1545 nm, with few exceptions [64]. While there are still many rare-earth transitions that are located across all the telecom bands, their utility is greatly hampered by non-radiative relaxation, with either very short (<<1 μs) T_1 lifetimes and/or immeasurably short T_2 coherence times. Fundamental materials research and spectroscopy of the alkali lead halides in the <4K regime could enable new optical applications at alternative wavelengths simply by suppressing the phonon relaxation and decoherence on the affected transitions. The utility of this approach has already been demonstrated in in chapters 3 and 4, where host materials were explored in detail for UOT on a transition conventionally viewed as uninviting for hole burning or coherence. While Tm^{3+}:LaF_3 was found to be an ideal choice for that particular application due to host material symmetry, growth sizes, and the $^3H_6$⇔$^3F_3$(1) absorption strength, the T_1 lifetime of the $^3F_3$ manifold of Tm^{3+}:KPb_2Br_5 was a hundred times longer. The large improvement in the T_1 lifetime alone warrants further investigations, and the limited toolkit of telecom-band rare-earth transitions should be expanded. An ideal candidate, the $^3H_4$⇔$^3F_3$(1) transition of Pr^{3+} at ~1584 nm and shown in fig. 39, has no reported optical coherence [159, 223]. To that end, that transition is investigated in RPb_2Br_5 at low temperature for classical and quantum signal processing.

The investigations of the $^3H_6$⇔$^3F_3$ transition of Tm^{3+}:KPb_2Br_5 also presented technical challenges that showcase the interplay of hardware development and fundamental research. The transition is located at 698.637 nm, beyond the immediate tuning range of the laser used to study

that transition in chapter 3. It is also a location where laser diodes are less readily available. Even so, the luminescence and SHB properties of the transition are effectively assured by both the previous results and the host material, and so the initial spectroscopy of this transition in this material was used to bootstrap the construction and characterization of a laser to study the same transition.

With these aims, two materials are grown and studied in this chapter: Pr^{3+}:$RbPb_2Br_5$ (RPB) and Tm^{3+}:KPb_2Br_5 (KPB). Both samples are grown in sealed, evacuated quartz ampules using a homemade Bridgman furnace and studied at low temperature. The growth procedure is briefly discussed. In Pr^{3+}:$RbPb_2Br_5$, the properties of the $^3H_4 \Leftrightarrow {}^3F_3(1)$ transition at ~1584 nm in the optical telecom L-Band (~1565-1625 nm) are explored. The spectroscopy certainly identifies four separate sites this material, with spacings of ~10 GHz and inhomogeneous broadenings ranging from 2-5 GHz, and each with T_1 lifetimes of $^3F_3$ ranging from ~500 μs to ~1 ms, measured with time-resolved fluorescence. Each site exhibits ground-state nuclear storage in zero external magnetic field due to the pseudoquadrupole interaction. Spectral hole lifetimes in sites 1-3 are on order of ~1 ms, but site 4's spectral hole lifetime extends out to ~2.25 seconds in zero field. Photon echoes measure phase memory times T_M of ~750 ns in all cases and are dominated by praseodymium nuclear spin modulations, with outlooks to improve them through better understanding of the magnetic environment. The impact of Pr^{3+}:$RbPb_2Br_5$ in particular is discussed in the context of telecom applications, especially in terms of quantum information and the development of other rare-earth ions with telecom transitions. Additionally, in Tm^{3+}:KPb_2Br_5, the work of chapter 3 is extended to construct and optimize a new homemade laser by using the $^3H_6 \Leftrightarrow {}^3F_3(1)$ transition as a ~1 MHz resolution, real-time spectrum analyzer

with the ability to sensitively track laser stability in holeburning; this laser is then used in turn to investigate the basic properties of the transition itself. Long-lived spectral holes are burned into the transition and are still measurable at ~100 ms. New directions for research into rare-earth doped alkali lead halides at low temperature are then briefly discussed.

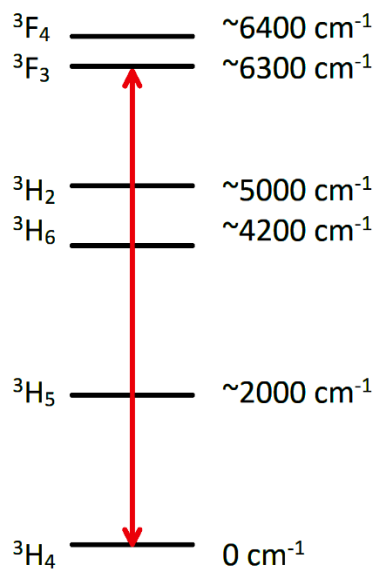

Figure 39. The $^3H_4 \Leftrightarrow {}^3F_3$ transition of Pr^{3+} and adjacent manifolds [75, 86, 87]. The transition is located at ~1584 nm in $RbPb_2Br_5$.

Experimental

Samples

The growth procedure, outlined in the following subsections, was implemented in-house to produce ~5mm transparent crystals for spectroscopy. The target dopant levels were 0.1% Pr:$RbPb_2Br_5$ and 0.2% Tm:KPb_2Br_5. A gemological polariscope identified that one of the dielectric axes of the crystals aligned readily with the growth axis; these crystal orientation techniques may be seen in the excellent text by Wood [224]. The samples were then cut and polished parallel and perpendicular to the axis of growth direction, denoted as the ***g***-axis. The ***g***-

axis has not been confirmed by other means to align with a particular crystal axis in KPB, but was shown through laser absorption to coincide with the crystal axes in RPB. The 0.1% Pr:$RbPb_2Br_5$ crystal was cut to 3.51 mm thick perpendicular to the ***g***-axis for absorption measurements, and the 0.2% Tm:KPb_2Br_5 sample used for absorption was cut to 3.43 mm thick. The essential structural crystal properties of both samples are reproduced in table 9. Examples of crystal growth results are shown in fig. 40.

It is essential to note that rare-earths have been shown to occupy one of the two Pb^{2+} sites in the alkali lead halide family of materials, but which of the two sites are occupied remains an open question [25]. The first lead site is surrounded by nine halide ions to form a tricapped trigonal prism of symmetry D_{3h}, while the second lead site is a tetragonal antiprism surrounded by eight halides for a symmetry of D_{4d}. However, in both cases, even the Pb^{2+} ion in any coordination (1.45 Å in octahedral coordination) is considered to be too small for the sites. The ion is shifted out of center to create a variety of low-symmetry sites of C_s or C_1 [159]. Therefore, it is assumed that the trivalent lanthanides will also occupy sites of low symmetry, regardless of which nominal lead site they occupy, as their effective radii (~1.01-1.14 Å) are even smaller than the radius of Pb^{2+}. Naively, the rare-earth ions appear more likely to occupy the D_{4d} site, because it has one less neighboring ion and is therefore a smaller site.

The charge difference between the 2+ lead ion and the 3+ lanthanide is compensated for by a 1+ alkali metal vacancy. However, Tm^{2+} would be a good candidate for study in these materials as the charge mismatch is removed and the ion's larger size better fits the site. This is considered in more detail in the discussion section.

Crystal	Symmetry	***a*** (Å)	***b*** (Å)	***c*** (Å)	***β***	Volume ($Å^3$)	Max Phonon Energy (cm^{-1})
KPb_2Br_5	Monoclinic ($P2_1/c$ or C_{2h}^5)	9.256(2)	8.365(2)	13.025(3)	90.00(3)	1008.4	138 [159]
$RbPb_2Br_5$	Tetragonal (I4/mcm or D_{4h}^{18})	8.43(1)	8.43(1)	14.54(1)	90	1033	

Table 9. Structural crystal properties of KPb_2Br_5 and $RbPb_2Br_5$, from ref. [159].

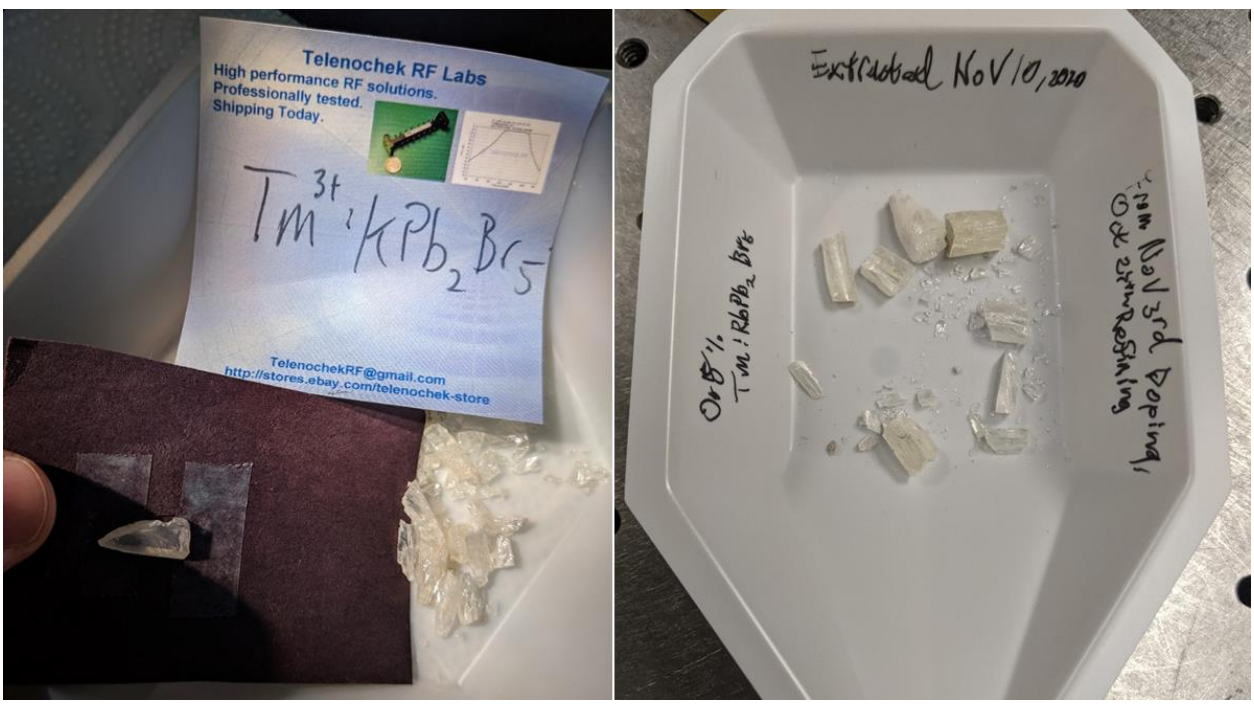

Figure 40. Examples of crystal growth results, with (left) pieces of 0.2% Tm^{3+}:KPb_2Br_5 and (right) of 0.1% Pr^{3+}:$RbPb_2Br_5$, used in these measurements.

Apparatus and Methods

To map out the $^3F_3$ excited manifold structure in both Tm^{3+}:KPb_2Br_5 and Pr^{3+}:$RbPb_2Br_5$, white light from a 12-Watt tungsten-halogen bulb was focused onto the samples in the Montana

Instruments (MI) C_2 cryostat cooled to 4 K. The absorption spectrum of Tm^{3+}:KPb_2Br_5 was measured with a SPEX 1401 double monochromator and detected with a Hamamatsu R928 PMT. The absorption spectrum of Pr^{3+}:$RbPb_2Br_5$ was measured with a SPEX 1000 monochromator, and detected with a liquid nitrogen-cooled Edinburgh Instruments germanium detector with ~10 ms response time and biased to 50V. Fluorescence spectra of the 0.1% Pr^{3+}:$RbPb_2Br_5$ sample were made using the same spectrometer and detector, but collected at 90 degrees relative to the propagation direction of the exciting 450 nm laser diode to minimize collected scatter. The sample temperature was also elevated to 10K to thermally broadening the $^3H_6 \Leftrightarrow {}^3P_0$, $^3P_1$, $^1I_6$, $^3P_2$ transitions of Pr^{3+} near 450 nm to assist with optically pumping the ions. In all these measurements, the signal from the detector was routed into a Tektronix TDS 754C oscilloscope and then recorded and analyzed with a computer program.

A commercial New Focus Velocity 1545-1636 nm model no. 6330 laser was used for high resolution measurements of the $^3H_4 \Leftrightarrow {}^3F_3(1)$ transitions of the 0.1% Pr^{3+}:$RbPb_2Br_5$ sample. Electrical pulses from DG645 were used to control all the instruments and synchronize timings, and the Burleigh WA-1500 wavemeter was used to calibrate all scans and read absolute laser wavelength. An alphaNov with CC-S Corvega Diode optical amplifier was used to pulse the laser and augment the low power from the cavity. Time-resolved fluorescence was measured by pulsing the amplifier and collecting the resulting fluorescence at 90 degrees relative to the laser beam onto a model 2053 IR New Focus detector. By tuning the laser with the motor across its range, T_1 lifetimes were measured to help sort the numerous transitions into separate sites. The nuclear states of Pr^{3+} in the $^3H_4$ manifold were optically pumped with ~600 μs burn times, producing ~10MHz holes, and these were read out using the internal piezo of the laser cavity.

Piezo scans were calibrated with the wavemeter. A malfunction in the laser electronics precluded current scanning for high-speed readouts, limiting ramp rates to ~1 kHz piezo scans. Photon echoes required the low temperature of the MI prototype xp100 cryostat, down to 1.6K, and the protocol for achieving low temperatures outlined in chapter 2 was closely observed. An additional Amonics L+C band amplifier was installed with the alphaNov amplifier to achieve the necessary intensity in the crystal. The ~100 mW beam was tightly focused onto the sample with an achromatic doublet. Optimal pulses were ~100 ns for both pulses and fine-tuned for each of the four sites from there.

A homemade laser was built and configured for reaching the $^3H_6 \Leftrightarrow {}^3F_3(1)$ transition of Tm^{3+}:KPb_2Br_5 at 698.637 nm through an appropriate choice of commercially available diode and diode temperature. The cavity was aligned according to refs. [225-228]. The spectrum and absolute wavelength of the laser was measured using a homemade 1.9 GHz free-spectral range (FSR) scanning Fabry-Perot (SFP) with a finesse of ~10 and a ~900 MHz resolution Advantest optical spectrum analyzer (OSA). Alignment was then fine-tuned by leveraging the hole burning spectrum of the Tm^{3+}:KPb_2Br_5 crystal itself at 4K in the MI C_2 closed-cycle cryostat. Burn times of ~250 μs were needed to produce a clear hole spectrum. The transmission of the laser was detected with a New Focus 1801 visible photodetector and the traces were recorded on the Tektronix TDS 754C oscilloscope. The homemade laser was tuned to read out the hole burning spectrum by externally sweeping a Crystal Technology Inc. 3080-125 acousto-optic modulator (AOM) driven at 80 MHz about its center drive frequency with a triangle ramp produced from an Stanford Research Systems DS345 function generator. Time-resolved fluorescence on the 0.2% Tm^{3+}:KPb_2Br_5 sample was also measured by using the AOM to rapidly chop the laser with a 20

ns response time, and fluorescence was collected at ninety degrees and focused onto the New Focus 1801 visible photodetector. The design, motivation, and setup of the homemade laser is described in more detail the following subsections.

Crystal Growth

The alkali lead halide class of materials consists of many stoichiometric variants. Many crystals described in literature follow the XPb_2Y_5 format, where X is an alkali metal such as potassium, sodium, rubidium, and cesium, and Y is a halogen, such as fluorine, chlorine, bromine, and iodine. That stoichiometry corresponds to the congruent melting point common across the family [159, 174]. A principal application of these materials is in producing room-temperature lasing cryogen-free lasers in the mid-IR (3-10 μm). In terms of SHB and signal processing, their low phonon cutoff energies should strongly suppress non-radiative, multiphonon relaxation pathways. The transitions in these materials should be immediately applicable to researchers looking to implement rare-earth quantum memories at different wavelengths as well. In this work, the growth, spectroscopy, and discussion of alkali lead halides are focused on KPb_2Br_5 and $RbPb_2Br_5$.

From the purely practical perspective of materials growth, the most attractive element of the majority of alkali lead halides is their low melting point (generally <1000K), chemical and mechanical stability, and very low hygroscopicity [159]. However, all the alkali lead halide growths suffer from the dissociation of PbY_2 (Y = halogen) in the presence of impurities, especially water and hydroxides. After dissociation, lead ions rapidly scavenge oxygen at elevated temperatures and release their halogen ions, resulting in large quantities of lead oxide dross and driving the melt far from the target stoichiometry. This is especially problematic when

considering many rare-earth salts are complexed with water. Consequently, all the starting materials themselves must be kept dry and oxygen free before and throughout the growth process and only doped at the very end as a separate growth stage [13, 16, 159, 205], which is generally true for the growth of all materials involving PbY_2. After the final crystal is grown, the material is insensitive to atmospheric water.

The most common growth procedure for this class in literature is through zone refinement, with the aim of producing large, high-quality, defect-free laser rods. However, in this work, only ~1-5 mm pieces are required, and so a simple Bridgeman system was constructed [229, 230], shown in fig. 41, and several refining steps were used to partly replicate the results of a full zone refining system. A streamlined growth procedure paralleling literature [13, 16, 159] was developed based on this simpler system. The parameters specific to the target crystals themselves are given in table 10.

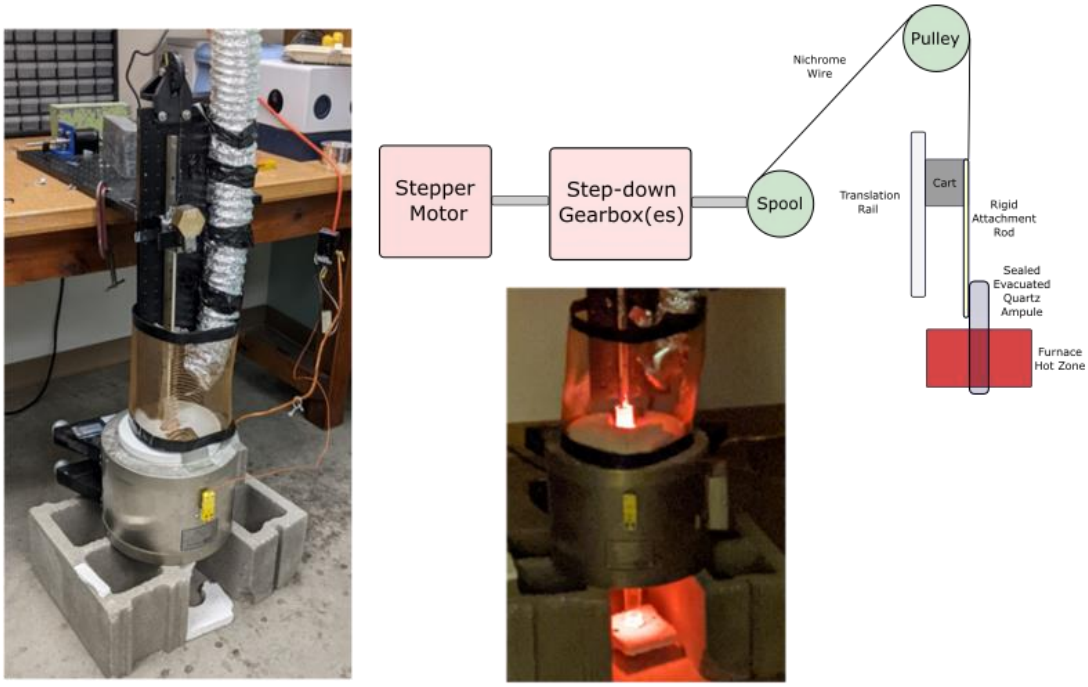

Figure 41. Homemade Bridgman growth system photo (a) and schematic (b). A stepper motor is geared down with 100:1 planetary gearboxes, travelling ~10 to 1 mm/hour or even less, depending on the specific requirements of the growth experiment. A critical aspect of the alkali lead halides was annealing and slow cooling for long periods. Poor quality vacuum in the ampule always resulted in opaque and polycrystalline masses. A fume extractor was implemented to remove fumes from ampules breaking open during the growth.

Crystal	Travel Rate	Melting Point (°C)	Growth Ampule Inner Diameter	Peak Furnace Temperature (°C)	Temperature Gradient (°C/cm)
$PbBr_2$	~1-10 mm/hr	370.6	1 cm	500	~15
KBr	~10 mm/hr	734		850	~27
RbBr		693		750	~23
KPb_2Br_5	~1-10 mm/hr	382		500	~15
$RbPb_2Br_5$					

Table 10. Crystal growth parameters used for all materials grown.

In the first stage of growth, the starting salt XBr and lead compounds $PbBr_2$ were independently crystallized in the Bridgman system in sealed, evacuated quartz tubes to ensure purity through recrystallization and to ensure accurate stoichiometry in the materials committed to the final growth. Sealed ampules were dropped through the hot zone at ~1-10 mm/hr. The melting zone was measured both with a thermocouple gauge, and by manually translating the quartz ampule through the furnace until there was a mass of solid and molten material indicating clearly where the molten and frozen zones were. Since the materials are grown congruently and the phase diagrams are known, this gives an accurate measurement of the temperature profile in the vicinity of the growth zones [159]. This stage resulted in two separate ampules of crystals of XBr and $PbBr_2$. Large pieces of XBr salts are easy to grow, but $PbBr_2$ requires extensive annealing and purification to control cracking. The $PbBr_2$ need for annealing and purification translates directly to the XPb_2Br_5 growth procedure. Furthermore, in many cases, the $PbBr_2$ growths and all subsequent regrowths involving it require a maximum pressure of ~10^{-3} torr, or else the material rapidly degrades as it dissociates and oxidizes. Pumping ~1 day after reaching

the base pressure greatly improved yields and quality. Finally, the $PbBr_2$ compounds are again emphasized as being especially sensitive to impurities, even in very pure starting materials, and growth of $PbBr_2$ crystals will invariably result in oxides of lead collecting on top of the melt or even throughout the bulk. The remaining lead oxide must be discarded before proceeding.

In the second growth, the crystals of XBr and $PbBr_2$ were then combined in a single evacuated quartz tube in the appropriate stoichiometric ratio. The materials were melted and recrystallized in the Bridgman system, using the growth parameters in table 10 and adhering to the same requirements as in growing $PbBr_2$. All of the materials used in growing XPb_2Br_5 were found to be relatively insensitive to travel speed and temperature gradient through the growth zone. Less than ~10 mm/hr of travel produced generally satisfactory results, the slower, the better. However, both $PbBr_2$ and the XPb_2Br_5 crystals were also found to be extremely sensitive to the cooling process. These crystals would readily shatter into fine, irregular pieces during cooling to room temperature unless left to anneal just outside of the growth zone for ~24 hours. Afterwards, the sample was allowed to descend. Because of the annealing requirements, significant improvements in growth size could certainly come in the form of a two-zone Bridgman furnace or very slow translations rates. Non-crystalline material and reject was thereafter separated from the good crystals.

Rare-earth salts (RX_3) are complexed with water and are hygroscopic, which mandates a separate growth stage from any of the host XPb_2Y_5 crystals. Since the crystalized host material XPb_2Br_5 is relatively insensitive to water, salts RX_3 are added on top of the host material in the final doping growth run. The sealed quartz tube is then evacuated until the water is removed, resulting in a fine dehydrated powder of RX_3 atop the XPb_2Br_5. This low-temperature approach

prevents the rare earth from simply oxidizing and becoming less soluble in the melt. This approach is especially necessary in cases of ions with low segregation coefficients. Lanthanides occupy one of the two lead sites in XPb_2Y_5, the segregation coefficient depends sensitively on the relative size of RE^{3+} ions to the larger Pb^{2+} ion. Therefore, ytterbium has a very low probability to enter the site, while neodymium is nearly 100% [159]. Excess doping of thulium and other lanthanides of similar size is essential to have measurable quantities of ions enter the host, and therefore, more water is added to the mix. Otherwise, the growth procedure is the same as for the undoped host crystal. In this work, doping also accounted for the segregation coefficient of thulium being ~20% in KPb_2Br_5, and the segregation coefficient of praseodymium being ~100% in $RbPb_2Br_5$. Growths of Tm^{3+}:RPB were attempted, but absorption was not measured.

Improvements to the growth could come about in several ways. First, a pumping system with a base pressure of ~10^{-3} mbar was used, and much more consistent, higher quality results were achieved with longer pumping times and lower pressures, indicating that it is a critical parameter. A lower base pressure system with a turbo or diffusion pump would likely improve yields and optical quality. Second, high-temperature annealing of the XPb_2Y_5 close to the melting point is also critical for producing larger samples. Contributing to this issue, many of the XPb_2Y_5 materials have solid state structural phase transitions below the melting point, requiring slow cooling to survive without embrittlement or cracking. The only certain exception to this is $RbPb_2Br_5$, which does not have this phase transition during cooling to room temperature [159].

Homemade Littrow Laser Design

A major hurdle for high-resolution studies of many transitions of ions doped into solids, both lanthanides as well as transition metals, is the lack of available lasers for high resolution spectroscopy. This deficit can take many forms. Generally, the commercial cost of a quality external cavity diode laser (ECDL) is prohibitive, becoming more so at wavelengths outside of mass-produced bands, such as the telecom wavelengths, where optical components such as diodes and gratings are commonly available. In cases where researchers are investigating the effects of host material modification on the transition properties, very frequently, interesting transitions can shift to outside the laser tuning range or happen to be located at the wavelengths of unfavorable laser modes. The limited availability of coherent light sources at needed wavelengths leads research groups to concentrate their efforts solely on one or two specific transitions in a specific material.

To escape these constraints, spectroscopists are incentivized to build their own tailored lasers to identify new luminescence and coherence properties at new wavelengths. The Littrow configuration is a common approach, because it is relatively simple to design, build, and align [225-228]. Lasers are frequently characterized with interferometers and delayed-self-heterodyne measurements. However, many available or homemade interferometers possess 100+ MHz resolution, and delayed self-heterodyne instruments are constrained to work at the operating bands of the delay lines and optics and generally are aimed at measuring peak widths and coherence, not necessarily diagnosing laser operation. In both cases, power loss and coupling efficiency are also issues. An alternative approach is to measure the spectrum of the laser directly in hole burning. Some clear benefits is that SHB is ideally performed in the low-power limit, and provides real-time feedback on both the laser spectrum and stability [65]. Combined with

interferometric techniques, gated holeburning enables very clear inspections of laser behavior with snapshots of the laser spectrum, integrated by the optical transition.

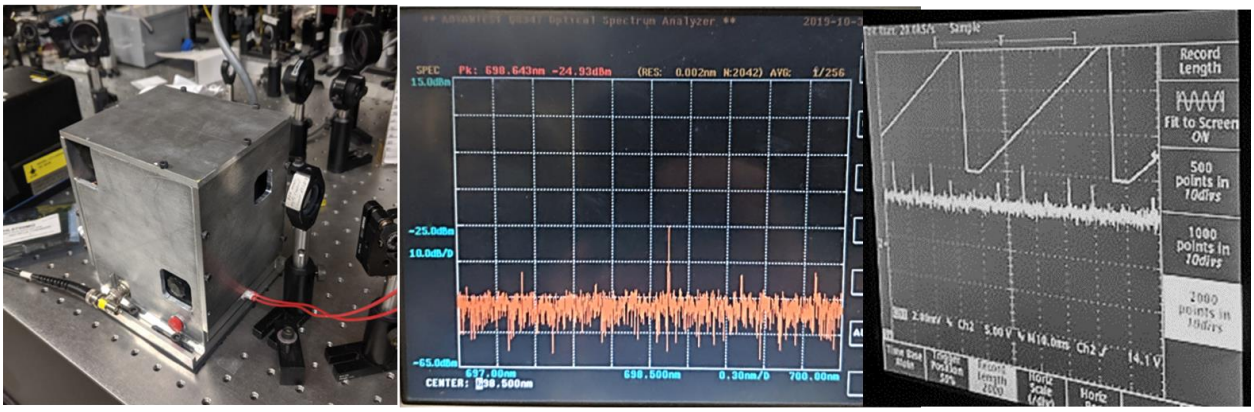

Figure 42. (Left) Homemade modular Littrow laser in use. The lasing cavity is a diode and grating in the Littrow configuration, and contained within the machined aluminum housing. The temperature-controlled baseplates float on rubber sheets for additional vibrational damping. (Center) Laser spectrum measured by the OSA. Main mode is center, and some side modes are visible adjacent to it. Note that in the OSA, the feedback is not in real time and limited to 900 MHz. (Right) Laser spectrum measured in a homemade confocal 1.9 GHz SFP. The Peaks of the SFP are ~200 MHz wide, providing real time feedback, but far above the actual laser linewidth and with low power. Transient multimode behavior ~10's of MHz would be difficult to identify this way.

The motivations behind the design choices were first and foremost to produce a thermally stabilized, acoustically sheltered, and massive, vibrationally-damped platform and box for the cavity to inhabit. Second, the cavity was to be modular so that new diodes and gratings could be swapped in and out for adjustments to new wavelengths could be made as needed for experimental agility. A modular, stable Littrow laser was constructed in accordance with those principles. Initial characterization was performed with an Advantest optical spectrum analyzer (OSA) and a homemade confocal scanning Fabry-Perot (SFP) with a free spectral range of 1.9 GHz and finesse of ~10. Examples of the laser spectrum are shown in fig. 42. The quality of the lasing action is reasonable, but it can still be difficult to identify pathological behavior below

instrument resolution and transient behaviors faster than the instrument refresh rate. The OSA or SFP also diverts power away from the main experiment itself.

In this case, the OSA provides broad-band spectral information and an absolute reference relative to a HeNe laser but is limited to ~900 MHz resolution. On the other hand, the SFP provides real time information on the laser spectrum, with transmission peaks being as narrow as ~200 MHz. Using the crystal to measure the laser improves on both cases by providing ~1 MHz resolution in real time, and absolute frequency references relative to the narrow rare-earth inhomogeneously broadened absorptions.

Spectroscopy of Pr^{3+}:$RbPb_2Br_5$

Absorption

White-light absorption spectroscopy of the sample of 0.1% Pr^{3+}:$RbPb_2Br_5$ at 3.5K, revealed many sharp lines below the spectrometer resolution, shown in fig. 43. The narrow lines of the praseodymium transitions motivated high resolution laser spectroscopy, which revealed many closely spaced transitions and inhomogeneous broadening on order of 2-5 GHz for the lowest-to-lowest transitions. These transitions, the lowest lines of the four sites, are shown in fig. 44, are strongly polarized parallel and perpendicular to the growth axis. This observation confirms the tetragonal symmetry of the sample and the crystal orientation relative to the ***g***-axis.

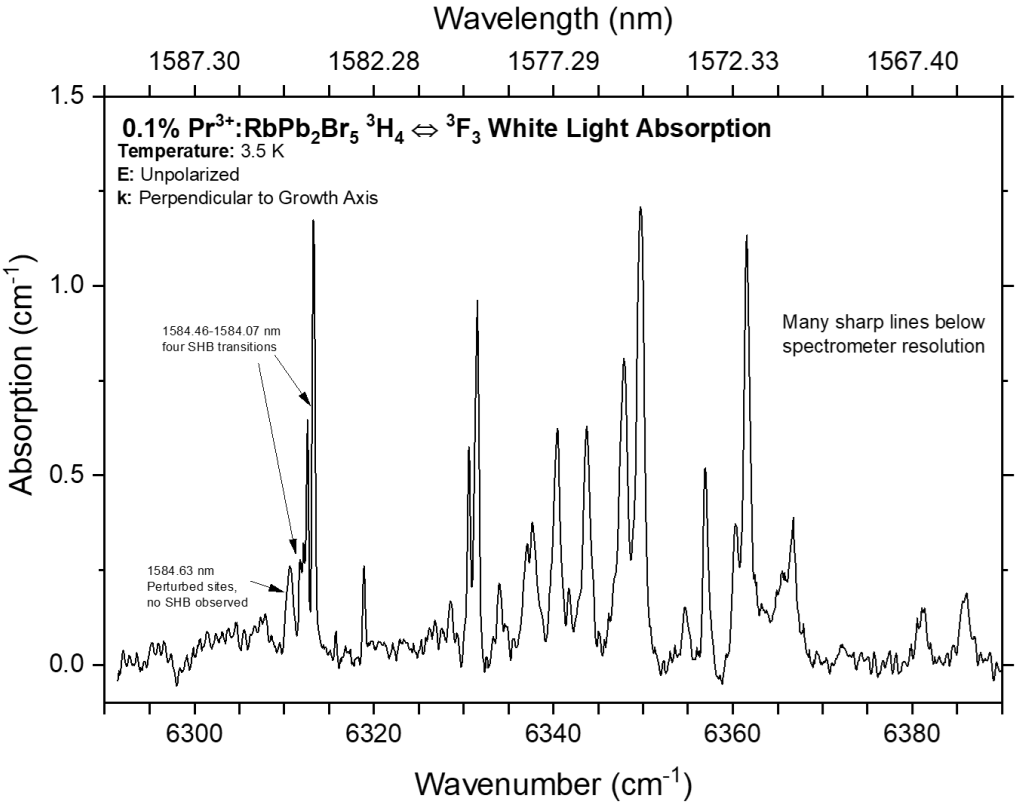

Figure 43. Liquid helium temperature absorption of 0.1% Pr^{3+}:$RbPb_2Br_5$ in the L-band. The resolution of the SPEX 1401 is limited to ~3 GHz in the most optimal case, but in practice this is difficult to achieve over large wavelength ranges and with low absorption.

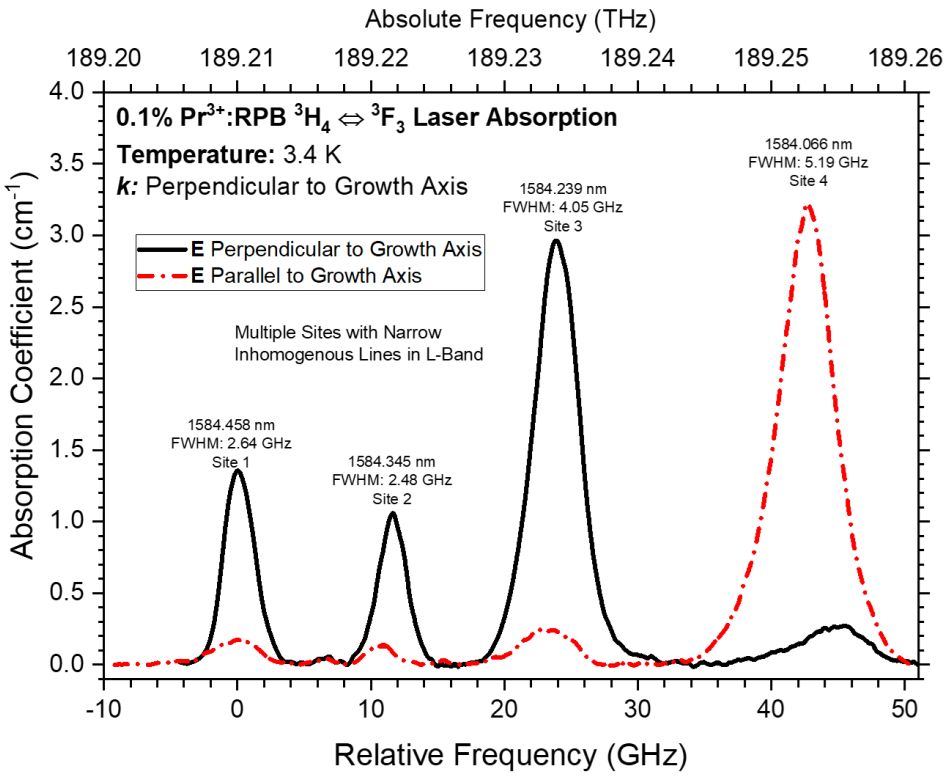

Figure 44. Laser absorption of the lowest-to-lowest transitions 0.1% Pr^{3+}:$RbPb_2Br_5$ at 3.5 K. The transitions of four separate sites are shown, which were positively identified with site-selective time-resolved fluorescence and holeburning. The inhomogeneously broadened lines are sharp, which is of interest for signal processing, quantum memories, and transduction [20, 30-32, 35, 42, 64, 67, 69, 70, 74, 127, 129-132].

Site Selective Spectroscopy

The overlapping level structures called for site-selective spectroscopies to measure the properties of each site. Time-resolved, gated SHB, time-resolved fluorescence, and photon echoes were performed on each level to sort each observed transition into sites and measure their properties. The results of that survey are summarized in table 11.

$^3F_3$	Level #	Energy (cm^{-1})	Comment
	1	6311.31	Site 1, T_1 = 642 μs, zero-field T_M = 760 ns
	2	6311.76	Site 2, T_1 = 550 μs, zero-field T_M = 760 ns
	3	6312.18	Site 3, T_1 = 665 μs, zero-field T_M = 792 ns
	4	6312.87	Site 4, T_1 = 981 μs, zero-field T_M = 725 ns
	5	6318.55	Site 4 (from T_1 and Hole Burning; excited crystal field level hole burning)
	6	6328.27	Site 2 (from T_1)
	7	6330.32	Site 1 (T_1)
	8	6331.10	Site 3 (T_1)
	9	6336.6	Site 1 (T_1)
	10	6340.0	Site 3 (T_1)
	11	6343.2	Site 3 (T_1)
	12	6347.5	T_1 - 827 μs
	13	6349.5	Site 4 (T_1)
	14	6354.4	T_1 - 877 μs
	15	6356.7	Site 1 (T_1)
	16	6361.4	Site 1 (T_1)
	17	6366.7	T_1 - 750 μs
	18	6381.0	Multi exponential convolution of sites 2 and 4?
	19	6385.7	T_1 - 915 μs
	20	6394.2	T_1 - 732 μs

Table 11. Summary of spectroscopy of $^3F_3$, through absorption (1-4) and site-selective time-resolved fluorescence (5-20). This list should not be regarded as exhaustive. 5-20 were assigned to sites based on the closest T_1 value measured. Some higher levels may also belong to $^3F_4$.

Time-Resolved, Gated Spectral Hole Burning

The New Focus Velocity laser was tuned across the wavelength range of the manifold 1.6 K to identify hole burning transitions. Four separate holeburning sites were identified, and their rough, single-exponential lifetimes were measured. Sites were labeled in order of their appearance from lowest to highest energy. Holes were burned on each site into the nuclear levels. Their traces were recorded and are shown in figs. 45-48. Holes broadened quickly above 2K, and holes were difficult to resolve at and above 3K. The width of the holes is ~10-30 MHz for each site, and is dictated by the long, heavy burns, over the course of which the laser drifts and jitters, randomly broadening out the hole. The long burn times are necessary because the cross-spin transition probability is low.

In the non-Kramers ion Pr^{3+}, the ground state nuclear storage is made possible by a Hamiltonian of the form:

$$H = H_0 + H_Z + H_z + H_{HF} + H_Q \tag{16}$$

In eq. (16), H_0 is the Hamiltonian of the central field, relativistic effects, spin-orbit coupling, and crystal field interactions, H_Z is the Zeeman interaction, H_z is the nuclear Zeeman interaction, H_{HF} is the magnetic hyperfine interaction, and H_Q is the nuclear electric quadrupole interaction. The full theoretical treatment of the last four terms is described in works by Macfarlane, Liu, Sun, Mossbauer, and others [83, 88, 109, 145, 149, 231]. In this particular case, where there is no Kramers degeneracy and there is no applied external field, the electronic and the nuclear Zeeman effects do not contribute to the energy of the system. However, both are very important cases in general for rare-earths, and the nuclear Zeeman effect is of great interest in non-Kramers ions [58, 72, 90, 91, 126, 179, 180, 182]. The magnetic hyperfine interaction H_{HF} describes the

interaction of the nuclear moments with the magnetic field at the nucleus produced by the spin and orbital angular momentum of electrons in unfilled shells. However, in cases where the site symmetry is low (C_2 or lower), the diagonal matrix elements of this interaction are zero. Therefore, there is no first order contribution from this term [88]. This applies to the perturbed lead sites that the rare-earths occupy in KPB and RPB where the symmetry low. The second-order term of H_{HF} gives rise to the pseudoquadrupole interaction [88], which enhances the nuclear Zeeman effect [83], and is of the same form as the nuclear electric quadrupole interaction. This can be also referred to as a Sternheimer anti-shielding effect the $4f^N$ electrons [83, 231]. H_Q models the interaction of the electric quadrupole moment of the praseodymium nucleus with the electric field gradient at the nucleus produced by the asymmetric distribution of the electron orbitals; the orbitals are disturbed by the ligands of the host material ions [83, 149].

The combination of the terms H_{HF} and H_Q splits the crystal field levels into what are generically termed quadrupole levels; praseodymium is dominated by the pseudoquadrupole contribution [88]. In the case of Pr^{3+}:RPB, there should be three quadrupole levels of spin doublets corresponding to $m_I = \pm 5/2$, 3/2, and 1/2. This is because there is only one stable isotope of praseodymium, ^{141}Pr, with nuclear spin I = 5/2, and because each crystal field level is otherwise non-degenerate because of the low site symmetry [83]. Supporting this argument are the three side holes visible in the hole burning spectrum of site 3, shown in fig. 47. The other sites do not display the expected structure as clearly. It is very likely the structure is simply not easily observed. This can be due to the delay between the write and read pulse sequences, the scale of the splittings being too large or too small to observe directly, or simply the structure being broad and faint.

The lifetimes of the holes range from ~400 μs in site 3 to as long as 2.25 seconds in site 4. The hole lifetime is the convolution of the lifetimes of $^3F_3$ and the intermediate states (~0.5-1 ms) with the nuclear spin lattice relaxation time in the ground state of $^3H_4$ [17, 66, 67, 117, 126, 141, 144, 200, 201]. The only exception is site 4, where the 2.25 second hole lifetime is much longer than the T_1 lifetime of $^3F_3$ (981 μs) and the intermediate states.

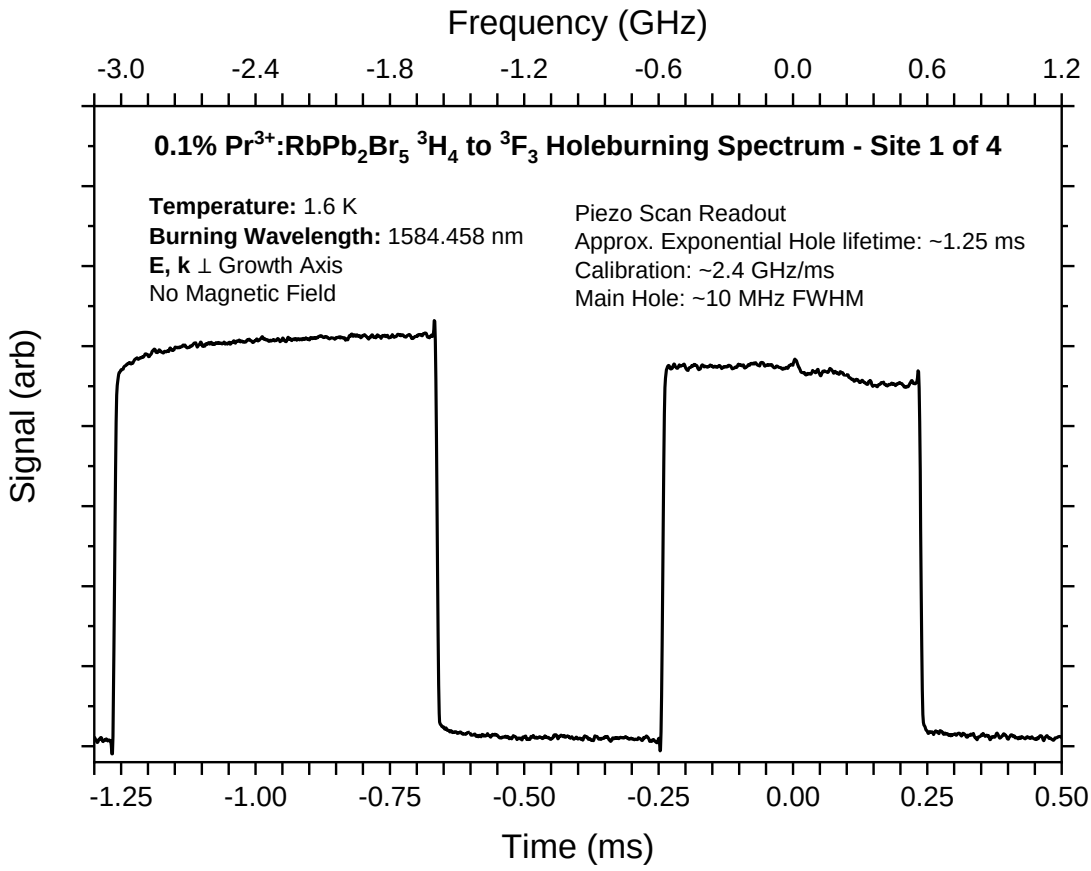

Figure 45. SHB on the ions designated site 1 of the $^3H_4 \Leftrightarrow {}^3F_3(1)$ transition of 0.1% Pr^{3+}:$RbPb_2Br_5$ at 1584.458 nm at 1.6 K.

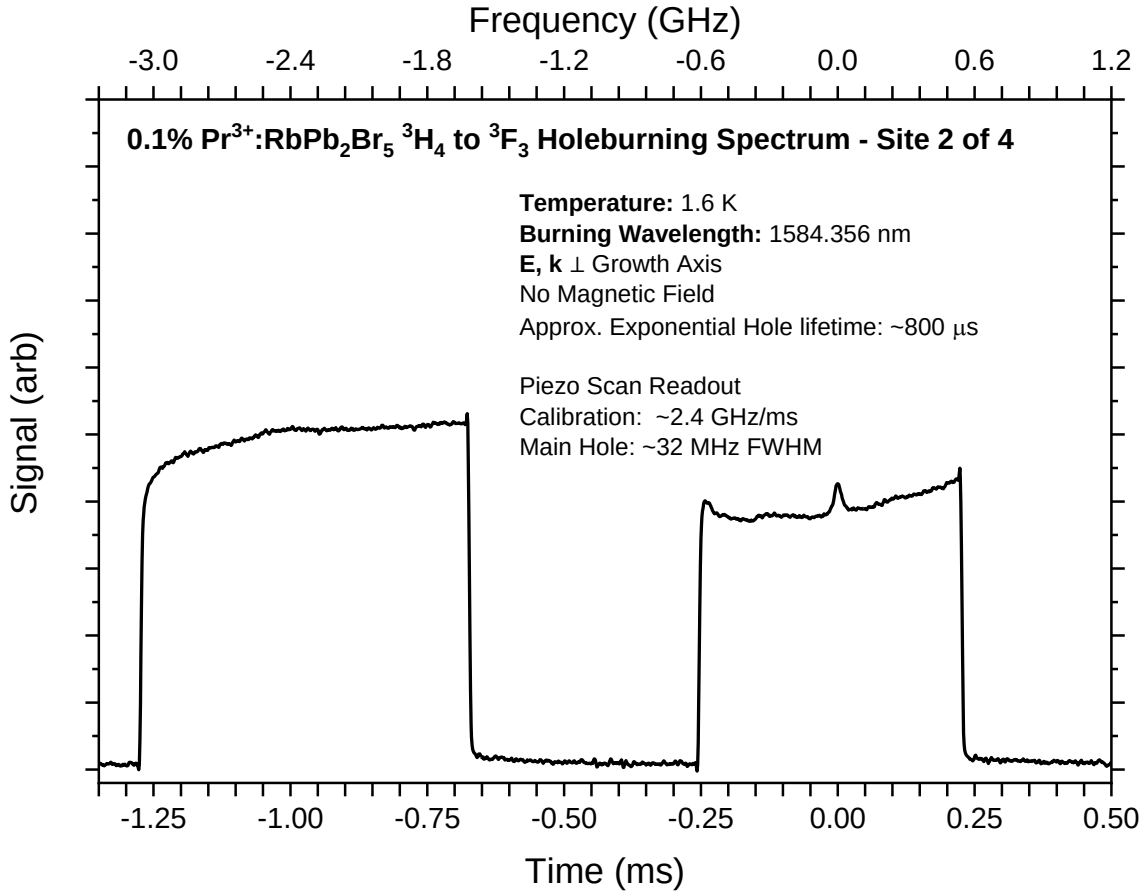

Figure 46. SHB on the ions designated site 2 of the $^3H_4 \Leftrightarrow {}^3F_3(1)$ transition of 0.1% Pr^{3+}:$RbPb_2Br_5$ at 1584.356 nm at 1.6 K.

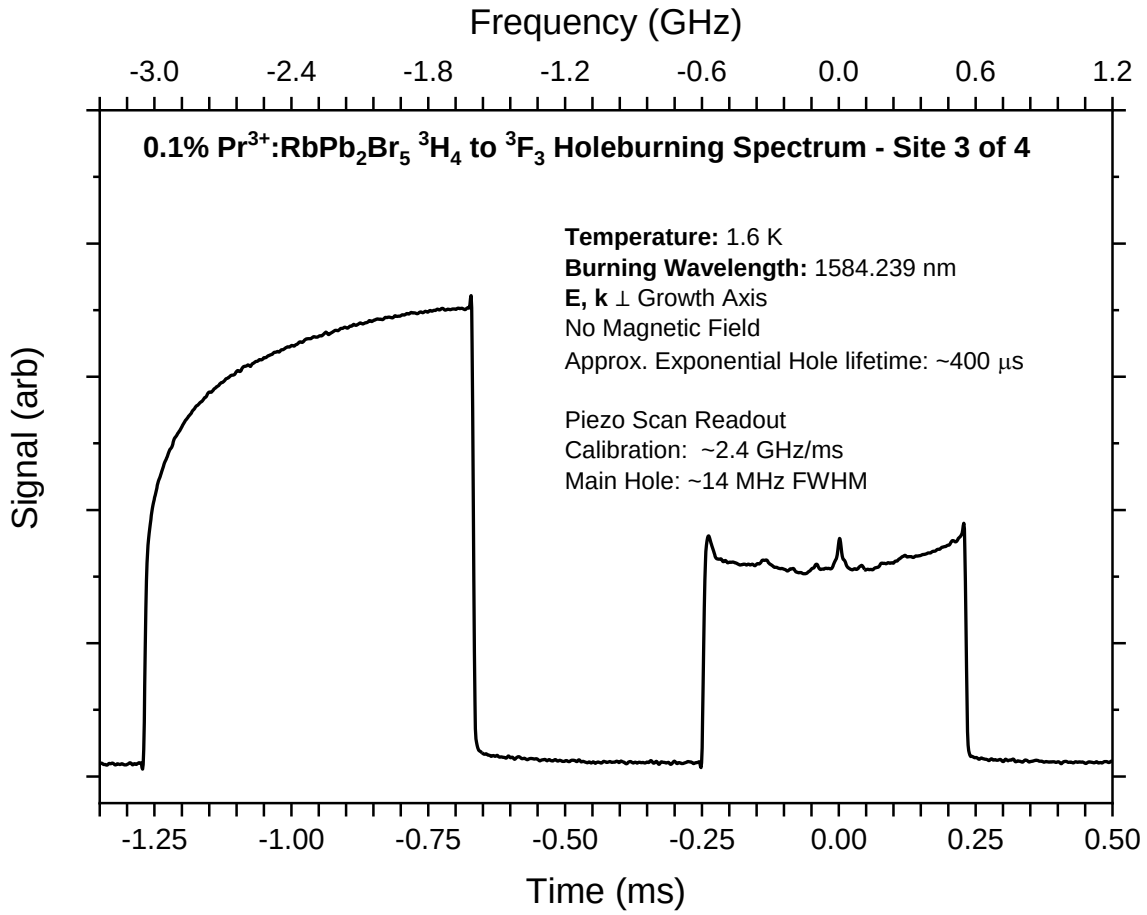

Figure 47. SHB on the ions designated site 3 of the $^3H_4 \Leftrightarrow {}^3F_3(1)$ transition of 0.1% Pr^{3+}:$RbPb_2Br_5$ at 1584.239 nm at 1.6 K.

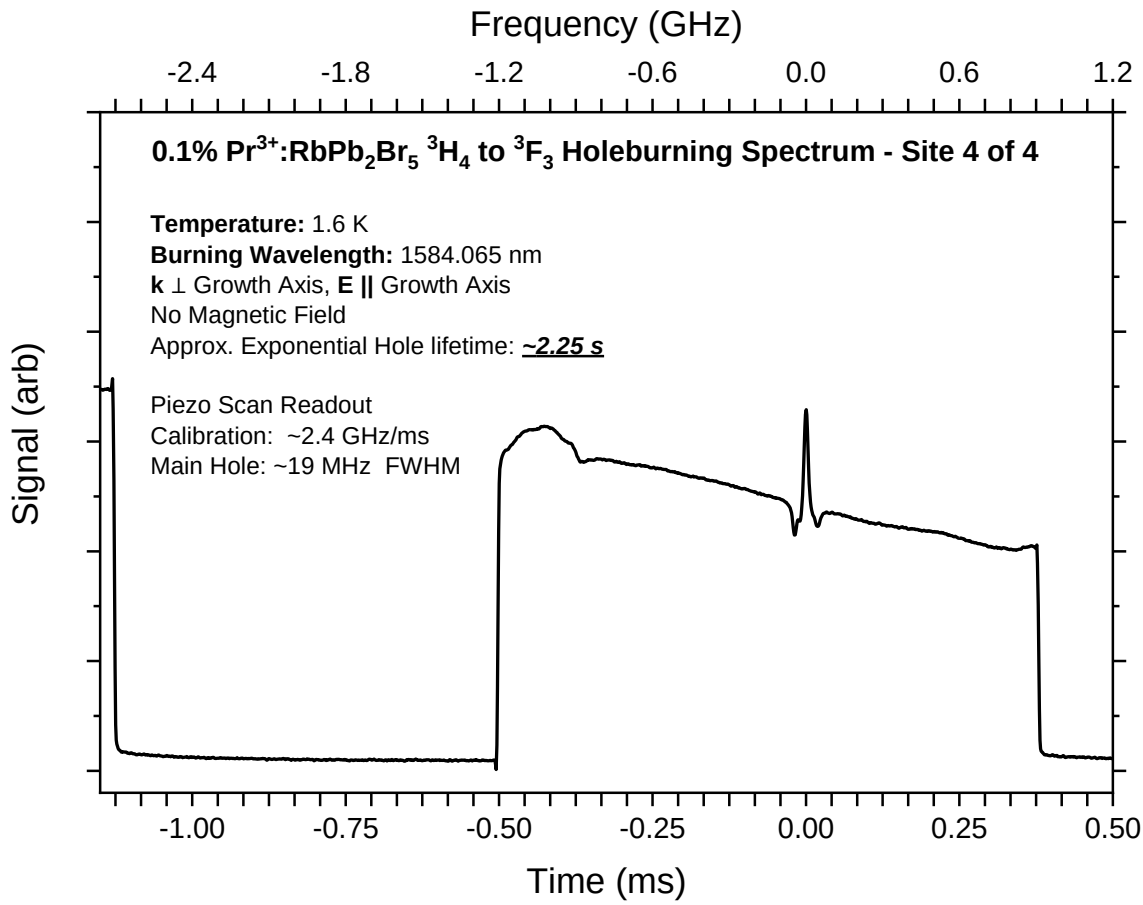

Figure 48. SHB on the ions designated site 4 of the $^3H_4 \Leftrightarrow {}^3F_3(1)$ transition of 0.1% Pr^{3+}:$RbPb_2Br_5$ at 1584.065 nm at 1.6 K.

The hole burning spectrum in fig. 49 indicates that the transition at 1582.645 nm is either a separate site altogether, site 5, or is another level in the structure of site 4. The latter interpretation can be made because of its identical T_1 fluorescence lifetime, the long hole lifetime characteristic of that site, and the phonon-broadened holes. It is noteworthy for quantum information applications such as microwave-optical transduction, that upper crystal field level hole burning transitions are of interest due to the potential use cases of multi-level systems not split by external fields [30-32, 34, 35, 69-72, 114, 127-132, 221, 232]. In this case, the ~170 GHz

splitting is possibly too large for direct use, but its presence implies that other transitions on other hole burning level structures with smaller spacings could certainly exist.

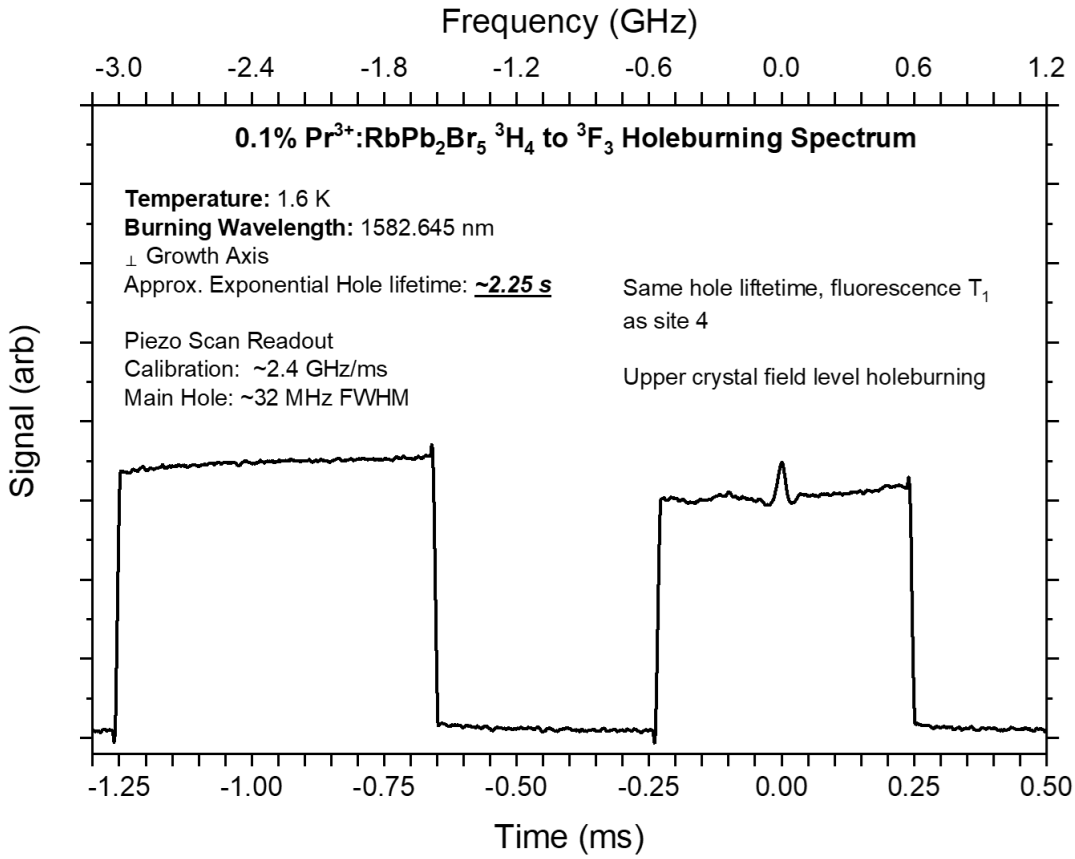

Figure 49. SHB on the ion designated site 4 of the $^3H_4 \Leftrightarrow {}^3F_3(2)$ transition of 0.1% Pr^{3+}:$RbPb_2Br_5$ at 1584.458 nm at 1.6 K. Note that this is an excited crystal field level of $^3F_3$ that is being burned. The broadening of the hole is in part due to non-radiative relaxation from $^3F_3(2)$ to $^3F_3(1)$.

Time Resolved Fluorescence

The New Focus Velocity laser was tuned across the manifold, and pulsed to produce time-resolved fluorescence decays. Decays for the lowest levels are shown in Figs. 50-53. This positively identified each site as having a unique structure and relaxation rate from $^3F_3$. The T_1 lifetimes range from 0.55-1.0 ms, indicating that the non-radiative relaxation pathways to nearby

adjacent manifolds such as $^3H_2$ are strongly suppressed in accordance with the concepts described in chapter 3. The multiphonon relaxation cutoff is approximately five times the maximum phonon energy of 138 cm^{-1}, or 690 cm^{-1}(14 μm), which is roughly half the ~1300 cm^{-1} (7.7 μm) spacing between $^3F_3$ and $^3H_2$. In the alkali lead halides, especially RPB, many of those Pr^{3+} transitions would be of great interest for 3-10 μm transitions due to the plethora of transitions in this range, though not all are not from the ground state $^3H_4$. Excited state transitions though are of practical interest for many applications, including quantum information. One such transition in Tm^{3+}:$YAlO_3$ is discussed in chapter 6.

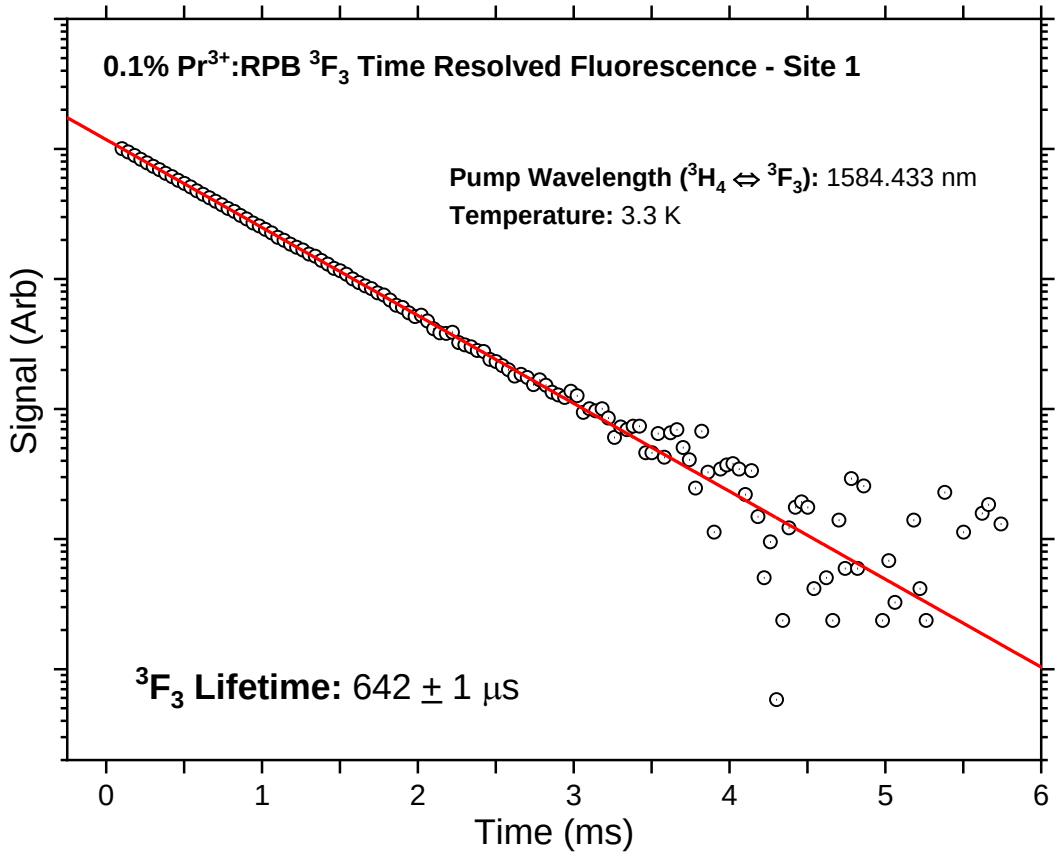

Figure 50. Time resolved fluorescence from $^3F_3$ in site 1 of 0.1% Pr^{3+}:RPB at 3.3 K.

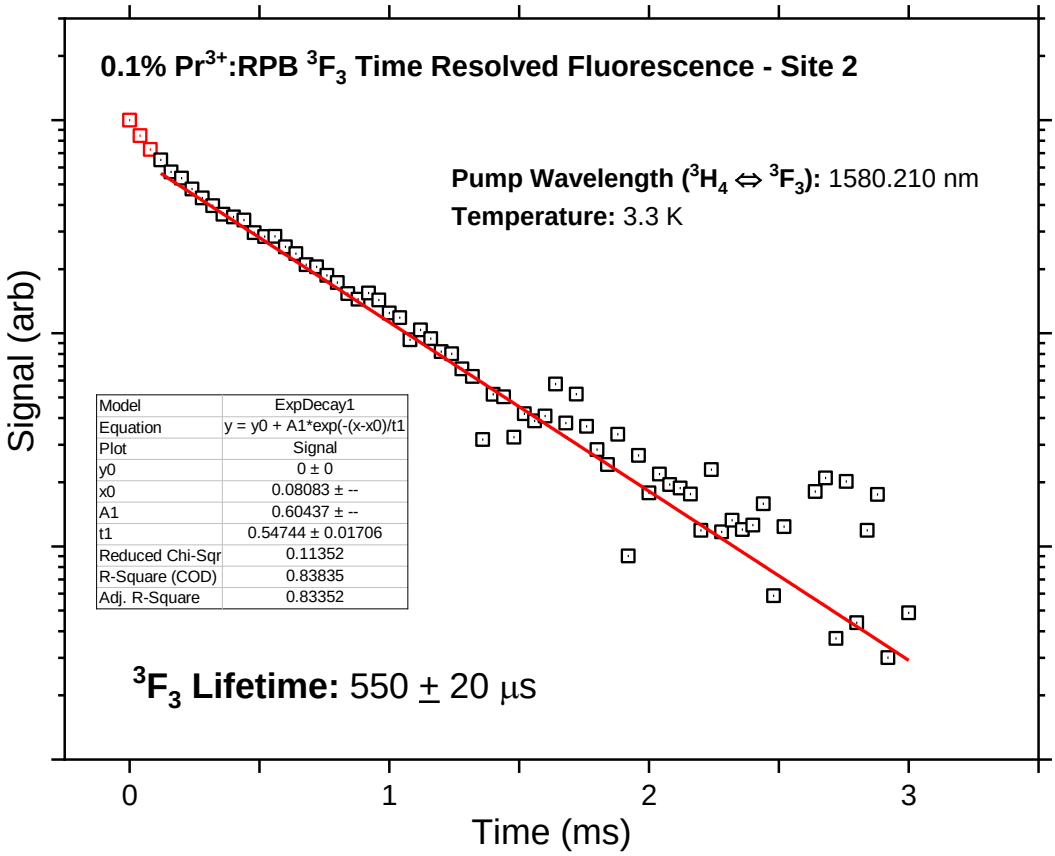

Figure 51. Time resolved fluorescence from $^3F_3$ in site 2 of 0.1% Pr^{3+}:RPB at 3.3 K.

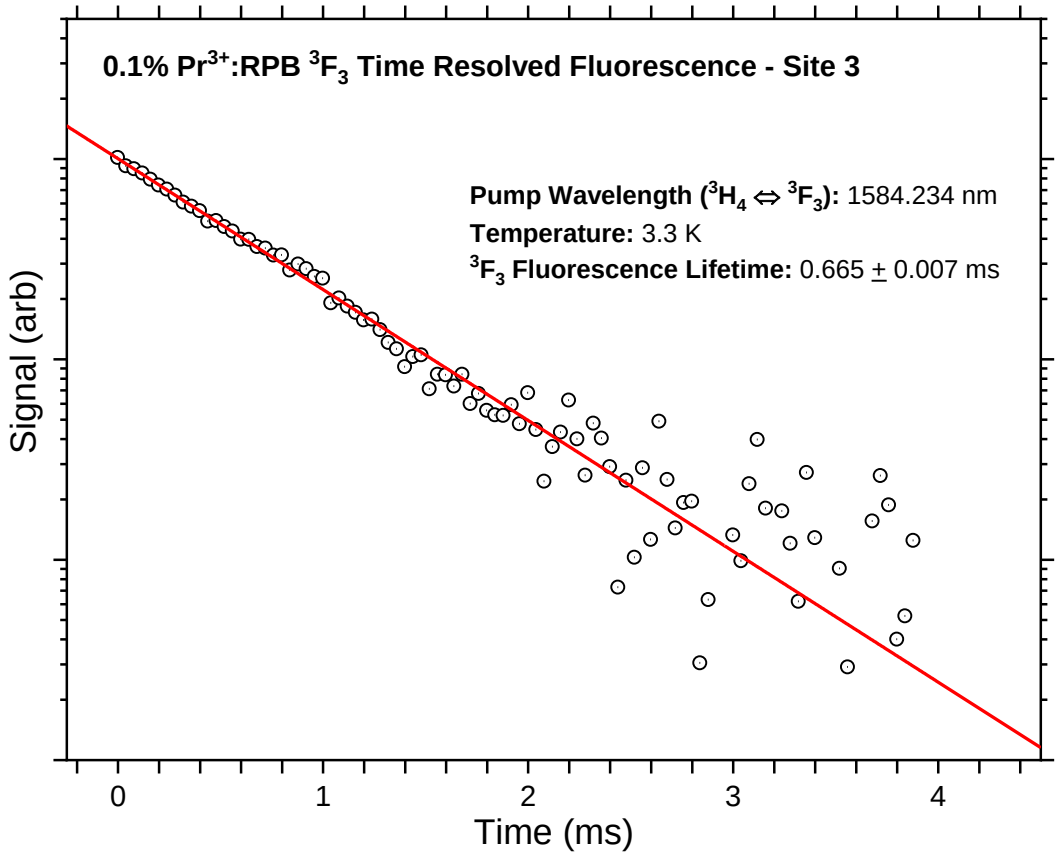

Figure 52. Time resolved fluorescence from $^3F_3$ in site 3 of 0.1% Pr^{3+}:RPB at 3.3 K.

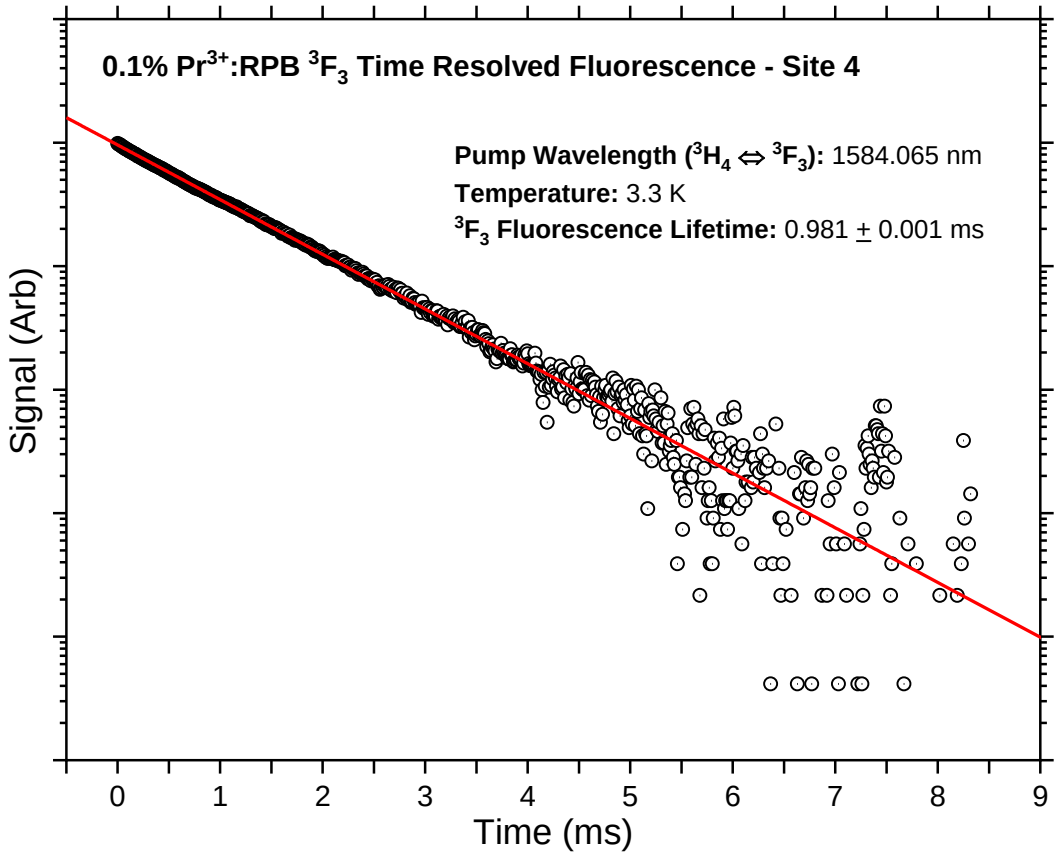

Figure 53. Time resolved fluorescence from $^3F_3$ in site 4 of 0.1% Pr^{3+}:RPB at 3.3 K.

The site assignments of the upper crystal field levels of $^3F_3$ were chosen primarily based on the closest T_1 fluorescence lifetimes observed from those levels. However, in several cases, the lifetimes were not exact or were convolutions of multiple decays, especially higher up in the manifold, and so the site assignment is subjective. The implication though is that in several cases the absorptions were not fully spectrally resolved, energy transfer excites different populations of ions in relaxation from the initial state, or these levels actually belong to $^3F_4$; further studies are needed to fully assign the transitions with total certainty.

Photon Echoes

Two-pulse photon echo measurements were made on all four holeburning sites in the $^3H_4 \Leftrightarrow {}^3F_3(1)$ transitions of Pr^{3+}:RPB at 1.6 K. Modulations due to the quadrupole levels of Pr^{3+} dominated the relaxation behavior of the coherence in all four cases, resulting in ~750 ns phase memory times T_M. The modulated photo echoes were fit to the following equation:

$$I = I_0 e^{-2\left(\frac{2(t-t_0)}{T_M}\right)^x)} \cdot \left[1 + \frac{\beta}{1+\beta^2}\begin{pmatrix} 2e^{-\pi\Gamma_g(t-t_0)} \cdot cos(\omega_g(t-t_0)) + \\ 2e^{-\pi\Gamma_e(t-t_0)} \cdot cos(\omega_e(t-t_0)) - \\ e^{-\pi(\Gamma_g+\Gamma_e)(t-t_0)} \cdot cos((\omega_g-\omega_e)(t-t_0)) - \\ e^{-\pi(\Gamma_g+\Gamma_e)(t-t_0)} \cdot cos((\omega_g+\omega_e)(t-t_0)) \end{pmatrix}\right]^2 \quad (17)$$

Eq. (17) is comprised of two factors. The first factor is the Mim's decay [17, 66, 67, 104, 106, 137, 141, 233], with delay t, phenomenological phase memory time T_M, and non-exponential decay factor x. The second factor are the modulations and beatings of the ground and excited nuclear levels in a four-level system, with spin flip probability β, inhomogeneous widths of the nuclear spin flip transition Γ_g and Γ_e for the ground and excited electronic states respectively, and angular frequencies ω_g and ω_e of the ground and excited electronic state spin transitions [115, 142, 143, 233, 234].

Fits to eq. (17) are limited in physical meaning in this context. The first reason is that the equation as written is a simplification of the real Pr^{3+} system. This is because there are three quadrupole levels in the ground and excited electronic states apiece, but the equation accounts for only two nuclear spin transitions altogether. Additional factors of beatings caused by other levels could be inserted, but this leads to the second issue. In eq. (17), there are already eight total unknown parameters, and several fits are possible. To adequately constrain the parameter space, the inhomogeneous broadening of the spin flip transitions and their transition energies must be measured in other ways, with other magnetic resonance techniques such as NMR or

ODMR [132, 149]. Overall, eq. (17) cannot capture the complete of the behavior of the echo modulations observed in Figs. 54-57. However, the phase memory time T_M and the dominant frequency components can certainly be determined. The power spectrum of each photon echo curve was inspected to determine the major frequency components as an initial guess to seed the fit. The peaks of the frequency components in the modulated decays are recorded in the captions of each trace, with the peaks being used as the starting points for the fits bolded and underlined.

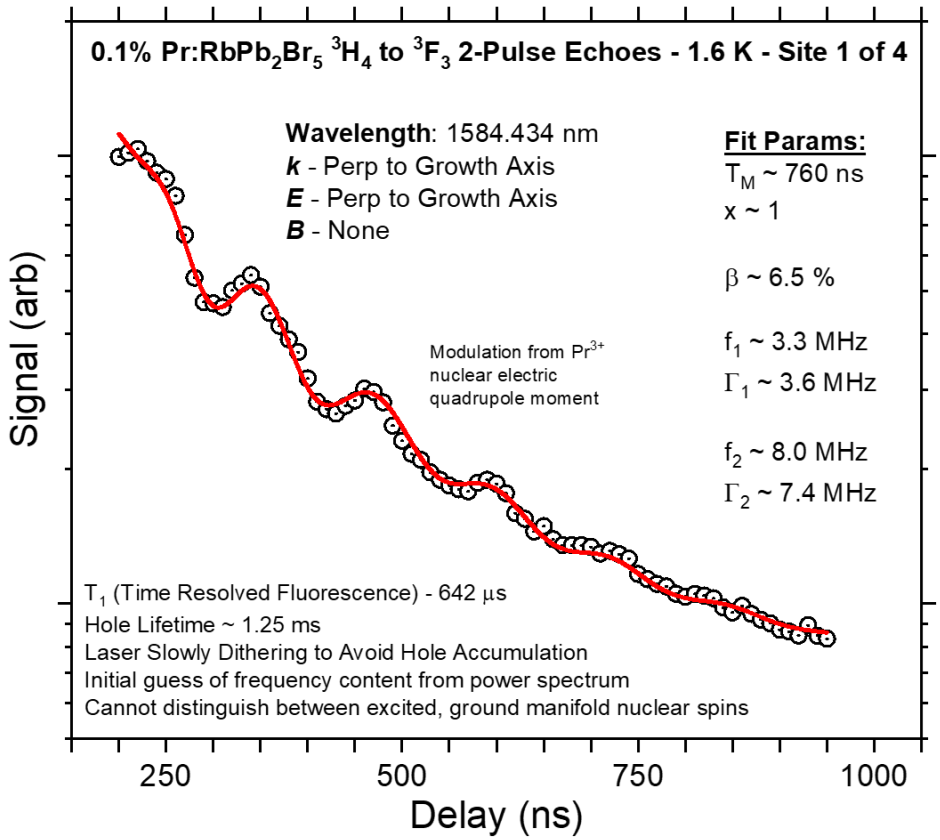

Figure 54. Modulated two-pulse photon echoes on the ions designated site 1 of the $^3H_4 \Leftrightarrow {}^3F_3(1)$ transition of 0.1% Pr^{3+}:RPB at 1584.458 nm at 1.6 K. Frequency components in this decay measured include **2.9 MHz**, **8.3 MHz**, 14.1 MHz, and 23.6 MHz.

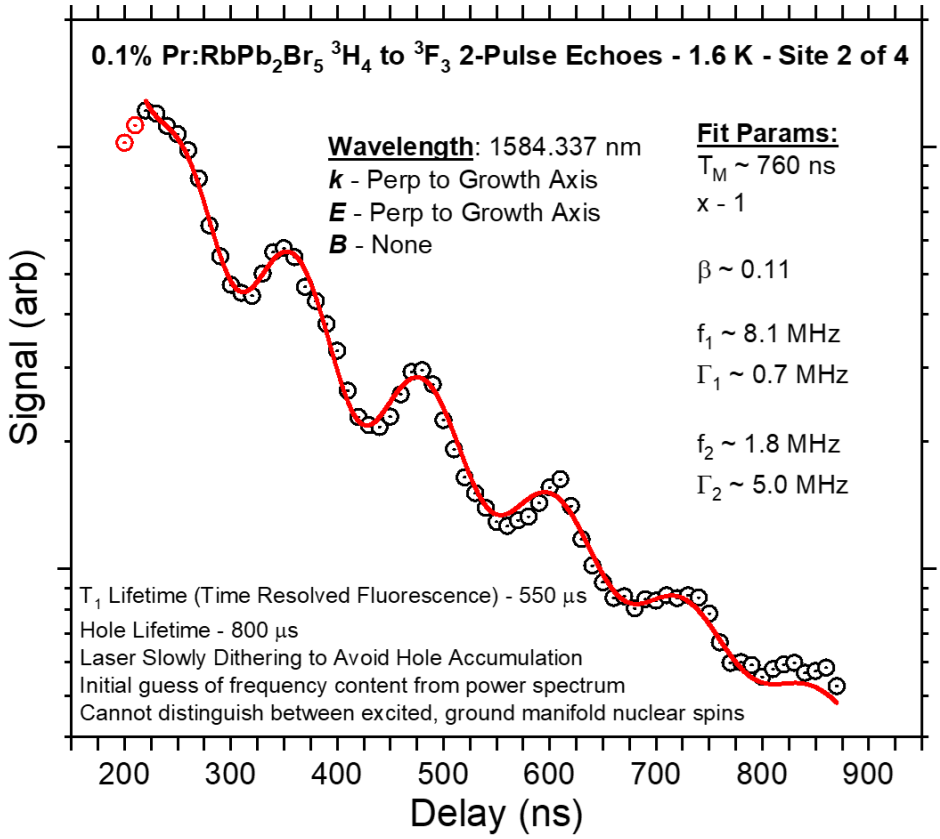

Figure 55. Modulated two-pulse photon echoes on the ions designated site 2 of the $^3H_4 \Leftrightarrow {}^3F_3(1)$ transition of 0.1% Pr^{3+}:RPB at 1584.337 nm at 1.6 K. Frequency components in this decay measured include **2.5 MHz**, **8.1 MHz**, 15.7 MHz, and 23.1 MHz.

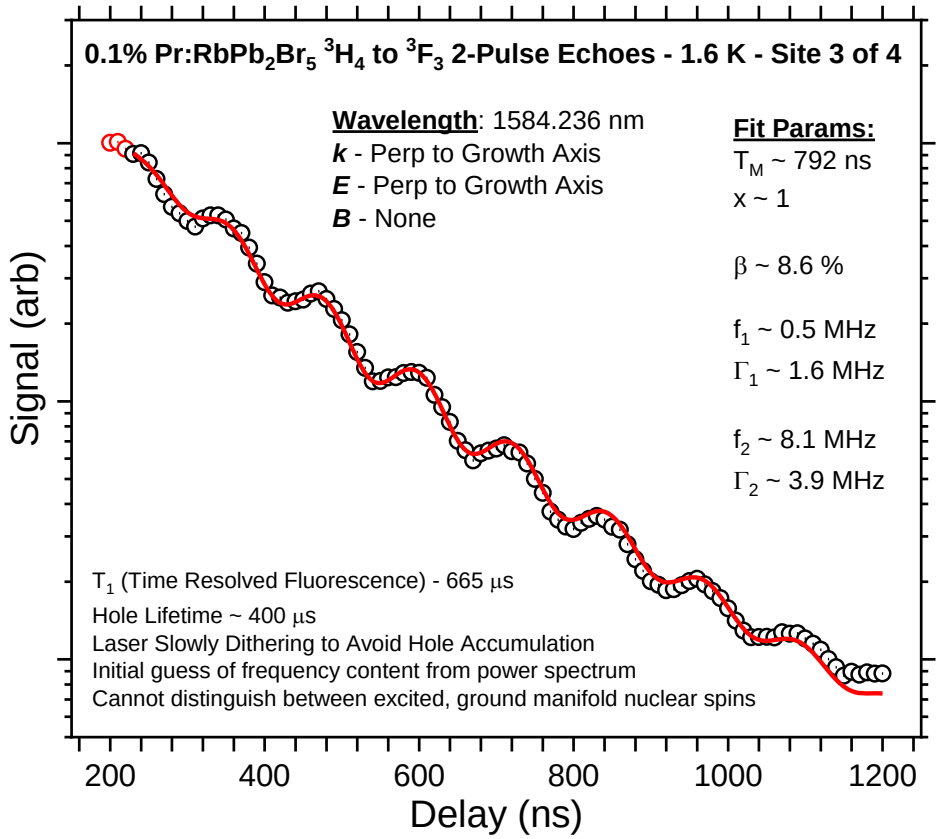

Figure 56. Modulated two-pulse photon echoes on the ions designated site 3 of the $^3H_4 \Leftrightarrow {}^3F_3(1)$ transition of 0.1% Pr^{3+}:RPB at 1584.236 nm at 1.6 K. Frequency components in this decay measured include **1.9 MHz**, **7.9 MHz**, 22.7 MHz, and 38.0 MHz.

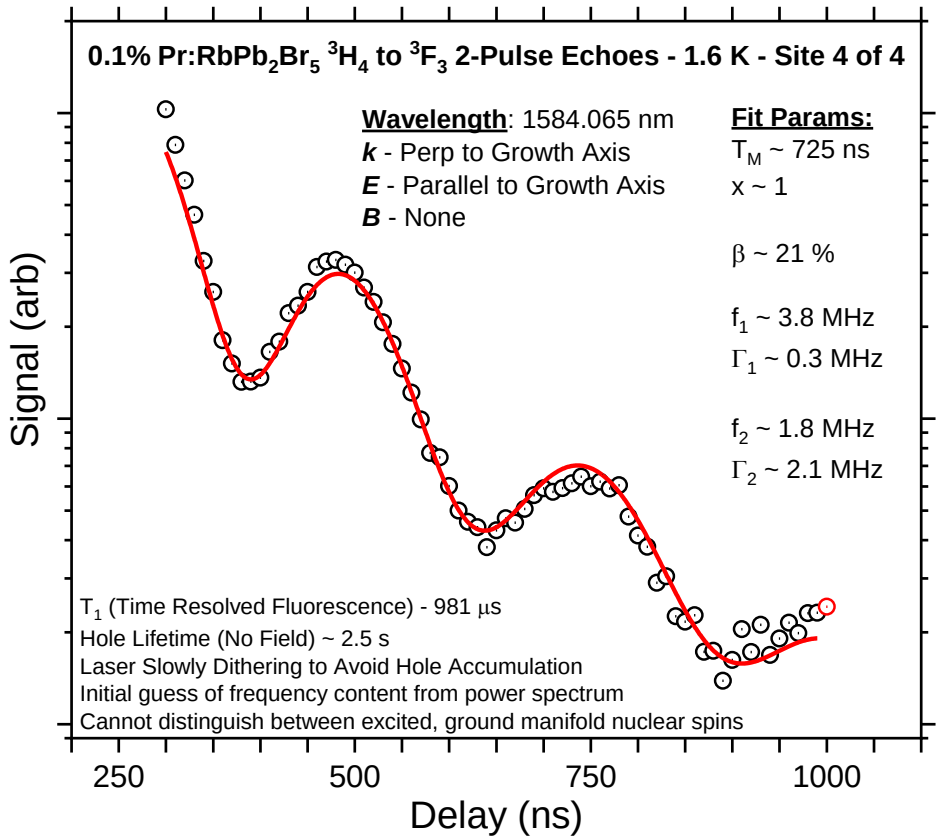

Figure 57. Modulated two-pulse photon echoes on the ions designated site 4 of the $^3H_4 \Leftrightarrow {}^3F_3(1)$ transition of 0.1% Pr^{3+}:RPB at 1584.065 nm at 1.6 K. Frequency components in this decay measured include **1.0 MHz**, **4.4 MHz**, 10.5 MHz, and 17 MHz.

Photon echoes in all sites exhibited strong responses to weak fields from bar magnets placed (~10 Gauss) parallel and perpendicular to the ***g***-axis. Fields made with Helmholtz coils (~100 G) would enable a more systematic study of the magnetism of the Pr^{3+} in RPB and lead to significant increases in the phase memory time T_M.

Fluorescence Spectrum

To map out the ground state structure, the praseodymium $^3H_6 \Leftrightarrow {}^3P_0$, $^3P_1$, $^1I_6$, $^3P_2$ levels were excited with a 450 nm laser diode in the MI C_2 cryostat at 10 K. Elevated temperature assisted with pumping by thermally broadening the excitation bands. Population relaxing to $^3F_3$ resulted in fluorescence revealed the structure of all four sites simultaneously identified in holeburning and time-resolved fluorescence and probed the general structure of the ground manifold $^3H_4$. The spectrum is shown in fig. 58. Site selective fluorescence spectra is needed to expose each site energy level structures, and many sharp lines are assumed to be unresolved due to the elevated temperature dependence measured in hole burning. The level structure is given in table 12.

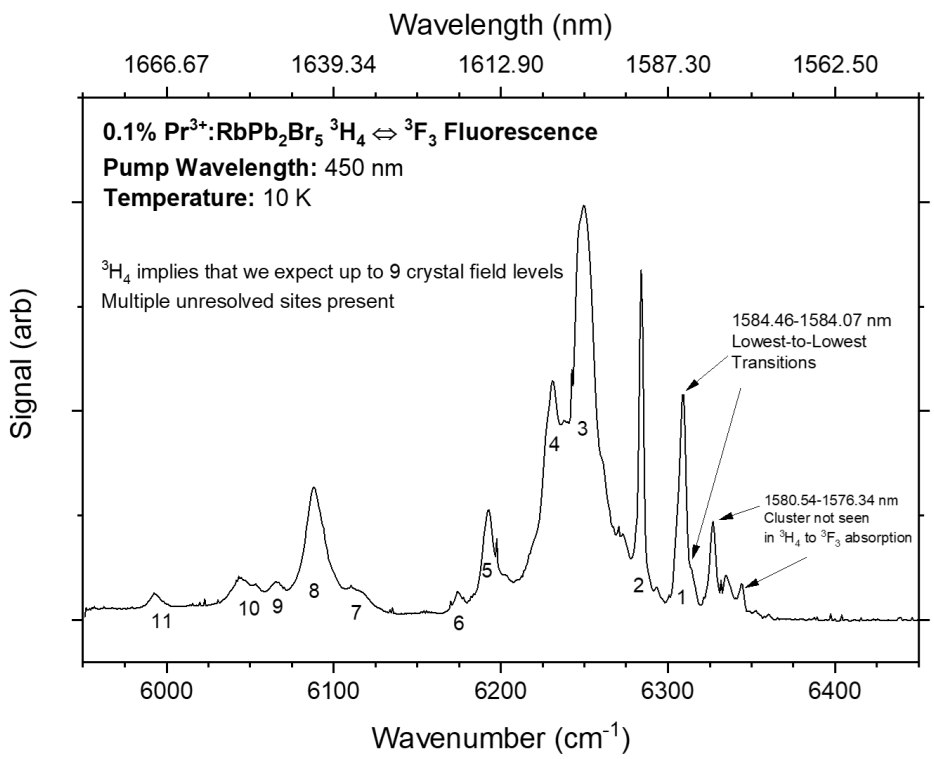

Figure 58. Fluorescence spectra pumped with a 450 nm laser diode ($^3H_6 \Leftrightarrow {}^3P_0$, $^3P_1$, $^1I_6$, $^3P_2$) in 0.1% Pr^{3+}:RPB at 10K to identify the structure of the ground manifold. Site-selective fluorescence is needed to map out the specific energy level structure of each particular site. The lowest-to-lowest transitions are known from the laser absorption in fig. 44.

$^3H_4$	Level #	Energy (cm^{-1})	Comment
	1	0	Unknown site assignments due to thermally broadened lines
	2	25	
	3	60	
	4	79	
	5	117	
	6	136	
	7	199	
	8	221	
	9	244	
	10	266	
	11	317	

Table 12. Observed energy levels from unpolarized fluorescence measured from $^3F_3$ in the sample of 0.1% Pr^{3+}:RPB, excited with 450 nm diode to ^3P_x and $^1I_6$ manifolds in that band. Levels measured are clusters of perturbed sites broadened by the measurement resolution and the temperature (10K). This table should be viewed as a rough estimate of the level spacings in $^3H_4$, Site-selective fluorescence is needed to discern which lines belong to which site.

Spectroscopy of Tm^{3+}:KPb_2Br_5

White light absorption measured the energies of the $^3F_3$ levels at 4K, shown in fig. 59 and enumerated in table 13. The propagation vector ***k*** was perpendicular to the growth axis, and low polarization dependence was detected with ***E*** either parallel or perpendicular to the sample growth axis.

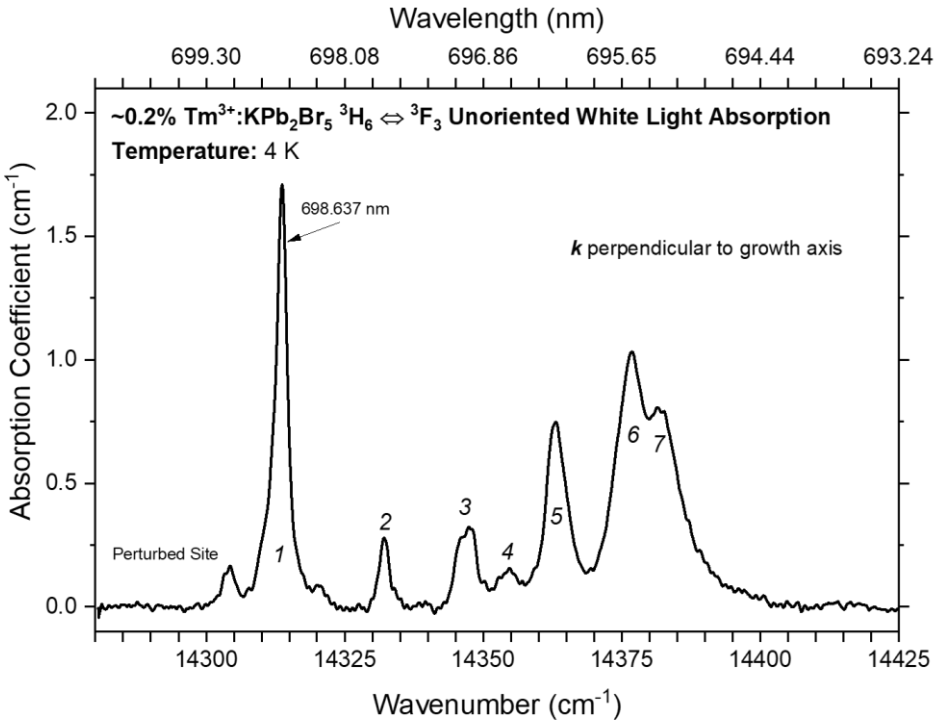

Figure 59. White light absorption spectra of 0.2% Tm^{3+}:KPb_2Br_5. Low polarization dependence was measured both in this spectrum and in the holeburning measurements, indicating that the propagation vector ***k*** was possibly close to the optical axis of the material, the axis at which light propagates as if it were in an isotropic material [224].

$^3F_3$ Level #	Energy (cm^{-1})	Comment
1	14313.59	Hole burning; Inhomogeneous Width: 71.9 GHz
2	14332.1	
3	14347.4	
4	14354.7	
5	14363.1	
6	14376.7	
7	14381.7	

Table 13. Observed $^3F_3$ levels of Tm^{3+}:KPb_2Br_5.

The homemade laser was used identify the lowest-to-lowest transition in the spectrum of $^3H_6 \Leftrightarrow {}^3F_3$ transitions by burning ~20 MHz holes into the $^3H_6 \Leftrightarrow {}^3F_3(1)$ transition. The large spectral hole width is the consequence of laser jitter and long burn times; it is not indicative of the homogeneous linewidth Γ_h. Long burn times were required to generate clear holes, because of the combination of low power from the homemade laser cavity and of the ~100 μs lifetime of $^3F_3$. The homemade laser was also measured to walk up to ~50 MHz in ~100 ms by measuring the variation of the oscilloscope trace of the spectral hole with time delay, which has consequences for the spectral hole decay shown in fig. 61. Overall, ~20 MHz holes are expected in this arrangement without laser stabilization or higher power. Low magnetic fields from button magnets (~10 G at the sample) sharpened these broad holes noticeably, indicating the scale and presence of the enhanced nuclear moment of thulium [126], and strongly implying the holes could be much narrower than those burned.

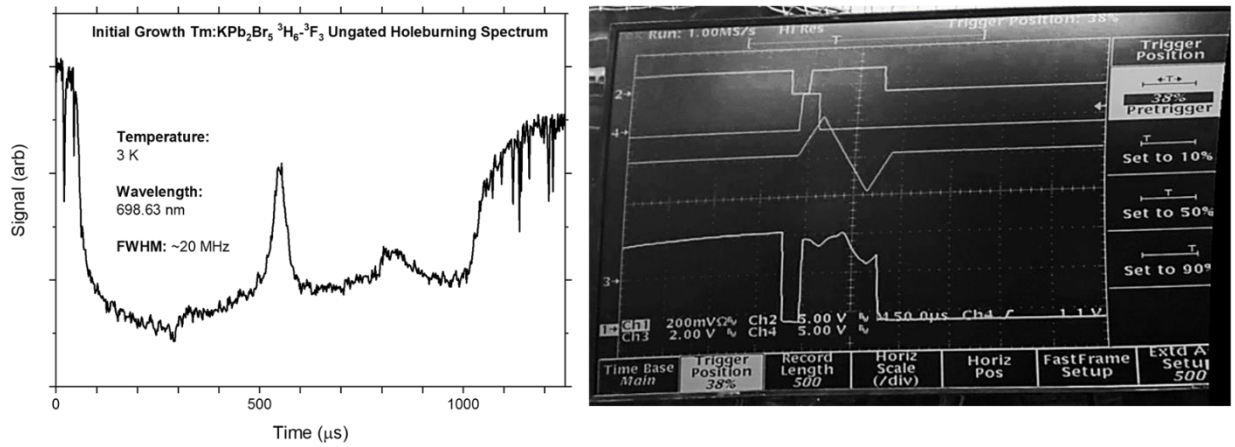

Figure 60. Examples of traces of (left) ungated and (right) gated spectral holeburning in Tm^{3+}:KPb_2Br_5. Long burn times and laser noise result in artificially broad holes, which are ideal for long spectral hole decay measurements.

Spectral hole decays were measured out to ~100 ms, where the first ~100 μs is the T_1 lifetime of the $^3F_3$ state, measured in chapter 3. The drift of the laser between the burn and the readout precluded longer decay measurements, and directly measured the laser stability over the course of the prescribed delays. The lifetime of the spectral holes measured here are consistent with those measured in chapter 3 in Tm^{3+}:LaF_3. They imply the lifetimes of the bottleneck states, especially $^3F_4$.

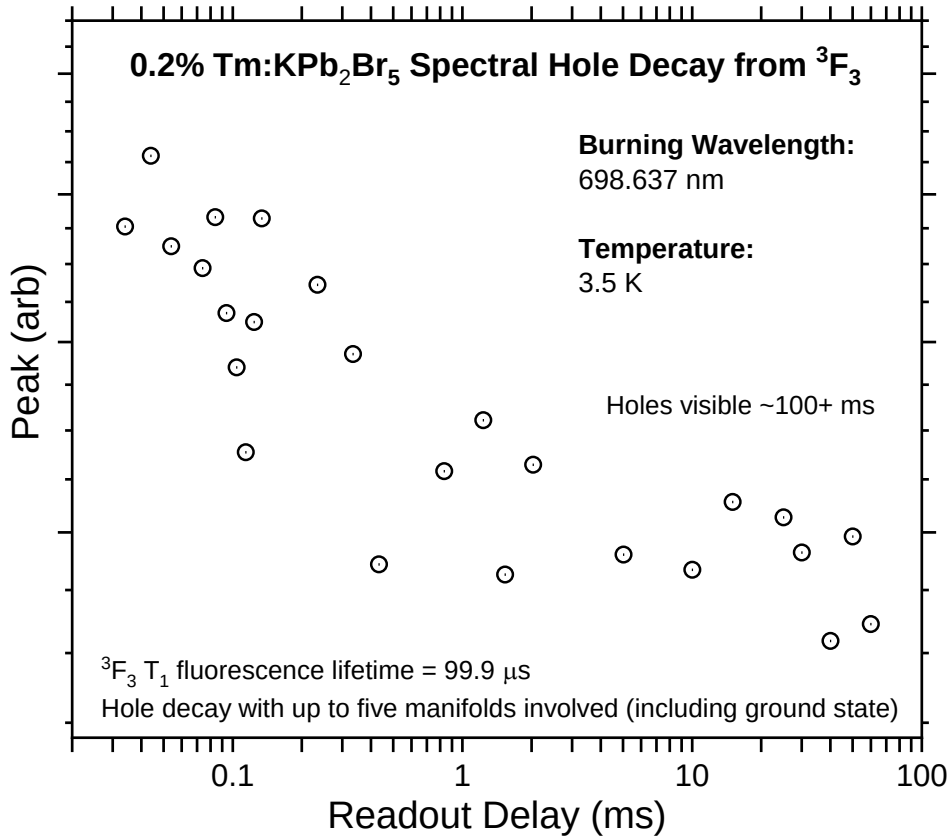

Figure 61. Spectral hole decay of trenches burned into the $^3H_6 \Leftrightarrow {}^3F_3(1)$ transition of Tm^{3+}:KPb_2Br_5. The decay not only measures the material properties but characterizes the laser behavior. The decay could not be measured longer than 100 ms due to the laser jitter and drift. Up to five separate manifolds are involved in the decay; a fit to extract lifetimes and population fractions of levels below $^3F_3$ requires spectroscopy on the levels below the $^3F_3$ and laser stabilization to reduce noise.

Discussion

Any simplification of a quantum memory systems is highly sought after to improve efficiency and bitrates by mitigating photon loss and multiplexing [30-35, 42, 52, 64, 69-71, 74, 114, 127, 128, 130, 132, 134, 136, 137, 148, 221, 222, 235]. Therefore, the detection of luminescence, holeburning, and photon echoes on the ~1584 nm transitions of 0.1% Pr^{3+}:RPB has several important implications.

Telecom optical transitions with any measurable coherence at least on order of a microsecond are few, and none of them are located near the optical L-band [64]. This feature alone makes this material of interest for quantum repeaters in long haul communication systems. A major advantage is that it can circumvent frequency conversion of single photons from memory operating wavelengths to telecom transmission bands [32, 74, 134, 148, 235]. Additionally, telecom hardware such as high-quality commercial lasers, amplifiers, optical fibers, and general optical components such as mirrors and lenses are commonly available.

The presence of four independent optical L-band transitions in Pr^{3+}:RPB, each with 2-5 GHz inhomogeneous linewidths and all within ~50 GHz of each other, is of interest for multiplexed quantum memories and microwave-optical transduction [35, 36, 74, 107, 129-132, 137, 148]. Narrower inhomogeneous lines should be possible through improvements in growth procedure to eliminate impurities present in this streamlined growth procedure and then through isotopic purification of the host ions [232]. Increased absorption, needed for assuring single photon absorption, could occur through increased Pr^{3+} doping. The intrinsic isotopic purity of ^{141}Pr is also an advantage as there are no complications from overlapping isotopic structures and the associated spin-spin interactions. The material also has flexibility in that it can be used in a zero-field operational mode near magnetically sensitive components in the confines of a cryostat. It is also certain that magnetic studies will enable improvements in the phase memory time by decoupling the Pr^{3+} spins which dominate the echo decays [32, 51, 52, 56, 58, 68, 72, 109, 117, 132, 142-144, 149, 179, 180, 236] and allow tuning of the inhomogeneous lines to better suit microwave-optical transduction [131, 132]. Lower temperature will also further suppress phonon-mediated decoherence to determine the limitations of performance. The zero-field, long-

lived ground state nuclear storage are also of interest for SHB applications in the telecom bands [17, 19, 20, 43-47, 49, 51-53, 61, 62, 65, 74, 88].

It is strongly emphasized that Pr^{3+} should not be the only ion of interest for telecom transitions either. In terms of rare-earths, neodymium, samarium, europium, terbium, dysprosium, holmium, and thulium all have transitions out of their ground states in these bands. They are all worth another look in the alkali lead halides or another low-phonon cutoff host, and excited state transitions are also of interest [75, 86, 87]. The utility of an excited state transition is also investigated in chapter 6. Regardless, between all of these ions as well as transition metals, there should be more than enough transitions to cover the telecom window, especially if techniques like compositional tuning are also used [46]. Additionally, there is no compelling reason that alkali lead halides must be used other than that their growths are logistically straightforward to execute and they are not hygroscopic. Any soft, dense material should be interesting for the low Debye temperature approach, including many semiconductors [11, 29, 189-192].

It should be noted that the halogens generally have sizeable nuclear gyromagnetic ratios, especially fluorine, while lead and rubidium also have non-negligible magnetism as well. Only potassium in the studied materials possesses a relatively small gyromagnetic ratio (~2 MHz/T for both isotopes). Additionally, the nuclear spin of fluorine and lead may be 1/2, but chlorine, bromine, potassium, and rubidium isotopes have spins of 3/2 and rubidium, iodine, and praseodymium isotopes have spins of 5/2. These facts pose a problem for quantum memories in that nuclear spin interactions that dominate decoherence phenomena even below 1K, because they are never fully frozen out due to their generally small-scale energy differences [68, 72, 117,

126, 141, 144, 145, 200, 201, 216]. The ideal approach is then to instead avoid having large nuclear moments in the first place, as they are more sensitive to fluctuations in the magnetic environment. YSO is a common choice, but it is unsuitable for the $^3H_4 \Leftrightarrow {}^3F_3$ transition due to crystal's high Debye temperature [74, 149, 163]. Therefore, a host with low-spin in conjunction with a low phonon cutoff energy should be used to suppress magnetically-mediated decoherence as well as enable luminescence of transitions like $^3H_4 \Leftrightarrow {}^3F_3$. Magnetic fields and dynamic decoupling protocols can suppress deleterious interactions, but also increase device complexity [72, 102]. Even so, these potential hesitations do not preclude Pr^{3+}:RPB from being used as a quantum memory material. Instead, they should be recognized and accounted for in implementations and be used to guide the next development of generation of quantum memories.

The spectroscopy of 0.2% Tm^{3+}:KPB with a homemade laser demonstrates how basic results can be acquired and the experimental hardware framework can be initiated by leveraging the time and frequency domain properties of rare-earths and engineering of the host material. The system itself warrants more extensive investigation for SHB applications due to its extended T_1 lifetime and its long spectral hole lifetime in zero field.

It should be noted that divalent thulium would have great advantages in the alkali lead halides. First, the additional electron of Tm^{2+} increases the ion size, and offsets the radius and charge mismatch from Pb^{2+}, enabling higher dopant concentrations. Second, Tm^{2+} is a well-known solar concentrator ion for improving solar cell efficiencies, and the alkali lead halides are already closely related to the host materials already used in those applications, but the alkali lead halides are comparatively chemically stable and not hygroscopic [63, 237, 238]. Third, Tm^{2+} is also of great interest as an analog of Yb^{3+}, which is already used for quantum information

applications [106, 130]. There is only one stable thulium isotope of spin 1/2, whereas there are seven stable ytterbium isotopes of roughly similar abundances with nuclear spins varying from 0 to 1/2 to 5/2. Using Tm^{2+} would lead to a drastic simplification in nuclear structure and isotopic purity for those approaches, while possessing a similar $^{2S+1}L_J$ level structure to Yb^{3+}. Intrinsic Tm^{2+} was not found in the investigated samples as grown, but Tm^{2+} may be created through reduction during the growth or through photoionization [239, 240].

Conclusions

Two alkali lead halides, RPB and KPB, have been explored with high resolution spectroscopy to expand the toolkit of rare-earth doped materials and transitions for advanced luminescence, laser, SHB, and quantum information applications. Pr^{3+}:RPB was found to have many attractive features, with coherence measured on four L-band transitions. Tm^{3+}:KPB demonstrated approaches for bootstrapping fundamental research and hardware simultaneously and demonstrating the power of rare-earth SHB to characterize lasers in both the time and frequency domain. These results are encouraging for more explorations in the alkali lead halide family of materials, and these new wavelengths should be the first step to enabling many exciting new applications.

CHAPTER SIX

INVESTIGATION OF THE TELECOM $^3F_4 \Leftrightarrow {}^3H_4$ TRANSITION IN TRIVALENT THULIUM FOR THE DEVELOPMENT OF EXCITED STATE TRANSITIONS FOR CLASSICAL AND QUANTUM SIGNAL PROCESSING

In this chapter, a third transition, disused due to its presence above the ground manifold of Tm^{3+}, is explored. The excited state transition of $^3F_4 \Leftrightarrow {}^3H_4$ in Tm^{3+}:$YAlO_3$ at ~1451 nm is surveyed for the purpose of identifying a suitable host for implementing quantum memories and hole burning applications in an excited state scheme. Experimental techniques for measuring the properties of this class of transition are presented and their analysis is discussed. Using two-wavelength approaches, a ~950 MHz inhomogeneously broadened absorption is measured, ~30 MHz holes are burned on $^3F_4 \Leftrightarrow {}^3H_4$, and time-resolved fluorescence reveals a ~5 ms $^3F_4$ bottleneck lifetime while observing the fluorescence from $^3H_4$. These results speak to the potential of the unexplored regime of excited state transitions in rare-earths.

This work was produced in conjunction with Dr. Wolfgang Tittel's group at TU Delft, who sent Dr. Josh Slater to study these transitions and crystals with the Cone-Thiel Rare-Earth Spectroscopy Group. Our group is grateful for his expertise, effort, and enthusiasm, even late into the night a few hours before his early morning flight.

Introduction

A second quantum revolution is underway in the 21st century because of the maturation of quantum computation, cryptography, and networking. These developments stand to increase computational power many-fold and provide completely secure communications, but reliable and practical implementations of these systems depend on materials that allow preservation and manipulation of quantum states. One promising class of materials for quantum information science (QIS) applications is rare-earth doped crystals [32, 64, 134-136]. Rare-earth ions experience the local environment as a small perturbation relative to the free-ion, even when included in a solid. This results from an electronic structure that isolates the optically-active unfilled $4f^N$ shell from the electronic states of the host material. The ensemble of dopant ions in a solid can be addressed using the weakly allowed $4f^N$-$4f^N$ optical transitions that can be engineered to have large bandwidths, long lifetimes, and low decoherence [1-5]. These materials are therefore ideal for the storage and recall of photons, a critical feature of quantum memories, if remaining intrinsic and extrinsic sources of decoherence are suppressed [6]. In rare-earth-based quantum memories, a programmed material can store and recall photons on demand using photon echo methods that causes the material to re-emit a photon with the same quantum state as the absorbed photon. The success of this read-write operation is limited by the fundamental lifetime of the transition and dynamic perturbations that corrupt the phase of the stored coherence. Storage lifetimes can be significantly increased through transfer of the quantum coherence to long-lived spin states of the rare-earth ion in an applied magnetic field. Characterization, modeling, and control of decoherence effects in rare-earth materials are critical for attaining high-efficiency quantum memories and an important focus of research.

One outstanding issue for the rare-earth ensemble approach to signal processing and quantum computation, memories, and transducers is the shortage of suitable optical telecom transitions with good T_1 lifetimes and measurable coherence [19, 64, 72, 131, 134, 220], even though many transitions exist in the range of the telecom window [75, 86, 87]. In chapters 3, 4, and 5 of this thesis, the Tm^{3+} $^3H_6 \Leftrightarrow {}^3F_3$ and the Pr^{3+} $^3H_4 \Leftrightarrow {}^3F_3$ transitions had non-radiative relaxation suppressed through understanding of the material dynamics at low temperatures and subsequent engineering of the host-material. Another approach to expanding the toolbox of lanthanide telecom transitions is to use excited state transitions, that is, between manifolds that do not include the atomic ground state. The disadvantage to this approach is the additional layer of complexity in pumping and preparing transitions to capture and store optical coherence before transfer to longer-lived spin levels. It also requires a long-lived bottleneck state $|0\rangle$ above the ground state $|g\rangle$ to use as the lower state of the memory. However, there are advantages to using the ground state $|g\rangle$ as a population shelving state, one of which is that the ground state possesses an infinite lifetime to store and retrieve population. In this scheme, an atomic frequency comb (AFC) or a controlled, reversible inhomogeneous broadening (CRIB) memory is prepared first by burning in population into the lower state $|0\rangle$ in the prescribed patterns of the memory, as opposed to burning it away into the shelving state [32, 69, 113, 114, 219, 241].

Trivalent thulium is known to possess a level structure that fits the desired pattern, shown in fig. 62. $^3F_4$ is a bottleneck state with long T_1 lifetimes in many materials [109], and the ~1451 nm $^3F_4 \Leftrightarrow {}^3H_4$ transition is attractive for its wavelength. Moreover, thulium possesses a simple magnetic structure, being a non-Kramers ion of nuclear spin 1/2 with a single stable isotope, making it an ideal test case. Due to its long history of use as a laser ion, especially ~2 μm

wavelengths, thulium-doped host materials abound [109, 242, 243]. The principle criteria for a useful quantum memory material are (1) that it possesses good coherence and hole burning properties, and (2) that the ensemble absorption be strong at relatively low concentrations, so that single photons are captured with ~100% probability while mitigating decoherence from other ions [64, 104, 108, 134, 136, 137]. However, observing hole burning on an excited state transition is an important first step, and demonstrates that excited state transitions have practical potential that is largely unexplored and even unconsidered.

Another complication is that the lifetimes of longer-lived bottleneck states can be awkward to measure as they typically are at long wavelengths or otherwise difficult to regimes for spectroscopy, and QIS labs focused on specific bands. In the case of thulium, measurements of the $^3F_4$ lifetime can be challenging. PMTs are drowned in thermal noise at ~2 μm without liquid nitrogen cooling and detectors tend to be less common than for wavelengths less than 1.8 μm. Excitation to a shorter lived level that also fluoresces to relax to the ground state above the bottleneck can overcome this difficulty by recognizing that the two fluorescence lifetimes are only convolved. The resulting decay may be used to extract the bottleneck lifetime indirectly.

In the course of this work, thulium doped laser crystals were surveyed, and the spectroscopy of Tm^{3+}:$YAlO_3$, lifetimes, and spectral hole burning observed on its $^3F_4 \Leftrightarrow {}^3H_4$ transition are reported. The level structures of the $^3H_6$, $^3F_4$, $^3H_5$, and $^3H_4$ are mapped out in absorption and emission at 4K to precisely locate the lowest-to-lowest transitions of interest. A double pumped time-resolved fluorescence measurement of the $^3F_4$ and $^3H_4$ levels, described by Thiel [244], is presented. The decay is analyzed to determine the bottleneck lifetime without measuring the fluorescence from $^3F_4$ directly. The T_1 lifetime of $^3F_4$ is found to be 5.94 ms, while the lifetime of

$^3H_4$ is found to be 889 μs. The same techniques are used to measure the ~1GHz inhomogeneously broadened absorption and to burn ~30 MHz ungated CW spectral holes on the excited state transition. The implications for classical and quantum signal processing applications and further research are briefly discussed.

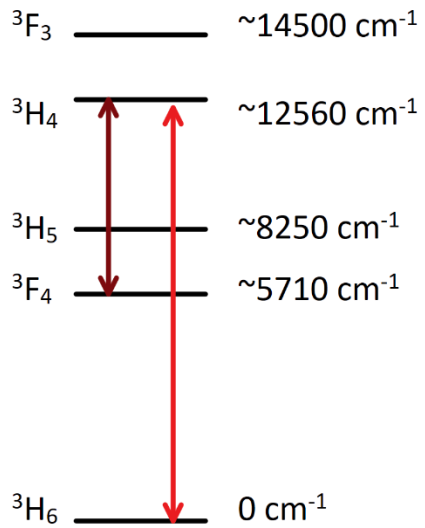

Figure 62. Energy level diagram of Tm^{3+}, with the 1451.363 nm $^3F_4 \Leftrightarrow {}^3H_4$ telecom transition marked with a wine color, and the 795.314 nm $^3H_6 \Leftrightarrow {}^3H_4$ transition marked in red.

Experimental

Samples of 4% and 0.1% Tm^{3+}:$YAlO_3$ were obtained from Scientific Materials in Bozeman, Montana. $YAlO_3$, or Yttrium Aluminum Perovskite (YAP), is an orthorhombic crystal. It has a unit cell of $\boldsymbol{a}$ = 5. 330(2) Å, $\boldsymbol{b}$ = 7. 375(2) Å, $\boldsymbol{c}$ = 5.180(2) Å, and is of space group D_{2h}^{16}. Rare earths mainly occupy the yttrium site of low C_{1h} symmetry [242, 243, 245]. The 4% sample was cut in a coin shape 0.98 mm thick, with that direction parallel to the $\boldsymbol{a}$-axis. The 0.1% sample was cut from the top of boule and not oriented, but the propagation vector $\boldsymbol{k}$ was parallel to the growth axis, denoted the $\boldsymbol{g}$-axis.

To map out the structure of the manifolds $^3F_4$, $^3H_5$, and $^3H_4$, white light from a 12-Watt tungsten-halogen bulb was focused onto the sample of 4% Tm^{3+}:$YAlO_3$ in the Montana Instruments (MI) C_2 cryostat cooled to 4 K. The absorption spectra of all three manifolds were measured with a SPEX 1000 monochromator, with a Newport 818-IR power meter fitted to the exit slits. The fluorescence spectra of $^3F_4 \Leftrightarrow {}^3H_6$ (1775-1800 nm), $^3H_4 \Leftrightarrow {}^3F_4$(1450-1540 nm) and $^3H_4 \Leftrightarrow {}^3H_6$ (795-850 nm) were measured in the 0.1% sample to locate the lowest-to-lowest transitions and map out the ground state structure of $^3H_6$. To ensure maximum signal strength, the temperature of the cryostat was raised to 10K to broaden the homogeneous lines and offset the loss of absorption from hole burning. Emission was collected 90 degrees relative to the excitation beam propagation vector $\boldsymbol{k}$ and passed through the SPEX 1000 onto a liquid nitrogen-cooled Edinburgh Instruments germanium detector with ~10 ms response time and biased to 50V. All signals were routed into a Tektronix TDS 754C oscilloscope and then traces were captured by a computer program.

Laser absorption of the $^3F_4 \Leftrightarrow {}^3H_4$ transition at ~1451 nm was carried out in the 0.1% Tm:$YAlO_3$ sample in the C_2 cryostat at 4K by pumping the upper crystal field level of $^3H_6 \Leftrightarrow {}^3H_4$ at 795.315 nm with a ~100 kHz linewidth Coherent 899-21 Ti:Al_2O_3 ring laser. $^3F_4$ was then populated through relaxation from $^3H_4$. A Photonetics Tunics-Plus, model number 3642 HE S, laser was scanned over the resulting absorption of $^3H_4 \Leftrightarrow {}^3F_4$ with a triangle ramp generated by a Stanford Research Systems DS345 function generator. To ensure adequate pumping, the beams were carefully focused and spatially overlapped to address the same populations of ions. Because the sample of 0.1% Tm:$YAlO_3$ was unoriented and rough cut, the signal was optimized by rotating polarization to maximize signal strength. The transmitted beam through the sample was passed through a Thorlabs FEL1000 1-μm longpass filter, which blocked the ~795 nm pump beam, but admitted the ~1451 nm probe beam, and then detected with a Newport 818-IG Power Meter. The ~795 pump laser wavelength was measured with a Burleigh WA-1500 wavemeter, while the ~1451 nm laser spectrum was measured by an Advantest Q8347 Optical Spectrum Analyzer with ~900 MHz resolution.

Measurements of the lifetime of the $^3F_4$ bottle neck state were made through time resolved fluorescence of the $^3H_4 \Leftrightarrow {}^3F_4$ transition in the 0.1% Tm:$YAlO_3$ sample, according to the dual-wavelength pumping scheme illustrated in fig. 63. The same lasers, temperatures, equipment, and considerations as in the laser absorption measurement were used, except pulses and timings were generated by a Stanford Research Systems DG645.

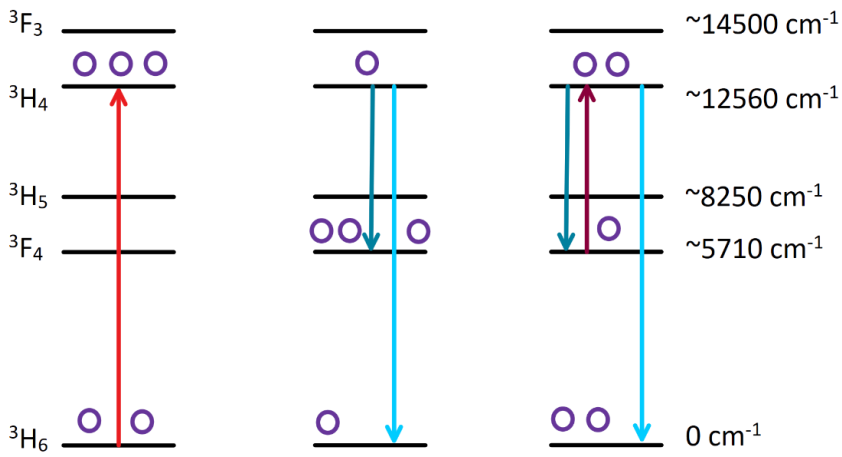

Figure 63. Pumping schematic of the double-pump time-resolved fluorescence measurement, proposed by Thiel [244]. (Left) Population is pumped at 795.315 nm to the $^3H_4$ state. (Center) Population has relaxed into the long-lived $^3F_4$ bottleneck state, and $^3F_4$ continues filling even after the 795.1 nm laser is shut off and the $^3H_4$ state empties entirely. The $^3H_5$ state is assumed to be short lived. (Right) After $^3H_4$ is empty, the second laser at 1451.363 nm is activated. Any population that relaxes to $^3F_4$ is excited once again to $^3H_4$, until $^3F_4$ has emptied entirely. The fluorescence of the $^3H_4 \Leftrightarrow {}^3H_6$ transition is detected, and its decay is a convolution of the $^3H_4$ and $^3F_4$ lifetimes.

Spectral hole burning was achieved on the $^3H_4 \Leftrightarrow {}^3F_4$ transition at 1451.2 nm by continuously pumping the $^3H_6 \Leftrightarrow {}^3H_4$ transition at 795.1 nm, and the absorption of the population that had relaxed from $^3H_4$ into $^3F_4$ was measured by scanning the piezo of the Phonetics laser with a single triangle ramp from a DS345 signal generator in a continuous burn, ungated SHB measurement. The scan transmission was detected by a New Focus 818 IG power meter.

Results

Little in the way of spectroscopy at liquid helium temperatures has been reported on Tm^{3+}:$YAlO_3$ [246, 247], with most being at room or liquid nitrogen temperature. Sun reports the T_2 coherence time is immeasurably short on the ~795 nm $^3H_6 \Leftrightarrow {}^3H_4$ transition in Tm^{3+}:$YAlO_3$ with photon echoes, and attributes the cause to the lowest level of $^3H_6$ having a close neighbor ~3

cm^{-1} (~90 GHz) away and the strong spin interactions of Al^{3+} [109]. Without detectable echoes on the most well-studied transition of thulium, $^3H_6 \Leftrightarrow {}^3H_4$, interest in the study of $Tm^{3+}:YAlO_3$ as a material for SHB and QIS appears to have remained low. Here, the issue is side-stepped in the use of $^3F_4 \Leftrightarrow {}^3H_4$.

A summary of the low-temperature absorption and emission spectroscopy on the levels of $Tm^{3+}:YAlO_3$ from this work is presented in table 14 and table 15, and the spectra follow. The positions of the lowest lines were confirmed with lasers on $^3F_4$ and $^3H_4$, but some ambiguity remains due to defect lines and broadening in the upper crystal field levels.

Manifold	Level	Energy (cm^{-1})	Manifold	Level	Energy (cm^{-1})
$^3H_6$	1	0	**$^3F_4$**	1	5622.44
	2	3.13		2	5712.2
	3	71.0		3	5722.1
	4	111.6		4	5815.9
	5	241.8		5	5840.2
	6	276.7		6	5932.5
	7	290.2		7	5956.2
	8	299.2		8	5960.5
	9	308.1		9	5981.9
	10	319.3			
	11	356.0			
	12	435			
	13	562			

Table 14. Observed energy levels in absorption and fluorescence of the $^3H_6$ and $^3F_4$ manifolds of Tm^{3+}:$YAlO_3$, chosen from the spectra in the next section.

Manifold	Level	Energy (cm^{-1})	Manifold	Level	Energy (cm^{-1})
$^3H_5$	1	7988.7	**$^3H_4$**	1	12512.50
	2	8033.0		2	12576.25
	3	8145.5		3	12661.1
	4	8169.5		4	12739.1
	5	8178		5	12783.8
	6	8184		6	12867
	7	8190		7	12883
	8	8197		8	12944
	9	8222			
	10	8237			
	11	8276			

Table 15. Observed energy levels in absorption and fluorescence of the $^3H_5$ and $^3H_4$ manifolds of Tm^{3+}:$YAlO_3$, chosen from the spectra in the next section.

White Light Absorption

The high concentration of thulium in the 4% sample was specifically chosen for absorption to locate all levels in $^3F_4$, $^3H_5$, and $^3H_4$, especially the weaker lines in $^3H_5$. The locations of $^3H_5$ must be known, as any fluorescence from those levels can easily overlap the fluorescence lines of $^3H_4 \Leftrightarrow {}^3F_4$. Some important consequences of the high concentration are the presence of defect lines, such as thulium pair sites, and additional inhomogeneous broadening hiding individual levels. Level assignments were therefore chosen based on position and absorption strength. Unpolarized white light absorption of $^3H_6 \Leftrightarrow {}^3H_5$ is shown in fig. 64, and absorption of $^3H_6 \Leftrightarrow {}^3H_4$ is shown in fig. 65. A hot line is visible in fig. 65, emerging from the closely spaced second crystal field level of $^3H_6$.

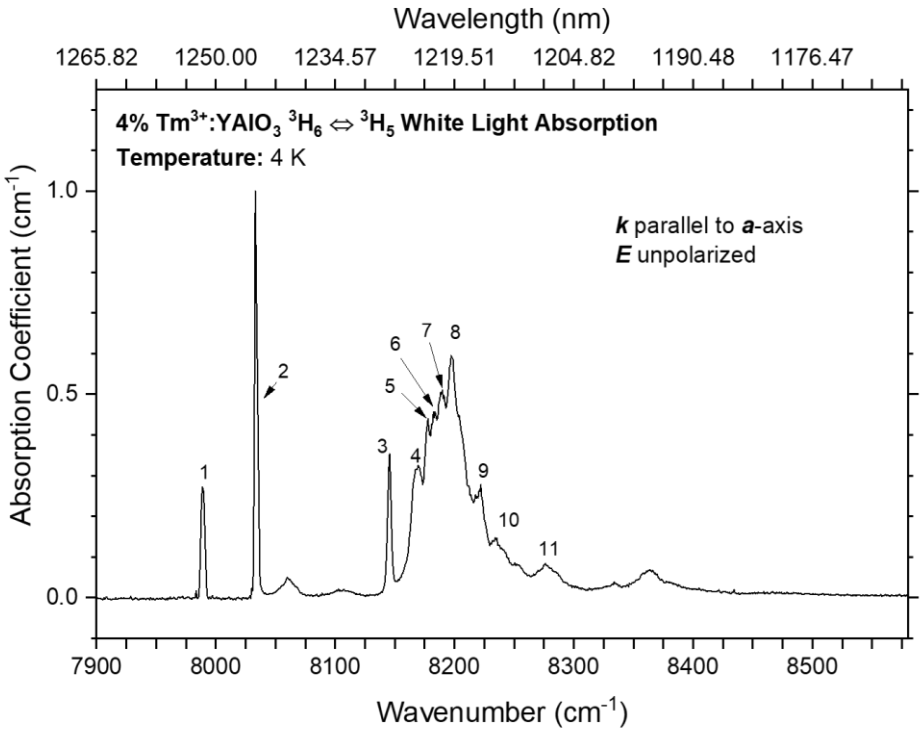

Figure 64. Unpolarized absorption spectrum of $^3H_6 \Leftrightarrow {}^3H_5$ in Tm^{3+}:$YAlO_3$ at 4K. Note that the relative absorption here is roughly ~15 times less than absorption observed on the other states, as in fig. 65. Conventionally, this state is known to be short lived, especially relative to $^3F_4$ and $^3H_4$.

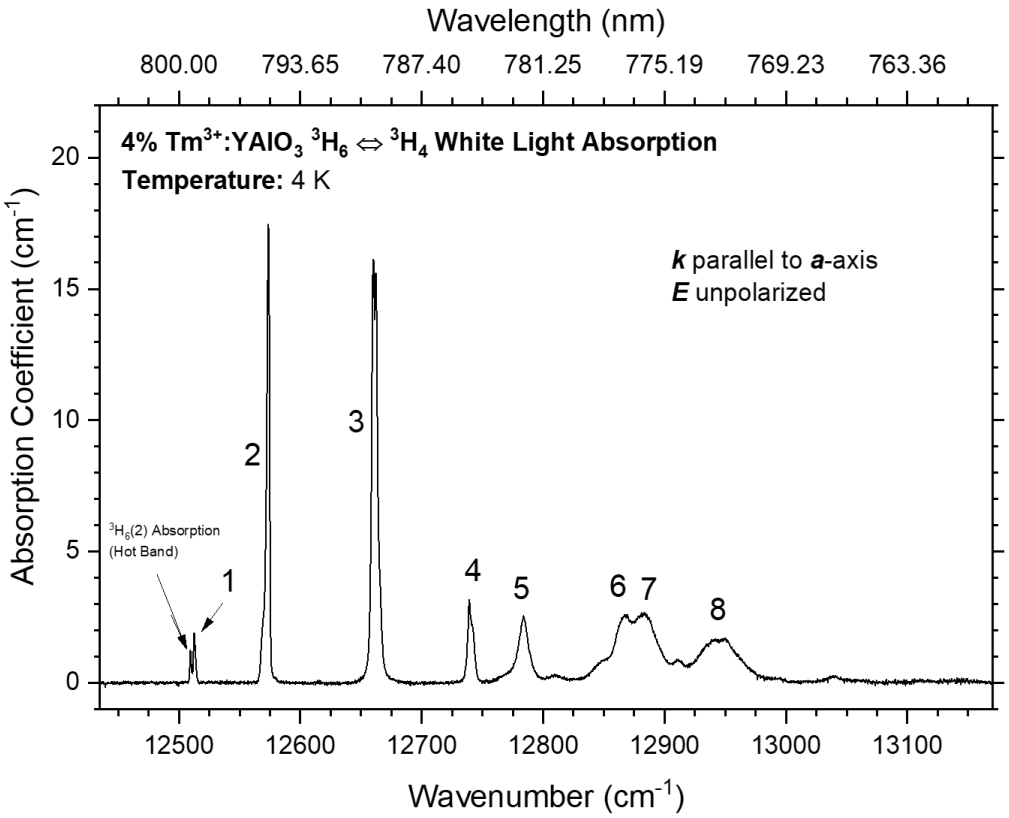

Figure 65. Unpolarized absorption spectrum of $^3H_6 \Leftrightarrow {}^3H_4$ in $Tm^{3+}:YAlO_3$ at 4K. There is a hot line emerging from the second crystal field level in $^3H_6$, which is about ~3 cm^{-1} (~90 GHz) away. Even at 4K, $^3H_6(2)$ is populated by phonons exciting $^3H_6(1)$.

Fluorescence Spectra

Spectrally resolved fluorescence was measured in the 0.1% Tm^{3+}:$YAlO_3$ to locate the levels of $^3H_6$ and $^3F_4$. The temperature was elevated to mitigate the unwanted effects of hole burning on the fluorescence intensity. The spacings of $^3H_6$(1) and (2), measured in absorption in fig. 65, are confirmed in the spectra of $^3F_4 \Leftrightarrow {}^3H_6$, shown in fig. 66 and fig. 67. The transition of interest, $^3F_4 \Leftrightarrow {}^3H_4$(1) is shown as the highest energy peak in fig. 68, and is below the spectrometer resolution.

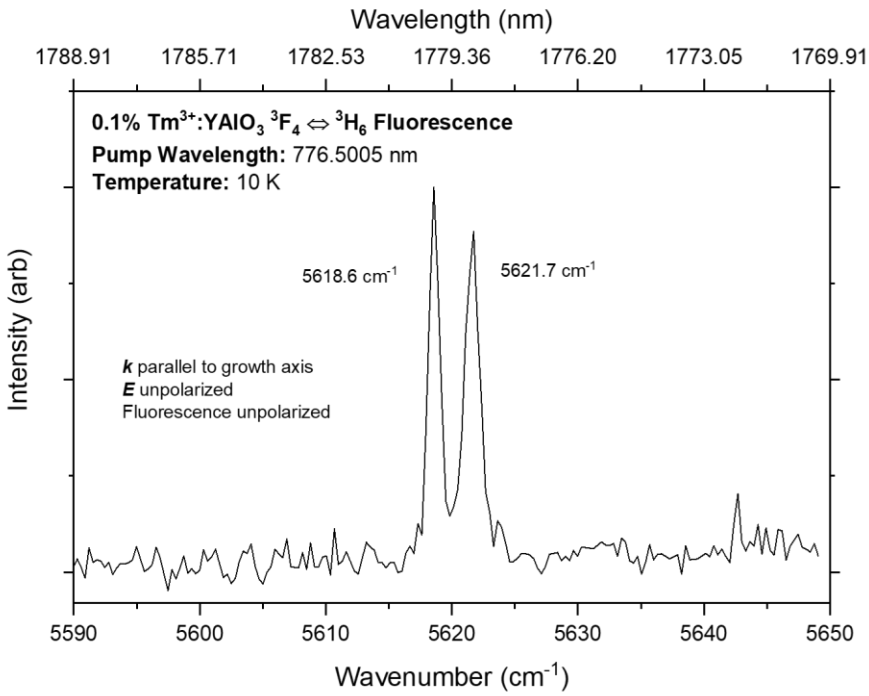

Figure 66. Unpolarized fluorescence spectra of $^3F_4 \Leftrightarrow {}^3H_6$ in Tm^{3+}:$YAlO_3$ at 10K. The second crystal field level in $^3H_6$ is ~3 cm^{-1} (~90 GHz) from the ground state, confirming the absorption and fluorescence on other manifolds.

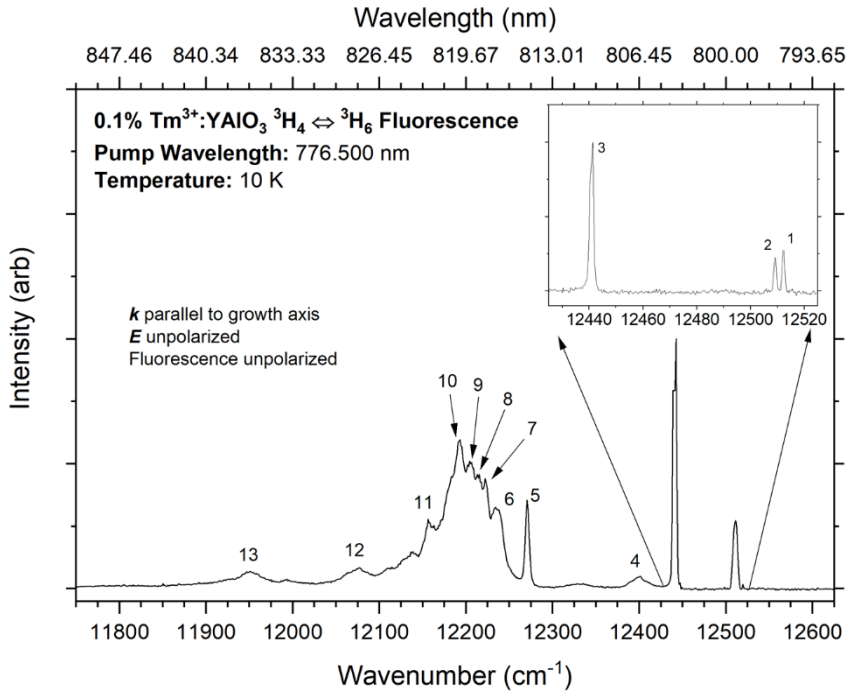

Figure 67. Unpolarized fluorescence spectra of $^3H_4 \Leftrightarrow {}^3H_6$ in Tm^{3+}:$YAlO_3$ at 10K. The second crystal field level in $^3H_6$ is also resolved in the inset.

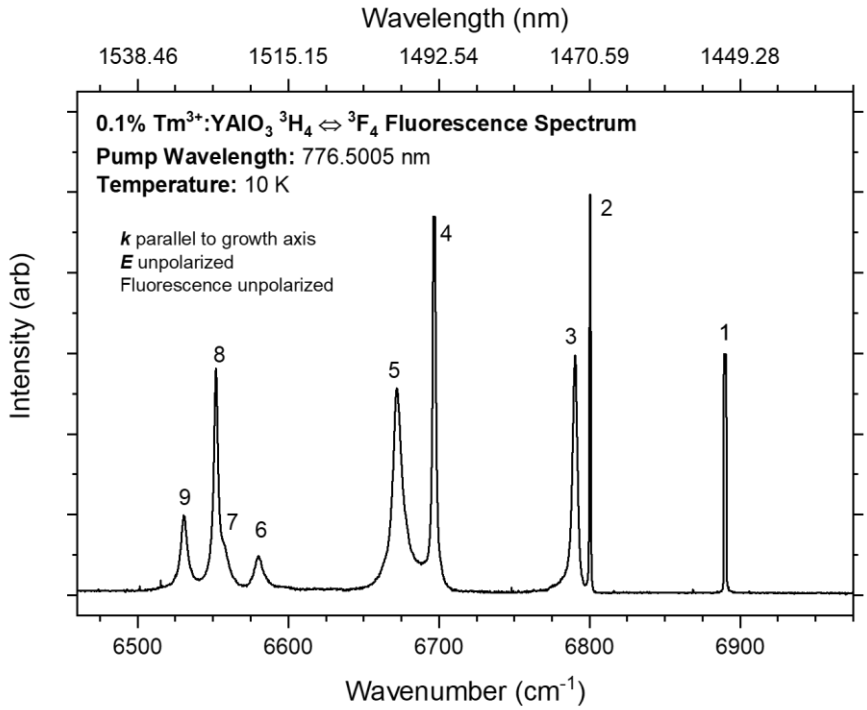

Figure 68. Unpolarized fluorescence spectra of $^3H_4 \Leftrightarrow {}^3F_4$ in $Tm^{3+}:YAlO_3$ at 10K. The transition of interest is labeled 1.

Laser Absorption

The sharp line measured in absorption and fluorescence, shown in fig. 68, motivated laser absorption of the $^3F_4 \Leftrightarrow {}^3H_4$ transition. The FWHM of the inhomogeneous line is ~950 MHz, with an absorption coefficient ~3 cm^{-1}, unpolarized. Further optimizations in polarization, pumping, and ion concentration could be made to increase the absorption depth. The width of the absorption however is interesting due to its sharpness, indicating that the enhanced nuclear levels might be spectrally resolved in magnetic fields, with implications for double-resonance techniques used in signal processing applications [30-32, 34, 64, 69-71, 113, 114, 127, 128].

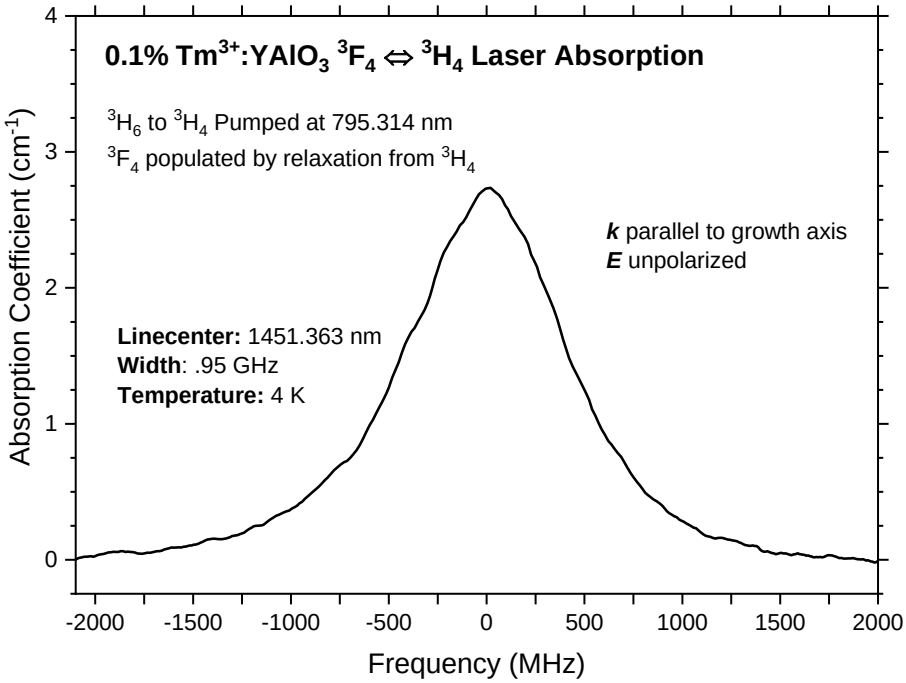

Figure 69. Unpolarized laser absorption of the $^3F_4 \Leftrightarrow {}^3H_4$ transition at 4K, produced through pumping at ~795 nm, and measured at ~1451 nm.

Time Resolved Fluorescence

The lifetime of $^3H_4$ in 0.1% Tm^{3+}:$YAlO_3$ has been reported as 0.76 ms by Sun at 2K [109], but as short as 53 μs in 4% Tm^{3+}:$YAlO_3$, indicating a strong concentration dependence. No value of T_1 has been reported for $^3F_4$ at liquid helium temperatures. However, the room temperature T_1 bottleneck lifetime has been reported as 7.2 ms in 0.5% Tm:$YAlO_3$ [248] and 4.2 ms at 2% concentration [249]. Consequently, measured values will reflect batch to batch variation in composition and concentration.

Time resolved fluorescence, shown in fig. 70, was measured on the $^3H_6 \Leftrightarrow {}^3H_4$ transition in accordance with the double pumped scheme shown in fig. 63. Beams were precisely overlapped and focused to ensure maximum pumping efficiency and addressing of the same ion populations. The first decay, resulting from the pumping to $^3H_4$, is a single exponential and elementary to fit and analyze. The full treatment of the second decay is more complicated. Thiel communicated that in the weak pumping limit of $^3F_4 \Leftrightarrow {}^3H_4$, the form of the population decay should be the convolution of the $^3F_4$ and $^3H_4$ lifetimes. The decay can also be calculated from standard rate equations [244]:

$$\text{(a)} \quad \dot{n}_1(t) = \frac{-n_1(t)}{T_1} + \left(n_B(t) - n_1(t)\right) * R$$

$$\text{(b)} \quad \dot{n}_B(t) = (-n_B(t) + n_1(t)) * R - \frac{n_B(t)}{T_B} + \frac{\beta * n_1(t)}{T_1} \qquad (18)$$

In coupled differential equations (16)a and b, the subscript 1 denotes the $^3H_4$ state, and the subscript B denotes $^3F_4$. The populations are n_i and the lifetimes T_i, while the fraction of the population that decays to $^3F_4$ from $^3H_4$ is β. Finally, the excitation rate from $^3F_4$ to $^3H_4$ is R. The initial conditions are set that $^3H_4$ is empty at when the ~1451 nm $^3F_4 \Leftrightarrow {}^3H_4$ laser is turned on, and

$^3F_4$ has $n_B = 1$. The ground state $^3H_6$ does not need to be accounted for in the related rates. Solving eq. (18) is straightforward, but the equations possess many terms and factors. They are readily simplified by requiring the excitation rate $R \rightarrow 0$ relative to the decay rates $1/T_i$ of the states: that is, no hole burning or stimulated emission takes place. The population $n_1(t)$ of the $^3H_4$ state then reduces to a simple form:

$$n_1(t) = Ae^{-t/T_B} - Be^{-t/T_1} \tag{19}$$

In eq. (19), A and B are fit parameters that depend on the pumping power and decay ratios. A very simple check to determine if the weak pumping limit holds is if the decay curve is exponential in form during the measurement.

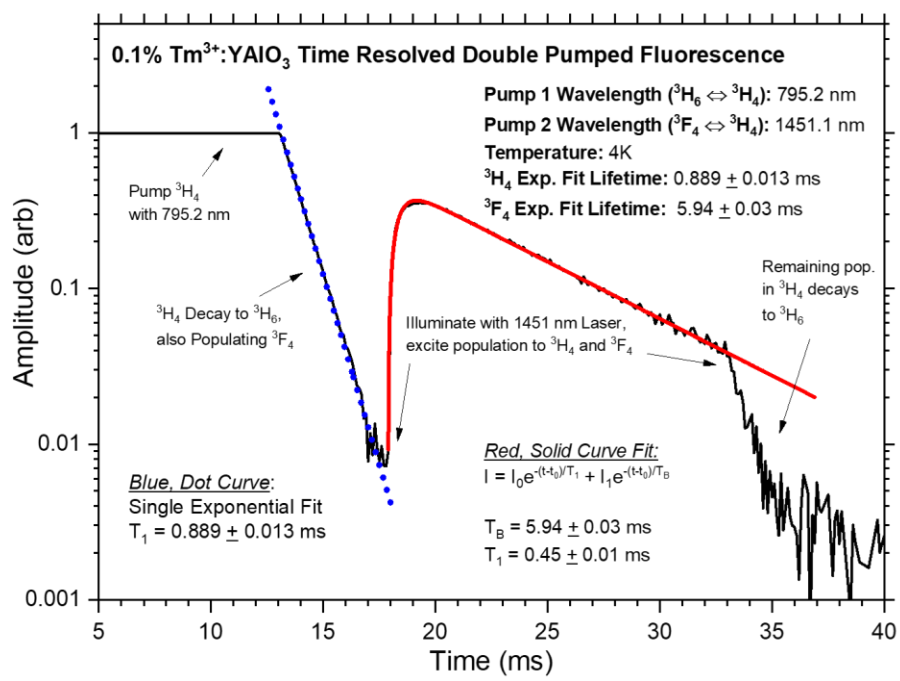

Figure 70. Double-pumped fluorescence decay of 0.1% Tm^{3+}:$YAlO_3$.

The decays, shown in fig. 70, were fit to the aforementioned models. In the second decay curve, the T_1 lifetime of $^3H_4$ was treated as a fit parameter to account for inaccuracies caused by

its convolution with the $^3F_4$ T_1 bottleneck decay. The decay of the first curve is taken as being more reliable. The measured 889 μs lifetime of $^3H_4$ is roughly ~100 μs longer than reported by Sun [109].

Excited State Spectral Hole Burning

Holes were burned on the $^3F_4 \Leftrightarrow {}^3H_4$ transition at 4K, with the ~1451 nm laser burning continuously. Holes, shown in the spectrum shown in fig. 71, were therefore broadened out by laser jitter, and are certainly much larger than the homogeneous linewidth. To maintain population in the bottleneck state, the ~795 nm $^3H_6 \Leftrightarrow {}^3H_4(2)$ transition was pumped continuously with the Ti:Al_2O_3 laser.

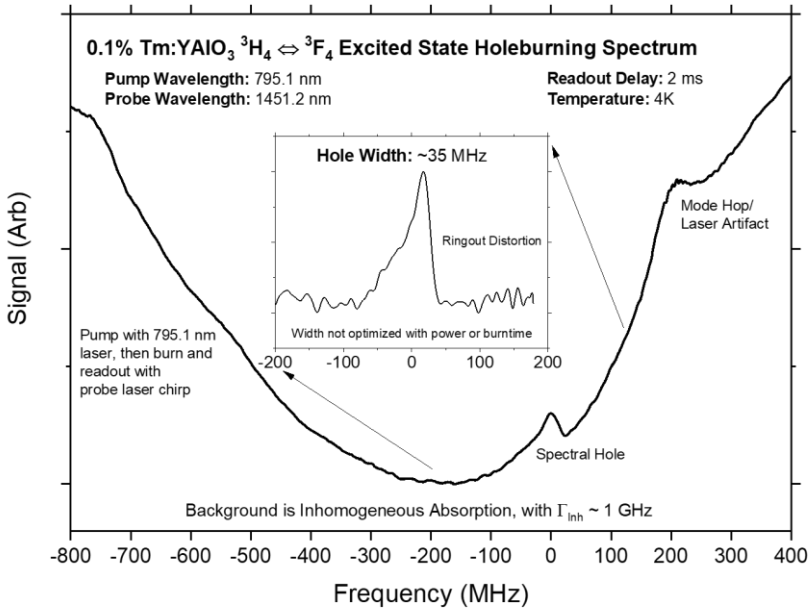

Figure 71. Ungated SHB spectrum burned onto the ~1451 nm telecom $^3F_4 \Leftrightarrow {}^3H_4$ transition at 4K.

Discussion

The SHB on the $^3F_4 \Leftrightarrow {}^3H_4$ transition strongly indicates that the homogeneous linewidth Γ_h is narrower than measured. If magnetic fields enable the Tm^{3+} nuclear levels to be spectrally resolved, the ~GHz width of the inhomogeneously broadened line is also of interest for spin-wave quantum memory protocols and double-resonance techniques [33, 113, 132, 221, 232]. It should be pointed out that optical coherence or good hole burning has not been reported on the standard ~795 nm $^3H_6 \Leftrightarrow {}^3H_4$ transition, but hole burning is readily observed on the excited state transition $^3F_4 \Leftrightarrow {}^3H_4$. The transition wavelength itself is also of great interest due to the lack of rare-earth hole burning transitions in the ~1450 nm bands. The measured properties of this excited state transition strongly suggest that explorations of other excited-state transitions might be equally or more fruitful for expanding the toolkit of available transition wavelengths. The dual-pumping approaches in time-resolved fluorescence and spectral hole burning also demonstrate that there is no great barrier to their study or use except equipment. The techniques and analytical approaches outlined for these levels and transitions are also more broadly useful to the general rare-earth research community.

The principal limitation of this transition in this material for QIS applications is the absorption coefficient of ~3 cm^{-1} at 0.1% concentration. However, if optimization from polarization of the light fields does not greatly improve the absorption, either more efficient pumping of $^3F_4$ or higher concentrations of thulium are required to ensure that single photon signals cannot be lost by transmission through the host material [32, 64, 69, 134]. Studies with photon echoes and Zeeman spectroscopy on this material would provide quantitative answers to determine a more optimal balance of properties. Conversely, for classical information processing

and spatial spectral holography, the absorption is not a great issue, though other materials exist with much wider inhomogeneous broadenings for maximum possible bandwidths [67, 109, 137]. However, it must be acknowledged that before this work, promising alternatives for transitions at this wavelength were likewise limited in scope if they existed at all [64]. There are also many other rare-earth materials and transitions for classical and quantum signal processing applications that are yet to be surveyed with the techniques and mindset described in this work.

Conclusion

The absorption and emission spectroscopy of Tm^{3+}:$YAlO_3$ has been reported, and spectral holes were burned on the excited state $^3F_4 \Leftrightarrow {}^3H_4$ transition at ~1451 nm. Techniques for studying these transitions above the ground state have been presented. The results of this study demonstrate that excited state transitions at liquid helium temperatures have much yet to offer to the rare-earth research community, particularly in the direction of developing new wavelengths for new spectral applications.

CHAPTER SEVEN

SUMMARY AND CONCLUSIONS

Many times in the course of the research presented here, the author was surprised to be suddenly staring into the machinery of lanthanide atoms in the middle of seemingly mundane measurements. In fact, the rare-earth doped materials research community is particularly fortunate in that the physics we study has direct application, but without sacrificing any richness or depth. In this case, three transitions, the Tm^{3+} $^3H_6 \Leftrightarrow {}^3F_3$ at ~690 nm, the Pr^{3+} $^3H_4 \Leftrightarrow {}^3F_3$ at ~1584 nm, and the Tm^{3+} $^3F_4 \Leftrightarrow {}^3H_4$ at ~1451 nm, have been presented with the aim of expanding the working toolkit of lanthanide optical transitions through the study of their fundamental properties. Along the way, experimental know-how and spectroscopic techniques have been simultaneously developed to better facilitate research geared for classical and quantum signal processing on rare-earth ions. The journey to this point was rewarding for the insight and success it enjoyed despite the technical challenges and long days and nights.

In chapter 2, the integration of rare-earth doped materials with their own cryogenic hardware and environment was investigated to develop all-optical approaches to sensing. Actual sample temperatures, fields, crystal damage and stress effects, and more were measured with the ultra-sensitive properties of the quantum memory materials Tm^{3+}:YGG and Er^{3+}:YSO. Those results encourage a mindset that the rare-earth crystals are as much a part of the measurement hardware as the entire apparatus itself. Useful ways of quantitatively measuring the effects of cryostats in situ were presented. Those techniques immediately improved the accuracy and reliability of the rest of the research presented in this thesis and the lab's work.

The survey presented in chapter 3 demonstrated a technique for engineering the phonon spectrum of materials doped with lanthanides. The effect of phonon-mediated relaxation and decoherence on the $^3H_6 \Leftrightarrow {}^3F_3$ transition was steadily dampened with hosts of decreasing Debye temperature. Strong absorption and ~380 kHz holes were observed with free induction decays in the material Tm^{3+}:LaF_3. That crystal was shown to have many good properties to serve as a spectral hole burning filter for a blood-oxygenation sensitive UOT medical imaging device. The $^3F_3$ lifetime was also extended to as long as ~100 μs in the alkali lead halide Tm^{3+}:KPb_2Br_5. The research shows the power of the low-phonon cutoff energy hosts to change the way non-radiative transitions are viewed to being interesting and viable for applications at new wavelengths.

Work in chapter 4 improved on the initial study of the $^3H_6 \Leftrightarrow {}^3F_3$ transition in Tm^{3+}:LaF_3 with photon echoes and Zeeman measurements. Echoes measured the homogeneous width down to the ~120 kHz lifetime limit with no other additional effects detected. Magnetic studies pushed the enhanced nuclear level lifetime out nearly two hours, greatly lengthening the lifetime of inscribed spectral filters. The simulations projected very optimistic outcomes for a new class of rare-earth enabled UOT device at a wavelength previously considered not practical in the lanthanides.

The alkali lead halides, initially studied in chapter 3, were revisited in more detail in chapter 5. The $^3H_4 \Leftrightarrow {}^3F_3$ transition of Pr^{3+}:$RbPb_2Br_5$ was investigated for telecom L-Band signal processing, while the study of the $^3H_6 \Leftrightarrow {}^3F_3$ transition in Tm^{3+}:KPb_2Br_5 was continued in high resolution. Four transitions were found in Pr^{3+}:RPB at ~1584 nm with ~0.5-1 ms $^3F_3$ optical lifetimes, 2-5 GHz inhomogeneous broadenings, and ~750 ns coherence times. Even more promising results are very likely possible through additional studies of magnetism and lower

temperatures. Similarly, the study of Tm^{3+}:KPb_2Br_5 showed how the SHB properties of the transition can be viewed as a time-resolved, high-resolution spectrum analyzer. The hole burning was used to characterize and align a homebuilt laser at its ~698 nm wavelength. The alkali lead halides and other low Debye temperature hosts were shown to be extremely promising for rare-earth signal processing applications at liquid helium temperatures at exciting new wavelengths.

Finally, in chapter 6, the last of the three transitions studied in this survey was presented, the $^3H_4 \Leftrightarrow {}^3F_3$ transition in Tm^{3+}:$YAlO_3$. The energy level structure was precisely mapped out, and two-laser absorption, fluorescence, and spectral hole burning were measured and analyzed. Narrow inhomogeneous broadening of ~950 MHz, bottleneck lifetimes of ~5 ms through excitation to a higher level, and ~30 MHz holes were presented. The work indicates that the excited state transitions possess equally intriguing properties as the more commonly studied transitions out of the ground state for luminescence, hole burning, and QIS.

These transitions studied in this thesis are not the final word by any means. They are interesting in their own right for further exploration for both the viewing of atomic-scale phenomena and the development of the techniques by which they are explored. But what these measurements truly indicate is that many unexplored or disused optical transitions of the lanthanides have much more to offer if the fundamental physics is understood. These exciting properties impact both scientific work and the development of cutting-edge applications at new wavelengths.

REFERENCES CITED

[1] H.M. King, REE - Rare Earth Elements and their Uses, https://geology.com/articles/rare-earth-elements/, Geology.com, 2020.

[2] V. Balaram, Rare earth elements: A review of applications, occurrence, exploration, analysis, recycling, and environmental impact, Geoscience Frontiers, 10 (2019) 1285-1303.

[3] T. Cheisson, E.J. Schelter, Rare earth elements: Mendeleev's bane, modern marvels, Science, 363 (2019) 489-493.

[4] X. Song, M.-H. Chang, M. Pecht, Rare-Earth Elements in Lighting and Optical Applications and Their Recycling, JOM, 65 (2013) 1276-1282.

[5] M.H.V. Werts, Making sense of Lanthanide Luminescence, Science Progress, 88 (2005) 101-131.

[6] K.A. Denault, J. Brgoch, S.D. Kloß, M.W. Gaultois, J. Siewenie, K. Page, R. Seshadri, Average and Local Structure, Debye Temperature, and Structural Rigidity in Some Oxide Compounds Related to Phosphor Hosts, ACS Applied Materials & Interfaces, 7 (2015) 7264-7272.

[7] B.M.J. Smets, Phosphors based on rare-earths, a new era in fluorescent lighting, Materials Chemistry and Physics, 16 (1987) 283-299.

[8] N.C. George, K.A. Denault, R. Seshadri, Phosphors for Solid-State White Lighting, Annual Review of Materials Research, 43 (2013) 481-501.

[9] C.R. Ronda, T. Jüstel, H. Nikol, Rare earth phosphors: fundamentals and applications, Journal of Alloys and Compounds, 275-277 (1998) 669-676.

[10] M.J. Digonnet, Rare-earth-doped fiber lasers and amplifiers, revised and expanded, CRC press, 2001.

[11] A.J. Kenyon, Recent developments in rare-earth doped materials for optoelectronics, Progress in Quantum Electronics, 26 (2002) 225-284.

[12] Z.W. Barber, C. Harrington, R. Krishna Mohan, T. Jackson, C. Stiffler, P.B. Sellin, K.D. Merkel, Spatial-spectral holographic real-time correlative optical processor with >100 Gb/s throughput, Appl. Opt., 56 (2017) 5398-5406.

[13] U. Hömmerich, E. Nyein, J.A. Freeman, P. Amedzake, S.B. Trivedi, J.M. Zavada, Crystal growth and optical properties of Dy-doped potassium lead bromide (KPb2Br5), Journal of Crystal Growth, 287 (2006) 230-233.

[14] Y. Wang, J. Li, C. Tu, Z. You, Z. Zhu, B. Wu, Crystal growth and spectral analysis of Dy^{3+} and Er^{3+} doped KPb_2Cl_5 as a mid-infrared laser crystal, Crystal Research and Technology, 42 (2007) 1063-1067.

[15] P. Amedzake, E. Brown, U. Hömmerich, S.B. Trivedi, J.M. Zavada, Crystal growth and spectroscopic characterization of Pr-doped KPb2Cl5 for mid-infrared laser applications, Journal of Crystal Growth, 310 (2008) 2015-2019.

[16] U. Hömmerich, E.E. Nyein, S.B. Trivedi, Crystal growth, upconversion, and infrared emission properties of Er^{3+}-doped KPb2Br5, Journal of Luminescence, 113 (2005) 100-108.

[17] T. Böttger, C.W. Thiel, Y. Sun, R.M. Macfarlane, R.L. Cone, Decoherence and absorption of Er^{3+}:$KTiOPO_4$ (KTP) at 1.5μm, Journal of Luminescence, 169 (2016) 466-471.

[18] Y. Li, P. Hemmer, C. Kim, H. Zhang, L.V. Wang, Detection of ultrasound-modulated diffuse photons using spectral-hole burning, Opt. Express, 16 (2008) 14862-14874.

[19] R.M. Macfarlane, High-resolution laser spectroscopy of rare-earth doped insulators: a personal perspective, Journal of Luminescence, 100 (2002) 1-20.

[20] T. Böttger, Y. Sun, C. Thiel, R. Cone, Material optimization of Er^{3+}:Y_2SiO_5 at 1.5 um for optical processing, memory, and laser frequency stabilization applications, in: Integrated Optoelectronics Devices, SPIE, 2003.

[21] K. Rademaker, W.F. Krupke, R.H. Page, S.A. Payne, K. Petermann, G. Huber, A.P. Yelisseyev, L.I. Isaenko, U.N. Roy, A. Burger, K.C. Mandal, K. Nitsch, Optical properties of Nd^{3+}- and Tb^{3+}-doped KPb_2Br_5 and $RbPb_2Br_5$ with low nonradiative decay, Journal of the Optical Society of America B, 21 (2004) 2117-2129.

[22] K. Rademaker, S.A. Payne, G. Huber, L.I. Isaenko, E. Osiac, Optical pump-probe processes in Nd^{3+}-doped KPb_2Br_5, $RbPb_2Br_5$, and KPb_2Cl_5, Journal of the Optical Society of America B, 22 (2005) 2610-2618.

[23] L.D. Merkle, M. Dubinskii, Pr:$RbPb_2Cl_5$: Temperature dependent spectra, dynamics and three-for-one excitation, Opt. Express, 25 (2017) 19780-19794.

[24] R. Capelletti, A. Baraldi, E. Buffagni, N. Magnani, M. Mazzera, Rare earth crystal field spectra as a probe of librational motions in BaY_2F_8solid state laser crystals, Journal of Physics: Conference Series, 249 (2010).

[25] N.W. Jenkins, S.R. Bowman, S. O'Connor, S.K. Searles, J. Ganem, Spectroscopic characterization of Er-doped KPb_2Cl_5 laser crystals, Optical Materials, 22 (2003) 311-320.

[26] A. Toncelli, M. Tonelli, A. Cassanho, H.P. Jenssen, Spectroscopy and dynamic measurements of a Tm,Dy:BaY_2F_8 crystal, Journal of Luminescence, 82 (1999) 291-298.

[27] U. Roy, R. Hawrami, Y. Cui, S. Morgan, A. Burger, K.C. Mandal, C.C. Noblitt, S. Speakman, K. Rademaker, S. Payne, Tb^{3+}-doped KPb_2Br_5: Low-energy phonon mid-infrared laser crystal, Applied Physics Letters, 86 (2005) 151911.

[28] C. Venet, M. Bocoum, J.-B. Laudereau, T. Chaneliere, F. Ramaz, A. Louchet-Chauvet, Ultrasound-modulated optical tomography in scattering media: flux filtering based on persistent spectral hole burning in the optical diagnosis window, Opt. Lett., 43 (2018) 3993-3996.

[29] J. Liu, X. Li, J. Feng, C. Zheng, Y. Wang, A. Wang, X. Liu, ZnS Nanospheres for Optical Modulator in an Erbium-Doped Fiber Laser, Annalen der Physik, 532 (2020) 1900454.

[30] M.P. Hedges, J.J. Longdell, Y. Li, M.J. Sellars, Efficient quantum memory for light, Nature, 465 (2010) 1052-1056.

[31] G. Brennen, E. Giacobino, C. Simon, Focus on Quantum Memory, New Journal of Physics, 17 (2015) 050201.

[32] W. Tittel, M. Afzelius, T. Chaneliére, R.L. Cone, S. Kröll, S.A. Moiseev, M. Sellars, Photon-echo quantum memory in solid state systems, Laser & Photonics Reviews, 4 (2010) 244-267.

[33] N. Kunkel, P. Goldner, Recent Advances in Rare Earth Doped Inorganic Crystalline Materials for Quantum Information Processing, Zeitschrift für anorganische und allgemeine Chemie, 644 (2018) 66-76.

[34] M. Nilsson, S. Kröll, Solid state quantum memory using complete absorption and re-emission of photons by tailored and externally controlled inhomogeneous absorption profiles, Optics Communications, 247 (2005) 393-403.

[35] M. Mirhosseini, A. Sipahigil, M. Kalaee, O. Painter, Superconducting qubit to optical photon transduction, Nature, 588 (2020) 599-603.

[36] A. Kinos, Q. Li, L. Rippe, S. Kröll, Development and characterization of high suppression and high etendue narrowband spectral filters, Appl. Opt., 55 (2016) 10442-10448.

[37] A. Walther, L. Rippe, L.V. Wang, S. Andersson-Engels, S. Kröll, Analysis of the potential for non-invasive imaging of oxygenation at heart depth, using ultrasound optical tomography (UOT) or photo-acoustic tomography (PAT), Biomed. Opt. Express, 8 (2017) 4523-4536.

[38] D.S. Elson, R. Li, C. Dunsby, R. Eckersley, M.X. Tang, Ultrasound-mediated optical tomography: a review of current methods, Interface Focus, 1 (2011) 632-648.

[39] J. Gunther, S. Anderson-Engels, Review of current methods of acousto-optical tomography for biomedical applications, Front. Optoelectron., 10 (2017) 211-238.

[40] H. Zhang, M. Sabooni, L. Rippe, C. Kim, S. Kroll, L.V. Wang, P.R. Hemmer, Slow light for deep tissue imaging with ultrasound modulation, Appl Phys Lett, 100 (2012) 131102-1311025.

[41] X. Xu, S.-R. Kothapalli, H. Liu, L.V. Wang, Spectral hole burning for ultrasound-modulated optical tomography of thick tissue, SPIE, 2010.

[42] Z.W. Barber, C. Harrington, K. Rupavatharam, C. Thiel, T. Jackson, P.B. Sellin, C. Benko, K. Merkel, Spatial-Spectral Materials for High Performance Optical Processing, in: 2017 IEEE International Conference on Rebooting Computing (ICRC), 2017, pp. 1-4.

[43] C. Arend, J.N. Becker, H. Sternschulte, D. Steinmüller-Nethl, C. Becher, Photoluminescence excitation and spectral hole burning spectroscopy of silicon vacancy centers in diamond, Physical Review B, 94 (2016) 045203.

[44] S.E. Beavan, E.A. Goldschmidt, M.J. Sellars, Demonstration of a dynamic bandpass frequency filter in a rare-earth ion-doped crystal, Journal of the Optical Society of America B, 30 (2013) 1173-1177.

[45] T. Böttger, Y. Sun, G.J. Pryde, G. Reinemer, R.L. Cone, Diode laser frequency stabilization to transient spectral holes and spectral diffusion in Er^{3+}:Y_2SiO_5 at 1536 nm, Journal of Luminescence, 94-95 (2001) 565-568.

[46] T. Böttger, C.W. Thiel, R.L. Cone, Y. Sun, Controlled compositional disorder in Er^{3+}:Y_2SiO_5 provides a wide-bandwidth spectral hole burning material at 1.5 μm, Physical Review B, 77 (2008) 155125.

[47] C.J. DeSantis, D. Huang, H. Zhang, N.J. Hogan, H. Zhao, Y. Zhang, A. Manjavacas, Y. Zhang, W.-S. Chang, P. Nordlander, S. Link, N.J. Halas, Laser-Induced Spectral Hole-Burning through a Broadband Distribution of Au Nanorods, The Journal of Physical Chemistry C, 120 (2016) 20518-20524.

[48] S. Dutta, E.A. Goldschmidt, S. Barik, U. Saha, E. Waks, Integrated Photonic Platform for Rare-Earth Ions in Thin Film Lithium Niobate, Nano Letters, 20 (2020) 741-747.

[49] O. Gobron, K. Jung, N. Galland, K. Predehl, R. Le Targat, A. Ferrier, P. Goldner, S. Seidelin, Y. Le Coq, Dispersive heterodyne probing method for laser frequency stabilization based on spectral hole burning in rare-earth doped crystals, Opt. Express, 25 (2017) 15539-15548.

[50] J.E. Gunther, A. Walther, L. Rippe, S. Kröll, S. Andersson-Engels, Deep tissue imaging with acousto-optical tomography and spectral hole burning with slow light effect: a theoretical study, SPIE, 2018.

[51] K. Holliday, M. Croci, E. Vauthey, U.P. Wild, Spectral hole burning and holography in an Y_2SiO_5:Pr^{3+} crystal, Physical Review B, 47 (1993) 14741-14752.

[52] D.O. Krimer, B. Hartl, S. Rotter, Hybrid Quantum Systems with Collectively Coupled Spin States: Suppression of Decoherence through Spectral Hole Burning, Physical Review Letters, 115 (2015) 033601.

[53] D.R. Leibrandt, M.J. Thorpe, C.-W. Chou, T.M. Fortier, S.A. Diddams, T. Rosenband, Absolute and Relative Stability of an Optical Frequency Reference Based on Spectral Hole Burning in Eu^{3+}:Y_2SiO_5, Physical Review Letters, 111 (2013) 237402.

[54] T. Lutz, L. Veissier, C.W. Thiel, P.J.T. Woodburn, R.L. Cone, P.E. Barclay, W. Tittel, Effects of fabrication methods on spin relaxation and crystallite quality in Tm-doped $Y_3Al_5O_{12}$ powders studied using spectral hole burning, Science and Technology of Advanced Materials, 17 (2016) 63-70.

[55] R.M. Macfarlane, Spectral hole burning in the trivalent thulium ion, Opt. Lett., 18 (1993) 829-831.

[56] R.M. Macfarlane, Photon-echo measurements on the trivalent thulium ion, Opt. Lett., 18 (1993) 1958-1960.

[57] R.M. Macfarlane, Direct process thermal line broadening in Tm:YAG, Journal of Luminescence, 85 (2000) 181-186.

[58] R.M. MacFarlane, A study of excited state dynamics of rare earth ions in solids by coherent transients and spectral holeburning, Journal of Luminescence, 40-41 (1988) 3-6.

[59] R.M. Macfarlane, M.J. Dejneka, Spectral hole burning in thulium-doped glass ceramics, Opt. Lett., 26 (2001) 429-431.

[60] E.S. Maniloff, F.R. Graf, H. Gygax, S.B. Altner, S. Bernet, A. Renn, U.P. Wild, Power broadening of the spectral hole width in an optically thick sample, Chemical Physics, 193 (1995) 173-180.

[61] S. Putz, A. Angerer, D.O. Krimer, R. Glattauer, W.J. Munro, S. Rotter, J. Schmiedmayer, J. Majer, Spectral hole burning and its application in microwave photonics, Nature Photonics, 11 (2017) 36-39.

[62] A. Rebane, R.N. Shakhmuratov, P. Mégret, J. Odeurs, Slow light with persistent spectral hole burning in waveguides, Journal of Luminescence, 127 (2007) 22-27.

[63] O.M. ten Kate, K.W. Krämer, E. van der Kolk, Efficient luminescent solar concentrators based on self-absorption free, Tm^{2+} doped halides, Solar Energy Materials and Solar Cells, 140 (2015) 115-120.

[64] C.W. Thiel, T. Böttger, R.L. Cone, Rare-earth-doped materials for applications in quantum information storage and signal processing, Journal of Luminescence, 131 (2011) 353-361.

[65] C.W. Thiel, R.L. Cone, T. Böttger, Laser linewidth narrowing using transient spectral hole burning, Journal of Luminescence, 152 (2014) 84-87.

[66] C.W. Thiel, R.M. Macfarlane, T. Böttger, Y. Sun, R.L. Cone, W.R. Babbitt, Optical decoherence and persistent spectral hole burning in Er3+:LiNbO3, Journal of Luminescence, 130 (2010) 1603-1609.

[67] C.W. Thiel, Y. Sun, T. Böttger, W.R. Babbitt, R.L. Cone, Optical decoherence and persistent spectral hole burning in Tm^{3+}:LiNbO3, Journal of Luminescence, 130 (2010) 1598-1602.

[68] R. Wannemacher, R.M. Macfarlane, Y.P. Wang, D. Sox, D. Boye, R.S. Meltzer, Nuclear spin-flip sidebands in optical spectral holeburning and fluorescence line narrowing of the Er3+ ion, Journal of Luminescence, 48-49 (1991) 309-312.

[69] M. Afzelius, C. Simon, H. de Riedmatten, N. Gisin, Multimode quantum memory based on atomic frequency combs, Physical Review A, 79 (2009) 052329.

[70] T. Zhong, J.M. Kindem, J.G. Bartholomew, J. Rochman, I. Craiciu, E. Miyazono, M. Bettinelli, E. Cavalli, V. Verma, S.W. Nam, F. Marsili, M.D. Shaw, A.D. Beyer, A. Faraon, Nanophotonic rare-earth quantum memory with optically controlled retrieval, Science, 357 (2017) 1392-1395.

[71] B. Kraus, W. Tittel, N. Gisin, M. Nilsson, S. Kröll, J.I. Cirac, Quantum memory for nonstationary light fields based on controlled reversible inhomogeneous broadening, Physical Review A, 73 (2006) 020302.

[72] M. Zhong, M.P. Hedges, R.L. Ahlefeldt, J.G. Bartholomew, S.E. Beavan, S.M. Wittig, J.J. Longdell, M.J. Sellars, Optically addressable nuclear spins in a solid with a six-hour coherence time, Nature, 517 (2015) 177.

[73] C.W. Thiel, Energies of rare-earth ion states relative to host bands in optical materials from electron photoemission spectroscopy, ProQuest Dissertations Publishing, 2004.

[74] R.W. Equall, Photon echo studies of rare-earth-activated materials for optical memory and signal processing devices, Montana State University - Bozeman, College of Letters & Science, 2015.

[75] W.T. Carnall, G.L. Goodman, K. Rajnak, R.S. Rana, A systematic analysis of the spectra of the lanthanides doped into single crystal LaF_3 The Journal of Chemical Physics, 90 (1989) 3443-3457.

[76] T.H. Maiman, Stimulated Optical Radiation in Ruby, Nature, 187 (1960) 493-494.

[77] A. Hussain, W. Petersen, J. Staley, E. Hondebrink, W. Steenbergen, Quantitative blood oxygen saturation imaging using combined photoacoustics and acousto-optics, Opt. Lett., 41 (2016) 1720-1723.

[78] P.N.T. Wells, Absorption and dispersion of ultrasound in biological tissue, Ultrasound in Medicine & Biology, 1 (1975) 369-376.

[79] R. Paschotta, https://www.rp-photonics.com/optical_fiber_communications.html, RP Photonics Encyclopedia, 2008.

[80] S.R. Bare, M. Lilly, J. Chermak, R. Eggert, W. Halperin, S. Hannahs, S. Hayes, M. Hendrich, A. Hurd, M. Osofsky, C. Tway, Responding to the U.S. Research Community's Liquid Helium Crisis, https://www.aps.org/policy/reports/popa-reports/helium-crisis.cfm, APS Physics.

[81] C. Evans, Episodes from the history of the rare earth elements, Springer Science & Business Media, 2012.

[82] B.M. Walsh, Judd-Ofelt theory: principles and practices, in: Advances in spectroscopy for lasers and sensing, Springer, 2006, pp. 403-433.

[83] G. Liu, Electronic Energy Level Structure, in: G. Liu, B. Jacquier (Eds.) Spectroscopic properties of rare earths in optical materials, Springer Science & Business Media, 2006.

[84] B.R. Judd, Optical absorption intensities of rare-earth ions, Physical review, 127 (1962) 750.

[85] G.S. Ofelt, Intensities of Crystal Spectra of Rare-Earth Ions, The Journal of Chemical Physics, 37 (1962) 511-520.

[86] G.H. Dieke, Spectra and Energy Levels of Rare Earth Ions in Crystals, (1968).

[87] G.H. Dieke, H.M. Crosswhite, The Spectra of the Doubly and Triply Ionized Rare Earths, Appl. Opt., 2 (1963) 675-686.

[88] R.M. Macfarlane, R.M. Shelby, CHAPTER 3 - Coherent Transient and Holeburning Spectroscopy of Rare Earth Ions in Solids, in: A.A. Kaplyanskii, R.M. Macfarlane (Eds.) Modern Problems in Condensed Matter Sciences, Elsevier, 1987, pp. 51-184.

[89] R.M. Shelby, C.S. Yannoni, R.M. Macfarlane, Optically Detected Coherent Transients in Nuclear Hyperfine Levels, Physical Review Letters, 42 (1979) 746-746.

[90] R.M. Shelby, R.M. Macfarlane, Measurement of the pseudo-stark effect in Pr^{3+}:LaF_3 using population hole burning and optical free-induction decay, Optics Communications, 27 (1978) 399-402.

[91] R.M. Shelby, C.S. Yannoni, R.M. Macfarlane, Optically Detected Coherent Transients in Nuclear Hyperfine Levels, Physical Review Letters, 41 (1978) 1739-1742.

[92] J.J. Sakurai, J. Napolitano, Modern Quantum Mechanics, Second Edition ed., Addison-Wesley, 2011.

[93] Y.V. Orlovskii, R.J. Reeves, R.C. Powell, T.T. Basiev, K.K. Pukhov, Multiple-phonon nonradiative relaxation: Experimental rates in fluoride crystals doped with Er^{3+} and Nd^{3+} ions and a theoretical model, Physical Review B, 49 (1994) 3821-3830.

[94] F. Ermeneux, C. Goutaudier, R. Moncorgé, Y. Sun, R. Cone, E. Zannoni, E. Cavalli, M. Bettinelli, Multiphonon relaxation in YVO_4 single crystals, Physical Review B, 61 (2000) 3915.

[95] M.J. Weber, Multiphonon Relaxation of Rare-Earth Ions in Yttrium Orthoaluminate, Physical Review B, 8 (1973) 54-64.

[96] M.J. Weber, Radiative and Multiphonon Relaxation of Rare-Earth Ions in Y_2O_3, Physical Review, 171 (1968) 283-291.

[97] A. de Bettencourt-Dias, Lanthanides: Electronic Structure, in: Encyclopedia of Inorganic and Bioinorganic Chemistry.

[98] E.P. Wigner, Über die Operation der Zeitumkehr in der Quantenmechanik, in: The Collected Works of Eugene Paul Wigner, Springer, 1993, pp. 213-226.

[99] H.A. Kramers, Théorie générale de la rotation paramagnétique dans les cristaux, Proc. Acad. Amst, 33 (1930).

[100] T. Böttger, Y. Sun, C.W. Thiel, R.L. Cone, Spectroscopy and dynamics of Er^{3+}:Y_2SiO_5 at 1.5 μm, Physical Review B, 74 (2006) 075107.

[101] T. Böttger, C.W. Thiel, R.L. Cone, Y. Sun, Effects of magnetic field orientation on optical decoherence in $Er^{3+}Y_2SiO_5$, Physical Review B, 79 (2009) 115104.

[102] T. Böttger, C.W. Thiel, Y. Sun, R.L. Cone, Optical decoherence and spectral diffusion at 1.5 μm in Er^{3+}:Y_2SiO_5 versus magnetic field, temperature, and Er^{3+} concentration, Physical Review B, 73 (2006) 075101.

[103] Y. Sun, T. Böttger, C.W. Thiel, R.L. Cone, Magnetic g-tensors for the $^4I_{15/2}$ and $^4I_{13/2}$ states of Er^{3+}:Y_2SiO_5, Physical Review B, 77 (2008) 085124.

[104] C.W. Thiel, W.R. Babbitt, R.L. Cone, Optical decoherence studies of yttrium oxyorthosilicate YSO codoped with Er^{3+} and Eu^{3+} for optical signal processing and quantum information applications at 1.5 microns, Physical Review B, 85 (2012) 174302.

[105] L. Allen, J.H. Eberly, Optical resonance and two-level atoms, Courier Corporation, 1987.

[106] T. Böttger, C.W. Thiel, R.L. Cone, Y. Sun, A. Faraon, Optical spectroscopy and decoherence studies of Yb^{3+}:YAG at 968 nm, Physical Review B, 94 (2016).

[107] C.W. Thiel, R.M. Macfarlane, Y. Sun, T. Böttger, N. Sinclair, W. Tittel, R.L. Cone, Measuring and analyzing excitation-induced decoherence in rare-earth-doped optical materials, Laser Physics, 24 (2014) 106002.

[108] C.W. Thiel, N. Sinclair, W. Tittel, R.L. Cone, Optical decoherence studies of Tm^{3+}:$Y_3Ga_5O_{12}$, Physical Review B, 90 (2014) 214301.

[109] Y.C. Sun, Rare Earth Materiais in Optical Storage and Data Processing Applications, in: R. Hull, J. Parisi, R.M. Osgood, H. Warlimont, G. Liu, B. Jacquier (Eds.) Spectroscopic Properties of Rare Earths in Optical Materials, Springer Berlin Heidelberg, Berlin, Heidelberg, 2005, pp. 379-429.

[110] D.L. McAuslan, P.M. Ledingham, W.R. Naylor, S.E. Beavan, M.P. Hedges, M.J. Sellars, J.J. Longdell, Photon-echo quantum memories in inhomogeneously broadened two-level atoms, Physical Review A, 84 (2011) 022309.

[111] N.A. Kurnit, I.D. Abella, S.R. Hartmann, Observation of a Photon Echo, Physical Review Letters, 13 (1964) 567-568.

[112] L. Allen, J.H. Eberly, Optical resonance and two-level atoms - Ch 9, Courier Corporation, 1987, pp. 195-220.

[113] V.C. Vivoli, N. Sangouard, M. Afzelius, N. Gisin, High-bandwidth quantum memory protocol for storing single photons in rare-earth doped crystals, New Journal of Physics, 15 (2013) 095012.

[114] P. Jobez, N. Timoney, C. Laplane, J. Etesse, A. Ferrier, P. Goldner, N. Gisin, M. Afzelius, Towards highly multimode optical quantum memory for quantum repeaters, Physical Review A, 93 (2016) 032327.

[115] W.B. Mims, Electron Spin Echoes, in: S. Geschwind (Ed.) Electron Paramagnetic Resonance, Plenum Press, New York, 1972, pp. 263-349.

[116] E.L. Hahn, Spin Echoes, Physical Review, 80 (1950) 580-594.

[117] A. Abragam, B. Bleaney, Enhanced Nuclear Magnetism: Some Novel Features and Prospective Experiments, Proceedings of the Royal Society of London. Series A, Mathematical and Physical Sciences, 387 (1983) 221-256.

[118] T. Lu, X. Miao, H. Metcalf, Bloch theorem on the Bloch sphere, Physical Review A, 71 (2005) 061405.

[119] L. Allen, J.H. Eberly, Optical resonance and two-level atoms - Bloch Equations and Bloch Sphere, Courier Corporation, 1987, pp. 28-77.

[120] G.S. He, Nonlinear optics and photonics, OUP Oxford, 2014.

[121] H.C. Torrey, Transient Nutations in Nuclear Magnetic Resonance, Physical Review, 76 (1949) 1059-1068.

[122] M. Tinkham, Group theory and quantum mechanics, Courier Corporation, 2003.

[123] G.F. Koster, J.O. Dimmock, R.G. Wheeler, H. Statz, Properties of the thirty-two point groups, MIT press, 1963.

[124] Montana Instruments Website, https://www.montanainstruments.com/, Montana Instruments, 2021.

[125] Quantum Information Science and Engineering Network, https://qisenet.uchicago.edu/, University of Chicago, 2021.

[126] L. Veissier, C.W. Thiel, T. Lutz, P.E. Barclay, W. Tittel, R.L. Cone, Quadratic Zeeman effect and spin-lattice relaxation of Tm^{3+}:YAG at high magnetic fields, Physical Review B, 94 (2016) 205133.

[127] K. Kutluer, M. Mazzera, H. de Riedmatten, Solid-State Source of Nonclassical Photon Pairs with Embedded Multimode Quantum Memory, Physical Review Letters, 118 (2017) 210502.

[128] M. Sabooni, Q. Li, S. Kröll, L. Rippe, Efficient Quantum Memory Using a Weakly Absorbing Sample, Physical Review Letters, 110 (2013) 133604.

[129] N. Lauk, N. Sinclair, S. Barzanjeh, J.P. Covey, M. Saffman, M. Spiropulu, C. Simon, Perspectives on quantum transduction, Quantum Science and Technology, 5 (2020) 020501.

[130] J.G. Bartholomew, J. Rochman, T. Xie, J.M. Kindem, A. Ruskuc, I. Craiciu, M. Lei, A. Faraon, On-chip coherent microwave-to-optical transduction mediated by ytterbium in YVO_4, Nature Communications, 11 (2020) 3266.

[131] J.R. Everts, M.C. Berrington, R.L. Ahlefeldt, J.J. Longdell, Microwave to optical photon conversion via fully concentrated rare-earth-ion crystals, Physical Review A, 99 (2019) 063830.

[132] S. Welinski, P.J.T. Woodburn, N. Lauk, R.L. Cone, C. Simon, P. Goldner, C.W. Thiel, Electron Spin Coherence in Optically Excited States of Rare-Earth Ions for Microwave to Optical Quantum Transducers, Physical Review Letters, 122 (2019) 247401.

[133] A. Compaan, L.Q. Lambert, I.D. Abella, Photon-Echo Dependence on Intensity, Physical review letters, 20 (1968) 1089-1091.

[134] R.L. Cone, C.W. Thiel, Y. Sun, T. Böttger, R.M. Macfarlane, Rare-earth-doped materials with application to optical signal processing, quantum information science, and medical imaging technology, SPIE, 2012.

[135] N. Sinclair, D. Oblak, E. Saglamyurek, R.L. Cone, C.W. Thiel, W. Tittel, Optical coherence and energy-level properties of a Tm^{3+}-doped $LiNbO_3$ waveguide at subkelvin temperatures, Physical Review B, 103 (2021) 134105.

[136] N. Sinclair, D. Oblak, C.W. Thiel, R.L. Cone, W. Tittel, Properties of a Rare-Earth-Ion-Doped Waveguide at Sub-Kelvin Temperatures for Quantum Signal Processing, Physical Review Letters, 118 (2017) 100504.

[137] C.W. Thiel, N. Sinclair, W. Tittel, R.L. Cone, Tm^{3+}:YGG Materials for Spectrally Multiplexed Quantum Memories, Physical Review Letters, 113 (2014) 160501.

[138] Y.C. Sun, Rare Earth Materials in Optical Storage and Data Processing Applications in: G. Liu, B. Jacquier (Eds.) Spectroscopic Properties of Rare Earths in Optical Materials, Springer, 2005, pp. 410.

[139] L. Allen, J.H. Eberly, Optical resonance and two-level atoms - echo pulse area, Courier Corporation, 1987, pp. 214-219.

[140] A. Franzen, Component Library, https://www.gwoptics.org/ComponentLibrary/.

[141] W.B. Mims, Phase Memory in Electron Spin Echoes, Lattice Relaxation Effects in $CaWO_4$: Er, Ce, Mn, Physical Review, 168 (1968) 370-389.

[142] W.B. Mims, Envelope Modulation in Spin-Echo Experiments, Physical Review B, 5 (1972) 2409-2419.

[143] W.B. Mims, Amplitudes of Superhyperfine Frequencies Displayed in the Electron-Spin-Echo Envelope, Physical Review B, 6 (1972) 3543-3545.

[144] N. Bloembergen, On the interaction of nuclear spins in a crystalline lattice, Physica, 15 (1949) 386-426.

[145] R.L. Mössbauer, General Aspects of Nuclear Hyperfine Interactions in Salts of the Rare Earths, Reviews of Modern Physics, 36 (1964) 362-371.

[146] Y. Sun, G.M. Wang, R.L. Cone, R.W. Equall, M.J.M. Leask, Symmetry considerations regarding light propagation and light polarization for coherent interactions with ions in crystals, Physical Review B, 62 (2000) 15443-15451.

[147] J. Stark, Observation of the Separation of Spectral Lines by an Electric Field, Nature, 92 (1913) 401-401.

[148] K. Heshami, D.G. England, P.C. Humphreys, P.J. Bustard, V.M. Acosta, J. Nunn, B.J. Sussman, Quantum memories: emerging applications and recent advances, Journal of Modern Optics, 63 (2016) 2005-2028.

[149] R.W. Equall, R.L. Cone, R.M. Macfarlane, Homogeneous broadening and hyperfine structure of optical transitions in Pr^{3+}:Y_2SiO_5, Physical Review B, 52 (1995) 3963-3969.

[150] C.W. Thiel, Crystal Damage Plastic Deformation Measurements, 2020.

[151] P. Zeeman, The Effect of Magnetisation on the Nature of Light Emitted by a Substance, Nature, 55 (1897) 347-347.

[152] Cryogenic Sample Mounting Guide, https://www.montanainstruments.com/help/Sample-Mounting-Guide/, Montana Instruments, 2020.

[153] Global Summary Estimates 2016: Deaths by Cause, Age, Sex, by Country and by Region, https://www.who.int/healthinfo/global_burden_disease/estimates/en/, World Health Organization, Geneva, 2016.

[154] S. Prahl, Optical absorption of hemoglobin, in: http://omlc.ogi.edu/spectra/hemoglobin, Oregon Medical Laser Center, 1999.

[155] Y. Haas, G. Stein, Radiative and nonradiative pathways in solutions. Excited states of the europium(III) ion, The Journal of Physical Chemistry, 76 (1972) 1093-1104.

[156] B. Henderson, G.F. Imbusch, Optical spectroscopy of inorganic solids, Oxford University Press, 2006.

[157] F. Auzel, A fundamental self-generated quenching center for lanthanide-doped high-purity solids, Journal of Luminescence, 100 (2002) 125-130.

[158] C. Kittel, Introduction to Solid State Physics, 8 ed., Jon Wiley & Sons, 2005.

[159] L. Isaenko, A. Yelisseyev, A. Tkachuk, S. Ivanova, New Monocrystals with Low Phonon Energy for Mid-IR Lasers, in: M. Ebrahimzadeh, I.T. Sorokina (Eds.) Mid-infrared coherent sources and applications, Dordrecht : Springer Verlag, Dordrecht, 2008.

[160] W.T. Carnall, P.R. Fields, J. Morrison, R. Sarup, Absorption Spectrum of Tm^{3+}:LaF_3, The Journal of Chemical Physics, 52 (1970) 4054-4059.

[161] M.G. Beghi, C.E. Bottani, V. Russo, Debye temperature of erbium-doped yttrium aluminum garnet from luminescence and Brillouin scattering data, Journal of Applied Physics, 87 (2000) 1769-1774.

[162] R.L. Aggarwal, D.J. Ripin, J.R. Ochoa, T.Y. Fan, Measurement of thermo-optic properties of $Y_3Al_5O_{12}$, $Lu_3Al_5O_{12}$, $YAlO_3$, $LiYF_4$, $LiLuF_4$, BaY_2F_8, $KGd(WO_4)_2$, and $KY(WO_4)_2$ laser crystals in the 80–300K temperature range, Journal of Applied Physics, 98 (2005).

[163] Z. Sun, M. Li, Y. Zhou, Thermal properties of single-phase Y_2SiO_5, Journal of the European Ceramic Society, 29 (2009) 551-557.

[164] M.J. Weber, Handbook of Optical Materials, CRC Press, New York, 2002.

[165] B. Di Bartolo, B.E. Bowlby, Spectroscopic properties of trivalent praseodymium in barium yttrium fluoride, Journal of Luminescence, 102-103 (2003) 481-486.

[166] D.K. Sardar, R.M. Yow, Inter-Stark Energy Levels and Effects of Temperature on Sharp Emission Lines of Nd^{3+} in $LiYF_4$, physica status solidi (a), 173 (1999) 521-534.

[167] R. Laiho, M. Lakkisto, T. Levola, Brillouin scattering investigation of the elastic properties of LaF_3, CeF_3,PrF_3, and NdF_3, Philosophical Magazine A, 47 (2006) 235-244.

[168] S. Hariyani, A.C. Duke, T. Krauskopf, W.G. Zeier, J. Brgoch, The effect of rare-earth substitution on the Debye temperature of inorganic phosphors, Applied physics letters, 116 (2020) 51901.

[169] K. Rademaker, E. Heumann, G. Huber, S.A. Payne, W.F. Krupke, L.I. Isaenko, A. Burger, Laser activity at 1.18, 1.07, and 0.97 μm in the low-phonon-energy hosts KPb_2Br_5 and $RbPb_2Br_5$ doped with Nd^{3+}, Opt. Lett., 30 (2005) 729-731.

[170] N.M. Strickland, G.D. Jones, Site-selective spectroscopy of Tm^{3+} centers in CaF_2, Physical Review B, 56 (1997) 10916-10929.

[171] S. Wang, Y. Ruan, T. Tsuboi, S. Zhang, Y. Wang, Z. Wu, H. Tong, Studies on the growth and optical characterization of Tm3+-doped BaY2F8 single crystals, Crystal Research and Technology, 47 (2012) 928-938.

[172] M. Dulick, G.E. Faulkner, N.J. Cockroft, D.C. Nguyen, Spectroscopy and dynamics of upconversion in Tm^{3+}: $YLiF_4$, Journal of Luminescence, 48-49 (1991) 517-521.

[173] A. Zalkin, D.H. Templeton, T.E. Hopkins, The Atomic Parameters in the Lanthanum Trifluoride Structure, Inorganic Chemistry, 5 (1966) 1466-1468.

[174] M. Ebrahimzadeh, I.T. Sorokina, Mid-infrared coherent sources and applications, Dordrecht : Springer Verlag, Dordrecht, 2008.

[175] L. Allen, J.H. Eberly, Optical resonance and two-level atoms - Ch 6, Courier Corporation, 1987, pp. 130-151.

[176] A.B. Matsko, I. Novikova, M.O. Scully, G.R. Welch, Radiation Trapping in Coherent Media, Physical Review Letters, 87 (2001) 133601.

[177] D.S. Sumida, T.Y. Fan, Effect of radiation trapping on fluorescence lifetime and emission cross section measurements in solid-state laser media, Opt. Lett., 19 (1994) 1343-1345.

[178] R. Moncorgé, M. Velazquez, P. Goldner, O. Guillot-Noël, H.L. Xu, M. Nilsson, S. Kröll, E. Cavalli, M. Bettinelli, Linear and non-linear spectroscopy of Ho^{3+}-doped YVO_4 and $LuVO_4$, Journal of Physics: Condensed Matter, 17 (2005) 6751-6762.

[179] R.M. Macfarlane, A.Z. Genack, S. Kano, R.G. Brewer, Optical FID measurement of low temperature dephasing in Pr^{3+}:LaF_3, Journal of Luminescence, 18-19 (1979) 933-936.

[180] A.Z. Genack, R.M. Macfarlane, R.G. Brewer, Optical Free-Induction Decay in LaF_3:Pr^{3+}, Physical Review Letters, 37 (1976) 1078-1080.

[181] R.M. Macfarlane, R.M. Shelby, Optical free induction decay of the 4G52 ↔ 6H52 transition of LaF3:Sm3+, Physics Letters A, 116 (1986) 299-301.

[182] R.M. Macfarlane, M. Zhu, Observation of coherent transients by use of current switching of a semiconductor diode laser, Opt. Lett., 22 (1997) 248-250.

[183] J. Hong, L. Zhang, M. Xu, Y. Hang, Optical characterization of Tm^{3+} in LaF_3 single crystal, Infrared Physics & Technology, 82 (2017) 50-55.

[184] D.E. McCumber, Theory of Vibrational Structure in Optical Spectra of Impurities in Solids. I. Singlets, Journal of Mathematical Physics, 5 (1964) 221-230.

[185] D.E. McCumber, Theory of Vibrational Structure in Optical Spectra of Impurities in Solids. II. Multiplets, Journal of Mathematical Physics, 5 (1964) 508-521.

[186] D.E. McCumber, M.D. Sturge, Linewidth and Temperature Shift of the R Lines in Ruby, Journal of Applied Physics, 34 (1963) 1682-1684.

[187] G.F. Imbusch, W.M. Yen, A.L. Schawlow, D.E. McCumber, M.D. Sturge, Temperature Dependence of the Width and Position of the E2→A24 Fluorescence Lines of Cr^{3+} and V^{2+} in MgO, Physical Review, 133 (1964) A1029-A1034.

[188] B.M. Walsh, G.W. Grew, N.P. Barnes, Energy levels and intensity parameters of Ho^{3+} ions in $Y_3Al_5O_{12}$ and $Lu_3Al_5O_{12}$, Journal of Physics and Chemistry of Solids, 67 (2006) 1567-1582.

[189] K.J. Bachmann, F.S.L. Hsu, F.A. Thiel, H.M. Kasper, Debye temperature and standard entropies and enthalpies of compound semiconductors of the type I-III-VI2, Journal of Electronic Materials, 6 (1977) 431-448.

[190] V. Kumar, V. Jha, A.K. Shrivastava, Debye temperature and melting point of II-VI and III-V semiconductors, Crystal Research and Technology, 45 (2010) 920-924.

[191] A.A. Bol, R. van Beek, A. Meijerink, On the Incorporation of Trivalent Rare Earth Ions in II−VI Semiconductor Nanocrystals, Chemistry of Materials, 14 (2002) 1121-1126.

[192] T. Gregorkiewicz, J.M. Langer, Lasing in Rare-Earth-Doped Semiconductors: Hopes and Facts, MRS Bulletin, 24 (1999) 27-32.

[193] E.E. Brown, A.G. Bluiett, U. Hommerich, A. Simmons, S.B. Trivedi, W.L. Boncher, M.P. Hehlen, A. Lindsey, M. Zhuravleva, Optical spectroscopy of rare-earth doped ternary lead based halides, Opt. Mater. Express, 7 (2017) 4415-4426.

[194] S. Mel'nikova, L. Isaenko, V. Pashkov, I. Pevnev, Phase Transition in a KPb_2Br_5 Crystal, Physics of the Solid State, 47 (2005) 332-336.

[195] A. Abragam, B. Bleaney, Electron Paramagnetic Resonance of Transition Ions - Spontaneous Emission, Dover Publications, Inc., New York, 1986.

[196] L. Allen, J.H. Eberly, Optical resonance and two-level atoms - Spontaneous Emission, Courier Corporation, 1987.

[197] J.H. Van Vleck, The theory of electric and magnetic susceptibilities, Oxford, The Clarendon press, Oxford, 1932.

[198] L.I. Schiff, H. Snyder, Theory of the Quadratic Zeeman Effect, Physical Review, 55 (1939) 59-63.

[199] A. Edmonds, THE THEORY OF THE QUADRATIC ZEEMAN EFFECT, Journal de Physique Colloques, 31 (1970) C4-71-C74-74.

[200] A. Abragam, B. Bleaney, Electron Paramagnetic Resonance of Transition Ions - Spin Lattice Relaxation, Dover Publications, Inc., New York, 1986.

[201] R. Orbach, B. Bleaney, Spin-lattice relaxation in rare-earth salts: field dependence of the two-phonon process, Proceedings of the Royal Society of London. Series A. Mathematical and Physical Sciences, 264 (1961) 485-495.

[202] R. Orbach, B. Bleaney, Spin-lattice relaxation in rare-earth salts, Proceedings of the Royal Society of London. Series A. Mathematical and Physical Sciences, 264 (1961) 458-484.

[203] A. Abragam, B. Bleaney, Electron Paramagnetic Resonance of Transition Ions, Dover Publications, Inc., New York, 1986.

[204] A. Bengtsson, UOT Performance Simulations on $^3H_4$ to $^3F_3(1)$ transition in Tm^{3+}:LaF_3, Personal Communication, 2020.

[205] K. Nitsch, V. Hamplová, M. Nikl, K. Polák, M. Rodová, Lead bromide and ternary alkali lead bromide single crystals — growth and emission properties, Chemical Physics Letters, 258 (1996) 518-522.

[206] C. Cascales, J. Fernandez, R. Balda, Investigation of site-selective symmetries of Eu^{3+} ions in KPb_2Cl_5 by using optical spectroscopy, Opt Express, 13 (2005) 2141-2152.

[207] R. Faoro, M. Tonelli, L.I. Isaenko, A.Y. Tarasova, V.M. Pashkov, Spectroscopy in the 1.4 and 1.8-μm wavelength regions of KPb_2Cl_5 single crystals doped with trivalent Thulium, Journal of Luminescence, 180 (2016) 140-145.

[208] A. Ferrier, M. Velázquez, J.-L. Doualan, R. Moncorgé, Midinfrared luminescence properties and laser potentials of Pr^{3+}-doped KPb_2Cl_5 and $CsCdBr_3$, Journal of Applied Physics, 104 (2008) 123513-123513-123514.

[209] A. Gabriel, A.D. Pelton, Phase diagram measurements and thermodynamic analysis of the $PbCl_2$–NaCl, $PbCl_2$–KCl, and $PbCl_2$–KCl–NaCl systems, Canadian journal of chemistry, 63 (1985) 3276-3282.

[210] L.I. Isaenko, I.N. Ogorodnikov, V.A. Pustovarov, A.Y. Tarasova, V.M. Pashkov, Optical and Photoelectron Spectroscopy Studies of KPb_2Cl_5 and $RbPb_2Cl_5$ Laser Crystals, Optical Materials, 35 (2013) 620-625.

[211] A.M. Tkachuk, S.E. Ivanova, A.A. Mirzaeva, L.I. Isaenko, Optical spectra and emission characteristics of terbium-doped potassium–lead double chloride crystals (KPb_2Cl_5:Tb^{3+}), Optics and Spectroscopy, 122 (2017) 735-748.

[212] M. Voda, M. Al-Saleh, G. Lobera, R. Balda, J. Fernández, Crystal growth of rare-earth-doped ternary potassium lead chloride single crystals by the Bridgman method, Optical Materials, 26 (2004) 359-363.

[213] P.C.d. Sousa Filho, J.F. Lima, O.A. Serra, From Lighting to Photoprotection: Fundamentals and Applications of Rare Earth Materials, Journal of the Brazilian Chemical Society, 26 (2015) 2471-2495.

[214] K. Zhang, A.N. Kleit, A. Nieto, An economics strategy for criticality – Application to rare earth element Yttrium in new lighting technology and its sustainable availability, Renewable and Sustainable Energy Reviews, 77 (2017) 899-915.

[215] T. Böttger, G.J. Pryde, C.W. Thiel, R.L. Cone, Laser frequency stabilization at 1.5 microns using ultranarrow inhomogeneous absorption profiles in Er^{3+}:$LiYF_4$, Journal of Luminescence, 127 (2007) 83-88.

[216] T. Kornher, D.-W. Xiao, K. Xia, F. Sardi, N. Zhao, R. Kolesov, J. Wrachtrup, Sensing Individual Nuclear Spins with a Single Rare-Earth Electron Spin, Physical Review Letters, 124 (2020) 170402.

[217] J.M. Boss, K.S. Cujia, J. Zopes, C.L. Degen, Quantum sensing with arbitrary frequency resolution, Science, 356 (2017) 837-840.

[218] E. Lee-Wong, J. Ding, X. Wang, C. Liu, N.J. McLaughlin, H. Wang, M. Wu, C.R. Du, Quantum Sensing of Spin Fluctuations of Magnetic Insulator Films with Perpendicular Anisotropy, Physical Review Applied, 15 (2021) 034031.

[219] S. Welinski, A. Tiranov, M. Businger, A. Ferrier, M. Afzelius, P. Goldner, Coherence Time Extension by Large-Scale Optical Spin Polarization in a Rare-Earth Doped Crystal, Physical Review X, 10 (2020) 031060.

[220] A. Kinos, D. Hunger, R. Kolesov, K. Mølmer, H. de Riedmatten, P. Goldner, A. Tallaire, L. Morvan, P. Berger, S. Welinski, Roadmap for Rare-earth Quantum Computing, arXiv preprint arXiv:2103.15743, (2021).

[221] R.L. Ahlefeldt, M.J. Pearce, M.R. Hush, M.J. Sellars, Quantum processing with ensembles of rare-earth ions in a stoichiometric crystal, Physical Review A, 101 (2020) 012309.

[222] J.H. Davidson, P. Lefebvre, J. Zhang, D. Oblak, W. Tittel, Improved light-matter interaction for storage of quantum states of light in a thulium-doped crystal cavity, Physical Review A, 101 (2020) 042333.

[223] Y.G. Choi, K.H. Kim, B.J. Park, J. Heo, 1.6 μm emission from Pr^{3+}:($^3F_3$,$^3F_4$)→$^3H_4$ transition in Pr^{3+}- and Pr^{3+}/Er^{3+}-doped selenide glasses, Applied Physics Letters, 78 (2001) 1249-1251.

[224] E.A. Wood, Crystals and Light: an introduction to optical crystallography, Second Revised Edition ed., Dover Publications, Inc, New York, 1977.

[225] P. McNicholl, H.J. Metcalf, Synchronous cavity mode and feedback wavelength scanning in dye laser oscillators with gratings, Appl. Opt., 24 (1985) 2757-2761.

[226] A.S. Arnold, J.S. Wilson, M.G. Boshier, A simple extended-cavity diode laser, Review of Scientific Instruments, 69 (1998) 1236-1239.

[227] C.J. Hawthorn, K.P. Weber, R.E. Scholten, Littrow configuration tunable external cavity diode laser with fixed direction output beam, Review of Scientific Instruments, 72 (2001) 4477-4479.

[228] J.J. Maki, N.S. Campbell, C.M. Grande, R.P. Knorpp, D.H. McIntyre, Stabilized diode-laser system with grating feedback anf frequency-offset locking, Optics Communications, 102 (1993) 251-256.

[229] P.W. Bridgman, Certain Physical Properties of Single Crystals of Tungsten, Antimony, Bismuth, Tellurium, Cadmium, Zinc, and Tin, Proceedings of the American Academy of Arts and Sciences, 60 (1925) 305-383.

[230] D. Nicoară, I. Nicoară, An improved Bridgman-Stockbarger crystal-growth system, Materials Science and Engineering: A, 102 (1988) L1-L4.

[231] R.M. Sternheimer, Shielding and Antishielding Effects for Various Ions and Atomic Systems, Physical Review, 146 (1966) 140-160.

[232] R.L. Ahlefeldt, M.R. Hush, M.J. Sellars, Ultranarrow Optical Inhomogeneous Linewidth in a Stoichiometric Rare-Earth Crystal, Physical Review Letters, 117 (2016) 250504.

[233] C.W. Thiel, Echo Data Analysis Notes, Personal Communication, 2008.

[234] L.Q. Lambert, Effects of Superhyperfine Interactions on Photon-Echo Behavior in Dilute Ruby, Physical Review B, 7 (1973) 1834-1846.

[235] A. Dréau, A. Tchebotareva, A.E. Mahdaoui, C. Bonato, R. Hanson, Quantum Frequency Conversion of Single Photons from a Nitrogen-Vacancy Center in Diamond to Telecommunication Wavelengths, Physical Review Applied, 9 (2018) 064031.

[236] Z. Liu, B. Qu, J.L. Doualan, B. Xu, H. Xu, Z. Cai, A. Braud, P. Camy, R. Moncorgé, Temperature effects on the main absorption and emission lines of the Pr^{3+}:$LiYF_4$ laser crystal, Journal of the Optical Society of America B, 32 (2015).

[237] E.P.J. Merkx, M.P. Plokker, E. van der Kolk, The potential of transparent sputtered NaI:Tm^{2+}, $CaBr_2$:Tm^{2+}, and CaI_2:Tm^{2+} thin films as luminescent solar concentrators, Solar Energy Materials and Solar Cells, 223 (2021) 110944.

[238] M.P. Plokker, E. van der Kolk, Temperature dependent relaxation dynamics of luminescent NaX:Tm^{2+} (X=Cl, Br, I), Journal of Luminescence, 216 (2019) 116694.

[239] G. Bosco, E. van der Kolk, Towards Tm^{2+} in Sialon Thin Films Grown by Sputtering Using the Gradient Deposition, ECS Transactions, 97 (2020) 17-26.

[240] J. Zhang, H. Riesen, Controlled Generation of Tm^{2+} Ions in Nanocrystalline BaFCl:Tm^{3+} by X-ray Irradiation, The Journal of Physical Chemistry A, 121 (2017) 803-809.

[241] C.W. Thiel, Quantum Memories: Shelving, Personal Communication, 2019.

[242] Yttrium Orthoaluminate in: Laser Materials, Scientific Materials, 2021.

[243] R. Diehl, G. Brandt, Crystal structure refinement of $YAlO_3$, a promising laser material, Materials Research Bulletin, 10 (1975) 85-90.

[244] C.W. Thiel, Double-Pumped Fluorescence, Personal Communication, 2019.

[245] R.C. Stoneman, L. Esterowitz, Efficient 1.94-µm Tm:YALO laser, IEEE Journal of Selected Topics in Quantum Electronics, 1 (1995) 78-81.

[246] T. Niedźwiedzki, J. Komar, M. Głowacki, M. Berkowski, W. Ryba-Romanowski, Luminescence and energy transfer phenomena in Gd^{3+}:$(Al,Ga)_5O_{12}$ crystals single doped with thulium and co-doped with thulium and holmium, Journal of Luminescence, 192 (2017) 77-84.

[247] C.A. Morrison, R.P. Leavitt, Spectroscopic properties of triply ionized lanthanides in transparent host crystals, in: Handbook on the Physics and Chemistry of Rare Earths, Elsevier, 1982, pp. 461-692.

[248] V. Sudesh, E.M. Goldys, Spectroscopic properties of thulium-doped crystalline materials including a novel host, $La_2Be_2O_5$: a comparative study, Journal of the Optical Society of America B, 17 (2000) 1068-1076.

[249] O.A. Buryy, D.Y. Sugak, S.B. Ubizskii, I.I. Izhnin, M.M. Vakiv, I.M. Solskii, The comparative analysis and optimization of the free-running Tm^{3+}:YAP and Tm^{3+}:YAG microlasers, Applied Physics B, 88 (2007) 433.

APPENDIX

SIMULATIONS OF SHB FILTERING FOR UOT

These simulations and details were graciously provided by Alexander Bengtsson [204].

Modeling the Tm^{3+}:LaF_3 Energy Level System

The energy level structure Tm^{3+}:LaF_3 is modeled with the ground state split into two nuclear levels g_1 and g_2 split in a magnetic field, and an excited state *e* and a bottleneck level *b*, as shown in fig. 72. The excited state represents $^3F_3$ and has a lifetime T_e =1 μs in the simulation. From this excited state, all ions decay to the bottleneck level, which has a lifetime T_b =10 ms and approximates the behavior of $^3H_4$ and $^3F_4$ and their respective lifetimes of 3.4 ms and 17.8 ms. The spin crossing likelihood was set by the branching ratio from the bottleneck state to either the ground state, which has the primary effect of changing the burn-in time. A ratio of 1% was used. The upper level of the ground state has a lifetime of T_g =1000 s, which is comparable to measured values for a 250 mT field (**B**⊥c). The splitting of the two ground states δg was set to 10 MHz in the simulation, which corresponds to the holeburning measurements for a 250 mT field (**B**⊥c). Because of the size of the ground state splitting, the off-resonance excitation rate should be low compared with the resonant rate and is therefore neglected. The linewidth of the optical transitions Γ_h is set to 140 kHz. In the inhomogeneously broadened absorption of the simulated sample, there are two distinct classes of ions, where the laser is resonant with either the $g_{1\text{-}e}$ or $g_{2\text{-}e}$ transitions, which will be called class 1 and class 2, respectively. Fig. 72 shows the case for class 1 ions. The number of ions belonging to each class is equal.

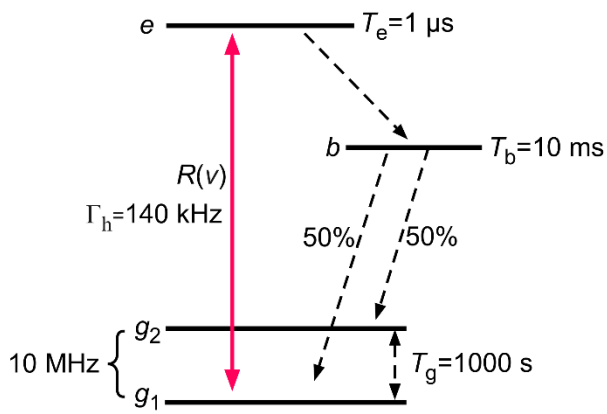

Figure 72: Level structure used in the filtering model.

The rate equations for the 4-level system depicted in fig. 4 are:

$$\begin{cases} \frac{dn_{g1}}{dt} = R(v)\left(n_e - n_{g1}\right) + \frac{n_b}{2T_b} + \frac{n_{g2} - n_{g1}}{T_g} \\ \frac{dn_{g2}}{dt} = \frac{n_b}{2T_b} - \frac{n_{g2} - n_{g1}}{T_g} \\ \frac{dn_b}{dt} = \frac{n_e}{T_e} - \frac{n_b}{T_b} \\ \frac{dn_e}{dt} = R_1(v)\left(n_{g1} - n_e\right) - \frac{n_e}{T_e} \end{cases} \tag{20}$$

In eq. (20), the populations of states g_1, g_2, b and e are denoted as n_{g1}, n_{g2}, n_b and n_e, respectively. The sum of all populations is 1 such that each population n_i is constrained between 0 and 1.

<u>Population Transfer Efficiency Expression</u>

Rectangular spectral holes are the most ideal filter shape for UOT, and hyperbolic secant pulses are the most efficient for burning these shapes. For this approach, the transfer efficiencies R_i can be described in terms of a convolution of the absorption spectrum, a Lorentzian with homogeneous linewidth Γ_h, with the spectrum of an infinitely long hyperbolic secant pulse:

$$R(\nu) = P(\nu) * \sigma(\nu) \tag{21}$$

In eq. (21), the normalized laser excitation spectrum multiplied by the peak single-ion excitation rate R_0 as a function of frequency ν is:

$$P(\nu) = R_0 \frac{\operatorname{sech}\left[\frac{\pi}{2}\left(\frac{\nu_0 - \nu}{\beta} + \mu\right)\right] \operatorname{sech}\left[\frac{\pi}{2}\left(\frac{\nu_0 - \nu}{\beta} - \mu\right)\right]}{\operatorname{sech}^2\left(\frac{\pi\mu}{2}\right)} \tag{22}$$

In eq. (22), the center frequency of the burn is denoted by ν_0, the parameter μ determines the frequency rolloff of the burn pulse spectrum, both β and R_0 are related to the burn-width and peak burn intensity, respectively, and are parameters that are freely set in the simulation to optimize the filter profile, and finally the filter bandwidth is tuned by changing β. This simulation uses μ =10, $R_0 = 0.25\ s^{-1}$, and $\beta = 5*10^4$ to achieve a ~2 MHz filter bandwidth.

<u>Absorption profile</u>

The system of eq. (20) is solved in steady-state for each frequency giving population differences $\Delta n_1(\nu)$ and $\Delta n_2(\nu+\delta g)$, corresponding to the population difference between level e and g_1 and level e and g_2, respectively. The absorption profile is finally obtained by taking the convolution with the atomic response and multiplying with the peak absorption coefficient α_0:

$$\alpha(\nu) = \alpha_0[\Delta n_1(\nu) + \Delta n_2(\nu + \delta g)]\sigma(\nu) \tag{23}$$

In the case of an optically thick medium, the crystal is divided into several slices. The absorption profile for the first slice is calculated, and thereafter used to modify the laser input in eq. (23) for the second slice using Beer-Lambert's law. The procedure is then repeated across the crystal length.